COLLECTED PAPERS

ON

NANO/ATOM PHOTONICS

Volume 15

August 1999 – July 2000

Professor

Motoichi OHTSU

TOKYO INSTITUTE OF TECHNOLOGY

Interdisciplinary Graduate School of Science and Engineering

4259 Nagatsuta, Midori-ku, Yokohama, Kanagawa 226-8502, JAPAN

TEL : +81 – 45 – 924 – 5455

FAX : +81 – 45 – 924 – 5599

E-mail : ohtsu @ ae. titech. ac. jp

PREFACE

In order to realize the ultimate status of light and matter, M. Ohtsu tries to control the spatial properties of light. The approach he has used is through the research of near-field optics and its application to nano-structure fabrication and atom manipulation. This will open up a new era of nano/atom photonics. It should be pointed out that the nano/atom photonics is closely related to quantum optics, atom optics, high density optical storage, nano-structure fabrication technology, and so on (see the figure on the next page). And for this relationship of near-field optics with a variety of fields, nano/atom photonics exhibits rapid progress. Further research will be done to realize novel nanometric materials and devices.

A "NEAR FIELD PHOTONICS" research group, which is executed in Kanagawa Academy of Science and Technology(KAST) and directed by Ohtsu, has started from April,1998 in order to transfer the results of the research of the previous "PHOTON CONTROL" project to industry so as to produce commercial near field optical spectrometers, optical memories, fiber probes, and so on(*). From October, 1998, a "LOCALIZED PHOTON" project, which is supported as ERATO (Exploratory Research for Advanced Technology) by Japan Science and Technology Corporation and directed by Ohtsu, has started for exploring a novel theory of optical near-field, for studying nano-photonics and atom-photonics.(+) Results of the recent research carried out by Ohtsu are reviewed in this issue of the COLLECTED PAPERS.

August 2000

Motoichi OHTSU

大津　元一

(*) Address: Near field photonics group,
Kanagawa Academy of Science and Technology
KSP East, Rm. 408, 3-2-1 Sakado, Takatsu-ku,
Kawasaki-shi, Kanagawa 213-0012, JAPAN
Phone: +81-44-819-2075
Fax: +81-44-819-2072

〒213-0012　神奈川県川崎市高津区坂戸３－２－１
ＫＳＰ東棟４０８号室
（財）神奈川科学技術アカデミー，光科学重点研究室
第２研究グループ

(+) Address: Localized photon project,
Japan Science and Technology
4th-floor, Tenko Building #17
687-1 Tsuruma, Machida-shi, Tokyo 194-0004
Phone: +81-427-88-6030
Fax: +81-427-88-6031
〒194-0004　東京都町田市鶴間 687-1
第１７天幸ビル４階
科学技術振興事業団　「局在フォトン」プロジェクト

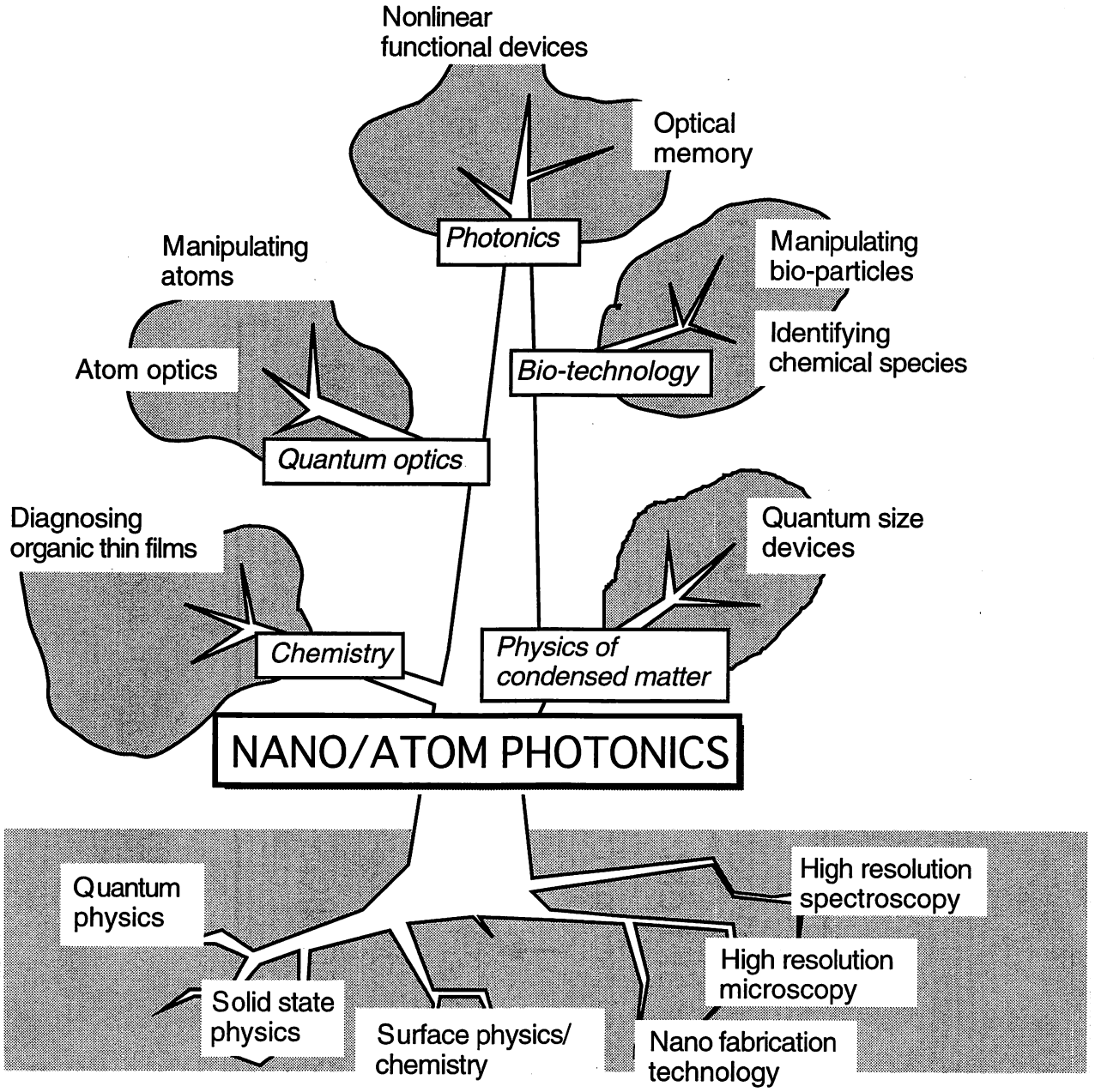

Nano/atom photonic tree with its roots and leaves covering a wide range of fields

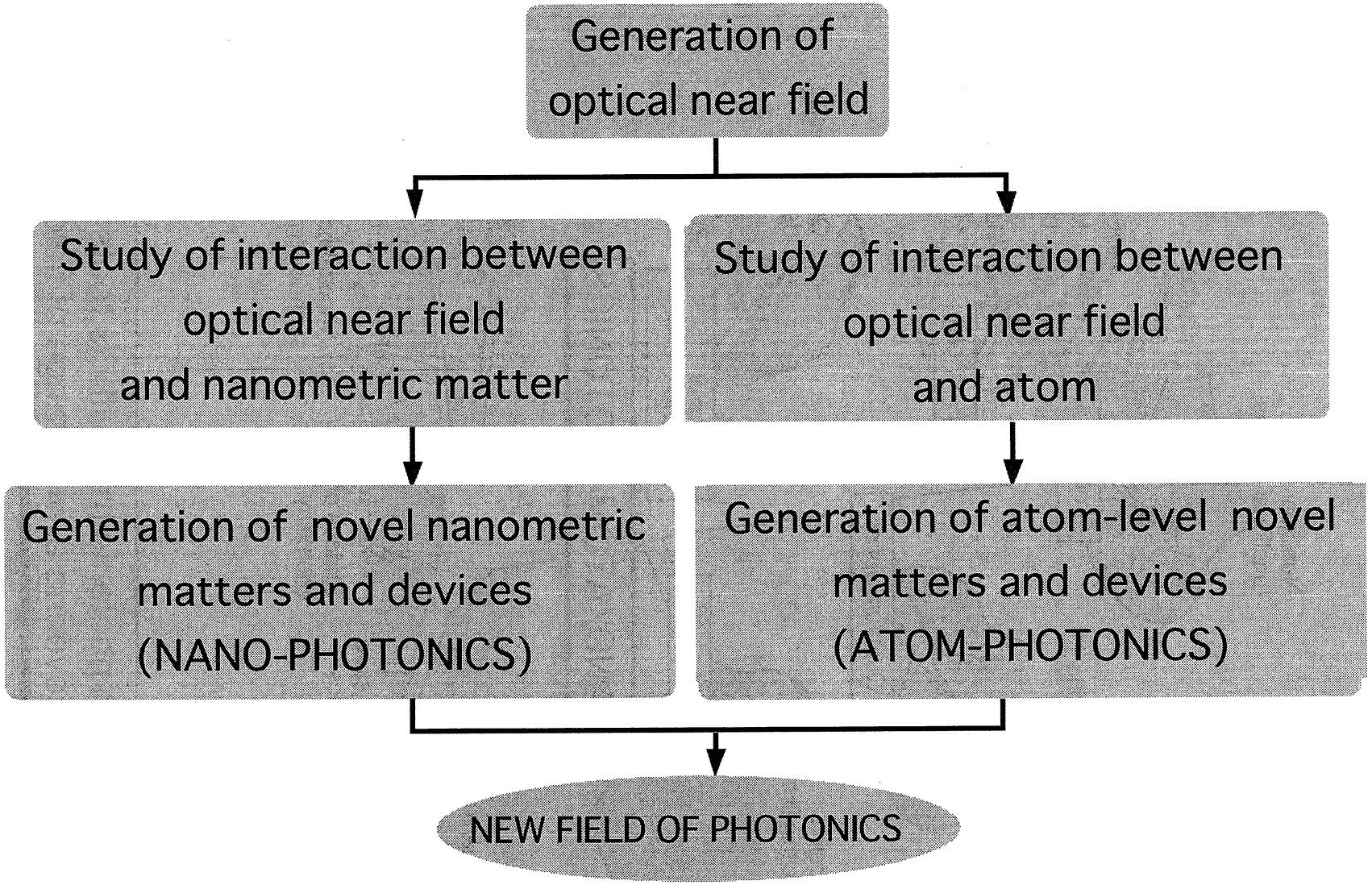
Generation of optical near field
Study of interaction between optical near field and nanometric matter
Study of interaction between optical near field and atom
Generation of novel nanometric matters and devices (NANO-PHOTONICS)
Generation of atom-level novel matters and devices (ATOM-PHOTONICS)
NEW FIELD OF PHOTONICS

MEMBERS

(From April 1, 2000)

[I] TOKYO INSTITUTE OF TECHNOLOGY

Professor

Motoichi OHTSU[a,b] (Dr. Eng.)

Associate Professor

Haruhiko ITO[c] (Dr. Sci.)

Research Associate

Motonobu KOUROGI[c,d] (Dr. Eng.)

Graduate Students (Doctor Candidates)

Yoh YAMAMOTO
Hiroaki FUKUDA[e]
Akifumi TAKAMIZAWA

Graduate Students (Master Course)

Shuko KOGISO
Takashi SHIMIZU
Tomoto KAWAMURA
Yusuke SUMITA
Hideaki TANIOKA
Tokiya ABE
Minoru UEDA
Masakazu YAMAGIWA
Nobuo SASAKI
Kazuhiko YAMADA

Undergraduate Students

Kazutaka ITSUMI
Jung-Shik LIM
Yuji ECHIGO
Kazuhiro KOSAKA

Visiting Scientists

Seok-Jeong LEE [f]	(PhD.)
Bambang WIDIYATMOKO	(Dr. Eng.)
Osamu NAKAMOTO	
Yoshinobu NAKAYAMA[e]	(Dr. Eng.)
Nariyoshi MISAWA[e]	(Dr. Eng.)
Takashi Yatsui[g]	(Dr. Eng.)

Secretaries

Chikako ISHIDA
Kaoru OGURA

a) Also with Kanagawa Academy of Science and Technology
(Director, "Near field photonics"group)
b) Also with ERATO, Japan Science and Technology Corporation
(Director, "Localized photon" project)
c) Also with "Localized photon" project, ERATO,
Japan Science and Technology Corporation
d) Also with Kanagawa Academy of Science and Technology
(Part-time researcher, "Near field photonics"group)
e) Permanent affiliation: RICOH Co.Ltd.
f) Permanent affiliation: Korea Maritime University
g) Permanent affiliation: "Localized photon" project, ERATO,
Japan Science and Technology Corporation

[II] "LOCALIZED PHOTON" PROJECT, ERATO, JAPAN SCIENCE AND TECHNOLOGY CORPORATION

Researchers

Theory Group

Kiyoshi KOBAYASHI[h]	(Dr. Sci.)	(Group Leader)
Suguru SANGU	(Dr. Eng.)	

Nano-photonics Group

Tadashi KAWAZOE	(Dr. Sci.)
Takashi YATSUI	(Dr. Eng.)
Hemantkumar N. AIYER	(Ph.D.)

Atom-photonics Group

Kouki TOTSUKA	(Dr. Sci.)

Visiting Researchers

Guen-Hyoung Lee[i]	(Dr. Eng.)

Managers

Akiyoshi ORIDE[j]
Takaaki MORIYAMA

Secretaries

Fumiko Ohta
Tomoko Ohta

h) Permanent affiliation: Japan IBM Co. Ltd.
i) Permanent affiliation: Dong-Eui University, Korea
j) Permanent affiliation: RICOH Co.Ltd.

[III] KANAGAWA ACADEMY OF SCIENCE AND TECHNOLOGY

Full-Time Researchers

Shuji MONONOBE (Dr. Eng.)

Part-Time Researchers

Motonobu KOUROGI[k] (Dr. Eng.)

Visiting Scientist

Hiroaki FUKUDA[l]

Secretary

Yumiko MIYAHARA

k) Permanent affiliation: Tokyo Institute of Technology
l) Permanent affiliation: RICOH Co.Ltd.

LIST OF PAPERS

[(pp.XX-XX; pages in this issue of the COLLECTED PAPERS]

[I] PAPERS IN ATOM PHOTONICS

(b) International Conferences

[II] PAPERS IN NANO PHOTONICS

(a) Journal Papers

"Electroless Nickel Plating for Nanofabrication in Optics", J. Electrochemical Soc., vol.147, no.3, March 2000, pp.1046-1049

(pp.16-19)

[3] T. Kobayashi, J. Ishibashi, H. Inaba, S. Mononobe, M. Ohtsu and H. Honma, "Electroless Nickel Plating to a Minute Area", Surface Technology, vol.51, no.2, February 2000, pp.193-198

【小林健、石橋純一、稲葉裕之、物部秀二、大津元一、本間英夫、「微小領域への無電解ニッケルめっき」、表面技術、第５１巻、第２号、２０００年２月、pp. 193-198】

(pp.20-25)

[4] U. Maheswari Rajagopalan, S. Mononobe, K. Yoshida, M. Yoshimoto and M. Ohtsu, "Nanometer Level Resolving Near Field Optical Microscope under Optical Feedback in the Observation of a Single-String Deoxyribo Nucleic Acid", Jpn. J. Appl. Phys., vol.38, part 1, no.12A, December 1999, pp.6713-6720

(pp.26-33)

[5] M. B. Lee, N. Atoda, K. Tsutsui and M. Ohtsu, "Nanometric aperture arrays fabricated by wet and dry etching of silicon for near-field optical storage application", J. Vac. Sci. Technol. B, vol.17, no.6, Nov/Dec. 1999, pp.2462-2466

(pp.34-38)

[6] T. Matsumoto, M. Ohtsu, K. Matsuda, T. Saiki, H. Saito and K. Nishi, "Low-temperature near-field nonlinear absorption spectroscopy of InGaAs single quantum dots", Appl. Phys. Lett., vol.75, no.21, November 1999, pp.3246-3248

(pp.39-41)

[7] K. Kurihara, M. Ohtsu, T. Yoshida, T. Abe, H. Hisamoto and K. Suzuki, "Micrometer-Sized Sodium Ion-Selective Optodes Based on a "Tailed" Neutral Ionophore", Analytical Chemistry, vol.71, no.16, August 1999, pp.3558-3566

(pp.42-50)

(b) International Conferences

[1] M. Ohtsu, "Near field optical technology for high density optical storage and nano-deposition", Abstracts of the International Union of Materials

Research Societies, - 6th International Conference in Asia, 23-26 July, 2000, Hong Kong, China, (paper number e3.1b) **[Invited presentation]**

(p.51)

[2] T. Ikeda, Y. Narita, T. Williams and M. Ohtsu, "Design and Application of an Ultra-high Spatial Resolution Mapping System Using Near-field Spectroscopy", Abstract of the Second Meeting of the International Union of Microbeam Analysis Societies, July 9-14, 2000, Hawai, USA, pp.117-118 **[Invited presentation]**

(pp.52-53)

[3] T. Yatui, S. Kogiso, M. Kourogi, K. Tsutsui, M. Ohtsu and J. Takahashi, "Extremely high throughput and resolution capability of an optical near field slider", Technical Digest of Conference on Lasers and Electro-Optics, May 7-12, 2000, San Francisco, CA, pp. 218-219 (paper number CtuI7)

(pp.54-55)

[4] G.H. Lee, Y. Yamamoto, M. Kourogi and M. Ohtsu, "*In-situ* fabrication of nanostructures by photo-enhanced chemical vapor deposition using optical near field", Technical Digest of Quantum Electronics and Laser Science Conference, May 7-12, 2000, San Francisco, CA, pp. 17-18 (paper number QMF4)

(pp.56-57)

[5] S. Sangu, K. Kobayashi and M. Ohtsu, "Nanometric probe-sample interactions via optical near fields: derivation and characteristics", Technical Digest of Quantum Electronics and Laser Science Conference, May 7-12, 2000, San Francisco, CA, pp. 60-61 (paper number QTuA23)

(pp.58-59)

[6] M. Ohtsu and G.H. Lee, "Chemical vapor deposition of nanometric materials by optical near field toward nano-photonic integration", Technical Digest of the NAIR/OITDA Workshop on Ultrahigh Density Optical Storage and Related Techniques, 7-8 March, 2000, Tsukuba, Japan, pp.1-23 **[Invited presentation]**

(pp.60-82)

[7] V. Polonski, Y. Yamamoto, G.H. Lee and M. Ohtsu, "Applicability of Otical Near-Field for Depositing Nanoscale Patterns in Virtual Photon Environment", Technical Digest of the 8th JST International Symposium on Molecular Processes in Small Time and Space Domains, 3-4 March, 2000, Nara, Japan, p.102 (paper number 204)

(p.83)

[8] M. Ohtsu, "Near-field nano-optics toward nano/atom deposition", Technical Digest of the 18th Congress of the International Comission for Optics, 2-6 August, 1999, San Francisco, CA, SPIE volume 3749, pp.478-479 **[Invited presentation]**

(pp.84-85)

[9] K. Kobayashi and M. Ohtsu, "Quantum theory and virtual photon model of near field optics", Technical Digest of the SPIE Conference on Near-Field Optics: Physics, Devices, and Information Processing, 22-23 July, 1999, Denver, Co., vol.3791, pp.10-20 **[Invited presentation]**

(pp.86-96)

[10] M. Kourogi, T. Yatsui and M. Ohtsu, "Phase-change recording/readout with a high throughput fiber probe", Technical Digest of the SPIE Conference on Near-Field Optics: Physics, Devices, and Information Processing, 22-23 July, 1999, Denver, Co., vol.3791, pp.68-75

(pp.97-104)

[11] T. Yatsui, M. Kourogi, K. Tsutsui, J. Takahashi and M. Ohtsu, "Subwavelength-sized phase-change recording with a silicon planar apertured probe", Technical Digest of the SPIE Conference on Near-Field Optics: Physics, Devices, and Information Processing, 22-23 July, 1999, Denver, Co., vol.3791, pp.76-84

(pp.105-113)

[12] Y. Yamamoto, V. Polonski, G.H. Lee, M. Kourogi and M. Ohtsu, "Photochemical vapor deposition by optical near-field", Technical Digest of the SPIE Conference on Near-Field Optics: Physics, Devices, and Information Processing, 22-23 July, 1999, Denver, Co., vol.3791, pp.124-131

(pp.114-121)

[13] G.H. Lee, Y. Yamamoto, M. Kourogi and M. Ohtsu, "Fabrication of ZnO nanostructure using near-field optical technology", Technical Digest of the SPIE Conference on Near-Field Optics: Physics, Devices, and Information Processing, 22-23 July, 1999, Denver, CO., vol.3791, pp.132-139

(pp.122-129)

[III] REVIEW PAPERS

[1] M. Ohtsu, "Preface", A monthly publication of the Jpn. Soc. Appl. Phys.,

vol.69, no.6, June 2000, p.629
【大津元一、「巻頭言」、応用物理、第６９巻、第６号、２０００年６月、p.629】

(p.131)

[2] M. Ohtsu, "Near-field Optical Technology and Its Overlook", J. Jpn. Soc. For Precision Eng., vol.66, no.5, May 2000, pp.661-666
【大津元一、「近接場光技術とその展開」、精密工学会誌、第６６巻、第５号、２０００年５月、pp.661-666】

(pp.132-137)

[3] S. Mononobe and M. Ohtsu, "Fabricatoin of Near-field Optical Probes", J. Jpn. Soc. For Precision Eng., vol.66, no.5, May 2000, pp.667-670
【物部秀二、大津元一、「近接場光学用プローブの作製法」、精密工学会誌、第６６巻、第５号、２０００年５月、pp.667-670】

(pp.138-141)

[4] H. Ito and M. Ohtsu, "Controlling Atoms by Optical Near field", J. Opt. Soc. Jpn., vol.28, no.11, November 2000, pp.610-615
【伊藤治彦、大津元一、「近接場光を用いた原子の制御」、光学、第２８巻、第１１号、１９９９年１１月、pp.610-615】

(pp.142-147)

[5] G.H. Lee, Y. Yamamoto, M. Kourogi and M. Ohtsu, "Deposition of Nanometer-Sized Materials by Optical Near-Field", Trans. IEE of Japan, vol.119-C, no.10, October 1999, pp.1113-1118
【李謹炯、山本洋、興梠元伸、大津元一、「近接場光によるナノメートル寸法物質の堆積」、電気学会論文誌Ｃ、第１１９－Ｃ巻、第１０号、１９９９年１０月、pp.1113-1118】

(pp.148-153)

[IV] PUBLISHED BOOKS

[1] M. Ohtsu and S. Kawata (ed.), *Introduction to Near-field Nano-photonics*, Optronics, Tokyo, April 2000 (133 pages)
【大津元一、河田聡編、「近接場ナノフォトニクス入門」、オプトロニクス社、２０００年４月（１３３頁）】

[2] M. Ohtsu and Y. Arakawa, *Handbook of Quantum Engineering*, Asakura-shoten Publishers, Tokyo, November 1999 (979pages)
【大津元一、荒川泰彦編、「量子工学ハンドブック」、朝倉書店、１９９９年１１月（９７９頁）】

[3] M. Ohtsu, "Chapter 13, Past and Present of the Information Storage", in *Electronics and Society* (ed. by H. Goto), Hoso-daigaku Shuppankai, Tokyo, March 2000, pp.168-176

【大津元一、「第１３章、情報の記録の過去と現在」、後藤尚久編、電子技術と社会（放送大学教材）、放送大学出版会、東京、2000年3月、pp.168-176】

[4] M. Ohtsu, "Chapter 14, Optical Storage", in *Electronics and Society* (ed. by H. Goto), Hoso-daigaku Shuppankai, Tokyo, March 2000, pp.177-187

【大津元一、「第１４章、光によるメモリ技術」、後藤尚久編、電子技術と社会（放送大学教材）、放送大学出版会、東京、2000年3月、pp.177-187】

[5] M. Ohtsu, "Chapter 15, Future of the Information Storage", in *Electronics and Society* (ed. by H. Goto), Hoso-daigaku Shuppankai, Tokyo, March 2000, pp.188-198

【大津元一、「第１５章、情報の記録の将来」、後藤尚久編、電子技術と社会（放送大学教材）、放送大学出版会、東京、2000年3月、pp.188-198】

[V] PRESENTED PH.D THESIS

[1] T. Yatsui, "Study on optial near field heads for high-density and high-speed storage and readout", January 2000

【八井崇、「超高密度・超高速光記録読み出し用光近接場ヘッドの開発」、２０００年１月】

[2] Bambang Widiyatmoko, "Study on the expansion of the span of optical frequency comb using nonlinear frequency conversion", January 2000

[3] S. Mononobe, "Study on fabricating fiber probes for near field optical microscopy", September 1999

【物部秀二、「近接場光学顕微鏡のためのファイバープローブの作製に関する研究」、１９９９年９月】

[I] PAPERS IN ATOM PHOTONICS

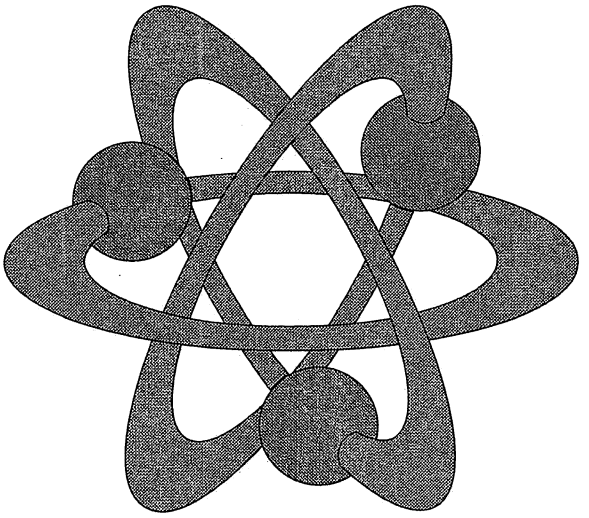

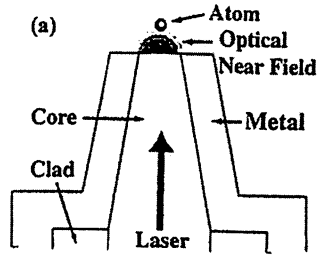

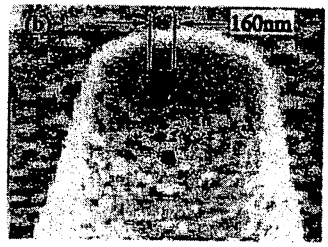

QMF5 Fig. 1. (a) Cross sectional profile and (b) scanning electron micrograph of an apertured-type fiber-probe. The flat aperture of the fiber-probe was fabricated with a focused ion beam technique.

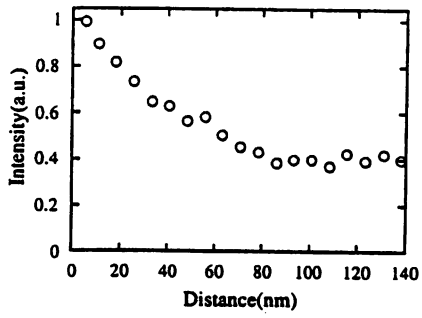

QMF5 Fig. 2. Experimental result of the measurement of optical near-field intensity. The light intensity picked up by the gold coated fiber-probe is plotted as a function of the distance from the surface of the tip of the apertured-type fiber-probe. The light intensity is normalized by the value at $r = 5$ nm.

QMF5 **11:15 am**

Evaluation of near-field optical potentials on a nanometric sharpened fiber probe for atom trapping

Kouki Totsuka, Hideaki Tanioka,* Haruhiko Ito,** Motoichi Ohtsu,† *ERATO, Japan Science and Technology Corp., 687-1 Tsuruma, Machida 194-0004, Japan*

Recently, atom manipulation by using optical near fields has been attracting a lot of interests. Optical near field can be localized in a nanometric region, being free from the diffraction limit in contrast to propagation light. The intensity distribution of optical near field decays rapidly as an exponential-like function. Because such a spatially inhomogeneous light field can affect the resonant force on an atom (so called dipole force), the optical near field produces the strong dipole force.[1] Using the dipole force of the optical near field, we can expect to manipulate an atom with high spatial accuracy. Moreover, due to the resonant character of dipole force, we can manipulate an atom species- and state-selectively. The optical near field localized in a nanometric region can be generated on the tip of a sharpened fiber-probe. This kind of fiber probes can be used for deflection of the atomic motion, and then trap of an atom.[2–5] To this end, it is very important to fabricate the fiber probe suitable for the atoms used. In this case, we must consider several parameters: a size and a shape of the tip, light intensity, frequency detuning, etc. In this paper, in order to examine the optimal conditions for the fabrication, we measured and evaluated the optical near-field intensity distribution of the fiber-probe.

Figure 1 shows the top of an apertured-type fiber-probe used in the experiment. We measured the intensity distribution of the optical near field generated on the tip of the apertured-type fiber-probe in a probe-to-probe configuration with the shear-force technique.[6] The light beam from a laser diode with a wavelength of 780 nm, which is a resonant wavelength of a Rb atom, was introduced to the apertured-type fiber probe with an aperture radius of 80 nm.[5] A gold-coated fiber-probe with a radius of curvature of 40 nm was approached to the tip of the apertured-type fiber-probe and picked up the light signal scattered from the tip. These fiber probes were fabricated by our group for the present work.[5]

Figure 2 shows the intensity distribution of the optical near field as a function of the distance from the surface of the tip. The light intensity is normalized to the value at a distance of 5 nm. In this figure, we find that the signal consists of fast- and slow-decay components. The signal within the region of 100 nm shows the change of the optical near field. On

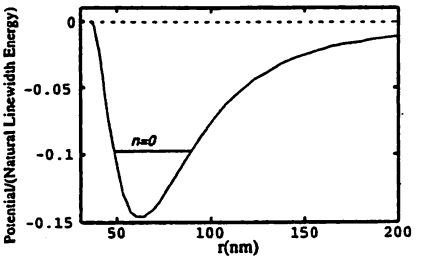

QMF5 Fig. 3. Calculated trap potential as a function of the distance from the surface of the tip. The potential is normalized by the natural linewidth energy of a Rb atom.

the other hand, the signal in the region of more than 100 nm contains the far-field component. The intensity distribution in the near-field region is fitted with an exponential function of $I(r) = \exp(-0.84r/a)$, where a is a radius of aperture and r is the distance from the surface of the tip. The decay length of the near-field component is comparable to the aperture size a.

It has been proposed that an atom can be trapped at a minimum point of a trap potential composed of the repulsive dipole force and the attractive van der Waals force in a certain condition.[4,5] To generate a stable trap potential for a Rb atom, we must pay attention to several parameters: van der Waals force, de Broglie wavelength and radius of the aperture. Here, in order to estimate the near-field optical potential for a Rb atom, we assume that the experimentally obtained function $I(r)$ can be applied to the case where the tip radius is smaller than 80 nm. When we consider the case of the optical near field power of 80 W/cm^2 and the frequency detuning of $\delta/2\pi$ of +1 GHz, we find the optimal trap potential can be formed if $a = 10$ nm. In this case, the minimum point of the potential is found at a distance 60 nm from the surface of the tip, as shown in Fig. 3. The atom can be trapped at one of the quantized vibrational levels with n, drawn with horizontal line in the trap potential. When we regard the trap potential as a harmonic potential, the minimum level with $n = 0$ corresponds to the kinetic energy of 30 μK in terms of the temperature. This temperature correspond to the de Broglie wavelength of 90 nm. If $a \geq 10$ nm, the trap potential become too shallow to trap a Rb atom by conventional laser cooling technique. On the other hand, if $a \leq 10$ nm, van der Waals force become dominant, and the trap potential disappears.

*Tokyo Inst. of Tech., Japan
**Tokyo Inst. of Tech. and Kanagawa Academy of Science and Tech., Japan
†Japan Science and Tech. Corp., Tokyo Inst. of Tech. and Kanagawa Academy of Science and Tech., Japan

1. J.P. Dowling and J. Gea-Banacloche, "Evanescent light-wave atom mirrors, resonators, waveguides, and traps," in *Advances in atomic, molecular, and optical physics*, B. Bederson and H. Walther, eds., Vol. 37 (Academic Press, San Diego, 1996), pp. 1–94.
2. M. Ohtsu, S. Jiang, T. Pangaribuan, M. Kozuma, "Nanometer resolution photon STM and single atom manipulation," in *Near-Field Optics*, D.W. Pohl and D. Courjon, eds. (Kluwer, Dordrecht, 1993), pp. 131–139.
3. H. Hori, "Quantum optical picture of photon STM and proposal of single atom manipulation," in *Near-Field optics*, D.W. Pohl and D. Courjon, eds. (Kluwer, Dordrecht, 1993), pp. 131–139.
4. H. Ito, K. Otake, M. Ohtsu, "Near-field optical guidance and manipulation of atoms," in *Far- and Near-Field optics*, (Society of Photo-Optical Instrumentation Engineers, Washington, 1998).
5. M. Ohtsu, eds., in *Near-field nano/atom optics and technology* (Springer-Verlag, Berlin, 1998).
6. T. Yatsui, M. Kourogi, M. Ohtsu, "Increasing throughput of a near-field optical fiber probe over 1000 times by the use of a triple-tapered structure," Appl. Phys. Lett. 73, 2090–2092 (1998).

The Second Asia-Pacific Workshop on Near Field Optics
Oct. 20-23, Peking University
Beijing, China

Effective probe-sample interaction: toward atom deflection and manipulation

K. Kobayashi and S. Sangu

ERATO Localized Photon Project
Japan Science and Technology Corporation
687-1 Tsuruma, Machida, Tokyo 194-0004, Japan
TEL: +81-42-788-6036, FAX: +81-42-788-6031
E-mail: kkoba@ohtsu.jst.go.jp

H. Ito and M. Ohtsu
Interdisciplinary Graduate School of Science and Engineering
Tokyo Institute of Technology
4259 Nagatsuta-cho, Midori, Yokohama, Kanagawa 226-8502, Japan
TEL: +81-45-924-5455, FAX: +81-45-924-5599

Using the projection-operator method, we have proposed a microscopic formulation of optical near-field systems that can be viewed as a hierarchical combination of the two subsystems: one is macroscopic matter and incident light, and the other is a microscopic probe tip and sample [1-3]. Such a formulation enables us to analyze quantum theoretical behavior or cavity QED effects of an atom, a molecule, and a quantum dot interacting with optical near fields, as well as fundamental properties of optical near-field microscopy and spectroscopy.

In this paper we discuss effective interactions between a probe tip and sample, in particular, functional forms of the interactions. Analyzing the wave number dependence of the coupling coefficients of the probe/sample coupled to the virtual photon or exciton-polaritons, we find that the major part of the interactions is Yukawa potential. We also examine the deviations from the Yukawa potential (see Fig. 1), depending on a variety of parameters such as the size and material properties (excitation energy, effective mass and so on). If the Yukawa potential is repulsive, the deviations produce the potential minimum that indicates the possibility of atom trapping by optical near-fields [4].

In order to demonstrate the application of our formulation with the effective interactions, we show two examples: one is the so-called size resonant effect as a conventional problem in optical near-field systems. The other is atom deflection by optical near fields as a quantum-mechanical problem.

References

[1] M. Ohtsu (ed.), Near-Field Nano/Atom Optics and Technology, (Springer-Verlag, Tokyo, 1998) Chap. 12.

[2] K. Kobayashi and M. Ohtsu, J. Microscopy 194, 249 (1999).

[3] K. Kobayashi and M. Ohtsu, to appear in Proc. SPIE.

[4] M. Ohtsu (ed.), Near-Field Nano/Atom Optics and Technology, (Springer-Verlag, Tokyo, 1998) Chap. 11.

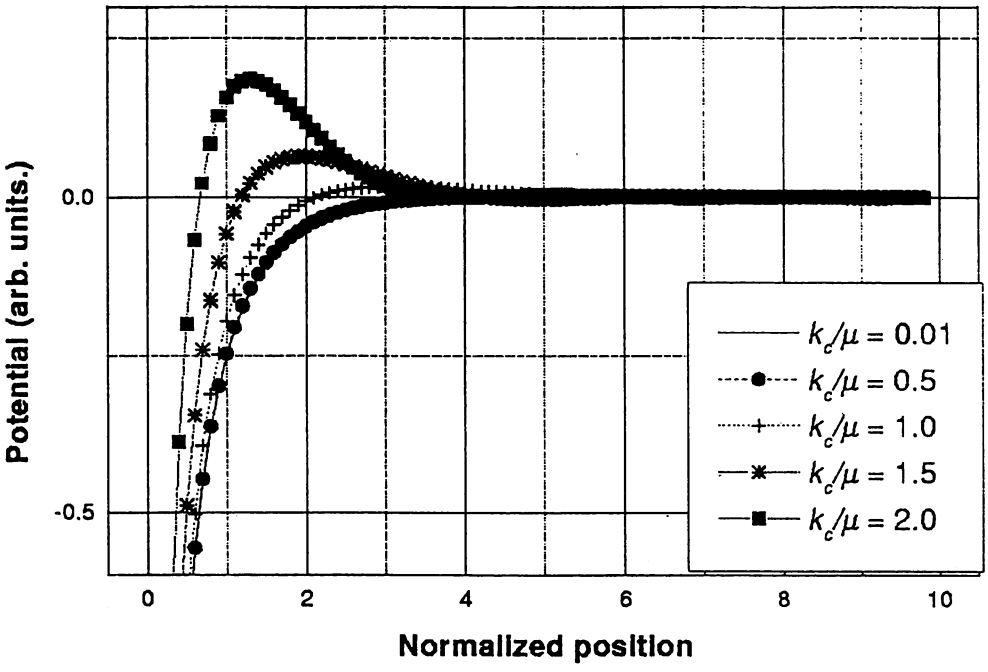

Fig.1 Effective potential between a probe tip and sample.

Invited Paper

Precise control of atoms with optical near fields: deflection and trap

Haruhiko Ito[a,b,c], Akifumi Takamizawa[b], Hideaki Tanioka[b], Motoichi Ohtsu[b,c]

[a]PRESTO, Japan Science and Technology Corporation,
KSP East 408, 3-2-1 Sakado, Takatsu-ku, Kawasaki 213-0012, Japan

[b]Interdisciplinary Graduate School of Science and Engineering
Tokyo Institute of Technology
4259 Nagatsuta, Midori-ku, Yokohama 226-8502, Japan

[c]Kanagawa Academy of Science and Technology
KSP East 408, 3-2-1 Sakado, Takatsu-ku, Kawasaki 213-0012, Japan

ABSTRACT

We present a new scheme of atom manipulation by means of a sharpened optical fiber with near-field light. In particular, we discuss the feasibility of deflecting and trapping Rb atoms. The optical potential produced by the dipole force is estimated from numerical calculations based on the Yukawa-type intensity distribution. We show that a slow Rb atom can be deflected at a large deflection angle. A static atom trap can be made near the tip of a sharpened fiber. A cold Rb atom is captured at the minimum of the trap potential composed of the repulsive optical potential and the attractive van der Waals potential. A spatial intensity distribution of an optical near field produced near the tip of a protrusion-type fiber is measured in the fiber-to-probe configuration with a shear-force technique. We also describe an atom funnel to form a cold atomic beam required for the near-field light manipulation.

Keywords: optical near field, atom deflection, atom trap, atom funnel, sharpened fiber, dipole force, van der Waals force, Yukawa-type intensity distribution

1. INTRODUCTION

Control of atomic motion with laser light[1] has attracted a lot of experimental attention. Now, thanks to the development of near-field optical techniques,[2–4] the possibility of manipulating a single atom, ion, and molecule has opened up.[3–7] In contrast to propagating light, near-field light is not affected by diffraction. Therefore, we can expect to use the optical near field localized in a nanometric region for controlling atoms with high spatial accuracy.

When the light frequency is tuned to an atomic resonant frequency, the near-field light exerts the dipole force on an atom. Since the dipole force is in proportion to the gradient of light intensity,[7,8] one of the near-field light is so strong as to greatly change the thermal atomic motion. In addition, owing to the resonant character, we can manipulate atoms species- and state-selectively. In this paper, we describe a new method with a sharpened fiber for precise control of neutral atoms.

Let us consider the two cases of the atom manipulation with a sharpened fiber. Figure 1 (a) schematically shows the deflection of an atom. In this scheme, an atom ballistically flying is deflected by the repulsive dipole force from the near-field light. On the other hand, Fig. 1 (b) shows the trap of an atom near the nanometric tip. The trap potential is made up of the repulsive dipole-force potential and the attractive van der Waals potential. In the following sections, we estimate the optical near field required for the deflection and the trap, assuming the Yukawa-type intensity distribution. We also report experiments now in progress: measurements of the spatial intensity distribution of near-field light and generation of a cold atomic beam through an atom funnel involving the Sisyphus cooling.

Other author information: (Send correspondence to H.I.)
H.I.: E-mail: ito@ae.titech.ac.jp
M.O.: E-mail: ohtsu@ae.titech.ac.jp

Part of the SPIE Conference on Near-Field Optics: Physics, Devices and Information Processing • Denver, Colorado • July 1999
SPIE Vol. 3791 • 0277-786X/99/$10.00

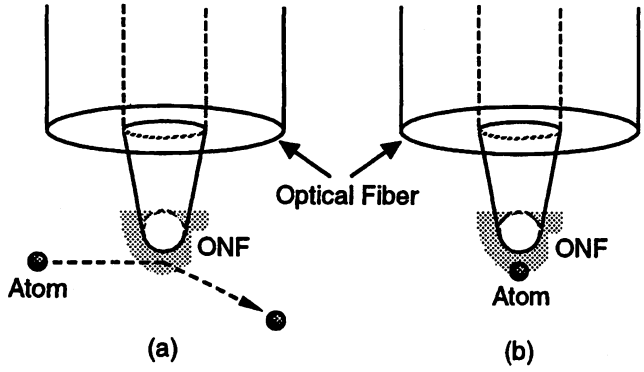

Figure 1. Sketches of atom manipulation with a sharpened fiber: (a) atom deflection, and (b) atom trap. In (a), an atom ballistically flying is deflected by the repulsive dipole force from the optical near field (ONF). In (b), an atom is trapped near the tip by achieving a balance between the repulsive dipole force and the attractive van der Waals force.

2. MECHANICAL POTENTIALS ON ATOMS

We basically deal with the dipole force to manipulate atoms with near-field light. The dipole force has the dispersion-like character on the frequency detuning. Figure 2 shows the dipole force plotted as a function of the detuning $\delta = \omega - \omega_0$ of the light frequency ω from a resonant atomic frequency ω_0. The dipole force becomes repulsive in the case of the blue detuning $\delta > 0$, while attractive in the case of the red detuning $\delta < 0$. The optical potential produced by the dipole force is given by[7,8]

$$U_{\rm opt}(r) = \frac{\hbar\delta}{2} \ln\left\{1 + \frac{\gamma^2}{4\delta^2 + \gamma^2}\frac{I(r)}{I_{\rm sat}}\right\}, \tag{1}$$

where γ, and $I_{\rm sat}$ are a natural linewidth, and a saturation intensity, respectively.

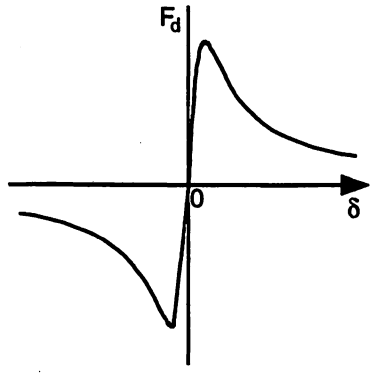

Figure 2. Dipole force plotted as a function of the detuning δ of the light frequency from a resonant atomic frequency. It becomes repulsive in the blue-detuning region ($\delta > 0$), while attractive in the red-detuning region ($\delta < 0$).

In order to estimate the intensity $I(r)$ of an optical near field, we introduce the Yukawa-type potential written as[3,6,9]

$$\phi(r) = \int\int \frac{\exp(-r/a)}{r} {\rm dS}, \tag{2}$$

where a is a radius of curvature of the tip and r is a distance from the tip surface. From this Yukawa-type potential,

we obtain the near-field light intensity distribution $I(r)$ given by[3,6]

$$I(r) \sim |\nabla\phi(r)|^2 + \frac{1}{a^2}|\phi(r)|^2 \,. \tag{3}$$

When the shape of the tip is hemispherical, the two components of $\phi(r)$ and $|\nabla\phi(r)|$ can be approximately written as

$$\phi(r) = \frac{2\pi a^2}{r}\left[\exp\left(-\frac{r-a}{a}\right) - \exp\left(-\frac{\sqrt{r^2+a^2}}{a}\right)\right], \tag{4}$$

$$|\nabla\phi(r)| = 2\pi\left[\left(\frac{a}{r}+\frac{a^2}{r^2}\right)\exp\left(-\frac{r-a}{a}\right) - \left(\frac{a}{\sqrt{r^2+a^2}}+\frac{a^2}{r^2}\right)\exp\left(-\frac{\sqrt{r^2+a^2}}{a}\right)\right], \tag{5}$$

where r is measured from the center of the hemispherical tip.

On the other hand, an atom feels the attractive van der Waals force in the vicinity of a dielectric surface. The van der Waals potential is written as[10–12]

$$U_{\rm vdw}(r) = -\frac{1}{16r^3}\sum_j \frac{n_j^2-1}{n_j^2+2}\frac{\hbar\gamma_j}{k_j^3}\,, \tag{6}$$

where n_j and k_j are a refractive index and a wave number. The summation is carried out about the possible dipole transitions.

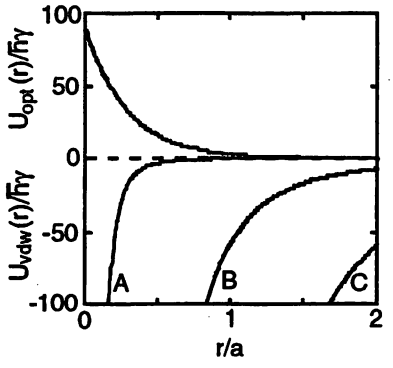

Figure 3. Optical and van der Waals potentials plotted as a function of the normalized distance r/a from the tip surface under a blue detuning condition of $\delta/2\pi = +1$ GHz. The three curves A, B, and C of the van der Waals potential are drawn for the cases of $a = 50$ nm, $a = 10$ nm, and $a = 5$ nm, respectively. Both of the potentials are normalized to the natural linewidth energy $\hbar\gamma$.

Figure 3 shows the optical potential $U_{\rm opt}(r)$ and the van der Waals potential $U_{\rm vdw}(r)$ on a Rb atom with a resonant wavelength of 780 nm near the hemispherical tip of a sharpened fiber. Both of the potentials normalized to the natural linewidth energy $\hbar\gamma$ are plotted as a function of the normalized distance r/a from the tip surface under a blue-detuning condition of $\delta/2\pi = +1$ GHz, where the near-field light power $P_{\rm onf}$ is 50 nW for $a = 50$ nm. The van der Waals potential is shown for the three values of $a = 50$ nm, 10 nm, and 5 nm. In the present case, from Fig. 3, we see that the repulsive optical potential can be comparable to the attractive van der Waals potential between $a = 10$ nm and $a = 50$ nm. The total potential on an atom is given by $U(r) = U_{\rm opt}(r) + U_{\rm vdw}(r)$.

3. NUMERICAL ESTIMATIONS

3.1. Atom Deflection

Let us consider the case of the deflection of an atom with a sharpened fiber as shown in Fig. 1 (a). If the repulsive dipole force is stronger than the attractive van der Waals force, an atom ballistically flying can be deflected in the

direction shown in Fig. 1 (a) by passing through the near-field region. Figure 4 shows the deflection angle θ plotted as a function of the impact parameter b, which is defined as the distance between the center of the hemispherical tip and the incident direction. In this calculation, we assume a moderate slow Rb atom with a velocity of 10 m/s under a condition of $a = 50$ nm, $\delta/2\pi = +2$ GHz, and $P_{\rm onf} = 50$ nW. The slow Rb atom can be supplied from an atomic beam with a mean temperature of 200 mK.

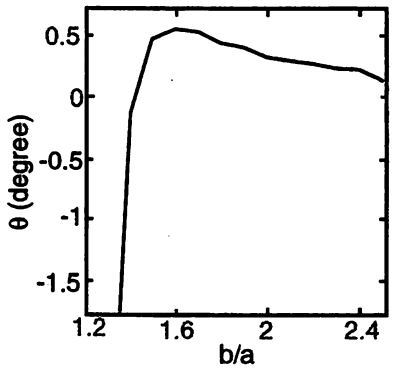

Figure 4. Deflection angle θ of a Rb atom with a velocity of 10 m/s plotted as a function of the normalized impact parameter b/a, where $a = 50$ nm, $\delta/2\pi = +2$ GHz, and $P_{\rm onf} = 50$ nW.

As shown in Fig. 4, the deflection angle is about 0.5 degree at $b/a = 1.6$. From this value, we find that the displacement of the atom from the incident axis is about 100 μm at a distance of 10 cm downstream the fiber. This result indicates that the atom can be easily detected with a commercial detector such as a microchannel plate.

3.2. Atom Trap

Next, let us consider the case of the trap of an atom with a sharpened fiber as shown in Fig. 1 (b). The original idea dealt with the balance of three forces: the attractive dipole force, the enhanced spontaneous force, and the centrifugal force.[5–7] A different type of atom trap has been also proposed.[13] Here, we describe a more static trap based on a balance between the repulsive dipole force and the attractive van der Waals force. In this scheme, an atom is trapped at the minimum point of the potential produced near the tip of a sharpened fiber.

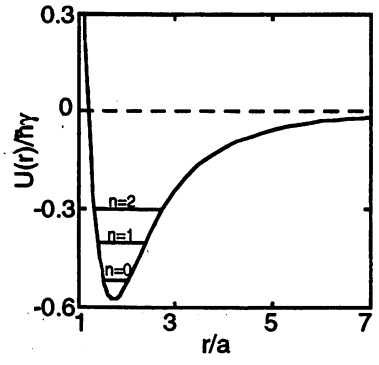

Figure 5. Trap potential on a ^{85}Rb atom in the upper ground state $F = 3$ produced near the hemispherical tip with $a = 20$ nm. The potential composed of the repulsive optical potential and the attractive van der Waals potential is plotted as a function of the normalized distance r/a from the tip surface, where $\delta/2\pi = +2$ GHz with respect to the lower ground state $F = 2$ and $P_{\rm onf} = 600$ nW. The horizontal lines shows the quantized vibrational levels with the quantum number n.

As mentioned in Sec. 2, the optical potential can be comparable to the van der Waals potential under a suitable condition. Figure 5 shows the trap potential on a ^{85}Rb atom composed of the repulsive optical potential and the attractive van der Waals potential. The potential curve for the hyperfine upper ground state $F = 3$ is plotted as a function of the normalized distance r/a from the hemispherical tip surface, where $a = 20$ nm and $P_{\rm onf} = 600$ nW. The frequency detuning $\delta/2\pi$ is taken to be +2 GHz with respect to the lower ground state $F = 2$, which is at about 3 GHz below the $F = 3$ state. The Rb atom can be trapped in one of the quantized vibrational levels indicated by the horizontal lines with the label n. For example, the lowest level with $n = 0$ corresponds to a temperature of 30 μK, at which the de Broglie wavelength is the order of 10 nm.

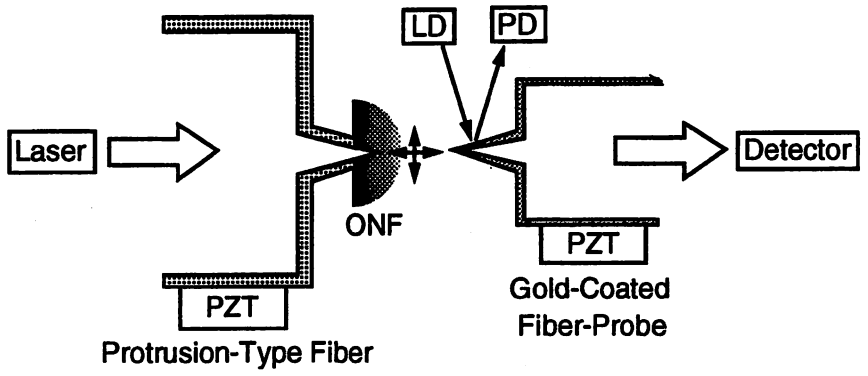

Figure 6. Experimental setup in the fiber-to-probe configuration. A protrusion-type fiber is used to produce an optical near field (ONF), while a gold-coated fiber-probe is used to pick up the signal. They are positioned with piezo-transducers (PZT) and controlled by means of the shear-force technique with an optical feedback system.

4. RELATED EXPERIMENTS

4.1. Measurements of Near-Field Light Intensity

For the atom manipulation experiments, it is fundamentally important to fabricate a sharpened fiber suitable for the atom used. There are several parameters to be determined: a shape of the tip, a radius of curvature, light intensity, frequency detuning, and so on. First of all, we measured the intensity distribution of near-field light in the fiber-to-probe configuration. Although this method is a destructive measurement of an optical near field, we can get a lot of information about the spatial distribution of near-field light.

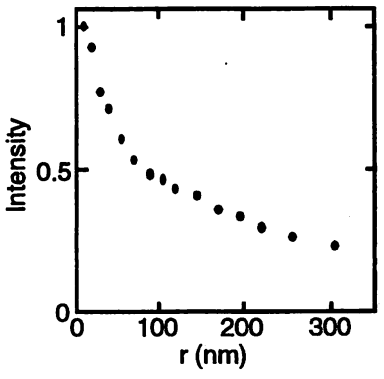

Figure 7. Measurement of a light field produced by a protrusion-type fiber with $a = 200$ nm in the fiber-to-probe configuration. The light intensity normalized to the value at $r = 10$ nm is plotted as a function of the distance r from the tip of the protrusion-type fiber.

Figure 6 shows the outline of the experimental setup. The spatial intensity distribution of the light field produced near the tip of a protrusion-type fiber is measured with a gold-coated fiber-probe placed face to face. The fiber-probe is controlled by the shear-force technique with an optical feedback system. The signal picked up by the fiber-probe is recorded as a function of the distance r from the tip of the protrusion-type fiber.

Figure 7 shows a result obtained from a measurement of the light field with a wavelength of 780 nm produced near the tip of a protrusion-type fiber[14,15] with $a = 200$ nm. Here, a gold-coated fiber-probe with a radius of curvature of 40 nm is used. The light intensity is normalized to the value at $r = 10$ nm. As shown in Fig. 7, the light field exponentially decays. We think that the intensity change is due to a near field in a region of less than 100 nm, while due to a far field in a region of more than 100 nm. The intensity distribution in the near-field region can be roughly fitted with $I(r) = I_0 \exp(-1.85r/a)$. When we estimate a trap potential by applying this experimental expression to the case of $a = 20$ nm, we find again that an atom with an energy of 30 μK in terms of temperature can be trapped.

4.2. Generation of Cold Atomic Beams

A thermal atomic beam has a mean velocity of more than 100 m/s. This velocity is too fast to manipulate with a nanometric sharpened fiber because such atoms go through the near-field region in a very short time. In addition, the thermal atomic density is low, so that the near-field light does not have many occasions to interact to the atoms. In order to improve the drawbacks, we consider the use of a cold atomic beam. In fact, such a cold atomic beam can be made with an atom funnel composed of a near-field light mirror.[16]

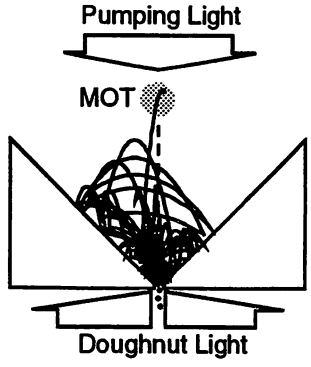

Figure 8. Atom funnel with a near-field light. Atoms supplied from a magneto-optical trap (MOT) are reflected by the atomic mirror excited on the inner wall surface via total reflection of a doughnut-shaped light beam shone upward. The reflected atoms are cooled down through the Sisyphus cooling process, which is reiterated by a weak pumping light shone downward. A trajectory is obtained from a Monte Carlo simulation performed for a Rb atom falling from an MOT with a mean temperature of 10 μK.

Figure 8 schematically shows the cross section of a funnel prism. Here, the near-field light mirror to reflect atoms is excited on the inner wall surface via total reflection of a doughnut-shaped light beam shone upward from the bottom. Furthermore, in this scheme, atoms inside the funnel are cooled down in the process of reflection based on the Sisyphus cooling mechanism with a weak pumping light.[17–19] In Fig. 8, a trajectory of a Rb atom falling from a magneto-optical trap (MOT) is also drawn as an example. The collected atoms go out of a small hole at the bottom, so that a collimated cold atomic beam can be produced. Figure 9 is the top view of an atom funnel composed of an inverse triangular hollow prism, in which cold Rb atoms with a mean temperature of about 100 μK are trapped at the center by an MOT. The funnel experiment is now in progress.

5. SUMMARY

We examined the possibility of fine control of neutral atoms with a nanometric sharpened fiber from numerical analyses with the Yukawa-type potential. When a sharpened fiber customized for Rb atoms is used, a cold Rb atom can be not only deflected at a large deflection angle but also captured with an trap composed of the repulsive dipole force and the attractive van der Walls force. The possibility of the trap was also illustrated by an experimental

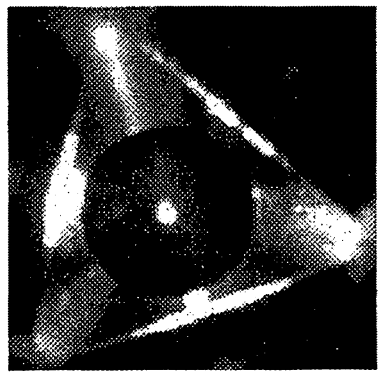

Figure 9. Top view of an atom funnel composed of an inverse triangular hollow prism. Cold Rb atoms with a mean temperature of about 100 μK are trapped with an MOT at the center.

measurement of the intensity distribution of an optical near field in the fiber-to-probe configuration. A cold atomic beam appropriate for the near-field light manipulation can be generated by means of an atom funnel involving the Sisyphus cooling.

The deflection technique with a sharpened fiber is also useful for the study of optical near fields. Using an atom as a probe, one can perform nondestructive measurements of the optical near fields. In addition, it can be used for the study of the cavity quantum electrodynamical effects including the van der Waals force in the near-field region. On the other hand, if the atom guidance technique with a hollow fiber[20,21] is employed together, one can carry atoms to an arbitrary point on a substrate and then make a small structure such as quantum dots atom by atom and species-selectively.[22] We think that the techniques presented here will be extremely useful for a single atom manipulation.

REFERENCES

1. V. I. Balykin and V. S. Letokhov, *Atom optics with laser light*, Harwood, Chur, 1995.
2. M. Ohtsu, "Progress of high-resolution photon scanning tunneling microscope due to a nanometric fiber probe", J. Lightwave Technol. **13**, pp. 1200-1221, 1995.
3. M. Ohtsu and H. Hori, *Near-field nano-optics*, Kluwer/Plenum, New York, 1999.
4. M. Ohtsu (ed.), *Near-field nano/atom optics and technology*, Springer-Verlag, Berlin, 1998.
5. M. Ohtsu, S. Jiang, T. Pangaribuan, and M. Kozuma, "Nanometer resolution photon STM and single atom manipulation", in *Near-Field Optics*, edited by D. W. Pohl and D. Courjon, pp. 131-139, Kluwer, Dordrecht, 1993.
6. H. Hori, "Quantum optical picture of photon STM and proposal of single atom manipulation", in *Near-Field Optics*, edited by D. W. Pohl and D. Courjon, pp. 105-114, Kluwer, Dordrecht, 1993.
7. J. P. Dowling and J. Gea-Banacloche, "Evanescent light-wave atom mirrors, resonators, waveguides, and traps", in *Advances in atomic, molecular, and optical physics*, edited by B. Bederson and H. Walther, Vol. 37, pp. 1-94, Academic Press, San Diego, 1996.
8. V. I. Balykin, V. S. Letokov, Yu. B. Ovchinnikov, and A. I. Sidorov, "Quantum-state-selective mirror reflection of atoms by laser light", Phys. Rev. Lett. **60**, pp. 2137-2140, 1988.
9. K. Kobayashi amd M. Ohtsu, "Quantum theoretical approach to near-field optical system", Journal of Microscopy **194**, pp. 249-254, 1999.

10. M. Chevrollier, M. Fichet, M. Oria, G. Rahmat, D. Bloch, and M. Ducloy, "High resolution selective reflection spectroscopy as a probe of long-range surface interaction : measurement of the surface van der Waals attraction exerted on excited Cs atoms", J. Phys. France II **2**, pp. 631-657, 1992.

11. W. Jhe and J. W. Kim, "Atomic energy-level shifts near a dielectric microsphere", Phys. Rev. A **51**, pp. 1150-1153, 1995; "Casimir-Polder energy shift of an atom near a metallic sphere", Phys. Lett. A **197**, pp. 192-196, 1995.

12. H. Nha and W. Jhe, "Cavity quantum electrodynamics between parallel dielectric surface", Phys. Rev. A **54**, pp. 3505-3513, 1996.

13. V. V. Klimov and V. S. Letokhov, "New atom trap configurations in the near field of laser radiation", Opt. Commun. **121**, pp. 130-136, 1995.

14. S. Mononobe and M. Ohtsu, "Fabrication of a pencil-shaped fiber probe for near-field optics by selective chemical etching", J. Lightwave Technol. **14**, pp. 2231-2235, 1996.

15. S. Mononobe and M. Ohtsu, "Development of a fiber used for fabrication application oriented near-field optical probes", IEEE Photonics Technol. Lett. **10**, pp. 99-101, 1998.

16. H. Ito, K. Sakaki, W. Jhe, and M. Ohtsu, "Atomic funnel with evanescent light", Phys. Rev. A **56**, pp. 712-718, 1997.

17. J. Söding, R. Grimm, and Yu. B. Ovchinnikov, "Gravitational laser trap for atoms with evanescent-wave cooling", Opt. Commun. **119**, pp. 652-662, 1995.

18. P. Desbiolles, M. Arndt, P. Szriftgiser, and J. Dalibard, "Elementary Sisyphus process close to a dielectric surface", Phys. Rev. A **54**, pp. 4292-4298, 1996.

19. N. Nha and W. Jhe, "Sisyphus cooling on the surface of a hollow-mirror atom trap", Phys. Rev. A **56**, pp. 729-736, 1997.

20. M. J. Renn, E. A. Donley, E. A. Cornell, C. E. Wieman, and D. Z. Anderson, "Evanescent-wave guiding of atoms in hollow optical fibers", Phys. Rev. A **53**, pp. R648-R651, 1996.

21. H. Ito, T. Nakata, K. Sakaki, M. Ohtsu, K. I. Lee, and W. Jhe, "Laser spectroscopy of atoms by evanescent waves in micron-sized hollow optical fibers", Phys. Rev. Lett. **76**, pp. 4500-4503, 1996.

22. H. Ito, K. Sakaki, M. Ohtsu, and W. Jhe, "Evanescent-light guiding of atoms through hollow optical fiber for optically controlled atomic deposition", Appl. Phys. Lett. **70**, pp. 2496-2498, 1997.

[II] PAPRES IN NANO PHOTONICS

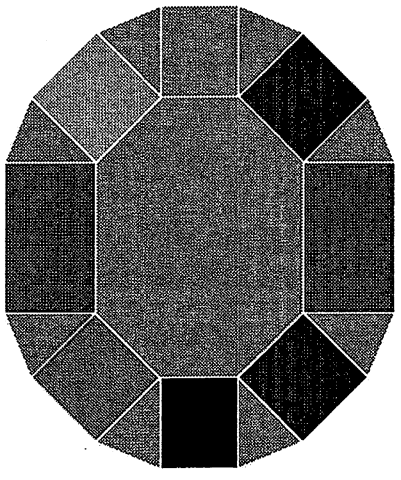

Fabrication of nanometric zinc pattern with photodissociated gas-phase diethylzinc by optical near field

Y. Yamamoto,[a] M. Kourogi,[b] and M. Ohtsu[b]
Interdisciplinary Graduate School of Science and Engineering, Tokyo Institute of Technology, 4259 Nagatsuta, Midori-ku, Yokohama, Kanagawa 226-8502, Japan

V. Polonski and G. H. Lee
Japan Science and Technology Corporation, 687-1 Tsuruma, Machida, Tokyo 194-0004, Japan

(Received 23 December 1999; accepted for publication 24 February 2000)

In situ patterning of zinc on a nanometric scale has been accomplished by photodissociation of gas-phase diethylzinc by optical near field. By using an ultraviolet optical fiber probe with an aperture diameter of 60 nm, dots with full width at half maxima of 60 and 70 nm were deposited, and were separated by 100 nm. The aspect ratio of the dots increased at the rate of 0.03/μJ, as the optical near field energy increased. A T-shape pattern was also fabricated by scanning the probe in an optical near field microscope system. © *2000 American Institute of Physics.* [S0003-6951(00)04616-7]

Optical near field has been reported to be applicable to various fields, such as spatially high resolution optical microscopy, spectroscopy, ultrahigh density optical memory, atom manipulation, and so on.[1] Recently, there has been interest in its application to nanostructure fabrication because of the possibility of realizing nanophotonic integration for metallic wires, light emitters, optical switches, and photodetectors, all controlled by nanoscale single dots.[2] For realization of such a device, which uses the optical near field as a carrier for signal transmission, various materials of nanometric size must be integrated laterally on a substrate. For this integration, we need an advanced nanostructure fabrication technique, which realizes spatially high resolution, precise control of size and position, and is applicable for various materials.

Conventional techniques popularly used for nanostructure fabrication are x-ray or electron beam lithography and the self-organized growth technique.[3] The former makes it easy to produce the desired pattern, but one disadvantage is the complexity associated with a multistep process that involves pattern definition and transfer. The latter easily produces high-quality nanoscale dots, but control over position and size is difficult.

Recently, as a nanostructure fabrication technique, we have proposed chemical vapor deposition (CVD) by optical near field.[4] Based on a photochemical reaction, this technique offers not only the possibility of lateral integration of different structures (different sequences of layers, materials, thicknesses and dopants) in a single growth run but also the option of chemical selective growth by varying the photon energy of the light source. In addition, using optical near field, it is possible to easily fabricate nanostructures having a controlled size and position. Thus we believe the technique is the most suitable technology for the realization of the nanophotonic integration.

For CVD using optical near field, we have proposed the prenucleation method[4,5] which involves the formation of nuclei by optical near field and the subsequent selective growth of the prenucleated pattern using conventional far field light (far field only prenucleation has been known since the 1980s[6]). With this method, we previously obtained a zinc (Zn) pattern with a minimum linewidth of 15 nm. This technique avoids deposition on the top of the probe tip, and is convenient for the fabrication of nanostructures of a single material (useful for the repair of photomasks). However, in the above method, lateral integration of various materials is not possible due to the diffraction of the far field light in the final step of pattern formation. To solve this problem, we propose as an extension to near field Optical-CVD (NFO-CVD); direct deposition of atoms by photodissociation of metalorganic gas with the optical near field. Since only the optical near field is utilized in this technique, it can be applied to deposit closely spaced nanostructures of various materials in a single step. In this letter, we demonstrate, to our best knowledge, the first result of nanoscale deposition of Zn by this method, i.e., photodissociation of gas-phase diethylzinc (DEZ) using optical near field generated at the probe tip.

The experimental setup is similar to one described previously.[4] Since the DEZ gas has strong absorption at $\lambda < 270$ nm (λ is the wavelength),[7] we used the second harmonic (SH) light of an argon ion laser ($\lambda = 244$ nm) as a light source for photodissociation of DEZ. The SH light was directed into the vacuum chamber through an ultraviolet (UV) fiber that had a pure silica core. The vacuum chamber was evacuated to below 1×10^{-5} Torr and then filled with a few mTorr of DEZ. Optically flat glass (Corning 7092) was used as the substrate.

Figure 1 shows the optical fiber probe fabricated for the present work. Although reliable fiber probes have conventionally been fabricated from an optical fiber with a germanium dioxide (GeO_2) doped core,[1] it is difficult to use for the present experiment due to high transmission loss (~ 96 dBm) for $\lambda = 244$ nm light. However, as shown in Fig. 1(a),

[a]Electronic mail: yoh@ae.titech.ac.jp
[b]Also with Japan Science and Technology Corporation, 687-1 Tsuruma, Machida, Tokyo 194-0004, Japan.

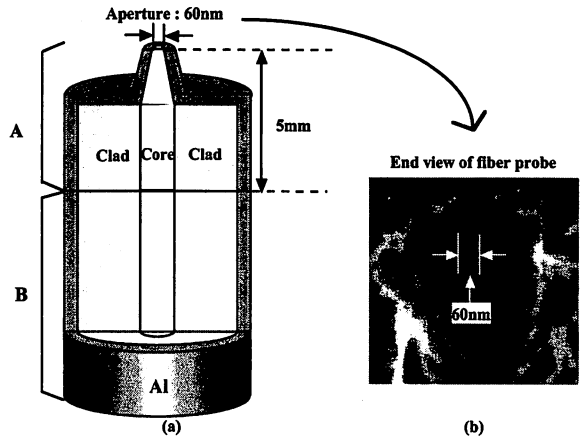

FIG. 1. Shape of the fiber probe. (a) Structure of fiber probe. A: Probe part made of a GeO_2 doped core fiber (transmission loss: 96 dBm at 244 nm). B: UV guide made of a pure silica core fiber (transmission loss: 1.1 dBm at 244 nm). (b) Scanning electron microscopy image of the fiber probe.

by splicing 5 mm of this fiber probe to an UV fiber with low transmission loss (~1.1 dBm), a low loss fiber probe was realized. After coating the fiber with 200 nm of aluminum film, an aperture formed using the focused ion beam.[8] The typical aperture diameter was 60 nm [Fig. 1(b)].

The shear-force technique[9] was employed to maintain the separation between the probe and the substrate to several nanometers during deposition. Upon deposition, the pattern was measured *in situ* by means of vacuum shear-force microscopy (VSFM).[5] All experiments were performed at room temperature.

Figure 2(a) shows the shear-force image of two closely spaced Zn dots deposited by the fiber probe shown Fig. 1(b). In Fig. 2(b), the cross-sectional profile taken along the white dashed line in Fig. 2(a), is presented. The DEZ gas pressure was 1 mTorr and the SH light power entering the fiber was 3 mW. The fiber probe was fixed at two positions on the glass substrate to illuminate with the optical near field. With an illumination time of 300 s, we fabricated two dots with full width at half maxima (FWHM) of 60 and 70 nm as is shown in Fig. 2(b). The FWHMs of the dots were comparable with the aperture diameter of the probe used which indicates that the lateral size of the dots is determined by the aperture diameter. Thus smaller dots can be expected in the future by using an optical fiber probe with a smaller aperture. Since the measured size of the fabricated dots includes the resolution

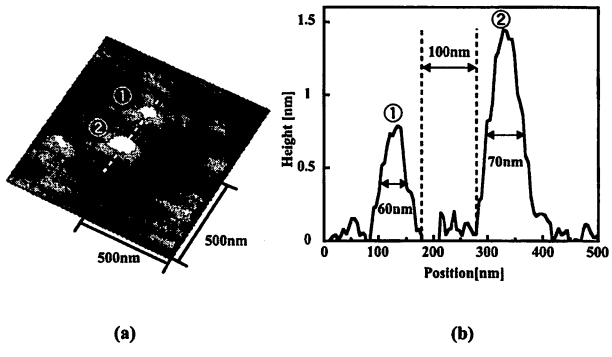

FIG. 2. Closely spaced Zn dots (① and ②) deposited on a glass substrate. (a) Shear-force image and (b) the cross-sectional profile along the white dashed line in (a).

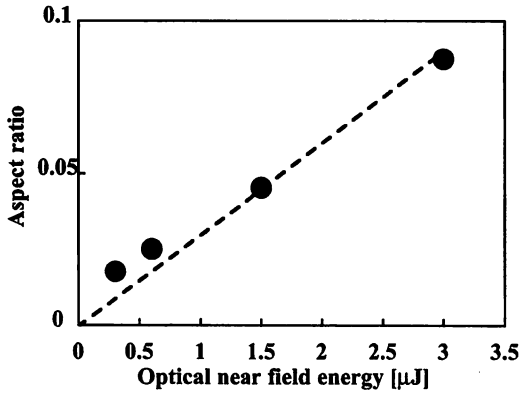

FIG. 3. Dependence of the aspect ratio of deposited dots on optical near field energy.

of VSFM, depending on the shape of the used probe, the intrinsic size of the dots in Fig. 2(a) may be smaller than the value estimated from Fig. 2(b). The distance between the two dots was 100 nm, close to the FWHMs of the dots. Such a contiguous deposition ability is essential to use this technique for realizing a nanophotonic integrated circuit in which a size-dependent optical near field is transmitted from one dot to the other. The separation is completely controllable using a nanopositioning system.

Next, we measured the growth rate by varying the illumination time while holding the gas pressure (1 mTorr) and input light power (15 mW) constant. The optical near field energy was estimated by SH light power×illumination time, where the SH light power at the fiber probe tip was measured with a broad-area Si photodiode (sensor area: 5.8 ×5.8 mm^2) placed in close proximity to the tip. Figure 3 shows the relation between the optical near field energy and the aspect ratio, i.e., the ratio of height to diameter of the dots. The aspect ratio increased in proportion to the optical near field energy, at the rate of ~0.03/μJ. The FWHM remained constant since it is determined by the aperture size, as was described above. Since, on the other hand, the height increased in proportion to the optical near field energy, the aspect ratio increased linearly as is shown in Fig. 3. These results show clearly that this technique makes it possible to control the size of the nanostructure.

One outstanding advantage of the present CVD is that various patterns can be fabricated using the scanning func-

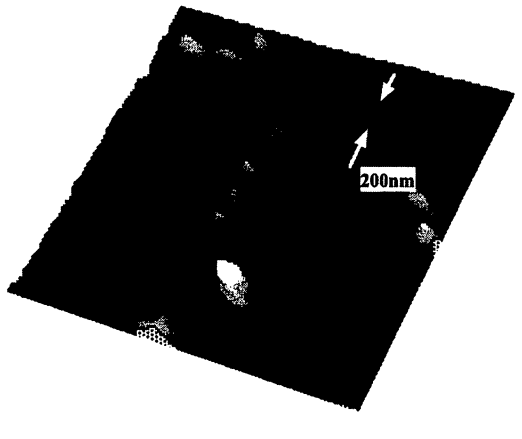

FIG. 4. Shear-force image of a T-shaped pattern of Zn deposited on a glass substrate.

tion of the probe in an optical near field microscope system. Figure 4 demonstrates this advantage. A T-shaped pattern was deposited by scanning the substrate at a speed of 10–50 nm/s. The height of this pattern was 16 nm. The width of the line in this pattern was 200 nm, including resolution of the VSFM. The FWHM is larger than that in Fig. 2(b) since a fiber probe with a larger aperture was used. Nevertheless, it illustrates the ability to deposit a variety of patterns.

One disadvantage of this method is that the probe tip is also gradually covered with deposited materials while fabricating a nanostructure on the substrate. In our experience, however, this only became a problem after a few hours of operation, during which time it would be possible to fabricate about 60 dots.

In conclusion, position specific nanoscale dots and a T-shaped pattern of Zn were fabricated by direct deposition with the optical near field. The lateral size of the dots depended exclusively on the aperture size of the fiber probe, with height being directly proportional to optical near field energy. Use of this technique makes possible the fabrication of various nanostructures with control over the position and size. In addition, since it is based on a photodissociation reaction, it is applicable to the deposition of not only Zn, but also of other metals, semiconductors, and insulators. As an example, we have demonstrated the deposition of zinc oxide, a semiconductor with blue light emission ability, on a sapphire substrate using this technique.[10]

The authors would like to thank Professor M. Konagai and Professor A. Yamada of Tokyo Institute of Technology for useful advice. They are grateful to S. Mononobe of Kanagawa Academy of Science and Technology for his irreplaceable help and advice in the art of making fiber probes and to H. Fukuda of Ricoh Co. Ltd. and Associate Professor J. D. White of Multimedia University (Malaysia) for useful discussions.

[1] *Near-Field Nano/Atom Optics and Technology*, edited by M. Ohtsu (Springer, Berlin, 1998).
[2] M. Ohtsu, Tech. Dig. Ser.-Opt. Soc. Am. **3749**, 478 (1999).
[3] D. Leonald, M. Krishnamurthy, C. M. Reaves, S. P. Denbaars, and P. M. Petroff, Appl. Phys. Lett. **63**, 3203 (1993).
[4] V. V. Polonski, Y. Yamamoto, M. Kourogi, H. Fukuda, and M. Ohtsu, J. Microsc. **194**, 545 (1999).
[5] V. V. Polonski, Y. Yamamoto, J. D. White, M. Kourogi, and M. Ohtsu, Jpn. J. Appl. Phys., Part 2 **38**, L826 (1999).
[6] D. J. Ehrlich, R. M. Osgood, Jr., and T. F. Deutsch, Appl. Phys. Lett. **38**, 946 (1981).
[7] R. R. Krchnavek, H. H. Gilgen, J. C. Chen, P. S. Shaw, T. J. Licata, and R. M. Osgood, Jr., J. Vac. Sci. Technol. B **5**, 20 (1987).
[8] T. Yatsui, M. Kourogi, K. Tsutsui, and M. Ohtsu, Proc. SPIE **3467**, 13 (1998).
[9] K. Karrai and R. D. Grober, Appl. Phys. Lett. **66**, 1842 (1997).
[10] G. H. Lee, Y. Yamamoto, M. Kourogi, and M. Ohtsu, Proc. SPIE **3791**, 132 (1999).

Journal of The Electrochemical Society, **147** (3) 1046-1049 (2000)
S0013-4651(98)10-118-0 CCC: $7.00 © The Electrochemical Society, Inc.

Electroless Nickel Plating for Nanofabrication in Optics

T. Kobayashi,[a] J. Ishibashi,[a] S. Mononobe,[c] M. Ohtsu,[c,d] and H. Honma[b,*,z]

[a]*Graduate School and* [b]*Faculty of Engineering, Kanto Gakuin University, Kanazawa-ku, Yokohama-shi, Kanagawa 236-0032, Japan*
[c]*Kanagawa Academy of Science and Technology, Takatsu-ku, Kawasaki-shi, Kanagawa 213-0012, Japan*
[d]*Interdisciplinary Graduate School of Science and Engineering, Tokyo Institute of Technology, Midori-ku, Yokohama-shi, Kanagawa 226-0027, Japan*

The electroless plating method has played an important role as an indispensable metallization technology for miniaturization of electronic components. This investigation discusses selective metallization on the fine area (nanometer size) by electroless plating. The experimental purpose is to fabricate a probe which is used for scanning near-field optical microscopy. The probe (cone angle 20°, probe size 4 μm) is comprised of an optical fiber covered with a metal film except for an aperture at the apex of the fiber. Nickel-plated probes with an aperture of 100 nm were fabricated by optimization of the plating conditions (dissolved oxygen concentration, bath temperature, and bath pH) and the addition of a catalytic poison into the plating bath.

Manuscript submitted October 29, 1998; revised manuscript received September 8, 1999.

Miniaturization and high efficiency of electronic devices depend heavily on advances in semiconductor-processing technologies. Currently, the semiconductor devices are scaled down to 0.25/0.18 μm as a design rule. Consequently, fine processing technology will enter into the nanosize fabrication stage in the near future. At present, thin-film formation by dry processes and pattern formation by lithographic techniques are applied widely. Application of electroless plating for fine wiring formation on semiconductor devices has been studied.[1-3] In this paper, we discuss the preparation of the fiber probe for a near-field optical microscope as a nanofabrication technique using electroless plating.

Resolution of an optical microscope is restricted by the wavelength of the incident light. According to the theory of the diffraction limit of Abbe, the limit of resolution is about 60% of the incident wavelength. However, the resolution of the optical microscope can be improved by detecting the evanescent field occurring at the vicinity of the surface of the object. Scanning near-field optical microscopy (SNOM) is realized based on this fact.[4,5] The resolution of SNOM depends on the size of the opening at the probe tip, which detects the evanescent field. When an optical fiber with a nanosized tip is used as the probe, the main factor determining the resolution of the SNOM imaging is the apex size of the probe. The sharp edges of the fiber must be coated with metal except for the apex region to suppress scattering and generation of low-spatial-frequency components of the near field. Vacuum deposition techniques, such as evaporation or sputtering, have been reported as methods for coating the fiber probe.[6,7] After the fiber is vacuum-coated with chromium and gold, the coating must be removed from the apex region. Conventionally, the fiber is dipped in an acrylic resin solution. When the fiber is withdrawn from the resin solution, a submicrometer apex region of the sharpened core is exposed, which is then etched by KI-I_2 solution. These procedures for probe-tip preparation are very complicated, however, and reproducibility is low. As a more efficient and simpler alternative, the applicability of electroless nickel plating for preparation of fine aperture on the protruded fiber is examined in this report.

Experimental

Protruded probe preparation method[8].—Optical fibers with 125 μm diameter cladding and 2 μm diam core, doped with GeO_2, were used. These fibers were sharpened by immersing them in an etching solution containing NH_4F (40 wt %), HF (50 wt %), and H_2O. We denote the volume ratio of etching solution as X, 1:1, which corresponds to the order of NH_4F, HF, and H_2O, respectively.

In this study, two types of etching processes were performed as shown in Fig. 1. For sharpening the core, the fibers were etched in a solution with a composition ratio of 10:1:1 for 90 min. Clad diameter could be reduced to 100, 50, and 25 μm by an etching solution with a composition ratio of 1.7:1:1. Figure 2 shows SEM micrographs of the sharpened fiber probe with a magnified view of the apex region. The radius of curvature is less than 5 nm and the cone angle is 20°. In this way, controlling the shape of the apex of the sharpened core can be achieved with high reproducibility. All treatments were performed at 25°C.

Electroless nickel plating process.—The sharpened fiber probes with flattened apex were coated with nickel by electroless plating. Pretreatment processes are shown in Table I. The basic bath composition and operating conditions of the electroless nickel plating bath are shown in Table II. The impurity in the electroless plating solu-

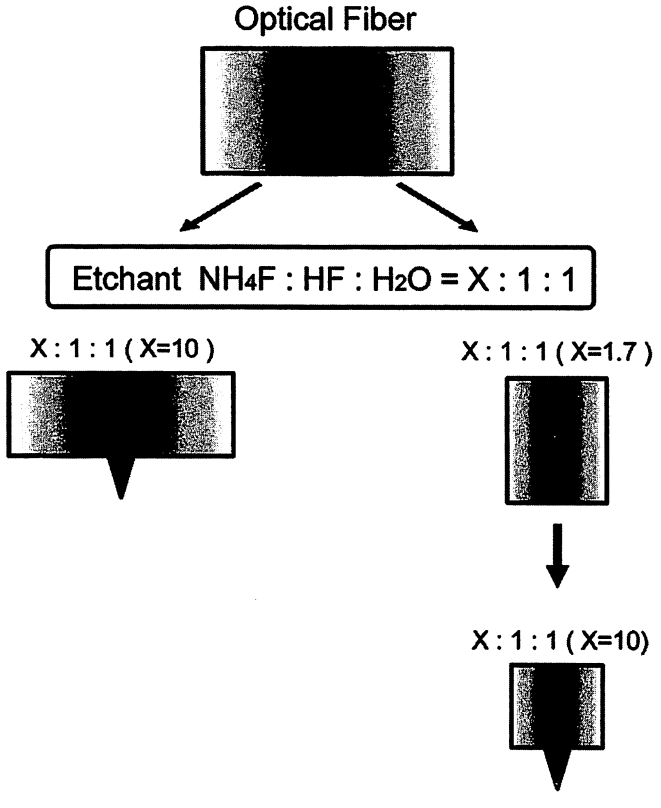

Figure 1. Schematic diagram of sharpening process for fiber probe.

* Electrochemical Society Active Member.
[z] E-mail: honma@kanto-gakuin.ac.jp

S0013-4651(98)10-118-0 CCC: $7.00

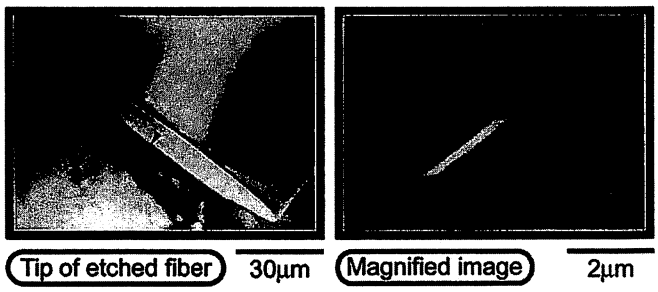

Figure 2. SEM micrographs of fine probe for SNOM.

tion could have influenced the deposition at the probe surface. To avoid this, the plating solution was filtrated through the membrane filter with a pore size of 0.2 μm.

The deposition morphology on the fine apex areas were observed by scanning electron microscopy (SEM). Dissolved oxygen concentration in the plating bath was measured under the plating condition using a dissolved oxygen (DO) meter (UD-1 type, Central Science Co., Ltd., resolution 0.01 ppm).

Results and Discussion

Influence of the DO concentration in plating solution.—It is a well-known fact that the deposition behavior on a small substrate area is influenced by the DO concentration in the plating bath.[9-11] The DO effect has been explained with a mixed potential theory.[12-14] Accordingly, we have examined the effect of DO in our plating solution. We have seen that when DO exceeds over 3 ppm, the entire area of protruded probe was not plated at all. This is because DO in the plating solution concentrates at the probe by nonlinear diffusion. Therefore, reduction of oxygen occurs preferentially and the nickel deposition reaction is suppressed. Nickel was deposited on the probe tip by introducing nitrogen gas in the bath before plating (DO 0.7 ppm) or by continuously purging with nitrogen during plating (DO 0.1 ppm) as shown in Fig. 3. The deposition configurations might have been delicately influenced by the several deposition-related factors at the protruded points of the probe, such as the differences of DO level, dynamics at the reaction interface, concentration of reaction species, etc.

Table I. Experimental conditions.

Optical fiber (ϕ 125 μm)	
↓	
Preparation for protruded probe	
↓	
Rinsing (25°C, 1 min)	
↓	
0.1 g/L $SnCl_2$ (25°C, 3 min)	Repeated two times
↓	
Rinsing (25°C, 1 min)	
↓	
0.05 g/L $PdCl_2$ (25°C, 3 min)	
↓	
Rinsing (25°C, 1 min)	
↓	
Electroless Ni plating	

Table II. Bath composition and plating conditions.

$NiSO_4 \cdot 6H_2O$	0.10 M
CH_3COONH_4	0.40 M
$NaH_2PO_2 \cdot H_2O$	0.20 M
Temperature	50°C
pH	5.0

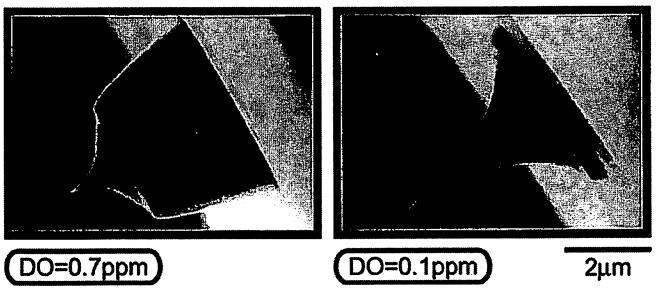

Figure 3. Effect of dissolved oxygen concentration on deposition configuration.

These are many differences between our observations and previously reported results,[10] which revealed that oxygen reduction did not inhibit metal deposition from an electroless nickel bath without any stabilizers. It is supposed that the oxygen is reduced only at the apex area of fiber below the order of submicron for electroless nickel plating. Moreover, the condition of nonlinear diffusion for DO is accelerated in this condition, since only three fiber probes are immersed into the 100 mL of plating bath. Thus, a lot of factors are involved to interpret these differences. Therefore, analysis of the electrochemical activity in this extremely small area is necessary to clarify these contradicting phenomena.

From these observations, DO was adjusted at 0.7 ppm by purging with nitrogen gas before plating to avoid the stirring effect and plating was performed for 15 min under the static condition in subsequent experiments.

Influence of the clad diameter.—We have studied the behavior of nickel deposition by using the fibers with different sizes of clad

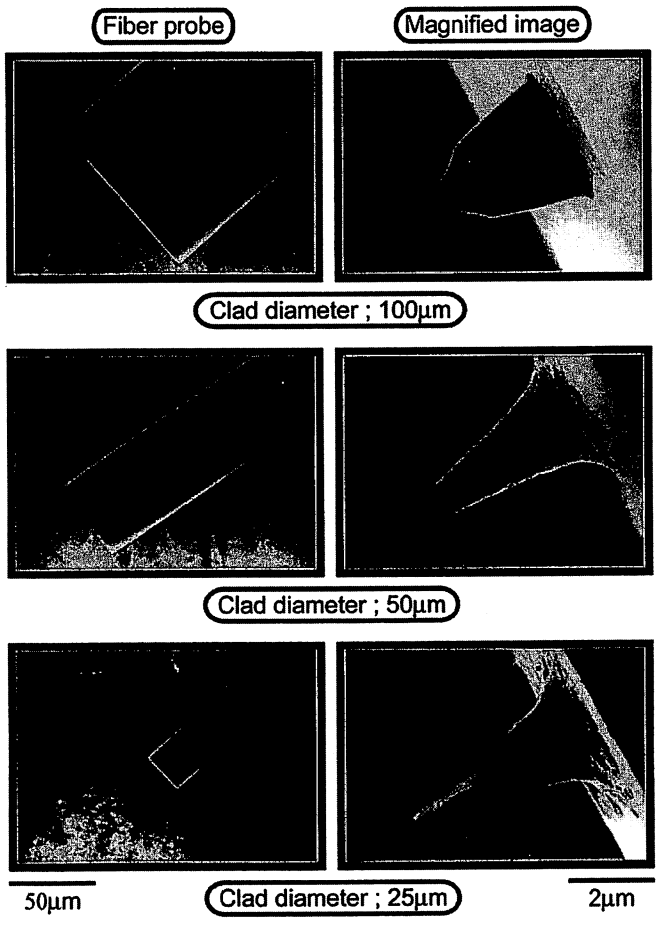

Figure 4. Influence of clad diameter on deposition configuration.

S0013-4651(98)10-118-0 CCC: $7.00

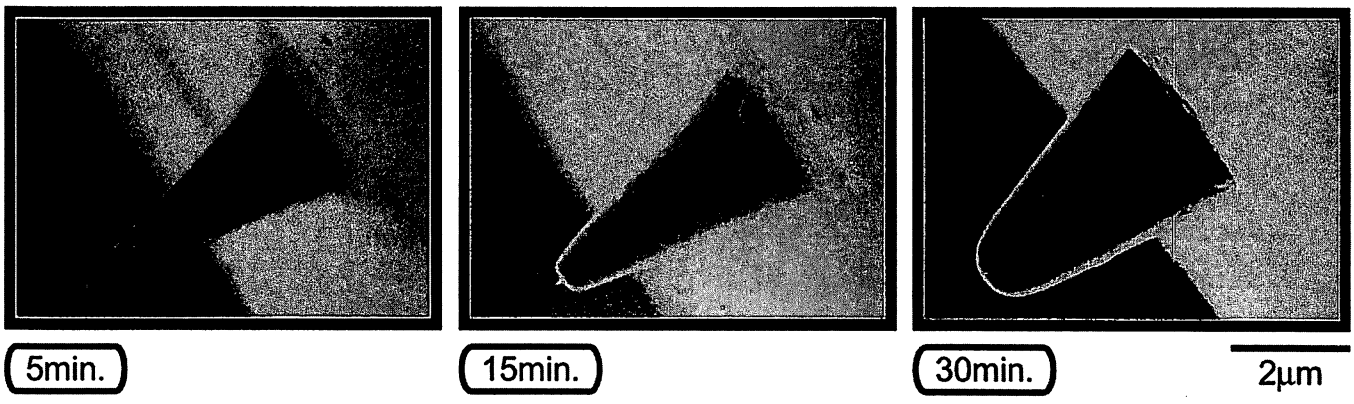

Figure 5. Relationship between plating time and deposition configuration.

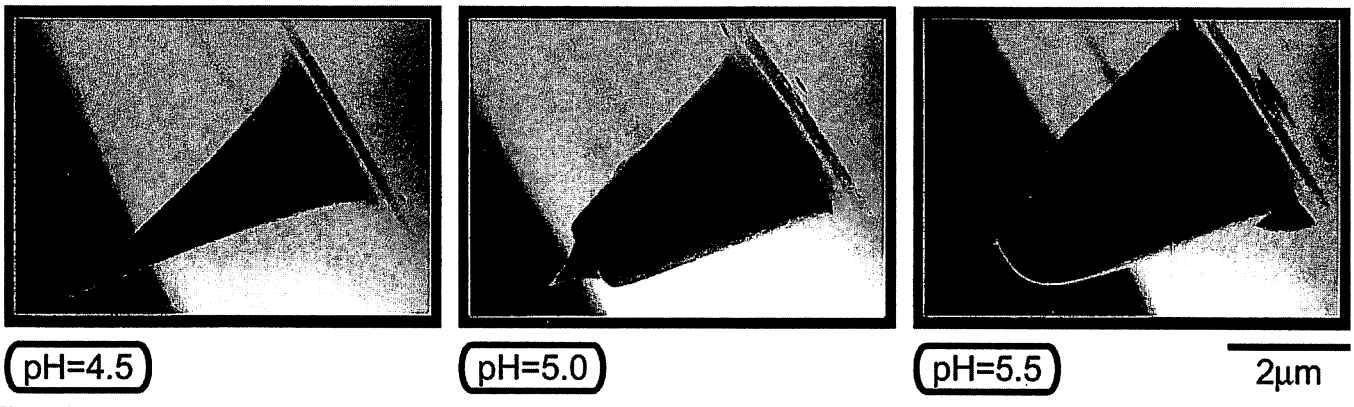

Figure 6. Relationship between bath pH and deposition configuration.

diameters, since reaction species and oxygen are concentrated by nonlinear diffusion at the protruded area. Figure 4 shows the dependence of plating on the clad diameter. Nickel coating was complete on the protruded area of the fiber probe with a clad diameter of 100 μm. However, no nickel deposition was observed up to a length of 1 μm from the apex at the protruded area for a 50 μm diam fiber. Nickel deposition at the protruded area did not occur at all with a clad diameter of 25 μm. These differences in deposition can be explained by the mixed-potential theory.[12-14] From these results we can conclude that when the clad diameter of the probe is greater than 100 μm, DO does not influence nickel deposition. However, the partial anodic current needed for oxygen reduction increases with the decrease in clad diameter. Therefore, the reduction of oxygen and the oxidation of reducing agent occur preferentially and nickel reduction is terminated.

From these results, we adjusted the DO to 0.1 ppm and 100 μm diameter of fiber was selected. Figure 5 shows the relationship between the plating time and deposition configuration. Ideal deposition configuration was obtained corresponding to 15 min. However, nickel gradually reached the apex area and all apex area was completely covered within 30 min.

Influence of pH and temperature of the plating solution.—The deposition morphology at the protruded area is greatly influenced by the condition of the plating solution. Accordingly, we studied the bath pH dependence of the deposition morphology at the probe tip at 50°C for 30 min. As shown in Fig. 6, nickel was not deposited at the apex of the protruded area below pH 4.5. On the other hand, thickness of deposition gradually increased with increasing pH. Ideal deposition for our purpose was achieved at the pH range 5-5.5.

Plating bath temperature is also a key factor for the deposition morphology at the protrusion area. Therefore, the bath temperature and pH dependence were investigated. As shown in Fig. 7, the ideal deposition morphology was obtained between the pH range 4.5-6 and temperature range 45-55°. Nickel was not deposited at the apex area below the bold line, nickel completely covered the apex area above the line.

Thus, the process window for our aimed shape is very narrow and reproducibility is low. These deposition differences can be attributed to various factors like chemical adsorption of reaction species, charge transfer, electrical double layer, adsorption and desorption of the

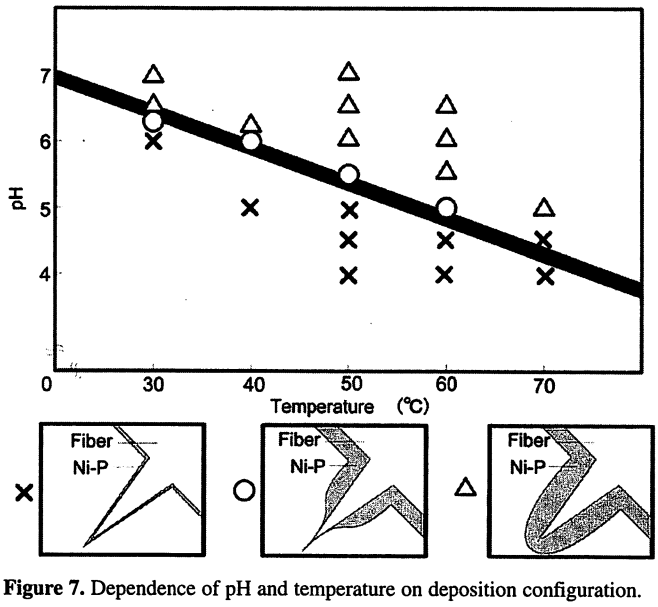

Figure 7. Dependence of pH and temperature on deposition configuration.

S0013-4651(98)10-118-0 CCC: $7.00

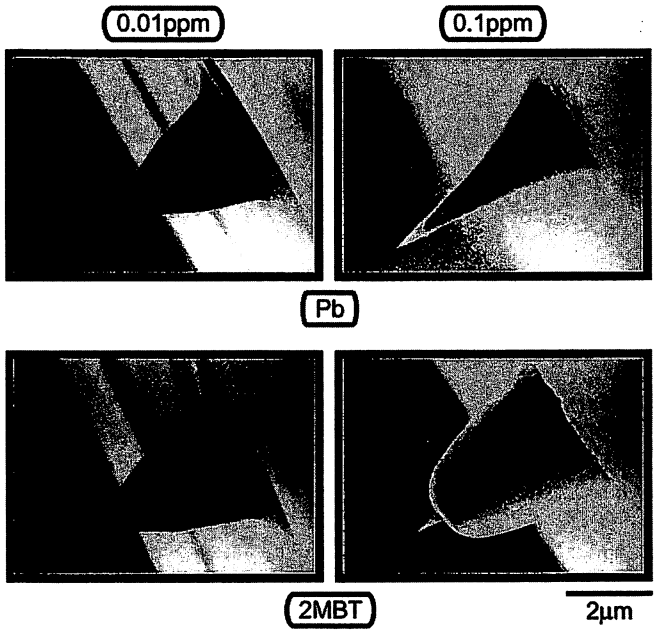

Figure 8. Effect of addition of catalytic poison on deposition configuration.

reducing agent, etc. These deposition-related factors at the vicinity of the protruded reaction site are greatly different from the bulk.

Effect of addition of inhibitors.—Our target is to shield the fiber by electroless nickel deposition except the apex region. To ensure controlability and reproducibility of the process, the effects of different catalytic poisons were evaluated. Lead (Pb) and 2-mercaptobenzothiazole (2-MBT) were selected as catalytic poisons. Effects of addition of lead are shown in Fig. 8. Appearance of the nickel deposit on the probe was not influenced by the addition of Pb below 0.01 ppm. Nickel deposition was inhibited only at the apex area when the amount of Pb was raised to 0.1 ppm. The plating reaction is completely inhibited at the protruded area by the addition of Pb over 0.5 ppm in the plating bath. Nickel was deposited on the fiber except the apex area by the addition of 1 ppm of 2 MBT. This configuration is ideal for our proposed purpose.

Thus, we confirmed that the addition of inhibitors in the plating bath which was reported elsewhere is an effective method for controlling the deposition condition even at the extremely fine area such as the apex of the fiber probe.

Conclusion

Preparation of the optical fiber probe for SNOM was studied as an application of electroless plating to coat a minute area. The following conclusions were reached

1. Nickel deposition occurred at the protruded area of the probe when the dissolved oxygen in the plating solution was lowered to 0.1 ppm.
2. Nickel deposition at the protruded area depends on the plating reaction area. The deposition morphology on the protruded point was greatly affected by the clad diameter of the fiber probe.
3. Shielding the fiber with electroless nickel, except the apex area, can be accomplished by the addition of a suitable catalytic poison into the plating solution.

Kanto Gakuin University assisted in meeting the publication costs of this article.

References

1. V. M. Dubin, Y. Shacham-Diamand, B. Zhao, P. K. Vasudev, and C. H. Ting, *J. Electrochem. Soc.*, **144,** 898 (1997).
2. H. Watanabe and H. Honma, *J. Electrochem. Soc.*, **144,** 471 (1997).
3. S. Abe, T. Fujinami, T. Aono, and H. Honma, *Hyomen Gijutsu*, **48,** 433 (1997).
4. S. Jiang, N. Tomita, H. Ohsawa, and M. Ohtsu, *Jpn. J. Appl. Phys.*, **30,** 2107 (1991).
5. S. Jiang, H. Ohsawa, K. Yamada, T. Pangaribuan, M. Ohtsu, K. Imai, and A. Ikai, *Jpn. J. Appl. Phys.*, **31,** 2282 (1992).
6. R. Uma Maheswari, S. Mononobe, and M. Ohtsu, *Appl. Opt.*, **35,** 6740 (1996).
7. S. Mononobe, M. Naya, T. Saiki, and M. Ohtsu, *Appl. Opt.*, **36,** 1496 (1997).
8. S. Mononobe and M. Ohtsu, *J. Lightwave Technol.*, **14,** 2231 (1996).
9. J. W. M. Jacobs and J. M. G. Rikken, *J. Electrochem. Soc.*, **135,** 2822 (1988).
10. A. M. T. van der Putten and J. W. G. de Bakker, *J. Electrochem. Soc.*, **140,** 2221 (1993).
11. A. M. T. van der Putten and J. W. G. de Bakker, *J. Electrochem. Soc.*, **140,** 2229 (1993).
12. M. Paunovic, *Plating*, **55,** 1161 (1968).
13. P. Bindra and J. Tweedie, *J. Electrochem. Soc.*, **130,** 1112 (1983).
14. P. Bindra and J. Roldan, *J. Electrochem. Soc.*, **132,** 2581 (1985).

微小領域への無電解ニッケルめっき

小林　健*，石橋純一*，稲葉裕之*，物部秀二**，大津元一**,***，本間英夫****

Electroless Nickel Plating to a Minute Area

Takeshi KOBAYASHI*, Junichi ISHIBASHI*, Hiroyuki INABA*, Shuji MONONOBE**, Motoichi OHTSU**,*** and Hideo HONMA****

The electroless plating method has played an important role as an indispensable metallization technology used in the miniaturization of electronic components. For example, it is applied to fabricate conductive patterns of fine circuits and via-holes in the PCB manufacturing process. In addition, since the mid-1980's it has often been reported that electroless plating is applicable for fine circuits of large scale integrations (LSIs).

In this study, we examined selective metallization on a minute area (size measured in nanometers) using electroless nickel plating. The experimental purpose was to fabricate a probe which is used in a scanning near-field optical microscope (SNOM). The probe (cone angle=20°, probe size=4 μm) is composed of optical fiber and has to be covered completely with metal film except for an aperture at its tip. The experimental results showed that nickel plated probes with an aperture of 100 nm could be fabricated by optimization of the plating conditions (dissolved oxygen concentration, bath temperature and bath pH) and the addition of catalytic poison into the plating bath.

Key Words: Electroless Nickel Plating, Optical Fiber, Dissolved Oxygen, Catalytic Poisoner

1．緒　言

半導体関連および半導体チップを搭載するプリント配線板関連技術の発展に伴い，電子機器の小型化・高性能化が急速に進んでいる。特に半導体関連技術では，設計ルールも0.35/0.25 μm から0.18 μm の微細加工へと移行しつつあり，今後の微細加工技術はまさしく“マイクロ・ファブリケーション”から“ナノ・ファブリケーション”へとシフトしてきた。

現時点における“ナノ・ファブリケーション”の主役は，ドライプロセスを用いた薄膜形成技術やパターン形成工程で利用されているリソグラフィー技術である。これらの技術に加え，数年前からは無電解めっきによる微細配線形成技術についても報告されており[1)-3)]，1997年にはIBMが電気めっきによる銅配線技術を実用化した。しかしながら，半導体関連分野以外での無電解めっきによる“ナノ・ファブリケーション”の報告例はほとんどない。

本報では，近接場光学顕微鏡で使用される光ファイバープローブをサンプルとして，無電解めっきによるnmオーダーの成膜性制御の可能性を検討した。

2．近接場光学顕微鏡について

光学顕微鏡の分解能は，Abbeの回折限界の理論から，測定光波長の約60%が限界と言われている。しかしながら，物質表面近傍(近接場領域：物質表面から光の波長以下の領域)に発生するエバネッセント場を検出することで，光の回折限界の制限を受けない光学顕微鏡が実現可能となる。これを近接場光学顕微鏡(Scanning Near-field Optical Microscope：SNOM)[4),5)]という。

物質表面に局在化しているエバネッセント場は光の波長と同程度であるため，これを検出するためには光の波長よりも小さな微小開口部(数十nm～数nm)を持つ光ファイバープローブを使用しなければならない。また，SNOMの測定分解能はプローブ先端の微小開口部の大きさに依存するため，開口部の微小径化に伴い高解像度化が実現できる。現在はSNOM用プローブとして先鋭角が小さいプローブが使用され，エバネッセント場を検出している。

*関東学院大学 大学院（〒236-0032 神奈川県横浜市金沢区六浦町4834）
Graduate School, Kanto Gakuin Univ. (4834, Mutsuura-cho, Kanazawa-ku, Yokohama-shi, Kanagawa 236-0032)
**神奈川科学技術アカデミー（〒213-0012 神奈川県川崎市高津区坂戸3-2-1 KSP E-408）
Kanagawa Academy of Sci. and Technology (KSP E-408, 3-2-1, Sakado, Takatsu-ku, Kawasaki-shi, Kanagawa 213-0012)
***東京工業大学大学院 総合理工学研究科（〒226-0027 神奈川県横浜市緑区長津田4259）
Interdisciplinary Graduate School of Sci. and Eng., Tokyo Inst. of Tech. (4259, Nagatsuta, Midori-ku, Yokohama-shi, Kanagawa 226-0027)
****関東学院大学 工学部（〒236-0032 神奈川県横浜市金沢区六浦町4834）
Fac. of Eng., Kanto Gakuin Univ. (4834, Mutsuura-cho, Kanazawa-ku, Yokohama-shi, Kanagawa 236-0032)

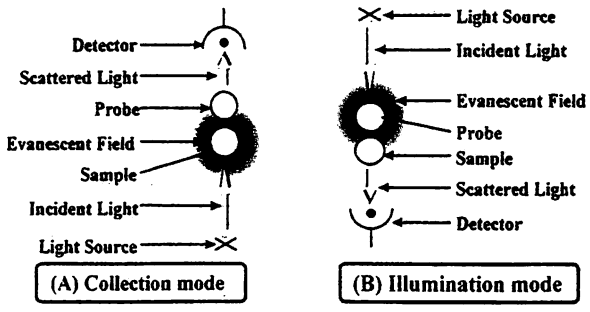

Fig. 1 Measurement principle of Scanning Near-field Optical Microscope(SNOM).

このように先鋭化された光ファイバープローブは，本用途以外に光メモリーディスクへの記録用素子[6)~9)]（ピット直径100 nm，記録密度45 Gb/inch^{2}が実現されており，将来的には100 Gb/inch^{2}までの記録密度が可能），発光形プローブ[10)]（GaAsのショットキー・コンタクトとしての利用），pHメーター等への適用が見込まれており，応用範囲は幅広い。

SNOMの測定原理を図1に示す。基本的な測定法として，(A)測定物質の裏面から固定波長の光を全反射で照射し，試料表面に発生するエバネッセント場を検出する方法(Collection mode)と，(B)プローブ先端にエバネッセント場を発生させ，STM同様，エバネッセント場の強度を減衰させないように測定物質表面をスキャンする方法(Illumination mode)の2種類がある。SNOMは高解像度の表面像が得られるだけでなく，微小領域における吸光度や発光強度分布等の分光特性の測定，生体試料および水溶液系内の観察にも応用可能である。

SNOMに使用するための光ファイバープローブは，プローブ側面に遮光膜を形成し，先端部に100 nm以下の微小開口部を形成しなければならない。これは，(1)測定物質表面近傍のエバネッセント場のみを検出する，(2)微小開口部と同サイズ程度で測定物質間と近接場相互作用を得る，という目的を達成するためである。このように，極めて小さな微小開口部を持つプローブを使用することで，SNOMの解像度は大幅に向上する[11)]。

プローブ側面の遮光膜形成および微小開口部形成法として蒸着法[12)]やSRC法[13)]が報告されているが，本報では生産性に有利な無電解めっき法を利用し，微小領域への成膜性について検討した。

3．実験方法

3．1 先鋭化プローブ作製法[14)]

本研究の評価試料として，クラッド部が純SiO_2（ϕ 125 μm），コア部はGeO_2を含有するSiO_2（ϕ 2 μm）により構成されている光ファイバーを使用した。この光ファイバーを5 cmに切断後，NH_4F(40 wt%)：

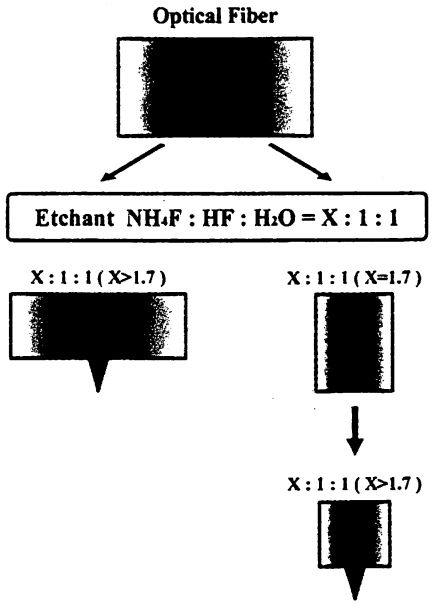

Fig. 2 Schematic diagram of optical fiber etching for probe manufacturing process[14)].

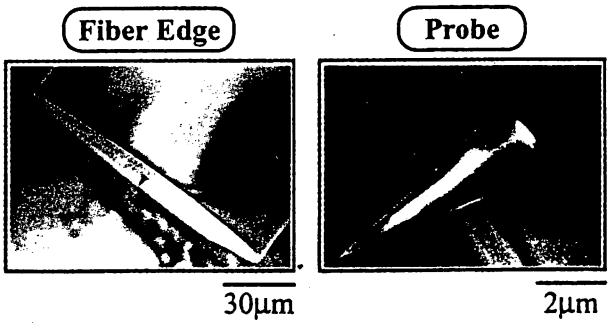

Fig. 3 SEM images of Scanning Near-field Optical Microscope(SNOM) probe.

HF(50 wt%)：H_2O＝X：1：1の体積比で調製したエッチング液に室温で90分浸せきすることにより，光ファイバー先端部の先鋭化を行った。

先鋭化のモデル図[14)]を図2に示す。エッチング後の光ファイバー先端の先鋭角は，エッチング液中のNH_4Fの体積比(X)に依存し，X>1.7の場合は光ファイバーの先鋭化が，X＝1.7でファイバー全体の小径化が可能となる。これは，NH_4Fの体積比がX>1.7ではコア部と比較してクラッド部のエッチング速度が速く，X<1.7ではコア部のエッチング速度が速いためである。なお，この先鋭化モデルからも類推できるように，光ファイバー先端部に形成した先鋭化プローブはファイバーのコア部のみから構成されている。

本実験ではNH_4Fの体積比をX＝10として光ファイバーのエッチングを行った。その結果，図3に示すように先鋭角20度，底部直径2 μm，全長4 μmのプローブを有する光ファイバーが作製可能となり，このサンプ

Table 1 Electroless nickel plating process.

Fiber etching
NH_4F:HF:H_2O=10:1:1 (25°C,90min.)
↓
Sensitizing
0.1g/L-$SnCl_2$ (25°C,3min.)
↓
Activating
0.05g/L-$PdCl_2$ (25°C,3min.)
↓
Electroless nickel plating

Repeated 2 times

Table 2 Basic bath composition and plating conditions.

$NiSO_4 \cdot 6H_2O$	0.10M
CH_3COONH_4	0.40M
$NaH_2PO_2 \cdot H_2O$	0.20M
Bath temperature	50°C
pH	5.0

ルを実験に供した。

3. 2 無電解ニッケルめっき工程

前節に示した工程により光ファイバーの先鋭化を行った後，表1に示す工程に基づき無電解ニッケルめっきを15分間行った。無電解ニッケルめっき浴の基本浴組成と操作条件を表2に示す。

本実験のような微小部への無電解めっきの場合，既報で述べたようにめっき液中の不純物が影響することが考えられる[15]。したがって，めっき液はポアサイズ0.2 μmのメンブランフィルターを用いてろ過を行った。めっき浴中の溶存酸素量はDOメーター(セントラル科学㈱製，UD-1，分解能：0.01 ppm)により測定した。また，析出形態，微小開口部の大きさは走査型電子顕微鏡(SEM)により観察した。

なお，ファイバープローブのニッケル成膜性は，めっき処理を行わないプローブサンプルのSEM像と比較することで，定性的に判断した。

4. 実験結果

4. 1 溶存酸素量の影響

微小領域への成膜において，析出状態はめっき液中の溶存酸素量(DO)に依存することが報告されている[16]。

そこで，成膜状態に及ぼすめっき液中の溶存酸素の影響について検討した。図4に示すように，DO=3.1 ppm以上では，プローブへのニッケルの析出は確認されなかった。これは，非線形拡散の影響によりめっき液中の溶存酸素が微小領域へ集中し，酸素の還元反応が優先的に起こり，金属の還元が抑制されるためと考えられる。

一方，めっき前に窒素を通気し，DOを0.7 ppmに制御した後，無かく拌状態でめっきを行うと，開口部は大きいものの，プローブ先端部の析出が抑制される傾向を確認した。また，めっき中も窒素を通気し続けることでDOを0.1 ppmに制御すると，無かく拌の場合と比較してニッケル析出の抑制部が拡大し，プローブの根本の部分のみが析出する形態を示した。これは，めっき液中の溶存酸素量の低下だけでなく，通気によるめっき液のかく拌効果のため，プローブ先端部での反応界面の拡散層の厚さや反応種の濃度等が異なることに起因すると推測している。

したがって，以下の実験ではめっき前に窒素を通気し，めっき中は無かく拌状態にすることでめっき浴中の溶存酸素量をおよそ0.7 ppmに制御してニッケルを成膜することとした。

4. 2 クラッド径の影響

このような微小領域への無電解めっきでは非線形拡散の影響を受けやすいため，金属の成膜状態が被成膜領域の面積に大きく依存すると考えられる。

そこで，図2に示したプローブ先鋭化工程において，まず光ファイバーの小径化を行うことで25，50，100 μmのクラッド径を持つファイバーを作製後，先端部に同一サイズのプローブを有するサンプルを作製し，成膜部面積と成膜状態の関係について検討した。その結果，

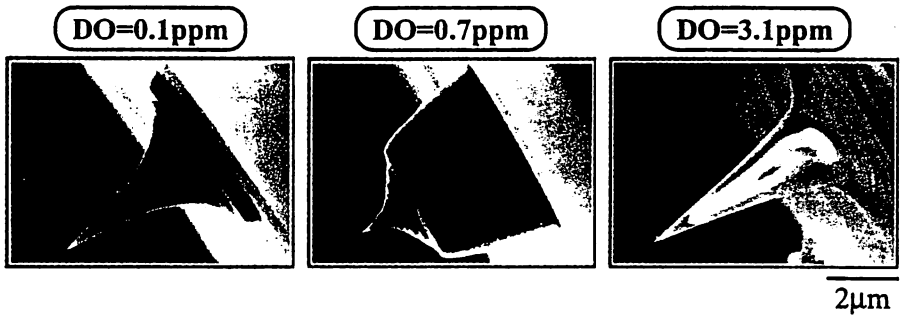

Fig. 4 Effects of DO concentration on deposits.

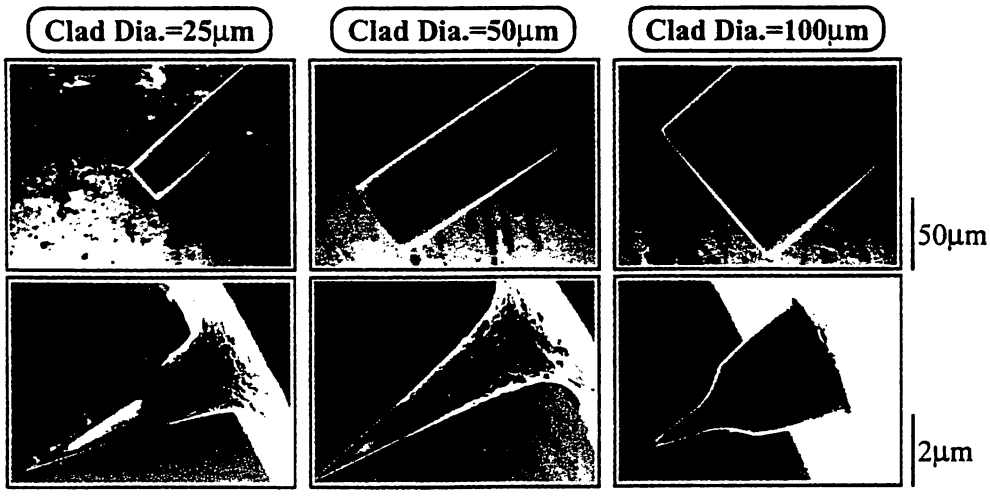

Fig. 5 Effects of clad diameter on deposits.

図5に示すように，クラッド径100μmのプローブの先端部の析出が抑制され，それ以外の領域はすべてニッケルで被覆することが可能であった。しかしながら，クラッド径が50μmの場合，プローブ先端からφ1μmまでの領域で，また，クラッド径が25μmのプローブではφ1.5μmまでの領域でニッケルはほとんど成膜されず，それ以外の部分の膜厚も極めて薄い成膜状態であることを確認した。

この現象を電気化学的に解釈すると，図6に示す混成電位モデルが考えられる。図6(A)のようにプローブ周辺のクラッド径が大きい場合，溶存酸素量を0.1 ppmに低下することで非線形拡散による酸素の影響が抑制され，プローブ先端部でニッケルが成膜する。しかしながら，図6(B)のようにクラッド径が小さくなると，相対的にプローブ先端での反応に関与する溶存酸素量が増加し，溶存酸素量を0.1 ppmまで低下させても酸素の局部アノード電流が増大し，酸素－還元剤系で混成電位が成立する。そのため，ニッケルの析出反応が抑制され，未析出部が生じたと考えられる。

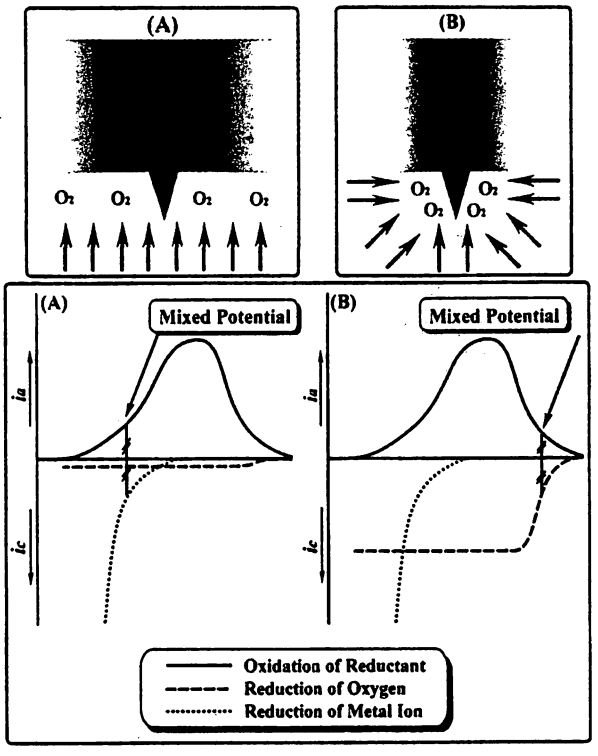

Fig. 6 Schematic diagram of DO dependence to the mixed potential.
(A) Bulk area (B) Small area

4. 3 めっき液のpHと温度の影響

以上の結果から，微小領域の析出状態がめっき浴中の溶存酸素量や反応部の面積に依存することを確認した。これらの条件以外に，無電解めっきの反応性に関与する因子，すなわちめっき液中の反応種の濃度やpH，温度も，この種のプローブ最先端部への析出に影響すると考えられる。

そこで，プローブ先端の析出形態に対するめっき浴pHの依存性について検討した。無電解ニッケルめっき浴のpHを4～7に変化した場合の各条件下における成膜状態を図7に示す。pH＝4.5以下ではプローブ先端部へのニッケルの析出は極めて少なかった。一方，pH＝5.0ではプローブの最先端部での析出量は少ないが，先端部よりφ0.5μm以上の部分でニッケルの析出量が増大し，析出膜厚は0.5μm以上となった。また，pH＝5.5以上の場合はプローブ全体がニッケルで被覆された。

以上の結果から，本実験のような微小領域への成膜の場合，めっき浴のpHに依存して図7に示す3種類の析出形態が得られた。

析出形態に及ぼすめっき浴成分以外の因子としてめっ

き浴温度が考えられる。そこで，浴温とpHを変化させた場合の析出形態の変化傾向を図8に示す。その結果，図中の○印で示した条件下で，図7のpH=5.0の場合のようにプローブ最先端部とそれ以外の部分で極端に膜厚が異なる析出形態を示すことを確認した。

このように，めっき条件により析出形態が変化する理由は，微小領域のめっきでは非線形拡散による反応種および反応阻害種の輸送，拡散層や電気二重層の分布状態が，バルク領域へのめっきと大きく異なるためと考える。

4. 4　触媒毒添加効果

以上のように，無電解めっきに関与する諸条件を最適化することにより，プローブ最先端部への成膜を制御することが可能であった。しかしながら，いずれも最先端部でニッケルが薄く成膜されているため，本実験の目的である微小開口部を有するプローブの作製には至らなかった。

そこで，めっき反応を抑制もしくは停止させる触媒毒作用を持つ化学種の添加により，微小開口部を有するプローブ作製を試みた。本実験では，無電解めっきの触媒毒として一般に知られている鉛および2-メルカプトベンゾチアゾール(2-MBT)を使用し，これらをめっき液に0.01～0.1 ppm添加することで，プローブ先端部のニッケル成膜状態を比較した。その結果を図9に示す。鉛を0.01 ppm添加した場合，無添加と同様の析出形態を示したが，鉛濃度を0.1 ppmとすると，プローブ全体で析出反応が抑制され，ニッケルの成膜が不可能となった。一方，めっき液中に2-MBTを0.01 ppm添加

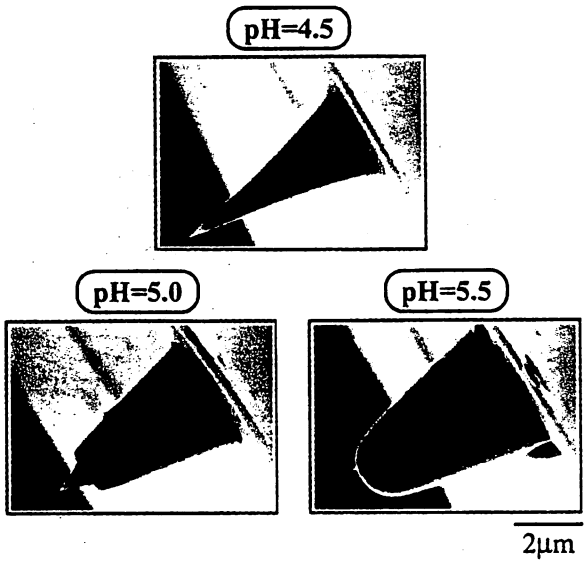

Fig. 7　SEM images of Ni plated probes with plating bath pH change.

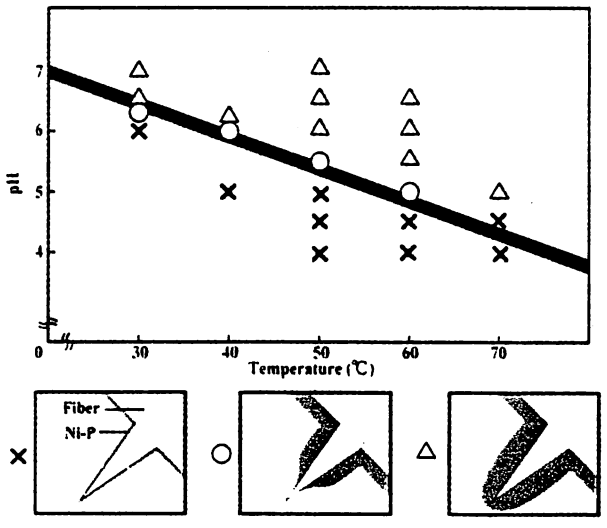

Fig. 8　Correlation between bath pH and temperature on plated probe.

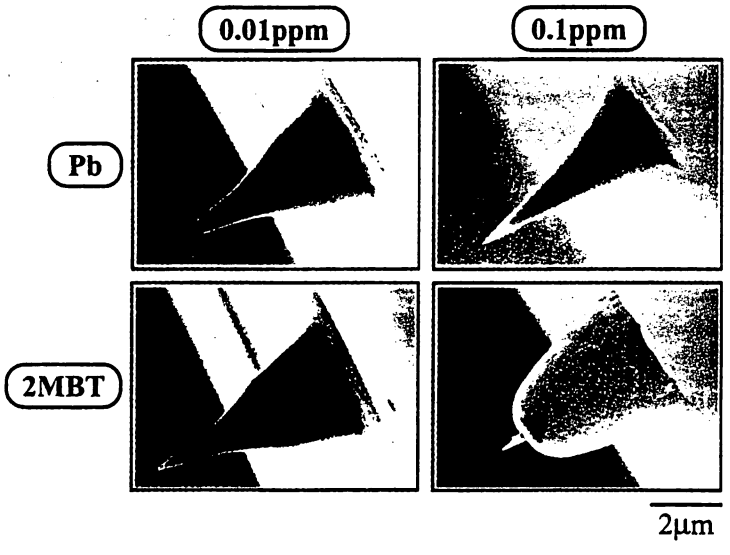

Fig. 9　Effects of catalytic poisoner on deposits.

して成膜した場合も無添加と同様の析出形態を示した。しかしながら，2-MBTの濃度を0.1ppmとすると，先端部からϕ100nmまでニッケルはほとんど析出せず，それ以外の部分でニッケルが1 μm以上の膜厚で成膜可能であった。

したがって，2-MBTのような触媒毒をめっき液中に微量添加することにより，微小開口部を有するプローブの作製が可能であることを確認した。また，この結果は触媒毒作用を持つ添加剤種の選択と，その濃度制御により微小開口部のサイズ制御の可能性も示唆している。

5. 結　論

微小領域への無電解めっきとして，SNOM用光ファイバープローブの作製について検討した結果，以下の結論を得た。

(1) めっき液中の溶存酸素量を0.1ppmに低下することにより，先鋭角20度，全長4 μmのプローブの先端部までニッケルが成膜された。

(2) ニッケルの成膜状態は析出反応部の面積に依存し，クラッド径100 μm以上のファイバープローブでは無電解ニッケルは先端部まで析出した。

(3) めっき液中に触媒毒として2-メルカプトベンゾチアゾール(2-MBT)を添加することにより，100nmの微小開口部を有するプローブを作製することが可能であった。

(Received July 12, 1999; Accepted October 15, 1999)

文　献

1) V. M. Dubin, Y. Shacham-Diamand, B. Zhao, P. K. Vasudev and C. H. Ting: *J. Electrochem. Soc.*, 144, 898 (1997)
2) H. Watanabe and H. Honma: *J. Electrochem. Soc.*, 144, 471 (1997)
3) 阿部真二, 藤波知之, 青野隆之, 本間英夫: 表面技術, 48, 433 (1997)
4) S. Jiang, N. Tomita, H. Ohsawa and M. Ohtsu: *Jpn. J. Appl. Phys.*, 30, 2107 (1991)
5) S. Jiang, H. Ohsawa, K. Yamada, T. Pangaribuan, M. Ohtsu, K. Imai and A. Ikai: *Jpn. J. Appl. Phys.*, 31, 2282 (1992)
6) E. Betzig, J. K. Trautman, R. Wolfe, E. M. Gyorgy, P. L. Fynn, M. H. Kryder and C.-H. Chang: *Appl. Phys. Lett.*, 61, 142 (1992)
7) Z. F. Liu, K. Hashimoto and A. Fujishima: *Nature*, 347, 658 (1990)
8) Z. F. Liu, K. Morigaki, T. Enomoto, K. Hashimoto and A. Fujishima: *J. Phys. Chem.*, 96, 1875 (1992)
9) S. Jiang, J. Ichihashi, H. Monobe, M. Fujihira and M. Ohtsu: *Opt. Commun.*, 106, 173 (1994)
10) 大津元一: 応用物理, 65, 2 (1996)
11) 物部秀二, 納谷昌之, R. ウママヘスワリ, 斎木敏治, 大津元一: Proceedings of 13th Meeting on Lightwave Sensing Technology, p. 83 (1994)
12) 物部秀二, R. ウママヘスワリ, 斎木敏治, 納谷昌之, 大津元一: 第55回応物予稿集, 2, 461 (1994)
13) 物部秀二, 大津元一: 第43回応物予稿集, 3, 885 (1996)
14) S. Mononobe and M. Ohtsu: *J. Lightwave Technol.*, 14, 2231 (1996)
15) 小林　健, 阿部真二, 石橋純一, 本間英夫: 回路実装学会誌, 12, 492 (1997)
16) J. W. M. Jacobs and J. M. G. Rikken: *J. Electrochem. Soc.*, 135, 2822 (1988)

Jpn. J. Appl. Phys. Vol. 38 (1999) pp. 6713–6720
Part 1, No. 12A, December 1999

Nanometer Level Resolving Near Field Optical Microscope under Optical Feedback in the Observation of a Single-String Deoxyribo Nucleic Acid

Uma Maheswari RAJAGOPALAN[1,*], Shuji MONONOBE[1], Kenji YOSHIDA[2], Mamoru YOSHIMOTO[2] and Motoichi OHTSU[1,2]
[1]*Kanagawa Academy of Science and Technology, KSP East 408, 3-2-1 Sakado, Takatsu-ku, Kawasaki 213-0012, Japan*
[2]*Tokyo Institute of Technology, 4259 Nagatsuda, Midori-Ku, Yokohama 226-0027, Japan*

(Received August 23, 1999; accepted for publication September 27, 1999)

We present the observation results of a single string deoxyribo nucleic acid (DNA) obtained by a collection mode near field optical microscope (NOM) operated under constant distance mode with the optical near field intensity as the feedback signal. The observed width of the narrowest string is around 4 nm. To our knowledge, this is not only the successful optical observation of a single string DNA by purely optical means but also under such high resolving capability. This high resolution is mainly attributed to the special care taken during the preparation of the sample and of the probe to avoid unwanted scattered light. The probe efficiently picks up the high spatial frequency component of the scattered near field and simultaneously rejects out effectively the lower spatial frequency components.

KEYWORDS: near-field optical microscope, collection mode, constant distance mode, optical feedback, efficient far-field rejection probe, ultra-flat sapphire surface, DNA string, nanometer resolution

1. Introduction

In recent times, the field of near-field optics has been gaining a lot of attention for its use as a microscope providing resolution comparable to that of the electron microscope[1–5] and in various other fields such as spectroscopy in investigating and diagnosing structural defects of p-n junction,[6] quantum dot and other semiconductor IC devices.[7–9] In the field of biology also, its potential as an investigative tool has been fairly established.[10–15] The smallest resolved feature that has been observed till now is in the order of 20 nm.[16–21] Based on our system function calculation of illumination-mode (i-mode) near-field optical microscope (NOM),[22] it has been found that our i-mode NOM system[21] has the capability of attaining subnanometer resolutions.

In actual biological applications, there is a need for example in the case of manipulating bio-molecules such as actin which forms the fundamental unit of muscles, the sizes involved are in the order of a few nanometer. Therefore, there is a strong need that the resolution or the smallest observable feature needs to be observed has to be increased to the level of a few nanometers. The current study has been done with the motivation of achieving the ultimate resolution of the current NOM system. For this purpose, deoxyribo nucleic acid (DNA) sample has been chosen as the sample. As it is well known, DNA forms the fundamental building block of life and also a lot of attention has been paid in manipulating at the level of a single string of DNA. A single DNA string of plasmid type has got an approximate lateral width of 4 nm and an height of around 2 nm.[24] The height and the width of the structure are just suitable in demonstrating the ultimate capability of our NOM system.

Till now, scanning probe microscopes such as scanning tunneling microscope (STM), atomic force microscope (AFM) have been successful in conducting observation of DNA under high resolution to the order of a few nm width.[25–27] Recently, the shear force microscope has also been successful in imaging DNA strings with the narrowest strings being around 20 nm.[28] With NOM, the only observation that has been reported is on chromosomes which are much larger structures (order of 100 s of nms).[28] In that observation, the chromosomes have been labeled with rhodamine dye and the observation has been done using fluorescence as the tool employing shear force feedback for control. Therefore, the imaging of a single string of DNA with NOM has not been reported yet. Such a study is extremely important as it will open up the possibility of conducting and manipulating at the molecular level by NOM in the near future. Moreover, it has been recently noticed that using shear force or any auxiliary type of signal for feedback has the effect of introducing artifacts into the image.[29] We recently noticed the effect of differentiating type effect due to shear force feedback which we will report separately.

In this study for conducting observation of DNA, collection-mode (c-mode) NOM has been chosen. The main reason for the choice of this mode of NOM operation is as follows: In c-mode NOM, the sample is illuminated under total internal reflection and an optical near field is generated on the sample surface and this field decays on going away from the surface. This optical near field is distributed only within a region determined by the size of the fine features of the sample.[30] This field is scattered by a probe for which generally a tapered fiber based sharpened tip is used. Collecting a part of the locally scattered field intensity and utilizing its decaying characteristic as an effective feedback control signal eliminates the need for an auxiliary feedback control signal. Using an efficient probe which can scatter and collect efficiently optical near field and at the same time rejecting the background scattered field from the substrate of the sample, we will demonstrate that a single string DNA could be observed with high resolution and high contrast. Section 2 gives the experimental details including the system, the probe and sample for which special care has been taken during the preparation. Section 3 discusses the results on high resolution observation and discusses about the importance of localized field interaction in enhancing the resolution by reducing the unwanted scattered light. Finally, summary is given in §4.

2. Experiments

2.1 *Experimental system*

Figure 1 shows a simple schematic view of the experi-

*Corresponding author. Present address: Integrative Neural Systems, Brain Science Institute, RIKEN, 2-1 Hirosawa, Wako, Saitama 351 0106, Japan. Email: uma@brain.riken.go.jp

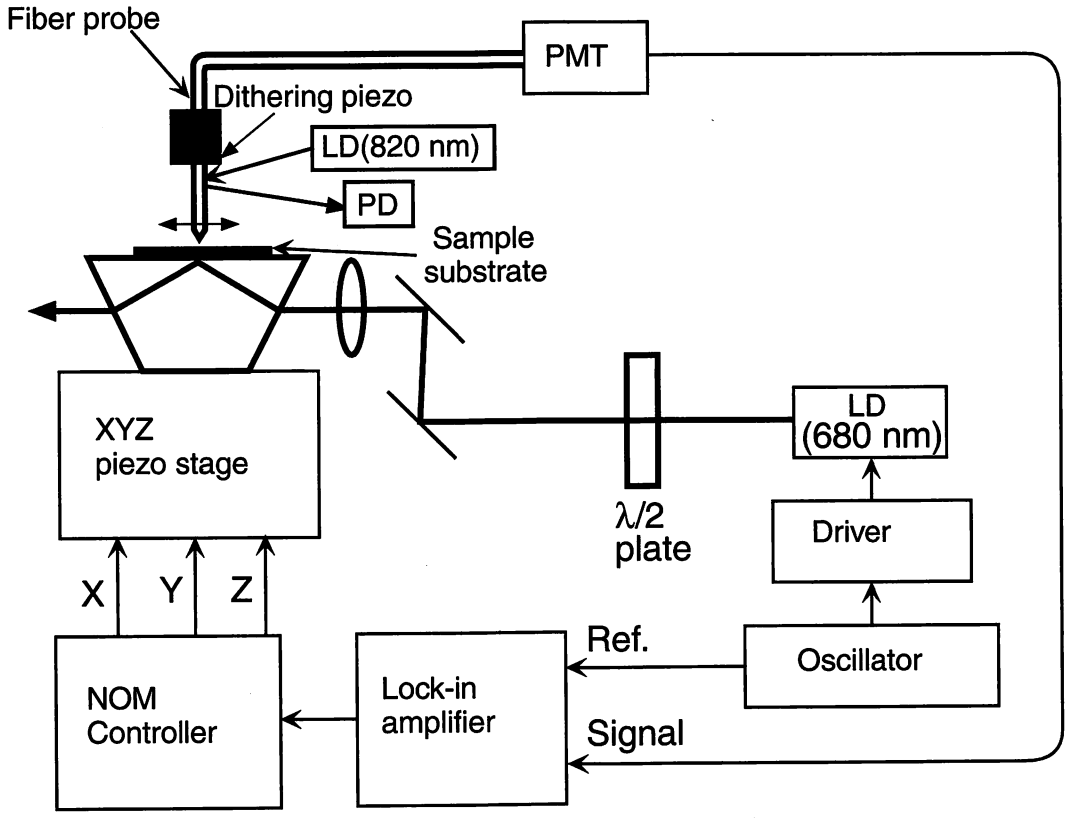

Fig. 1. A schematic of the experimental system of a collection mode NOM. Here the laser diode LD (820 nm) and the photodetector (PD) have been used for shear force detection to perform only the initial calibration of sample-probe observation by dithering the piezo transducer attached to the probe. During the actual conduction of the observation of DNA, the dithering had been stopped and the LD (820 nm) was not used in order not to introduce any artifacts.

mental arrangement of a collection mode NOM. The sample substrate was mounted on an xyz piezo stage operated under closed loop with the built-in sensors (PI-Polytec) having a span of 100 μm × 100 μm in the lateral direction and a span of 5 μm in the vertical direction. A dove prism was used for generating the optical near field on the sample surface. Sample is mounted on the prism with a sandwich of index matching oil. Light from a laser diode (LD) of wavelength 680 nm is made to incident normally on the surface of the prism and the optical near field is generated on the sample surface, which is localized over the prism surface.

The optical near field is scattered by bringing the probe closer to the surface of the sample. A lens was used so that the light is focused onto a spot in the vicinity of the probe. During the experiments, the spot size was approximately around 70 μm and a half-wave plate was used to control the state of polarization of the light incident on the sample. Here the fiber probe was attached with a dithering piezo device to monitor shear force[31,32] for initial calibration of the sample-probe separation. The dithering with its direction as indicated in the figure, was monitored by an additional LD of 820 nm and the dithering vibration detected by a pin photodiode attached with a cylindrical lens.

The scattered optical near field is picked up by the same probe to be detected by a photomultiplier tube. In order to improve the signal to noise ratio, the light from LD was modulated at 20 kHz and the detection was done with a lock-in amplifier. The detected lock-in output signal of optical near field intensity variation as a function of the sample-probe separation is shown by the dashed line in Fig. 2. The solid line

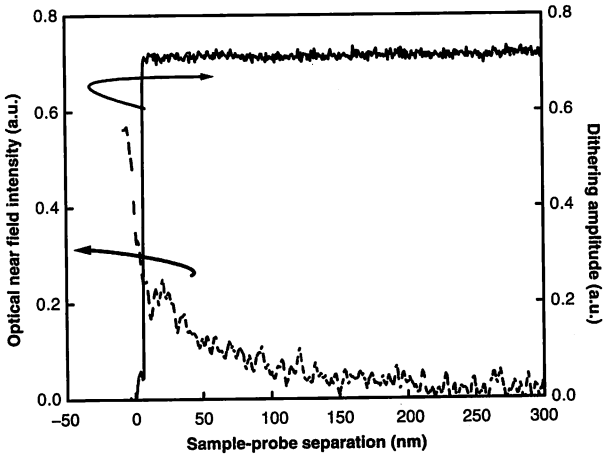

Fig. 2. Variation of the optical near field and the dithering amplitude as a function of the sample-probe separation. The solid line indicates the dithering amplitude and the dashed line indicates the optical near field intensity.

corresponds to the variation of the dithering amplitude taken simultaneously for reference.

As seen the variation of the optical near field intensity shows two kinds of slope: one slowly varying tail part beyond 20 nm extending upto around 100 to 150 nm and the other one steeply varying part that is localized very close to the sample surface. The steep variation is quite sensitive to the sample-probe separation and is localized within a region of around 10 nm of the surface. This curve is quite reproducible. This steep linearly varying region of the optical near

field intensity variation was used for maintaining the sample-probe separation constant during the two dimensional lateral scanning of the sample surface.[33] It should be pointed out that during the scanning operation, the lateral dithering was stopped in order not to cause any interference with the actual scanning operation. The resulting two dimensional scanning gives information about the surface variation of the sample which corresponds to the local field scattering enhancements happening between the probe and the sample.

2.2 *Probe*

The probe fabrication involves two steps: first sharpening of an optical fiber into pencil shaped structure and second coating in a vacuum evaporation unit.

2.2.1 *Fabrication of a pencil shaped probe*

Figure 3 shows a scanning electron micrograph of a typical pencil shaped probe with (b) showing the magnified view of the top most region shown in (a) used in the observations. In figure (a), the area between two the dashed lines corresponds to the core. The probe consists of two tapered structures with the initial taper having a cone angle of 62° and a further tapered apex region with a cone angle of 17°. The method of fabrication involves selective chemical etching based on buffered hydrofluoric acid usually employed in IC fabrication.[34] This probe was fabricated from a specially designed fiber having a germanosilicate doped core, pure silica and a fluorine doped silica support. The design was done by Mononobe *et al.* so as to control the shape of the etched fiber into a shape suitable for experimental applications of NOM. A detailed description of the design procedure and the results of etching could be found in ref. 35. In spite of the fact that, it is possible to fabricate various types of probes with the designed fiber,[36] the pencil shaped structured probe has been chosen for the following reasons:

(1) Reproducibility of the apex diameter, taper angle and the length of the tapered apex part with almost 100%;
(2) Based on experimental experience, after coating, the apex region is found to be mechanically strong;
(3) Further, pencil shape has been found to be just suitable for its efficient blocking of scattered background from the substrate for during the metal coating process this shape is found to be efficiently coated to its sides.

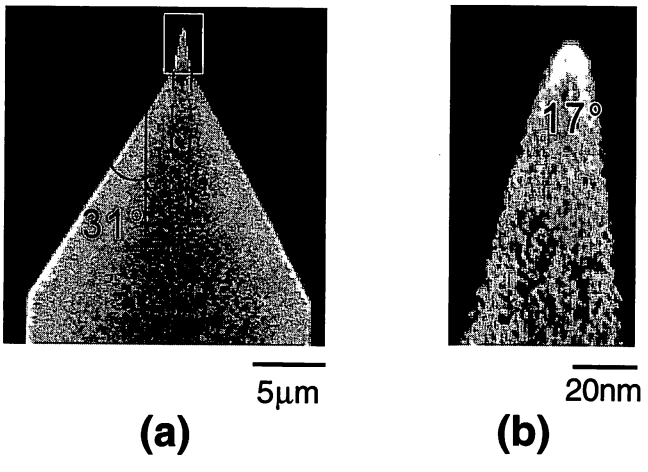

Fig. 3. A SEM micrograph of the pencil shaped probe showing (a) the double tapered structure and (b) a magnified view of the tapered apex region. The area between the two dashed lines in (a) corresponds to the fiber core.

The pencil shaped probe is etched in such a way that till around 500 nm to the apex region, the cone angle is larger around 60° to 80° so as to reduce the optical transmission loss during propagation inside the fiber. Around the apex region, where the probe comes into close contact with the sample surface, the cone angle was optimized to be less than 40° to have increased scattering efficiency for high spatial frequency components of the optical near field and at the same time to be mechanically stable. In actual experiments of successful observations, probe with a cone angle of 30° was used.

2.2.2 *Metal-dielectric-metal coating to fabricate efficient far-field rejection probe*

The pencil shaped probe fabricated by etching, is next coated in a vacuum evaporation unit. The coating consists of three layers with an outer aluminum (Al) coat, a middle layer of magnesium fluoride (MgF_2) and an inner thin coating of silver (Ag). A schematic of the coated apex region of the coated probe is shown in Fig. 4 with the respective thickness of each substance. The above materials have been chosen based on the following facts:

(1) The outer most Al coating with a fairly high thickness of 200 nm in comparison with the skin depth which is of the order of a few tens of nanometers[37] is coated for blocking background unwanted scattered light;
(2) The middle layer of MgF_2 has a lower refractive index of 1.3 compared with that of the sharpened core and forms an efficient cladding. It not only protects the deterioration of the innermost thin layer of silver on exposure to air but also plays some role in suppressing the far-field. Based on experimental experience, adding a coat of MgF_2 strongly improves the scattering efficiency of the probe and also due to its soft nature, the robustness of the probe.
(3) The innermost thin layer of Ag is mainly for enhancing the scattering efficiency of the three dimensionally localized near field around the sample. Ag has got an high reflectivity at the region of wavelength used and also has got a higher dielectric constant. Further, based on the MMP expansion method based calculations of Novotony *et al.*,[38,39] the field confinement for a tapered probe (equivalent to our structure) with a thin layer of silver coating till the apex, i.e., an entirely Ag coated tapered structure, is highly concentrated in both the lateral and vertical or z-directions (refer to Fig. 4 of ref. 38).[40] The field confinement of our probe in the z-direction could be inferred directly from Fig. 2 where there is a strong near field intensity enhancement very close to the sample surface. In order to avoid any misunderstanding, we would like to point out that the field is parallel with respect to the prism surface and hence perpendicular with respect to the metal coating. Therefore, the field confinement referred in our case is believed to be originating from the edge of the protruding Ag tip against its surround. Furthermore, it should be pointed out that the results of the calculations of ref. 38 could not be exactly applied as the actual probe used in our experiments differs considerably a lot from the one used in the model. Such field enhancement effects by purely metal probes have also been reported.[41,42] We have also found other experimental evidence for the near field intensity enhancement

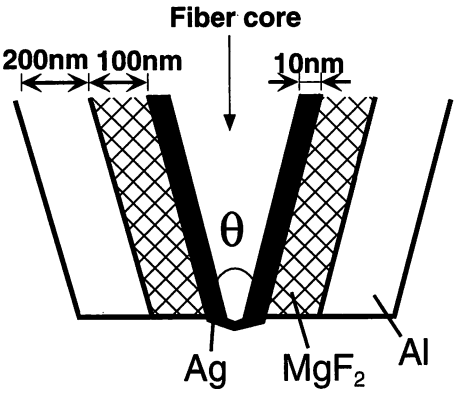

Fig. 4. A schematic view of the coated apex region with the inner most region being Ag film. The middle layer corresponds to MgF_2 and the outer most layer corresponds to Al coat.

for probes having entire metal coating.[43]

2.3 *Sample preparation*

The double stranded plasmid DNA with a ring structure (puc 18 and 2868 base pairs) has been used as the sample. It was diluted with distilled water to a final concentration of 5 ng/μl. A quantity of 2 μl of this diluted DNA solution was dropped onto the center of a wet-treated sapphire surface. Next this surface was blown dried with compressed air.

In AFM observations, generally, cleaved mica surface is used for its atomic smoothness. However, mica plate is unstable on exposure to air or water. Recently, Yoshimoto *et al.*,[44] have succeeded in producing ultrasmooth sapphire surface reproducibly by epitaxial growth which is stable both in air and water for a considerable duration. The surface has a staircase like step structure whose step height and terrace width can be controlled by a careful choice of the experimental conditions. However, as such the sapphire surface is hydrophobic while the organic DNA molecules are hydrophilic. So, it is necessary to first make the surface of the sapphire substrate hydrophilic. For this purpose, the sapphire surface was treated with sodium diphosphate (0.5 mol/l) for a few minutes and then rinsed with distilled water and then naturally dried in air (for details, refer to ref. 27).

Here, the sapphire surface itself is highly homogeneous having regular staircase like structure. There is very small or almost nil random height variations of the surface. The variation of the surface mainly is from the distribution of sodium diphosphate. This variation leads only to the formation of DNA strings of different structures on different places of the surface. There are also parts on the surface where there is no DNA strings getting attached leaving the sapphire surface free. Actually, We could get very clear image of sapphire surface showing the staircase like structure. Details about the imaging of sapphire surface structure is under preparation.

Figure 5 shows the atomic force microscope image of the ring structure DNA fixed on the wet-treated sapphire surface. The multi-step underneath structure of the sapphire substrate is seen on the background and step edge is indicated by the dashed white line with the double headed arrow. In this case, the step height is around 0.2 nm and the terrace width varies from 100 to 120 nm. Depending on the surface conditions, the DNA strings form into either a single loop or complicated supercoiled structures. Various looped or coiled ring structures of DNA could be clearly seen to be scattered on the surface. The long white arrows indicate the supercoiled structure while the short white arrow indicates a simple loop structure. The observed height of the DNA string was found to be 1 to 1.5 nm. The width of the narrowest string as indicated by the two black unfilled arrows is found to be less than 10 nm.

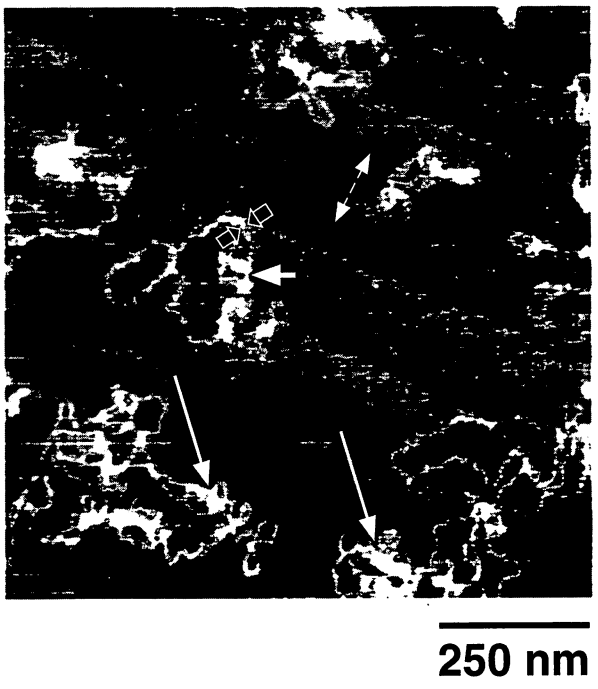

Fig. 5. Atomic force image of DNA fixed on a sapphire substrate. The long white arrows indicate the supercoiled structure. The short white arrow indicates a simple loop structure. The dashed double headed arrow indicates step edge of the substrate. The width of the string as indicated by the two black arrows is less than 10 nm.

3. Results and Discussion

In order to conduct the observation of DNA, the terrace width and step height of the surface have been chosen carefully. The terrace width of 100 nm with a step height of 0.2 nm used in AFM observations introduce strong scattered background in optical observations indicating on the other hand the high sensitivity of our probe even to atomic level variations of the optical near field. In order to avoid such scattered contributions, the terrace width had been adjusted to be 1 to 1.5 μm and the step height to be around 2 nm by varying the annealing conditions while fabricating the sapphire substrate.

Figure 6(a) shows the near field optical image of DNA. The image was obtained under a constant sample-probe separation of around 5 nm with the optical near field intensity as the control signal (refer to Fig. 2). Based on imaging sapphire step structure where DNA rings are absent, it has been found that the optimum sample-probe separation to observe the step surface with good contrast has been found to be approximately the step height or less than that. The results of the investigation regarding the criterion for optimum sample-probe separation will be published elsewhere.

In the image, the bright string structures correspond to DNA strings. The short white arrow corresponds to a single string structure while the long white arrow indicates a supercoiled structure. The pixel size is 7 nm × 7 nm. The direction of the electric field vector ($\boldsymbol{E}$) and the direction of propaga-

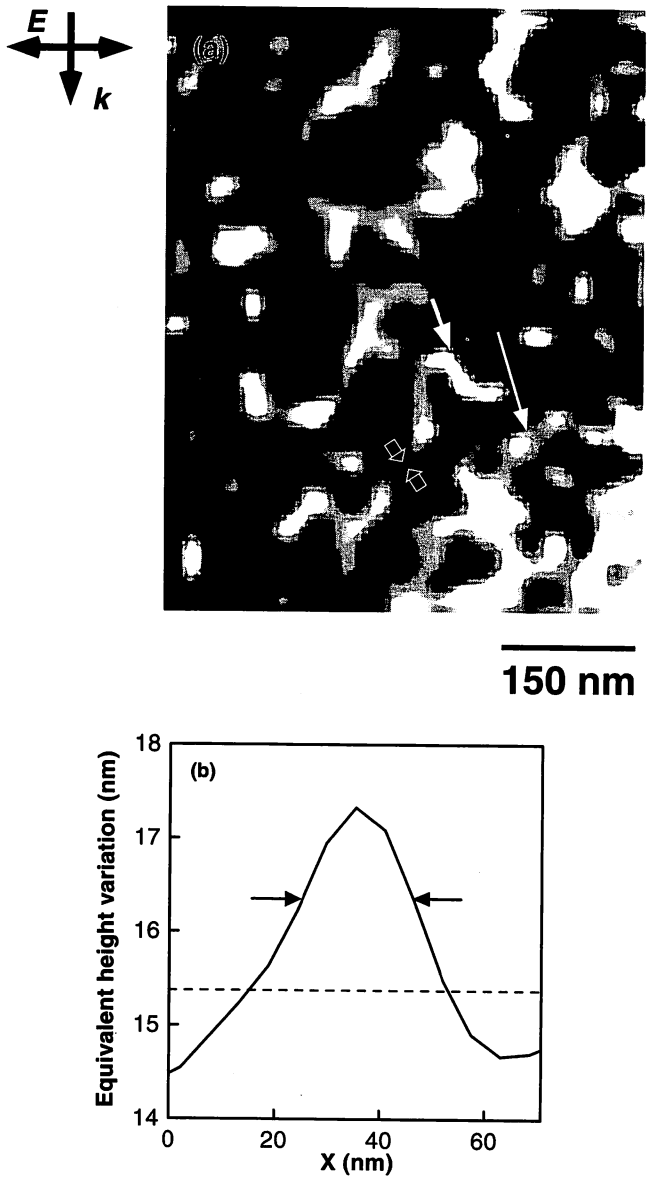

Fig. 6. (a) c-mode NOM image obtained under optical near field intensity feedback control with the electric field being parallel to the sample surface. E and k represent the electric field vector and the wave vector of the incident light, respectively. The long white arrow indicates a coiled loop structure while the short white arrow indicates a single string. The pixel size is 7 nm × 7 nm. (b) Variation across the single string as indicated by the two black arrows in (a). Here, the vertical axis is calibrated in terms of equivalent height or the distance that the sample had to be moved to have the detected intensity constant. The dotted line indicates the base level. The full width at half maximum (FWHM) of the string is around 20 nm measured with respect to the base level.

tion (k) of the incident light are shown on the left, i.e., the image was taken under the incident electric field being parallel to the sample surface s-polarization. Due to the difficulty in gaining enough S/N ratio, the image obtained under the state of p-polarization is very noisy and difficult to interpret.

The following image processing techniques have been applied to all the near field images obtained. In order to enhance the contrast of the image, first tilt introduced due to scanning was first corrected. Next, to adjust the dynamic range, histogram modification has been used for scaling. Finally, to remove the grain noise, a smoothing filter has been applied.

The bright structures present in the image correspond to the DNA string structures. This is because of the fact that the probe used can selectively scatter and pick up the field from the nano-protruding DNA structures against the relatively scattered field from the ultraflat substrate surface. The contributions of the scattered fields from the DNA structures and the background structure will ultimately decide the capability of our NOM in imaging the DNA strings and hence the contrast of the images. Here, it should be pointed out that, the noise level is determined by the detector's quantum noise which is much below the signal level. The information content of the image includes the topographical and dielectric properties of the sample.

Further, we have found that based on our experimental experience that the shape of the probe, the coating material and the thickness of the different layers used in enhancing the near field and blocking the far field play a far greater role in obtaining the final images as presented here. When the probes were not fabricated up to their optimum, we could image only the underneath sapphire substrates with some difficulty but not the string structures at all. This demonstrates the sensitivity of conducting nano-meter level resolution by our NOM system.

Figure 6(b) shows a section of the one dimensional variation across the two black arrows as indicated in Fig. 6(a). The vertical axis is calibrated in terms of equivalent height or the distance that the sample had to be moved to have the detected intensity constant. The line indicates the base level with respect to which the width of the string was measured. This is done by taking the Fourier transform of the one-dimensional line data containing the string as indicated by arrows. Next, the zero frequency or the dc level is taken as the average level. The average level is considered as the base level. The full width at half maximum of the bright string as indicated by arrows is around 20 nm. The fluctuations about the average level is less than 1%. The sample-probe separation during this observation is less than 10 nm.

As the pixel size used in this observation is still large in comparison to the lateral width of a single string DNA structure, the pixel size was reduced to around 1.9 nm × 1.9 nm. The sample-probe separation had been further reduced to less than 5 nm and observations have been conducted. The incident electric field is in the state of s-polarization. Due to the resolution limitations of the sensors of the scanner which is around 1 nm in the lateral directions and 0.1 nm in the vertical direction, the reliability of the observation of the image is limited to the scanner capabilities. The narrowest string observed is shown in Fig. 7. As seen, along with the single string structures as indicated by a short white arrow, complex loop structure as indicated by the long white arrow could also be seen.

Figure 7(b) shows the one dimensional variation across the two black arrows as indicated in Fig.7(a). The vertical axis is calibrated in terms of equivalent height or the distance that the sample had to be moved to have the detected intensity constant. The base level is indicated by the line in the figure. The full width at half maximum of the narrowest string measured with respect to this mean level is around 4 nm as indicated by the arrows. The dotted line indicates the base level with respect to which the width of the string was measured. This is done in the same way as of Fig. 6(b), by taking the Fourier transform of the one-dimensional line data containing the string as indicated by arrows. Next, the zero frequency or

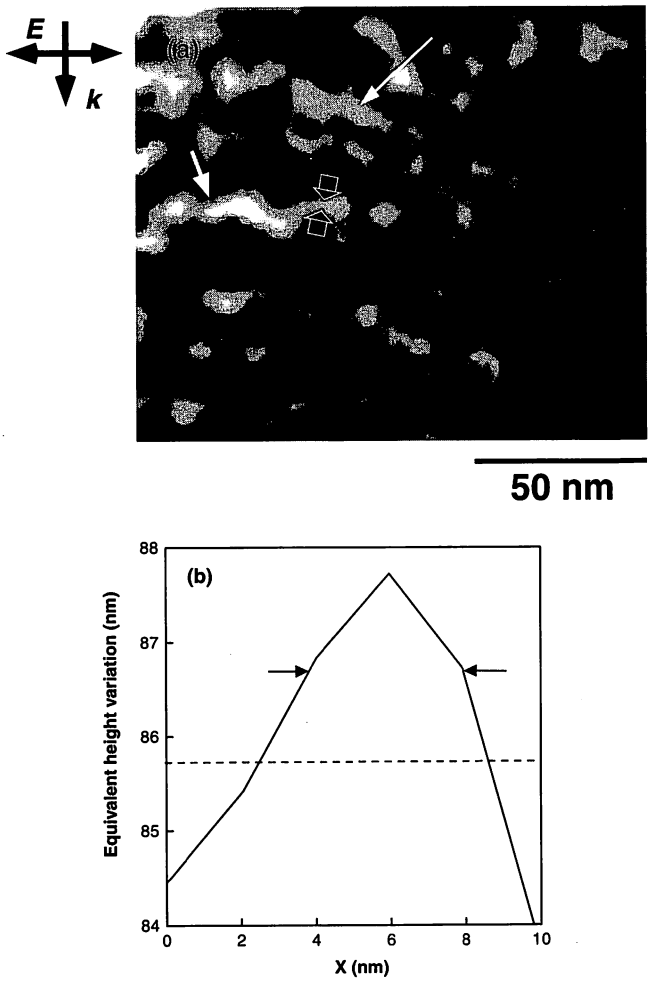

Fig. 7. c-mode NOM image obtained under a reduced pixel size of 1.9 nm × 1.9 nm. E and k represent the electric field vector and the wave vector of the incident light, respectively. The long white arrow indicates a complex loop structure. The short arrow indicates a single string. (b) The variation across the two black arrows in (a). Here, the vertical axis is calibrated in terms of equivalent height or the distance that the sample had to be moved to have the detected intensity constant. The dotted line indicates the base level. The FWHM as indicated by the arrows is approximately 4 nm.

the dc level is taken as the average level and hence the base level. To our knowledge, this is the narrowest structure that has been observed by NOM only by purely optical means.

As the DNA strings were just lying on the sapphire substrate and not fixed to the substrate, when scanning is performed again over the same area, it is difficult to reproduce the same image as the scanning operation damages the sample structure. But, we could reproduce similar kind of images when the center of scanning area is shifted demonstrating the reproducibility of our system. Further, it should be pointed out that both obtaining the image and its reproducibility highly depends on the condition of the probe. When the probe gets damaged due to prolonged scanning or due to mechanical bumping, the images presented in Fig. 6 and Fig. 7 could no longer be obtained. Therefore the condition of the probe plays a highly important role in obtaining the image and this in turn indicates the stage till which the probe can be used for scanning purpose in obtaining good images.

Further, in the actual case, when almost the same areas obtained in Fig. 6 or Fig. 7 were scanned by atomic force microscope, we could get similar kind of images containing looped structures like in Fig. 6 or Fig. 7. This shows that the bright structures presented in both Fig. 6 (and Fig. 7) correspond to DNA single strings. Hence, based on the looped structures, the width and formation of the structures and its comparison with the lot of images obtained using the atomic force microscope of the same sample, it can be concluded that what we have observed and reporting in this paper are nothing but DNA strings.

Though there exists reports on sub-nanometer resolved optical images by apertureless NOM,[45] it uses atomic force microscope as a control signal for maintaining constant sample-probe separation. It has been recently noticed that such an auxiliary control mechanism not only greatly influences the contrast of the near field optical image but also introduces some additional artifact into the image.[29] This artifact results from the differential changes in the intensity due to the probe movement. In our case, as the intensity itself is used as the control signal, there is no such case for worrying about the artifact effects. The image represents the purely optical variations which come from various sources with main contribution from edge effects of the probe and also of the sample which are both of nanometric dimensions. Apart from these, there are intensity variations introduced by the macroscopic properties such as the dielectric and topographic variations of the sample.

Finally, after finishing the observations, the probe has been observed under the electron microscope. Figure 8 shows the SEM micrographs of with the upper one showing the probe and the lower one showing the apex region encircled in the upper one. As seen from the magnified view, a very small protrusion as indicated by the arrow could be seen. Due to the soft nature of the MgF_2, while scanning the MgF_2 layer gets deformed so that a very small Ag coated tip region protrudes out at the apex region. The size of the protrusion as estimated from the SEM image is less than 10 nm. The size of this tip is still large in comparison with the dimensions of DNA single string. The following factors are believed to responsible for the high resolution: (1) Some very fine structure of the protrusion acting as an edge confining very high frequency; (2) Presence of Ag film enhancing the scattering efficiency of the probe; (3) Sample-probe separation being made very small.

Further, because of the high reflectivity of Ag film, the field around the sample is efficiently scattered and further confined by the MgF_2 layers at the surround and propagated through the fiber probe to be detected. The surrounding Al coating of the probe efficiently rejects the scattered field due to background coming mainly from low spatial frequency structures. Hence, in overall, the probe acts as a band pass filter with a narrow pass band with frequency mainly tuned to the efficient detection of high spatial frequency components. This paves a way for conducting nanometer level resolving observation of DNA for the first time.

4. Summary

In this paper, we reported on the successful observation of a single string structure of DNA by a collection mode NOM operated under optical feedback control for the first time. The width of the narrowest string has been estimated to be around 4 nm. Such a high resolving capability was made possible due to the special care taken for the preparation of the sample and the probe. The probe used is specially designed which

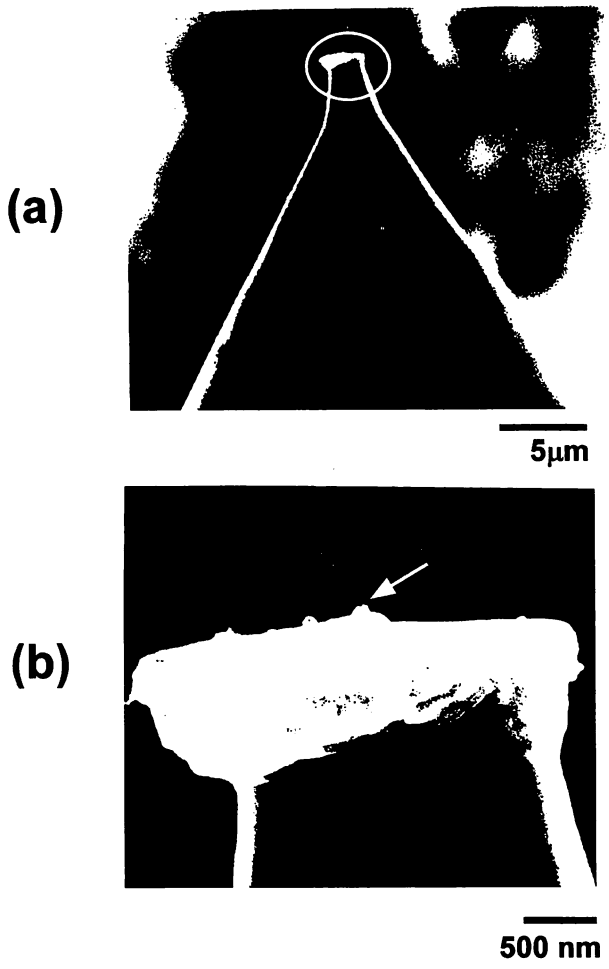

Fig. 8. SEM micrograph of the probe after scanning with (a) under low magnification and (b) magnified view of the encircled region shown in (a). The white arrow indicates the nanometric protrusion.

not only optimizes the local near field interaction between the probe and the sample but also picks up the higher spatial frequency components of the scattered near field efficiently. In future, we hope, with further improvement in the system including scanner and other mechanical components, it is possible to observe the double stranded or double helix of DNA by purely optical means. As the control is done optically, it is easier to extend the operation in liquid or fluid environments[11–14] which again opens up the possibility of directly manipulating the DNA structure or conducting investigating the individual segment of the double helix structure itself.

Acknowledgements

The authors would like to thank Dr. T. Ushiki of Niigata University for providing with the DNA solution.

1) D. W. Pohl: *Scanning Near-field Optical Microscopy (SNOM)*, eds. C. J. R. Sheppard and T. Mulevy (Academic, London, 1991) Advances in Optical and Electron Microscopy, Vol. 12, p. 243.
2) E. Betzig and J. K. Trautman: Science **257** (1992) 189.
3) R. Uma Maheswari, H. Tatsumi, Y. Katayama and M. Ohtsu: Opt. Commun. **120** (1995) 325.
4) M. Naya, S. Mononobe, R. Uma Maheswari, T. Saiki and M. Ohtsu: Opt. Commun. **124** (1996) 9.
5) *Near-field Nano/Atom Optics and Technology*, ed. M. Ohtsu (Springer-Verlag, Tokyo, 1998).
6) T. Saiki, S. Mononobe, N. Saito, J. Kusano and M. Ohtsu: Appl. Phys. Lett. **67** (1995) 2191.
7) T. Saiki, K. Nishi and M. Ohtsu: Jpn. J. Appl. Phys., **37** (1998) 1638.
8) S. Mononobe, T. Saiki, T. Suzuki, S. Koshihara and M. Ohtsu: Opt. Commun. **146** (1998) 45.
9) Y. Toda, M. Kourogi, M. Ohtsu, Y. Nagamune and Y. Arakawa: Appl. Phys. Lett. **69** (1996) 827.
10) E. Betzig, R. J. Chichester, F. Lann and D. L. Taylor: Bioimaging **1** (1993) 129.
11) P. J. Moyer and S. B. Kammer: Appl. Phys. Lett. **68** (1996) 3380.
12) R. Uma Maheswari, S. Mononobe, H. Tatsumi, Y. Katayama and M. Ohtsu: Opt. Rev. **3** (1996) 463.
13) H. Muramatsu, N. Chiba, H. Homma, K. Nakajima, T. Ataka, S. Ohta, A. Kusumi and M. Fujihira: Appl. Phys. Lett. **68** (1996) 3380.
14) M. Naya, R. Micheletto, S. Mononobe, R. Uma Maheswari and M. Ohtsu: Appl. Opt. **36** (1997) 1681.
15) A. V. Zvyagin, J. D. White and M. Ohtsu: Opt. Lett. **22** (1997) 955.
16) U. T. Durig, D. W. Pohl and F. Rohner: J. Appl. Phys. **59** (1986) 3318.
17) U. Ch. Fischer, U. T. Durig, D. W. Pohl: Scan. Microsc. **3** (1989) 1.
18) E. Betzig, J. K. Trautman, T. D. Harris, J. S. Weiner and R. L. Kostelak: Science **251** (1991) 1468.
19) N. F. van Hulst, M. H. P. Moers and B. Bolger: J. Microsc. **171** (1996) 95.
20) B. Hecht, H. Heinzelmann and D. W. Pohl: Ultramicroscopy **57** (1995) 228.
21) R. Uma Maheswari, H. Kadono and M. Ohtsu: Opt. Commun. **131** (1996) 133.
22) In our discussion, we have used the terminology NOM for the following reason: The optical counterpart of scanning probe microscopes which include the scanning tunneling microscope (STM), atomic force microscope (AFM), scanning electron microscope (SEM), etc is called under different names. Emphasizing the analogy with other scanning probe microscopes, scanning near-field optical microscope (SNOM) has been commonly used with various other names near-field scanning optical microscope (NSOM), scanning tunneling optical microscope (STOM) and photon scanning tunneling microscope (PSTM) depending on their technically different operating conditions. For details regarding the names and acronyms, refer to the compilation done.[23] In general, the NOM is operated either under collection mode in which the sample is illuminated under total internal reflection and the three dimensionally confined evanescent field generated over the sample is scattered by a sharpened probe. This mode of operation is called the collection mode (c-mode). In the other mode of operation, the sample is illuminated by light from a nanometer sized aperture sharpened probe and the scattered field is collected by a conventional optical microscope and this mode of operation is called the illumination mode (i-mode). Both the modes of operation involve scanning operation either of the sample or of the probe with the basic underlying principle being the same. In our paper, we have used the common and general term NOM with the specification of c-mode or i-mode depending on the mode used.
23) *Near-field Optics*, eds. D. W. Pohl and D. Coujourn (Kluwer, Dordrecht, 1993) NATO ASI Series E, Vol. 242.
24) *Molecular Biology of the Cell*, eds. B. Alberts, D. Bray, J. Lewis, M. Raff, K. Roberts and J. D. Watson (Garland Publishing, New York, 1983).
25) H. G. Hansma, D. E. Laney, M. Bezanilla, R. L. Sinsheimer and P. K. Hansma: Biophys. J. **68** (1995) 1672.
26) J. Yang and Z. Shao: Micron. **26** (1995) 35.
27) K. Yoshida, M. Yoshimoto, K. Sasaki, T. Ohinishi, T. Ushiki, J. Hitomi, S. Yamamoto and M. Sigeno: Biophys. J. **74** (1998) 1654.
28) N. F. van Hulst, M. F. Garcia-Parajo, M. H. P. Moers, J. A. Veerman and A. G. T. Ruiter: J. Struct. Biol. **119** (1997) 222.
29) B. Hecht, H. Bielefeldt, Y. Inoue, D. W. Pohl and L. Novotony: J. Appl. Phys. **81** (1997) 2492.
30) T. Saiki, M. Ohtsu, K. Jang and W. Jhe: Opt. Lett. **21** (1996) 674.
31) E. Betzig, P. L. Finn and J. S. Weiner: Appl. Phys. Lett. **64** (1995) 2484.
32) M. Vaez-Iravani, T. Toledo-crow and Y. Chen: J. Vac. Sci. Technol. A **11** (1993) 742.
33) S. Mononobe and M. Ohtsu: *Probe Fabrication Near-field Nano/Atom Optics and Technology*, ed. M. Ohtsu (Springer-Verlag, Tokyo, 1998).
34) In general, the NOM is operated under constant distance mode (refer to Chap. 6 of ref. 5) where the distance between the probe and the sample is kept constant by either moving the probe or the sample along the vertical direction. In order to estimate the sample-probe separation, an auxiliary mechanism such as shear force or atomic force technique is used and is kept constant while scanning. In case of i-mode NOM, use

of such an auxiliary mechanism is completely necessary as there is no way of estimating the sample-probe separation. However, in the case of c-mode NOM, it is possible to take advantage of the monotonous variation of signal intensity with respect to the sample-probe separation as a control signal for estimating the sample-probe separation. Hence, the optical signal itself can be used also as a feedback control signal eliminating the need for an auxiliary control signal.

35) S. Mononobe and M. Ohtsu: J. Lightwave Technol. **15** (1997) 1051.
36) S. Mononobe and M. Ohtsu: IEEE Photon. Technol. Lett. **10** (1998) 99.
37) M. A. Ordal, L. L. Long, R. J. Bell, S. E. Bell, R. R. Bell, R. W. Alexander, Jr. and C. A. Ward: Appl. Opt. **22** (1983) 1099.
38) L. Novotony, D.W. Pohl and B. Hecht: Ultramicroscopy **61** (1995) 1.
39) L. Novotony, D.W. Pohl and B. Hecht: Opt. Lett. **20** (1995) 970.
40) In the case of c-mode NOM, the optical near field scattered and picked up by the fiber probe could excite both modes inside the fiber and also in the outer metal cladding. However, it can be expected that the contribution from the outer modes would be very much negligible in comparison with the guided mode propagating through the fiber as the field overall excited propagating into the fiber would be very small. However, it should be pointed out that in the case of i-mode NOM as light is introduced into the metal coated apertured sharpened fiber probe, due to the presence of metal cladding, the guided mode in the fiber also excites modes in the metal cladding. The outer modes of the cladding interfere with the internal guided field localized around the aperture.
41) H. Furukawa and S. Kawata: Opt. Commun. **148** (1998) 221.
42) O. J. F. Martin and C. Girard: Appl. Phys. Lett. **70** (1997) 705.
43) M. Ashino and M. Ohtsu: Appl. Phys. Lett. **72** (1998) 1299.
44) M. Yoshimoto, T. Maeda, T. Ohinishi, H. Koinuma, O. Ishiyama, M. Shinohara, M. Kubo, R. Miyura and A. Miyamoto: Appl. Phys. Lett. **67** (1995) 2615.
45) F. Zenhauserin, Y. Martin and H. K. Wickramasinghe: Science **269** (1995) 1083.

Nanometric aperture arrays fabricated by wet and dry etching of silicon for near-field optical storage application

M. B. Lee[a] and N. Atoda[b]
Advanced Optical Memory Group, National Institute for Advanced Interdisciplinary Research, Tsukuba, Ibaraki 305-8562, Japan

K. Tsutsui and M. Ohtsu
Interdisciplinary Graduate School of Science and Engineering, Tokyo Institute of Technology, Midori, Yokohama 226-8502, Japan

(Received 2 April 1999; accepted 20 August 1999)

We fabricated nanometric aperture arrays in order to apply to an optical probe in high-density near-field optical storage for increase of data-transmission rate. The aperture arrays were fabricated by forming concave pyramidal grooves on a silicon-on-insulator wafer with electron beam lithography and wet anisotropic etching. Modification of the apex shape of the grooves by re-oxidation and subsequent reactive ion dry etching was able to increase the uniformity of the aperture size remarkably. The light transmission efficiency of the fabricated apertures was measured to be $\sim 10^{-3}$ when the aperture size was 100 nm, which was higher than that of a conventional optical fiber probe by several orders of magnitude. © *1999 American Vacuum Society.* [S0734-211X(99)01506-1]

I. INTRODUCTION

Near-field optical recording is currently regarded as one of the most promising technologies that can dramatically increase the storage density because it can circumvent the diffraction limit of light. Several groups have successfully demonstrated near-field optical recording that achieved an areal storage density as high as ~100 Gb/in^2.[1–3] Typically, a sharpened and metal-coated optical fiber probe with a subwavelength aperture on its tip is employed in near-field optical recording. The probe is scanned by a piezoelectric actuator while regulating the tip-medium separation to as close to an order of 10 nm with shear force, atomic force, or tunneling current feedback mechanism, etc.[4]

Extension of the near-field optical recording technique to actual optical storage systems, however, is difficult because the data-transmission rate is too low using the optical fiber probe, as is also the case for other ultrahigh-density recordings based on a scanning probe method. This is mainly because a high-speed scanning mechanism is not available while maintaining a narrow gap with the surface of a medium for the fiber probe. The very low optical power generated on the tip of the fiber probe also limits the scanning speed.[5] To overcome this problem, we have proposed a planar-type apertured probe array for an optical probe in ultrahigh-density near-field optical storage, illustrated schematically in Fig. 1.[6,7] The probe array has concave pyramid-shaped grooves with nanometric apertures in their bottom end that play the role of a generator or receiver of the optical near field on a recording medium. The probe array can realize a high data-transmission rate because high-speed scanning is possible by combining it with the drive technology of a contact-type slider head of a hard disk, and also by a simultaneous data processing with the multiple probes. Moreover, the planar structure of the probe array is much more stable and durable compared with the weak protruded tip of the fiber probe.

For simultaneous recording or readout of tiny marks using multiple probes, a fabrication technique for a probe array with a small and uniform aperture size should be established first because distributions of the aperture size may induce fluctuations of scattered-light intensity from each aperture, which could damage the reliability of the signal detected. In this study, we develop two fabrication processes of the proposed planar-aperture near-field optical probe array and evaluate the two processes in view of the size uniformity of the nanometric apertures formed. The light transmission efficiencies of the apertures were also measured.

II. FABRICATION PROCESS AND EFFICIENCY MEASUREMENT

Figure 2 shows the fabrication process for our probe array. A thermally bonded silicon-on-insulator (SOI) wafer with a 9-μm-thick top layer [Si(100)] and a 2-μm-thick buried oxide layer was used as the starting material [Fig. 2(a)]. First, the SOI wafer was thermally oxidized in wet O_2 at 1100 °C to form a 1.2-μm-thick SiO_2 film. Then, a photoresist (OFPR-8600, Tokyo Ohka) was spin coated on and window regions with areas of 0.5–1 mm^2 were patterned on the back side of the wafer. After removal of the SiO_2 film with a buffered hydrofluoric acid ($HF:NH_4F = 1:9$), the thick base silicon was anisotropically etched with a 10% KOH aqueous solution at 80 °C until the etching rate slowed down at the buried oxide layer [Fig. 2(b)]. The wet etching condition was determined to maximize the etching rate ratio of Si(100) to SiO_2. The thin silicon membrane in the window region in

[a]Electronic mail: mblee@nair.go.jp
[b]On leave from Electrotechnical Laboratory, AIST, Japan.

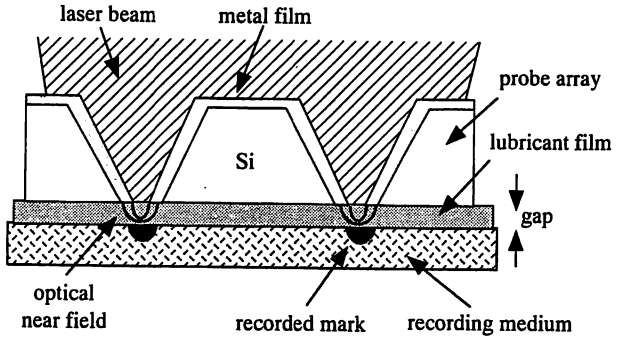

FIG. 1. Schematic diagram of the cross-sectional structure and the operating principles of the planar-apertured probe array.

Fig. 2(b) usually bulges out because of a stress imbalance between the top silicon and the two SiO_2 layers. Therefore we stripped away the oxides with buffered hydrofluoric acid and again oxidized the wafer to form a 0.1-μm-thick SiO_2 film. The formation of the new thin oxide film makes the surface flat and clean and thus increases adhesion of a resist.

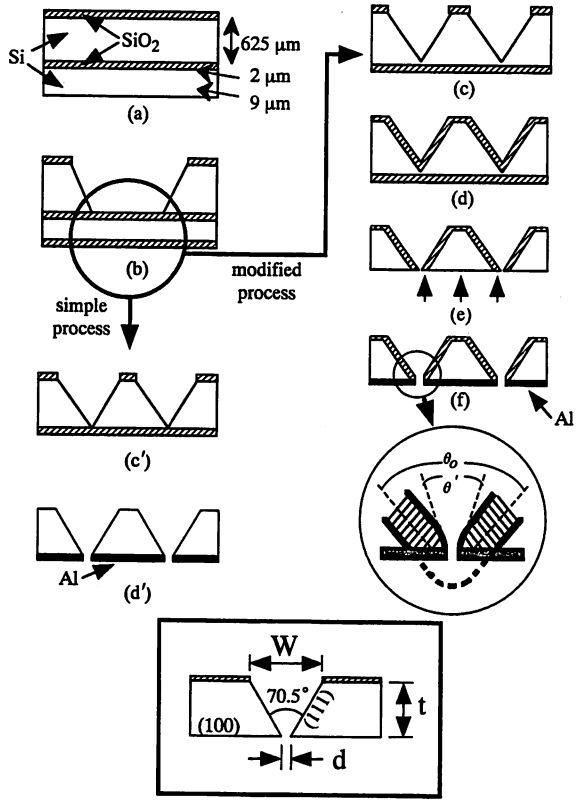

FIG. 2. Fabrication processes of the simple and modified-type planar-apertured probe arrays. Simple-type probes: (a) the initial SOI wafer, (b) formation of the window regions, (c′) formation of the concave pyramidal grooves, (d′) oxide removal and aluminum deposition. Modified-type probes: following steps (a) and (b), (c) formation of the concave pyramidal grooves, (d) re-oxidation, (e) dry etching of SiO_2 and Si, and (f) aluminum deposition. The enlargement of (f) shows the apex of the groove. The apex angle reduces from $\theta_0(=70.5°)$ to θ' by re-oxidation. The bold face dotted curve indicates the original profile of the oxide before the dry etching. The rectangular inset shows that the aperture size d is determined by the pattern size w and the SOI wafer thickness t.

The oxide film on the window was patterned in an array of squares with an electron beam exposure system (ELS-5000, Elionix). For the patterning process, a 0.2-μm-thick electron beam resist (ZEP-520, Nippon Zeon) was spin coated onto the window area. The resist could be coated uniformly over the whole area of the small window except for a very narrow region along the edge lines that defined the boundary between the (111) facet planes and the (100) plane. At the edge region, the resist thickens due to its recoil by the (111) wall. The area of the edge region with nonuniform thickness can be minimized by increasing the spin rotation speed and/or by decreasing the viscosity of the resist. Again the wafer was etched anisotropically [Fig. 2(c) or 2(c′)] in the same way as described above. In one process (we call it the simple process), etching of the silicon continued until the apexes of the grooves reached the oxide layer at the bottom surface [Fig. 2(c′)]. Then the oxides were stripped away with buffered hydrofluoric acid to generate small apertures in the apexes of the concave pyramids. Finally, a 100-nm-thick aluminum film was deposited by vacuum evaporation onto the bottom side to block far-field light transmission [Fig. 2(d′)].

In the other process (that we call the modified process) we modified the shape of the apexes of the concave pyramidal grooves by re-oxidation and a subsequent dry etching process to obtain the apertures. It is shown as a sequence of steps, (c)–(f) following steps (a) and (b), in Fig. 2. The square patterns formed by the electron beam lithography on the window are a bit smaller than those of the simple process. The apexes, therefore, do not reach the oxide at the bottom surface, leaving the silicon unetched by about 1 μm [Fig. 2(c)]. The wafer is re-oxidized thermally to form a 0.8-μm-thick SiO_2 film [Fig. 2(d)]. The oxide film at the bottom surface and the remaining silicon are removed by reactive ion etching. The sample was etched by CF_4 gas with a flow rate of 15 sccm and a rf power of 100 W under an ambient pressure of 5 Pa. According to the preliminary experiments, the etching rates of silicon and SiO_2 were found to be equal within the experimental error of the surface profile measurements at the above condition. Therefore the SiO_2 tip and the peripheral silicon around the tip are etched simultaneously to generate the aperture array on a flat surface [Fig. 2(e)]. Finally, a 100-nm-thick aluminum film was deposited on the bottom side to block far-field light transmission [Fig. 2(f)]. The expected feature of the apexes of the grooves, as shown in the enlargement of the circled region in Fig. 2(f), will be discussed later.

We evaluated the light transmission efficiency of the silicon planar-apertured probe array. For this, we fabricated aperture arrays with a range of aperture sizes by serially varying the square pattern size in the electron beam lithography within one sample. The incident light from a laser diode (5 mW power with 670 nm wavelength) was focused onto each aperture with an objective lens of 0.4 numerical aperture (NA). The sample, mounted on an X-Y stage, was moved to make each concave pyramidal groove coincide with the focused laser spot while being observed through an optical microscope. The output power of the far-field light emitted

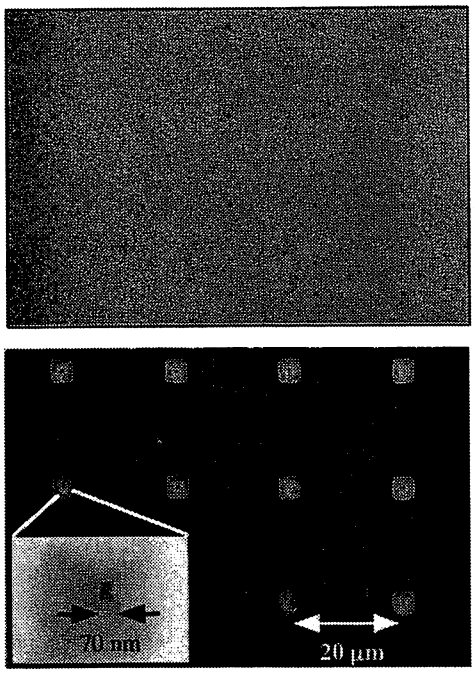

FIG. 3. SEM micrographs of the fabricated probe array by (a) the simple process and (b) the modified process, viewed from the bottom side before aluminum film deposition.

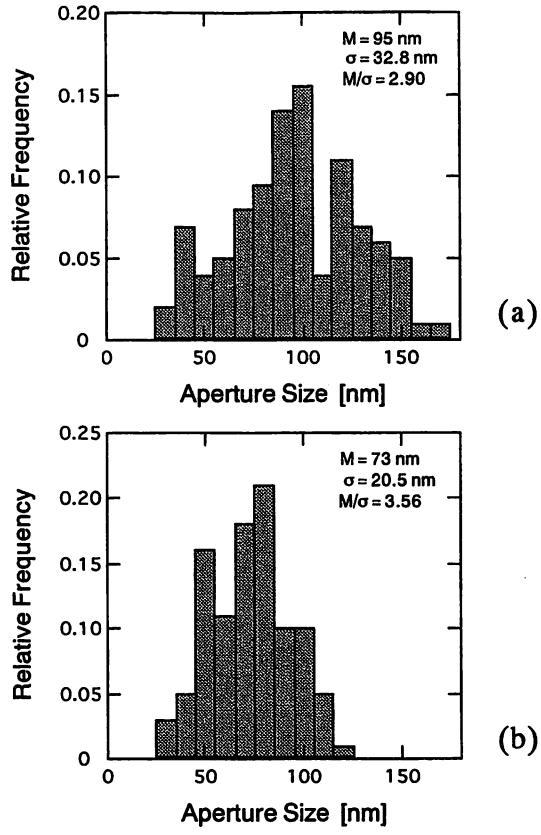

FIG. 4. Distribution of the aperture size in the aperture array fabricated by (a) the simple process and (b) the modified process. The number of the apertures measured was $n = 100$ in each case.

from the aperture was measured with an optical-power meter located in the proximity of the aperture. The light transmission efficiency is defined as the ratio of the collected output power to the input power measured just in front of the concave pyramidal grooves.

III. RESULTS AND DISCUSSION

Figures 3(a) and 3(b) show typical scanning electron micrographs of the aperture arrays fabricated by the simple and the modified processes, respectively, taken before aluminum film deposition. Homogeneous aperture arrays are formed. As shown in the enlarged view of Fig. 3(b), an aperture as small as 70 nm has formed on the center of oxide pad in the modified-type probe array. This dimension is as small as one tenth of the wavelength of light, which is two to three orders of magnitude smaller than conventional micromachined aperture arrays based on the wet anisotropic etching technique of silicon.[8] The sizes of the apertures of the fabricated probe arrays were measured before aluminum film deposition by scanning electron microscopy (SEM) in a sample area of $300\,\mu m \times 300\,\mu m$. Figures 4(a) and 4(b) show the distribution of the aperture size for the aperture arrays fabricated by the simple and the modified processes, respectively. The mean value M and the standard deviation σ of the aperture size, and the value of M/σ as a measure of the size uniformity are also indicated in Fig. 4. We see that the modified process achieved a higher uniformity (M/σ) in spite of the smaller aperture size (M) compared to that of the simple process.

The improvement of the uniformity in the modified process is considered to be caused by the oxidation characteristics at the apex of the groove. The apex angle θ_0 of the concave pyramid indicated in Fig. 2(f) is fixed to 70.5° by the crystallographic orientation of (111) planes in the simple process. In this case the aperture size d, shown in the inset of Fig. 2, is given in terms of the thickness t of the wafer and the edge length w of basal plane of the concave pyramid as $d = w - \sqrt{2}t$. Hence the absolute values of deviations of W and t are reflected directly to the deviation of d with a factor of $1[=(\partial d/\partial w)_t]$ and $\sqrt{2}[=(\partial d/\partial t)_w]$, respectively, in the simple process. We obtained deviations of $\sigma = 0.079\,\mu m$ for w and $\sigma = 0.24\,\mu m$ for t from a SEM measurement of the fabricated arrays.

It was reported that oxidized V-shaped grooves and concave pyramidal grooves provide a sharpened feature in the inner corner of oxide surfaces.[9] This structure results in a reduction of the effective apex angle from θ_0 to θ', as shown in Fig. 2(f). Figure 5 shows an example of a cross section of an oxidized V-shaped groove faceted with only two (111) planes observed in our other experiment where the oxidation condition was almost the same as that employed in the modified process. Figure 5 shows that the corner of the oxide is sharpened and has a reduced oxide thickness. Because this phenomenon is considered to result from the decrease of the oxidation rate at the corner due to a stress effect,[10] it is expected to appear stronger in concave pyramidal grooves that are faceted with four (111) planes. The height, indicated by h in Fig. 5, over which the sharpening occurrs due to the

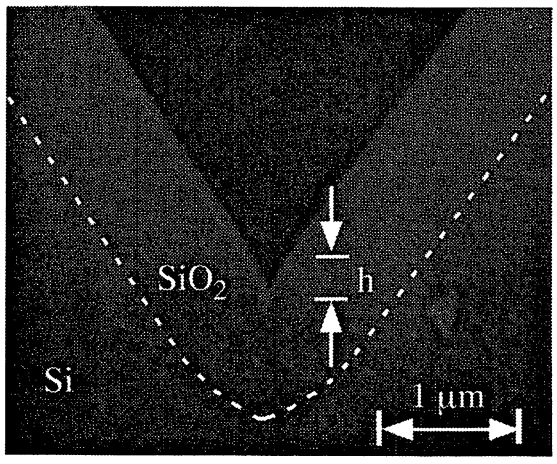

FIG. 5. Cross-sectional SEM micrographs of a V-shaped groove after oxidation process. The white dotted line was drawn to delineate the boundary of the Si and SiO_2 phases. The height h is the range where sharpening of the corner occurs.

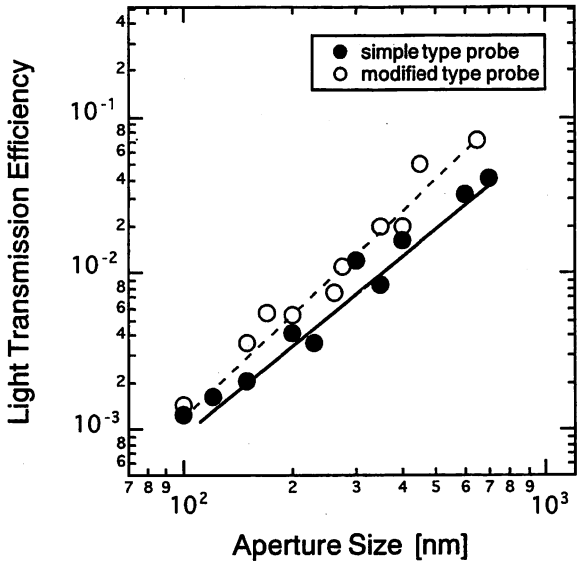

FIG. 6. Light transmission efficiencies of the two types of probe with variations of the aperture size.

oxide thickness reduction at the corner would be at least larger than 0.4 μm in our concave pyramidal grooves, as can be inferred from Fig. 5. The deviations in w and t in the concave pyramids in the modified process were measured to be the same degree of magnitude as those of the simple process. The height h is much larger than w and t. Furthermore, it is obvious that within the range of h the sensitivity of the aperture size to the wafer thickness fluctuation reduces significantly compared with that of the concave pyramid without a sharpened apex when the tips of the oxide are etched away from the bottom side to generate the aperture array. Therefore the mechanism of the increase of the aperture size uniformity in the modified process can be said to be the change of the apex shape by re-oxidation. With a longer oxidation, the oxide thickness at the apex is saturated and the oxide feature becomes sharper, leading to a further increase of the tolerances in the dimension of w and t in determining the deviation of d. Thus the aperture size is self-regulated in the modified process. It is considered that optimization of the re-oxidation condition, such as the oxidation temperature and the doping of the wafer, can further reduce the aperture size deviation by forming a sharper apex angle.[10]

Figure 6 shows the light transmission efficiencies of the two types of probe with variations of the aperture size. The light transmission efficiency of the modified-type probe array was a little higher than that of the simple type one. This is presumedly caused by delivery of the light to the apertures with less attenuation by a wider optical cavity region near the aperture in the modified probe.[11,12] The deposition of aluminum films from the bottom side is preferable to that from the patterned side not only to avoid the partial occlusion of small apertures but also to increase the light transmission efficiency. The light transmission efficiencies of our probes were $\sim 10^{-3}$ at an aperture size of 100 nm. It should be noted that the transmission efficiency of the new fabricated planar-apertured probes is several orders of magnitude higher than that of a conventional fiber probe. Typically, the transmission efficiency of a fiber probe is reported to be 10^{-5}–10^{-7} when the aperture diameter is 100 nm.[5] The reasons for the high light transmission efficiency of our probes are considered to be a large apex angle (70.5°) and less coupling loss compared to the fiber probe due to direct transmission of light in free space from the source light to the groove. This shows that our probe array is more advantageous for high-speed recording and readout in near-field optical storage than the fiber probe. We also conclude that the modified fabrication process is effective for the planar-apertured probe array because higher uniformity in the aperture size can be obtained by the addition of a few process steps while slightly increasing the light transmission efficiency of the aperture.

IV. CONCLUSIONS

In order to apply to near-field optical probe in place of a conventional fiber probe in ultrahigh density near-field optical storage, we have fabricated aperture arrays with an aperture size of 100 nm or smaller on flat silicon substrates using electron beam lithography and an anisotropic wet etching technique. A modified process employing a change of the apex shape of the concave pyramidal grooves with re-oxidation is able to increase the uniformity of the aperture size due to the self-limited oxidation profile. The transmission efficiency of the probe array was $\sim 10^{-3}$ at an aperture size of 100 nm, higher than that of the typical fiber probe by several orders of magnitude.

ACKNOWLEDGMENTS

The authors wish to acknowledge Dr. M. Komuro and Dr. J. Itoh (Electrotechnical Laboratory, AIST, Japan) for their support in the fabrication process, and A. Sato (Minlota Co., Ltd.) for his help in the measurement of the light transmission efficiency.

[1]E. Betzig, J. K. Trautman, R. Wolfe, E. M. Gyorgy, P. L. Finn, M. H. Kryder, and C.-H. Chang, Appl. Phys. Lett. **61**, 142 (1992).
[2]S. Jiang, J. Ichihasi, H. Monobe, M. Fujihira, and M. Ohtsu, Opt. Commun. **106**, 173 (1994).
[3]S. Hosaka, T. Shintani, M. Miyamoto, A. Hirotsune, M. Terao, M. Yoshida, K. Fujita, and S. Kammer, Jpn. J. Appl. Phys., Part 1 **35**, 443 (1996).
[4]*Near-field Nano/Atom Optics and Technology*, edited by M. Ohtsu (Springer, Tokyo, 1998), pp. 107–114; M. A. Paesler and P. J. Moyer, *Near-field Optics* (Wiley, New York, 1996), pp. 117–125.
[5]G. A. Valaskovic, M. Holton, and G. H. Morrison, Appl. Opt. **34**, 1215 (1995).
[6]M. Ohtsu, K. Tsutsui, M. Kourogi, and M. B. Lee, Electron. Commun. Jpn., Part 2: Electron. **81**, 41 (1998).
[7]M. B. Lee, M. Kourogi, T. Yatsui, K. Tsutsui, N. Atoda, and M. Ohtsu, Appl. Opt. **38**, 3566 (1999).
[8]E. Bassous, IEEE Trans. Electron Devices **ED-25**, 1178 (1978).
[9]T. Asano and J. Yasuda, Jpn. J. Appl. Phys., Part 1 **35**, 6632 (1996).
[10]D. Kao, J. P. McVittie, W. D. Nix, and K. C. Saraswat, IEEE Trans. Electron Devices **ED-35**, 25 (1988).
[11]T. Saiki, S. Mononobe, M. Ohtsu, N. Saito, and J. Kusano, Appl. Phys. Lett. **68**, 2612 (1996).
[12]L. Novotny, D. W. Pohl, and B. Hecht, Opt. Lett. **20**, 970 (1995).

Low-temperature near-field nonlinear absorption spectroscopy of InGaAs single quantum dots

Takuya Matsumoto and Motoichi Ohtsu
Interdisciplinary Graduate School of Science and Engineering, Tokyo Institute of Technology, 4259 Nagatsuta, Midori-ku, Yokohama 226-8502, Japan

Kazunari Matsuda and Toshiharu Saiki[a)]
Kanagawa Academy of Science and Technology, KSP East 408, 3-2-1 Sakado, Takatsu-ku, Kawasaki 213-0012, Japan

Hideaki Saito and Kenichi Nishi
Optoelectronics and High Frequency Device Research Laboratories, NEC Corporation, 34 Miyukigaoka, Tsukuba, Ibaraki 305-8501, Japan

(Received 30 April 1999; accepted for publication 21 September 1999)

Nonlinear absorption spectroscopy of InGaAs single quantum dots (QDs) was realized by means of a low-temperature near-field optical microscope. The spatial distribution of the nonlinear absorption change in single QDs was determined. The dependence of the nonlinear absorption change on the pump power density demonstrates that the nonlinearity originates from the state filling of the ground state. The nonlinear absorption spectrum showed a homogeneous broadening of the ground state of about 5 meV. Furthermore, the change in the absorption cross section of the single QD when the ground state is saturated with carriers is estimated to be $2.8 \pm 0.6\,\mathrm{nm}^2$, which agrees with the result predicted on the basis of theoretical consideration. © *1999 American Institute of Physics.* [S0003-6951(99)00547-1]

Semiconductor quantum dots (QDs) are quite attractive for optical devices used in information processing and transmission systems, since they have large optical nonlinearity due to atomic-like discrete energy levels.[1,2] For the precise evaluation of their optical nonlinearity, we must observe a single QD to eliminate the inhomogeneous broadening caused by size and shape fluctuations. However, the spatial resolution of conventional far-field optical microscopy is insufficient for the observation of the single QD due to the diffraction limit of light; the size of the focusing spot (limited to $\lambda/2$) is much larger than the absorption or scattering cross section of the QD, and the nonlinear signal is buried in a large background.

This problem can be solved by using a near-field optical microscope (NOM), in which light is confined to a subwavelength area by an optical fiber probe having a subwavelength aperture at the apex.[3–5] The NOM provides spatial information of the nonlinear response of single QDs as well as their spectra. The nonlinear response of single QDs can also be studied by irradiating the single QDs through a submicron-sized aperture in a metallic film deposited directly on the sample surface. By this method, Bonadeo *et al.* have successfully established a nonlinear spectroscopy method for analysis of localized excitons in QD-like potentials formed in a GaAs quantum well.[6] However, spatial information on the nonlinear response cannot be obtained, since the aperture is fixed at one position. In this letter, we demonstrate observation of the nonlinear absorption change in single QDs by using a NOM. We describe the spatial distribution of the nonlinear absorption change, and the nonlinear absorption spectrum of single QDs. The change in the absorption cross section of the single QD is also estimated from the experiment.

The sample investigated in this experiment is $In_{0.5}Ga_{0.5}As$ self-assembled QDs grown on a (100) GaAs substrate by gas-source molecular beam epitaxy. Atomic force microscope studies confirm that the average dot diameter is 30 nm and the height is 15 nm. The dot density is about $2 \times 10^{10}\,\mathrm{dots/cm}^2$. These dots are covered with cap layers with a total thickness of 180 nm.

To measure the nonlinear absorption change in the QDs, a continuous wave pump-probe technique is employed. As shown in Fig. 1, probe light (Ti:sapphire laser light, wavelength=900–980 nm) is introduced into the back of the

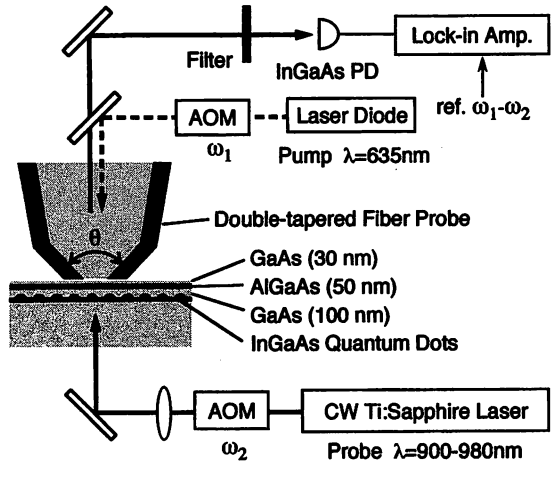

FIG. 1. Schematic of the experimental setup for the nonlinear absorption spectroscopy of single QDs and the sample structure. AOM: acoustooptic modulator.

a)Electronic mail: saiki@net.ksp.or.jp

sample, and the transmitted light is collected by a fiber probe placed in the vicinity of the sample surface using shear force feedback.[7,8] The collected probe light is detected by an InGaAs photodiode. When the sample is illuminated by pump light (laser diode, wavelength=635 nm) passing through the fiber probe, carriers are generated in the barrier layer, and flow into the QDs. Then the ground states of the QDs are occupied with the carriers. The resultant reduction of the absorption coefficient of the QDs is measured by detecting the transmission change in the probe light. To achieve high sensitivity in detection of the transmission change, both the pump light power and the probe light power are modulated, and the difference frequency component of the detected signal is extracted by synchronous lock-in detection. The modulation frequencies of the pump and probe light are $\omega_1 = 110$ and $\omega_2 = 100$ kHz, respectively. Furthermore, as the fiber probe, we use a double tapered fiber probe fabricated by chemical etching.[9] The throughput of the fiber probe (=light power ejected from the aperture/light power coupled into the fiber) is an important factor for high sensitivity. This fiber probe realizes a throughput as large as 10^{-2} (aperture diameter=150–200 nm) due to a large cone angle at the apex (θ in Fig. 1). The minimum detectable differential transmission (T) of this system is $\Delta T/T = 2 \times 10^{-5}$. The sample, scanner, and fiber probe are mounted in a continuous He-gas flow optical cryostat and all measurements are performed at 5–10 K.

For comparison, photoluminescence (PL) measurement is also performed. QDs are excited by light passing through a fiber probe (wavelength=635 nm), and the PL is collected by the fiber probe. To measure the spatial distribution, the collected PL is detected by an InGaAs photodiode through a bandpass filter. To measure the spectrum, the collected PL is sent into a monochromator equipped with a charge coupled device detector.

Figure 2(a) shows the spatial distribution of the nonlinear absorption change. The wavelength of the probe light is fixed at 940 nm, and the power density of the pump light at the apex of the fiber probe is 300 W/cm^2. Figure 2(b) shows the spatial distribution of the PL taken in the same scanning area. The center wavelength and bandwidth of the bandpass filter are 940 and 10 nm, respectively. The power density of the excitation light is the same as the pump power density of the nonlinear absorption image. Since the nonlinear absorption change and PL are strong at the same positions indicated by arrows, it is confirmed that the nonlinear absorption change originates from single QDs. The full width at half maximum of the bright spot A in Fig. 2(a) is 200 nm, which is 1/5 of the wavelength.[10]

To confirm that the nonlinear absorption change originates from the state filling of the ground state, the dependence of the nonlinear absorption change and PL intensity on the pump (excitation) power density was measured. The closed circles and the open circles in Fig. 3 show the pump power dependence of the nonlinear absorption change and the PL intensity, respectively. The PL intensity increases linearly in the weak excitation region, and reaches saturation above about 300 W/cm^2. From this behavior, we confirm that the PL is the ground state emission.[5] The nonlinear absorption change also increases linearly in the weak excitation region, and reaches saturation at the same pump power density as the PL intensity. Therefore, we confirm that the nonlinear absorption change originates from the state filling of the ground state. Here, we roughly estimate the saturation power density. By considering the parameters, i.e., the aperture diameter (d=200 nm), the carrier diffusion length (L

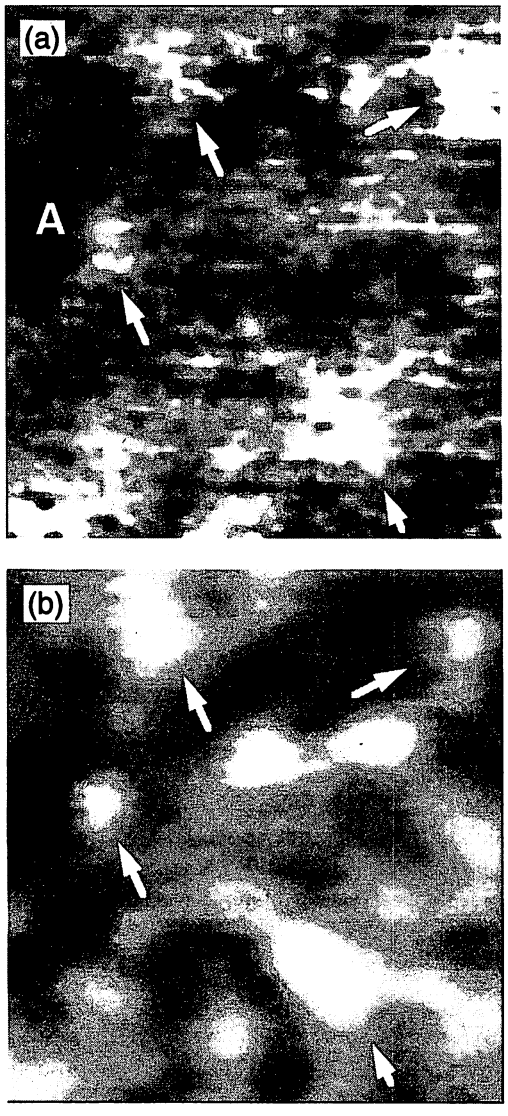

FIG. 2. Spatial distribution image of (a) the nonlinear absorption change and (b) PL. The scanning range is 2.2 μm×2.2 μm.

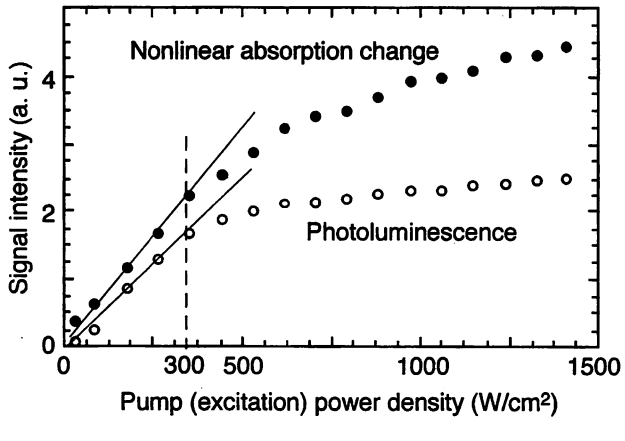

FIG. 3. Dependence of the nonlinear absorption change and the PL intensity on the pump (excitation) power density.

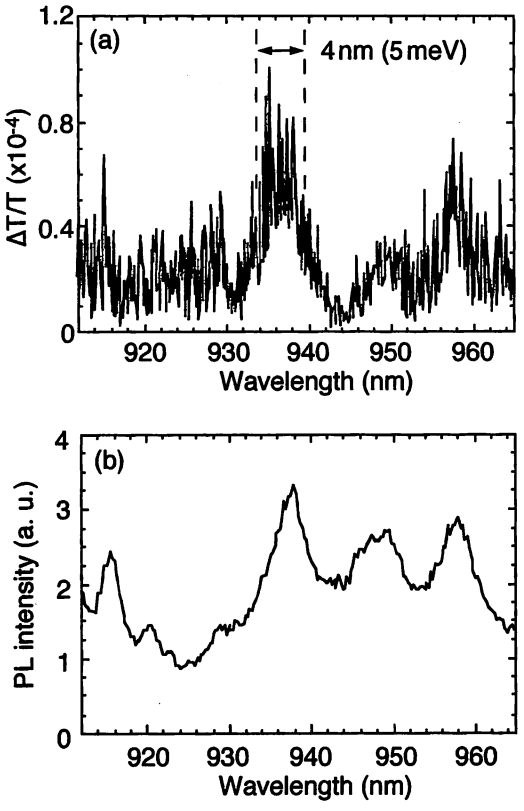

FIG. 4. (a) Nonlinear absorption and (b) PL spectrum of single QDs. The pump (excitation) power density is 300 W/cm^2.

=400–600 nm), the density of QDs ($n=2\times10^{10}$ dots/cm^2) and the recombination life time ($\tau=1$ ns), we can estimate the saturation power density (I_s) as $I_s=2\times(2L/d)^2 nh\nu/\tau$ = 100–300 W/cm^2, where $h\nu$ is photon energy. This value is in agreement with the experimental value.

Figure 4(a) shows the nonlinear absorption spectrum of single QDs obtained by changing the probe light wavelength continuously.[11] The pump power density is 300 W/cm^2. Figure 4(b) shows the PL spectrum taken with the same excitation power. The peaks in the nonlinear absorption spectrum are also seen in the PL spectrum at the same wavelengths. These peaks correspond to the ground states of single QDs, as confirmed by observing the pump power dependence described earlier. The homogeneous broadening of the peak is about 5 meV.

Here, we estimate the change in the absorption cross section of a single QD when the ground state is saturated with carriers ($\Delta\sigma_{sat}$). This value is an important parameter when we apply the nonlinear absorption change in the QDs to optical devices, and is given by $\Delta\sigma_{sat}=S\times(\Delta T/T)_{sat}$, where S is the detection area and $(\Delta T/T)_{sat}$ is the differential transmission change observed when the ground state is saturated with carriers. In this experiment, the diameter of the detection area is estimated to be about 200 nm from the spot image in Fig. 2(a), and $(\Delta T/T)_{sat}=(0.9\pm0.2)\times10^{-4}$ (for the pump power density=300 W/cm^2). Therefore, $\Delta\sigma_{sat}$ is estimated to be 2.8 ± 0.6 nm^2. $\Delta\sigma_{sat}$ corresponds to the linear absorption cross section of the single QD, if we neglect the Coulomb interaction between carriers. Theoretically, this linear absorption cross section of the single QD is estimated to be 1.5 nm^2, assuming that the QD has a homogeneous broadening of 5 meV and the shape of a sphere with a diameter of 30 nm.[1,12,13] This theoretical value is in agreement with the experimental one estimated in the present study. Recently, fabrication of QDs with much smaller homogeneous broadening (<20 μeV) has been reported.[14] For such QDs, a much larger change in the absorption cross section is expected.

Finally, we would like to claim that we can establish novel optical devices operated with single QDs utilizing the near-field technique for sending light power into the single QDs efficiently. For example, a single dot optical modulator is realized if we use the pump light as the modulation signal and the probe light as the carrier. Such single dot operation is advantageous to reduce the size and operation power of the devices.

In summary, we have succeeded in observing the nonlinear absorption change in single QDs by means of a NOM, and its spatial distribution image having a correlation with the PL image is obtained. The dependence of the nonlinear absorption change on the pump power density shows that the nonlinear absorption change originates from the state filling of the ground state. The nonlinear absorption spectrum showed homogeneous broadening of the ground state is about 5 meV. The change in the absorption cross section of the single QD when the ground state is saturated with carriers is estimated to be 2.8 ± 0.6 nm^2 from the experiment. This value agrees with the theoretical value calculated with the assumption that the QD has the homogeneous broadening of 5 meV.

The authors are grateful to Y. Arakawa for fruitful discussions.

[1] S. Schmitt-Rink, D. A. B. Miller, and D. S. Chemla, Phys. Rev. B **35**, 8113 (1987).
[2] H. Sakaki, K. Kato, and H. Yoshimura, Appl. Phys. Lett. **57**, 2800 (1990).
[3] *Near-field Optics*, edited by D. W. Pohl and D. Courjon (Kulwer, Dordrecht, 1993).
[4] *Near Field Nano/Atom Optics and Technology*, edited by M. Ohtsu (Springer, Tokyo, 1998).
[5] T. Saiki, K. Nishi, and M. Ohtsu, Jpn. J. Appl. Phys., Part 1 **37**, 1638 (1998).
[6] N. H. Bonadeo, G. Chen, D. Gammon, D. S. Katzer, D. Park, and D. G. Steel, Phys. Rev. Lett. **81**, 2759 (1998).
[7] R. Toledo-Crow, P. C. Yang, Y. Chen, and M. Vaez-Iravani, Appl. Phys. Lett. **60**, 2957 (1992).
[8] E. Betzig, P. L. Finn, and J. S. Weiner, Appl. Phys. Lett. **60**, 2484 (1992).
[9] T. Saiki, S. Mononobe, and M. Ohtsu, Appl. Phys. Lett. **68**, 2612 (1996); T. Saiki and K. Matsuda, *ibid.* **74**, 2773 (1999).
[10] In NOM, the resolution becomes higher with decreasing separation between the sample and the aperture. Therefore, the diameter of the spot seen in the image is expected to be made smaller by decreasing the thickness of the cap layer.
[11] We observe several QDs simultaneously since the dot density is rather high. The number of dots in the detection area is estimated to be 5–6, which is in agreement with the number of peaks in the spectrum.
[12] H. C. van de Hulst, *Light Scattering by Small Particle* (Dover, New York, 1957).
[13] J. J. Wynne and N. Bloembergen, Phys. Rev. **188**, 1211 (1969).
[14] N. H. Bonadeo, J. Erland, D. Gammon, D. Park, D. S. Kstzer, and D. G. Steel, Science **282**, 1473 (1998).

Anal. Chem. **1999**, *71*, 3558–3566

Micrometer-Sized Sodium Ion-Selective Optodes Based on a "Tailed" Neutral Ionophore

Kazuyoshi Kurihara[†] and Motoichi Ohtsu*[,†,‡]

Kanagawa Academy of Science and Technology, 3-2-1 Sakado, Takatsu-ku, Kawasaki 213-0012, Japan, and Interdisciplinary Graduate School of Science and Engineering, Tokyo Institute of Technology, 4259 Nagatsuta, Midori-ku, Yokohama 226-8502, Japan

Takeo Yoshida,[§] Toshihito Abe,[§] Hideaki Hisamoto,[§] and Koji Suzuki[†,§]

Department of Applied Chemistry, Keio University, 3-14-1 Hiyoshi, Kohoku-ku, Yokohama 223-8522, Japan

The preparation and response features of a micrometer-sized sodium ion-selective fiber optode based on a liquid membrane were described. The sensing membrane is a plasticized poly(vinyl chloride)-based copolymer with a neutral sodium ionophore and an anionic dye. To fabricate a micrometer-sized fiber optode, a "micropipet fabrication method" was proposed to fix a liquid membrane-based optode on the small tip of an optical fiber probe, in which the optode size can be varied from ~1 μm to more than 10 μm. Our first optode incorporated a 16-crown-5 derivative as the neutral sodium ionophore and a dibromofluorescein derivative as the single-emission anionic dye. The sensor response was monitored by measuring the fluorescence intensity under a time-resolved photon-counting method. At the first stage of the investigation, it was found that the ionophore including a sodium ion in its cavity leached from the membrane phase. However, we have discovered that the problem can be resolved by using a "tailed" ionophore, which is an ionophore possessing a lipophilic long alkyl chain. The "tail" of the ionophore functions as an "anchor" that prevents leaching of the ionophore from the membrane phase into the water phase. The anchor effect of the tailed ionophore was clearly demonstrated with 6-μm-sized sodium ion-selective optodes. Using a 3-μm-sized optode, the sensor response was examined and successfully explained by the response theory. The size limitation of the optode was also examined using the response features of a 1.5-μm-sized fiber optode. The second optode incorporated a tailed 16-crown-5 derivative as the neutral sodium ionophore and a coumarin derivative as the dual-emission anionic dye. The second optode is more practical than the first optode because the problem of fluorescence distortion due to photobleaching and solvent effect is resolved by ratiometric calibration where the sensor response is monitored by the spectral shift of the dual-emission fluorescence. The sensor response of an 8-μm-sized fiber optode having ratiometric calibration was examined and successfully explained by the response theory.

Much interest has been focused on the miniaturization of a fiber-optic chemical sensor (fiber optode), which is expected to carry out in vivo analyte measurements in a living cell. Recent improvements in miniature fiber optodes are mainly due to the development of a fabrication technique for optical fiber probes for scanning near-field optical microscopy (SNOM), whose spatial resolution is much higher than the diffraction limit.[1-3] Optodes have three major advantages in miniaturization over electrodes; First, optodes require only a one-unit device while electrodes require two (reference electrode and working electrode). Second, optodes can perform a highly sensitive measurement by utilizing a photon-counting method. Third, optodes are more advantageous with respect to electrostatic and magnetic noise than electrodes.[4] Despite these advantages, the miniaturization of optodes has not been easily possible, because there has been no suitable transducer for a miniature optode. However, the recent SNOM fiber probe can be applicable as a transducer for the miniature optode.

A pioneering study of miniature optodes has been carried out by Kopelman and his colleagues.[5-7] They demonstrated the usefulness of submicrometer-sized optodes for pH and dissolved oxygen measurements by preparing the optode membrane on the tip of an optical fiber using a photoinitiated polymerization based on a water-soluble polymer of acrylamide–methylenebis(acrylamide) copolymer. Indicator molecules were immobilized in the water-soluble polymer by covalent bonding or physical entrapment. Their immobilization technique produced satisfactory spatial selectivity of the sensing membrane attached on the tip of an SNOM fiber probe. The aperture size of the probe was 0.1 μm; however, their immobilization method limited the membrane to preparation with a photoinitiated polymer such as an acrylamide–methylenebis(acrylamide) copolymer, which is hard to use in constructing a flexible sensor because only a few indicator

[†] Kanagawa Academy of Science and Technology.
[‡] Tokyo Institute of Technology.
[§] Keio University.

(1) Ohtsu, M. *J. Lightwave Technol.* **1995**, *13*, 1200–1221.
(2) *Near-field nano/atom optics and technology*; Ohtsu, M., Ed.; Springer-Verlag: Berlin, **1998**.
(3) Ohtsu, M.; Hori, H. *Near-Field Nano-Optics*; Plenum: New York, 1999.
(4) Suzuki, K.; Hisamoto, H. *Bunseki* **1995**, *2*, 112–120.
(5) Tan, W.; Shi, Z.-Y.; Kopelman, R. *Anal. Chem.* **1992**, *64*, 2985–2990.
(6) Tan, W.; Shi, Z.-Y.; Smith, S.; Birnbaum, D.; Kopelman, R. *Science* **1992**, *258*, 778–781.
(7) Rosenzweig, Z.; Kopelman, R. *Anal. Chem.* **1995**, *67*, 2650–2654.

10.1021/ac981206+ CCC: $18.00
Published on Web 07/17/1999

molecules are known for the photoinitiated water-soluble polymer.

One of the most practical optodes for the miniaturization is a liquid membrane-based optode,[8-12] whose response mechanism was the ion-pair extraction/ion-exchange principle, first described by Suzuki et al. and Simon et al., independently.[13-19] The great advantage of the liquid membrane-based optode is the large number of ionophores known, which are selective for Li^+, Na^+, K^+, NH_4+, Mg^{2+}, Ca^{2+}, Zn^{2+}, Ag^+, Hg^+, Pb^+, Al^{3+}, and so on.[20] Another advantage is that delicate controls are possible such as tunability of the dynamic range and extension of the detection limit.

Recently, we have developed a new fabrication method for the liquid membrane-based optode, where the optode membrane cocktail (THF solution) is injected in a micropipet and fixed on the probe tip using a micromanipulator system.[2,10] This fabrication method ("micropipet fabrication method") can control the optode size to the precision of 1 μm, which is absolutely impossible by the dip-coating method. In most cases, a plasticized poly(vinyl chloride) (PVC) is used as the liquid membrane, but a better selection for the present method is replacement of the PVC with OH−PVC, a copolymer of vinyl chloride including vinyl alcohol and vinyl acetate. The replacement strengthens the adsorption of the membrane on the glass surface of the probe tip because of hydrogen bonding. The present paper describes the preparation and response features of micrometer-sized sodium-selective optodes based on the liquid membrane.

Miniaturization of the liquid membrane-based optode involves significant problems of leaching and fluorescence distortion. In our case, the most critical problem was the leaching of the ionophore including an ion to be sensed in its cavity; however, a solution was found by using an ionophore that has a lipophilic alkyl chain (a "tailed" ionophore). The leaching of the ionophore can be reduced due to the "anchor effect" of the tailed ionophore, whose tail is used to contact the liquid membrane like an anchor because of its hydrophobic force. The anchor effect indicates that, in a micrometer-sized optode, the lipophilicity value used in a bulk optode is not the only criterion for judging the leaching of the ionophore. On the other hand, the fluorescence distortion was another problem caused mainly by indicator dye molecules, whose fluorescence intensity changed according to photobleaching due to a strong excitation and solvent effect in the sensing membrane. In our case, the photobleaching was not a critical problem because of weak excitation and a highly sensitive measurement but was observed to reduce the optode performance.[12] The solvent effect in the membrane was as much a problem as the photobleaching. A solution for the fluorescence distortion is ratiometric calibration to measure the ratio of the two fluorescence intensities from a dual-emission dye and eliminate the intensity distortion of the fluorescence. The response theory indicates that the optode having the ratiometric calibration shows a high performance especially when the concentration of the dye is lower than that of the ionophore. The ratiometric calibration was demonstrated by carrying out a ratiometric measurement using a coumarin derivative as the dual-emission anionic dye. These results will contribute to the development of a micrometer-sized ion optode for practical use.

PRINCIPLE OF OPERATION AND THEORY

The operation mechanism of the optode based on a liquid membrane incorporating a cation-selective neutral ionophore, S, and a fluorescent anionic dye, AH, is divided into two parts: chemical response and fluorescence measurement. The former is based on the ion-exchange principle given by[13-15]

$$S_o + i^+ + AH_o \rightleftharpoons SiA_o + H^+ \qquad (1)$$

where the subscript o represents the existence of a chemical species in the organic phase (liquid membrane), i^+ is the ion to be sensed, SiA is the produced association (ion pair), and H^+ is a hydrogen ion. Equation 1 gives a chemical response equation that enables one to measure the ion concentration with a relative portion of the deprotonated anionic dyes. The latter fluorescence measurement is an optical method to estimate the relative portion of the deprotonation of the dyes. Here, we describe two methods: an intensity measurement using a single-emission dye and a ratiometric measurement using a dual-emission dye.

Chemical Response Equation. The ion-exchange equilibrium for eq 1 is given by

$$K = \frac{[SiA_o][H^+]}{[S_o][i^+][AH_o]} \qquad (2)$$

where the brackets represent the concentration of the chemical species and K is the ion-exchange equilibrium constant. Equation 2 can be transformed with a relative portion of deprotonated anionic dyes, α, the total ionophore concentration, $[S_{tot}]$, and the total anionic dye concentration, $[A_{tot}]$, resulting in the chemical response equation:

$$[i^+] = \frac{[H^+]\alpha}{K(1-\alpha)([S_{tot}] - [A_{tot}]\alpha)} \qquad (3)$$

This equation indicates important features of the liquid membrane-based optode: the detection limit and the dynamic range are controllable by the hydrogen ion concentration and the dissociation constant of the anionic dye.

Intensity measurement using a single-emission dye is a simple and useful method for evaluating the relative protion of

(8) Shortreed, M.; Bakker, E.; Kopelman, R. *Anal. Chem.* **1996**, *68*, 2656–2662.
(9) Shortreed, M. R.; Bakker, S. L. R.; Kopelman, R. *Sens. Actuators* **1996**, *B35–36*, 217–221.
(10) Kurihara, K.; Ohtsu, M.; Yoshida, T.; Abe, T.; Hisamoto, H.; Suzuki, K. *The Proceedings of Europt(r)ode IV* **1998**, 49–50.
(11) Koronczi, I.; Reichert, J.; Heinzmann, G.; Ache, H. J. *The Proceedings of Europt(r)ode IV* **1998**, 151–152.
(12) Shortreed, M.; Monson, E.; Kopelman, R. *Anal. Chem.* **1996**, *68*, 4015–4019.
(13) Suzuki, K.; Ohzora, H.; Tohda, K.; Miyazaki, K.; Watanabe, K.; Inoue, H.; Shirai, T. *Anal. Chim. Acta* **1990**, *237*, 155–164.
(14) Watanabe, K.; Nakagawa, E.; Yamada, H.; Hisamoto, H.; Suzuki, K. *Anal. Chem.* **1993**, *65*, 2704–2710.
(15) Hisamoto, H.; Watanabe, K.; Nakagawa, E.; Siswanta, D.; Shichi, Y.; Suzuki, K. *Anal. Chim. Acta* **1994**, *299*, 179–187.
(16) Morf, W. E.; Seiler, K.; Rusterholz, B.; Simon, W. *Anal. Chem.* **1990**, *62*, 738–742.
(17) Seiler, K.; Simon, W. *Anal. Chim. Acta* **1992**, *266*, 73–87.
(18) Bakker, E.; Simon, W. *Anal. Chem.* **1992**, *64*, 1805–1812.
(19) Bakker, E.; Buhlmann, P.; Pretsch, E. *Chem. Rev.* **1997**, *97*, 3083–3132.
(20) Buhlmann, P.; Pretsch, E.; Bakker, E. *Chem. Rev.* **1998**, *98*, 1593–1687.

the dye deprotonation, α, because only one photodetector is necessary and many single-emission fluorescent anionic dyes are known so far. In this case, α is given by

$$\alpha = (F - F_N)/(F_A - F_N) \quad (4)$$

where F_N and F_A are theoretical values for the fluorescent intensity when all the dyes are in a neutral form and an anionic form, respectively, and F is the observed value of the fluorescence intensity from dyes excited by the light source. By substituting eq 4 into eq 3, the sensor response equation is finally given by

$$[i^+] = \frac{[H^+](F - F_N)(F_A - F_N)}{K(F_A - F)\{[S_{tot}]F_A + ([A_{tot}] - [S_{tot}])F_N - [A_{tot}]F\}} \quad (5)$$

This equation characterizes the essential response feature of the optode. In assuming a case of $F_A > F_N$ and the activities of all the chemical species being equal to the respective concentration, the profile of log[i^+] vs F gave an S-shaped response curve. In the case where $[A_{tot}] \leq [S_{tot}]$, the minimum of F is F_N at $[i^+] = 0$, while the maximum of F is F_A at $[i^+] = +\infty$. On the other hand, when $[A_{tot}] > [S_{tot}]$, the minimum of F is F_N at $[i^+] = 0$, while the maximum of F is $F_A - (1 - [S_{tot}]/[A_{tot}])(F_A - F_N)$ at $[i^+] = +\infty$. The optode operating under the intensity measurement becomes a little stronger toward the fluorescence distortion when $[A_{tot}] > [S_{tot}]$, but a more effective solution is given by the ratiometric measurement described in the following section.

Ratiometric measurement using a dual-emission dye is an extremely effective method for resolving a serious problem of fluorescence distortion especially in the intensity measurement because the ratiometric measurement evaluates the relative portion of the dye deprotonation, α, with a spectral shift of the dual-emission fluorescence. The fluorescence distortion problem can be attributed to an optical system and a fluorescent dye. As examples of the former problem, the drift and fluctuation in intensity of the laser light and the change and instability in the optical alignment of optical elements such as mirrors and lenses are provided. The former problem can be completely resolved in principle by the ratiometric measurement although it was hardly observed in our experiment. The latter problem due to the fluorescent dye involves photobleaching, leaching, and solvent effects, among which leaching of the dye was not observed. The photobleaching and leaching problem of the dye cannot be completely resolved by the ratiometric measurement because it causes a change in the dye concentration in the sensing membrane, but the following theoretical consideration indicates that they can be substantially resolved when the concentration of the dye is lower than that of the ionophore. The solvent effect problem causes an intensity change and a spectral shift of the dual-emission fluorescence; the former can be compensated for by the ratiometric measurement while the latter cannot in principle. The latter is however so small as to pose no problem in the ratiometric measurement because the spectral shift usually happens over the whole spectram. The only disadvantage of the ratiometric measurement is that few dual-emission anionic dyes are known so far. In the following, mathematical expressions of the ratiometric measurement are given.

Assuming that the deprotonation of the dual-emission dye increases with increasing fluorescence intensity F_1 at wavelength λ_1 and with decreasing fluorescence intensity F_2 at wavelength λ_2, the relative portion of the deprotonated dual-emission dyes, α, is given in two ways:

$$\alpha = (F_1 - F_{1min})/(F_{1max} - F_{1min}) \quad (6)$$

and

$$\alpha = (F_{2max} - F_2)/(F_{1max} - F_{2min}) \quad (7)$$

where F_{1min} and F_{1max} are the minimum and maximum values of F_1, respectively, and F_{2min} and F_{2max} are the minimum and maximum values of F_2, respectively. The ratio R of the fluorescence intensities, F_1 and F_2, is defined as follows,

$$R = F_1/F_2 \quad (8)$$

By substituting F_1 and F_2 of eq 6 and eq 7, respectively, into eq 8, α can be expressed as follows.

$$\alpha = \frac{RF_{2max} - F_{1min}}{(F_{1max} - F_{1min}) + R(F_{2max} - F_{2min})} \quad (9)$$

This equation can be transformed into a more universal form with the fluorescence constants of the dual-emission anionic dye. Besides eqs 6 and 7, the fluorescence intensities, F_1 and F_2, are described as

$$F_1 = S_{1N}[A_N] + S_{1A}[A_A] \quad (10)$$

and

$$F_2 = S_{2N}[A_N] + S_{2A}[A_A] \quad (11)$$

where $[A_N]$ and $[A_A]$ are the anionic dye concentrations in the neutral form and the anionic form, respectively, and S_{1N}, S_{1A}, S_{2N}, and S_{2A} are proportional constants. On the basis of ideal experimental conditions, the following relations are assumed;

$$[A_N] + [A_A] = [A_{tot}] \quad (12)$$

and

$$\alpha = [A_A]/[A_{tot}] \quad (13)$$

The comparison of eqs 10 and 11 with eqs 6 and 7 under the

conditions of eqs 12 and 13 results in the following relations:

$$F_{1min} = S_{1N}[A_{tot}] \quad (14)$$

$$F_{1max} = S_{1A}[A_{tot}] \quad (15)$$

$$F_{2min} = S_{2A}[A_{tot}] \quad (16)$$

and

$$F_{2max} = S_{2N}[A_{tot}] \quad (17)$$

By substituting eqs 14–17 into eq 9, α is given by

$$\alpha = \left(1 + \frac{S_{2A}(R_{max} - R)}{S_{2N}(R - R_{min})}\right)^{-1} \equiv \left(1 + \frac{1}{F(R)}\right)^{-1} \quad (18)$$

where $R_{max} = F_{1max}/F_{2min} = S_{1A}/S_{2A}$ and $R_{min} = F_{1min}/F_{2max} = S_{1N}/S_{2N}$. $F(R)$ is a function newly defined as follows.

$$F(R) = \frac{S_{2N}(R - R_{min})}{S_{2A}(R_{max} - R)} \quad (19)$$

By substituting eq 18 into eq 3, the sensor response equation is finally given by

$$[i^+] = \frac{[H^+]}{K}\left(\frac{[S_{tot}]}{F(R)} - \frac{[A_{tot}]}{1 + F(R)}\right)^{-1} = \frac{[H^+]}{K[S_{tot}]}\left(\frac{1}{F(R)} - \frac{r}{1 + F(R)}\right)^{-1} \quad (20)$$

where the value of r is the concentration ratio of the anionic dye relative to the neutral ionophore, defined as follows.

$$r = [A_{tot}]/[S_{tot}] \quad (21)$$

Equation 20 characterizes some features of the ratiometric measurement. The significant feature is that, in the case where $[A_{tot}] < [S_{tot}]$ ($r < 1$), the optode becomes stronger toward decreasing changes in the anionic dye concentration, $[A_{tot}]$. This is explained by the fact that eq 20 approaches a certain value independent of $[A_{tot}]$ by decreasing the value of r to zero:

$$[i^+] = \frac{[H^+]}{K[S_{tot}]}F(R) \quad (r \to 0) \quad (22)$$

Figure 1 shows the sensor response profiles calculated by eq 20 when $S_{2N} = S_{2A}$. These response profiles show that, in eq 20, the profile of $0 < r < 0.5$ can be approximated by the profile of $r = 0$; in addition, the optode of $0 < r < 0.5$ is extremely effective in handling the problems of decreasing changes in the relative concentration, r, such as photobleaching and leaching of the anionic dye. It should be mentioned that, when $[A_{tot}] < [S_{tot}]/2$, the ratiometric measurement gives a excellent solution to the fluorescence distortion problem due to the photobleaching and leaching of the anionic dye.

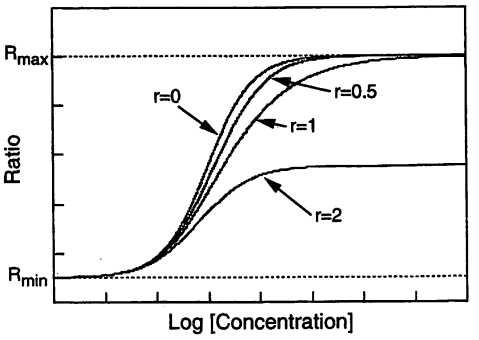

Figure 1. Theoretical response curves of the optode based on the ratiometric measurement using a dual-emission dye. The value, r, is the concentration ratio of the dye relative to the ionophore. The curves are calculated as a function of r by eq 20 under the condition of $S_{2N} = S_{2A}$. These profiles illustrate that the profiles of $0 < r < 0.5$ can be approximated by the profile of $r = 0$.

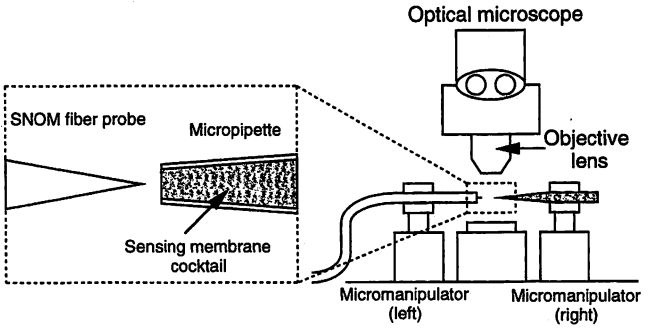

Figure 2. Schematic diagram of the micromanipulator system used for the micropipet fabrication method. The system consists of two micromanipulators and an optical microscope. Fixation is performed under observation through the optical microscope.

EXPERIMENTAL SECTION

Optode Membrane Fabrication. The micropipet fabrication method is briefly described because its details were given in chapter 5 of the monograph edited by Ohtsu.[2] The method employs a micropipet with a micromanipulator system, which consists of two micromanipulators (Shimazu MMS-77, Kyoto, Japan) and an optical microscope (Olympus BX60, Tokyo, Japan). Figure 2 shows a schematic diagram of the method. The SNOM fiber probe was held on the holder of one micromanipulator while a micropipet filled with the sensing membrane cocktail was set on the holder of the other. The fiber probe was fabricated from a quartz-core optical fiber with a micropipet puller (Sutter Instrument Co. P-2000) by the heat-pulling process. No further modifications such as metal coating and silanization were done to the fiber probe. The micropipet was fabricated from a glass tube (Narishige Scientific Instrument Lab. GD-1, Tokyo, Japan) using a micropipet puller (Narishige Scientific Instrument Lab. PP-83). The micropipet had an inner diameter of 2–5 μm and was filled with the cocktail using a syringe, whose needle was put into the glass tube at the other side of the micropipet. By controlling the micromanipulators under visual observation through the optical microscope, the cocktail was immobilized on the tip of the fiber probe. This immobilization procedure had to be done as quickly as possible because the solvent evaporation caused the cocktail to

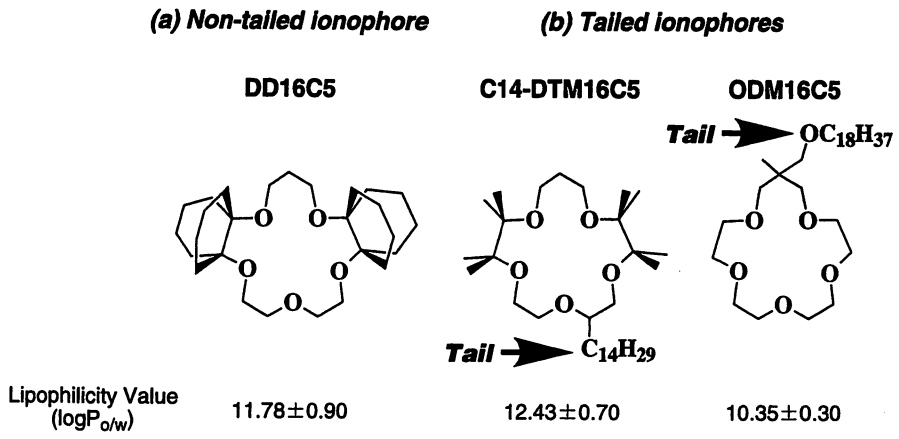

Figure 3. Chemical structures of three kinds of sodium-selective neutral ionophores: (a) nontailed ionophore of DD16C5; (b) two tailed ionophores of C14-DTM16C5 and ODM16C5. The lipophilicity is given by the value of log $P_{o/w}$, where $P_{o/w}$ is the distribution coefficient between the organic liquid and water (see refs 13 and 21).

rapidly become very hard. Sometimes, air pressure on the cocktail in the micropipet, whose other side was connected to a plastic tube with a syringe, was useful for moving the cocktail to the outside of the micropipet. Fixation size varied from ~1 μm to more than 10 μm, which was controllable mainly by varying the diameter of the micropipet and the viscosity of the cocktail. The final micrometer-sized optode was obtained after the fiber probe with the cocktail was dried in a 300-Torr container pumped by a vacuum pump for more than 10 min in order to fully evaporate the solvent THF of the cocktail.

Preparation of Membrane Cocktail. The liquid membrane-based optode was prepared to incorporate a neutral ionophore and a fluorescent anionic dye into the liquid membrane with a solvent of tetrahydrofuran (THF) (Wako Pure Chemical Industries, Ltd., Osaka, Japan, Type Infinity Pure). The liquid membrane consisted of 66 wt % bis(2-ethylhexyl)sebacate (BEHS) (Tokyo Chemical Industry, Tokyo, Japan) and 33 wt % copolymer (OH–PVC) of 90 wt % vinyl chloride, 6 wt % vinyl alcohol, and 4 wt % vinyl acetate (Aldrich Chemical Co., Inc., Milwaukee, WI). The reason for using OH–PVC instead of PVC is the enhancement of adhesion between the glass surface of the fiber probe and the liquid membrane, which is caused by hydrogen bonding between silanol group of the glass surface and hydroxyl group of OH–PVC. Figure 3 shows the chemical structures of sodium-selective neutral ionophores, which are classified according to the existence of a long alkyl chain ("tail"). All the ionophores were synthesized by the authors according to the previous report.[21] The non-tailed ionophore (Figure 3a) is 2,6,13,16,19-pentaoxapentacyclo-[18.4.4.4.^{7,12}0.^{1,20}0^{7,12}]dotriacontane (DD16C5) with a lipophilicity of 11.78 ± 0.90, whereas the tailed ionophores were 2,2,3,3,11,-11,12,12-octamethyl-1,4,7,10,13-pentaoxa-6-tetradecylcyclohexadecane (C14-DTM16C5, Figure 3b) and (1-methyl-3,6,9,12,15-pentaoxacyclohexadecyl)octadecyloxymethane (ODM16C5, Figure 3b) with lipophilicities of 12.43 ± 0.70 and 10.35 ± 0.30, respectively.[21] The value of the lipophilicity is indicated as log $P_{o/w}$, which is the distribution coefficient between the organic liquid and water determined using the R_f values from reversed-phase thin-layer chromatography (RP-TLC) according to the method

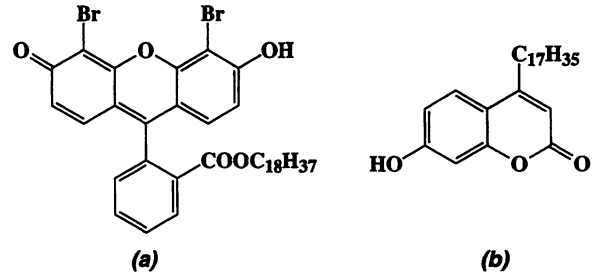

Figure 4. Chemical structures of fluorescent anionic dyes: (a) single-emission dye of 4′,5′-dibromofluorescein octadecyl ester; (b) dual-emission dye of 4-heptadecyl-7-hydroxycoumarin.

reported by Simon et al.[22] The nontailed ionophore, DD16C5, has a value of lipophilicity between those of the two tailed ionophores, C14-DTM16C5 and ODM16C5. The single-emission and dual-emission anionic dyes were 4′,5′-dibromofluorescein octadecyl ester (Fluka Chemical Corp., Ronkonkoma, NY) and 4-heptadecyl-7-hydroxycoumarin (Molecular Probes, Inc., Eugene, OR), respectively. The chemical structures of the anionic dyes are shown in Figure 4. The dibromofluorescein derivative and the coumarin derivative were incorporated at 1.7 and 1.4 wt % relative to the liquid membrane, respectively, while each sodium-selective neutral ionophore was at 200 mol % relative to the anionic dye. The optode components were mixed uniformly with more than 20 times their amount of the solvent THF. The viscosity of this optode membrane cocktail was appropriate for injection into a micropipet and immobilization on the probe tip.

Optical Measurement. Parts a and b of Figure 5 show a schematic diagram of the experimental setup for the intensity measurement and the ratiometric measurement, respectively. The optical measurement system was constructed chiefly from an inverted optical microscope (Olympus IX70). The micrometer-sized optode was vertically held on an *xyz* stage (Narishige Scientific Instrument Lab.) and immersed in Tris-HCl buffer solution at pH 7.4 or 9, which was kept in a culture dish (MatTek Corp.) on the inverted optical microscope. The beam of a single-mode cw Ar^+ laser (Coherent, Inc.) was coupled with a fiber coupler (Newport Corp.) into the optical fiber at the backside of

(21) Suzuki, K.; Sato, K.; Hisamoto, H.; Siswanta, D.; Hayashi, K.; Kasahara, N.; Watanabe, K.; Yamamoto, N.; Sasakura, H. *Anal. Chem.* **1996**, *68*, 208–215.

(22) Laubli, M. W.; Dinton, O.; Pretsch, E.; Simon, W. *Anal. Chem.* **1985**, *57*, 2756–2758.

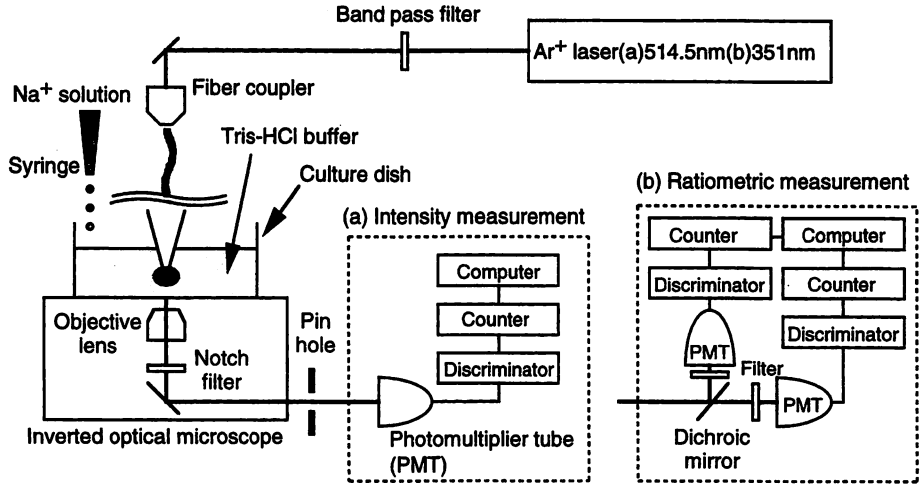

Figure 5. Experimental setups of the miniature optode for (a) intensity measurement using a single-emission dye and (b) ratiometric measurement using a dual-emission dye. The miniature optode is excited by the light of an Ar^+ laser system, and its fluorescence is measured with the time-resolved photon-counting method. The optode is immersed in a buffer solution, whose Na^+ concentration is changed by adding droplets of NaCl solution into the culture dish with a syringe.

the fiber optode. The fluorescent anionic dye in the optode membrane was excited by the laser light at a power of ~1 μW propagating through the optical fiber. The excitation wavelength was 514.5 and 351 nm for the single-emission dye of the dibromofluorescein derivative and the dual-emission dye of the coumarin derivative, respectively. The fluorescence of the dibromofluorescein derivative was at a peak of ~540-nm wavelength. On the other hand, the fluorescence of the coumarin derivative had two peaks at ~380- and ~430-nm wavelength and an emission isosbestic point at ~400 nm wavelength. The fluorescence from the excited dye was collected with a 10× objective lens of the inverted optical microscope and then passed through a holographic notch-plus filter (Kaiser Optical Systems, Inc.) in a mirror unit cassette (Olympus IX-RFAC) to reject the laser light by a factor of 10^6. In addition, the fluorescence passed through a pinhole in the cassette (Olympus OSP-MST) connected to the side port of the inverted optical microscope in order to reject the background light collected by the objective lens. For the intensity measurement (Figure 5a), the fluorescence was measured with a photomultiplier tube (PMT) (Hamamatsu R464, Shizuoka, Japan) by means of the photon-counting method with an accumulation time of 1 s. Data were stored on a personal computer (NEC Corp. PC-9821Xa, Tokyo, Japan) through a photon-counting board (Hamamatsu M3949) and a photon-counting unit (Hamamatsu C3866). On the other hand, for the ratiometric measurement (Figure 5b), with a dichroic mirror (Olympus U-MWU) in a cassette (Olympus OSP-DMU1), the fluorescence from the dual-emission dye was divided at the emission isosbestic point of ~400 nm into two beams, each of which was detected by PMT. The signals were measured by the photon-counting method. The data were successively stored on the computer through the photon-counting boards and the photon counting units. Finally, the ratio of the two counts was calculated on the computer. Both fluorescence measurements were carried out in a completely dark room. The Na^+ concentration in the sample solution was varied by adding droplets of NaCl solution (10^{-3}–1 M) into the culture dish using a syringe. To check visually whether the droplets fell into the culture dish, a light flash was used, which was recorded in the sensor response profiles as a signal for adding droplets of NaCl solution.

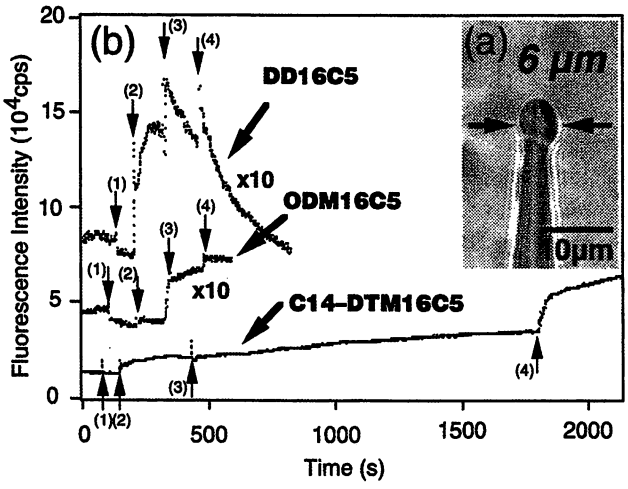

Figure 6. Comparison of dynamic response profiles of 6-μm-sized optodes based on different types of ionophores: (a) micrograph of the 6-μm-sized optode; (b) dynamic responses of three optodes based on the nontailed ionophore, DD16C5, and the two tailed ionophores, C14-DTM16C5 and ODM16C5. The arrows with numbers indicate the time when Na^+ droplets were added. The peaks accompanying the marks are due to a light flash to check the droplets falling into the culture dish. Na^+ concentrations in the solution: (initial state) 0, (1) 3.8×10^{-4}, (2) 4.1×10^{-3}, (3) 4.0×10^{-2}, and (4) 2.9×10^{-1} M.

RESULTS AND DISCUSSION

Ionophore with a "Tail Effect". Using the micropipet fabrication method and the dip-coating method, the Na^+ optodes were prepared in several sizes ranging from 1 μm to more than 100 μm. The optode was based on the liquid membrane incorporating DD16C5 as the neutral ionophore and dibromofluorescein derivative as the single-emission dye. Experimental results showed that optodes of 10–100-μm size worked with good reproducibility. On decreasing the size of the optode to less than 10 μm, the response of the optodes became unstable; especially, the 1-μm-sized optode did not show any response to the addition of sodium ion in the

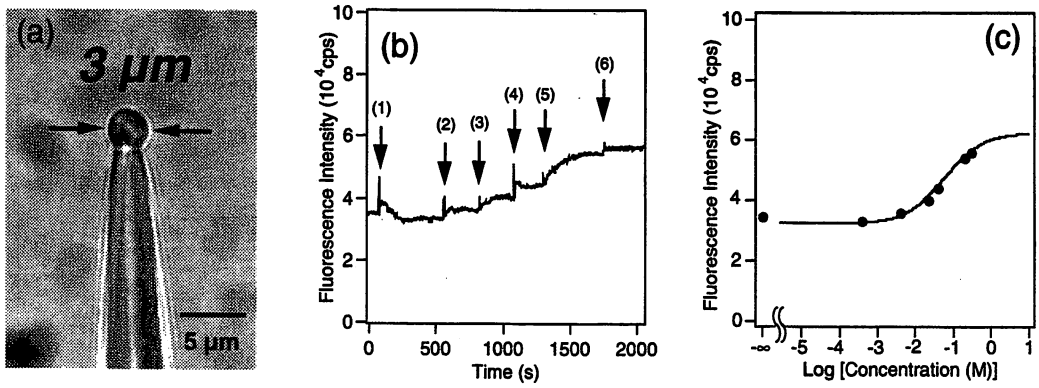

Figure 7. Characterization of a 3-μm-sized optode based on the tailed ionophore C14-DTM16C5: (a) micrograph of the 3-μm-sized optode; (b) dynamic response profile of the optode. Arrows with numbers indicate the time when Na^+ droplets were added. Peaks accompanying the marks are due to a light flash to check the droplets falling into the culture dish. Na^+ concentrations in the solution: (initial state) 0, (1) 3.8×10^{-4}, (2) 4.1×10^{-3}, (3) 2.2×10^{-2}, (4) 4.0×10^{-2}, (5) 1.9×10^{-1}, and (6) 2.9×10^{-1} M. (c) Plots of the sensor responses. The response curve is obtained by fitting the plots using the theoretical response equation (eq 5).

sample solution. After a number of careful experiments for over one year, we understand that the ionophore structure affects the sensor response of the optode. A typical case is the following; three kinds of sodium-selective optodes of 6-μm size were prepared employing two kinds of a tailed ionophore of C14-DTM16C5 and ODM16C5 and one kind of a nontailed ionophore of DD16C5 (for its chemical structure, see Figure 3a). Figure 6a shows a micrograph of the 6-μm-sized optode. The response profiles of the three optodes were obtained by time-resolved fluorescence intensity measurement. Figure 6b shows dynamic response profiles of the three optodes to various concentrations of Na^+ at pH 7.4. Arrows with numbers 1–4 indicate the point of changing sodium ion concentrations in the sample solution. A drastic difference in the three profiles was observed between the optodes using the tailed ionophore and the nontailed ionophore; The responses of the tailed ionophores of C14-DTM16C5 and ODM16C5 gradually reached a certain constant value after adding sodium ion; whereas, the response of the optode using the nontailed ionophore, DD16C5, was so unstable as to show a decay behavior at a Na^+ concentration of higher than 4.0×10^{-2} M. This decay behavior is simply attributed to the dynamics of the leaching of the nontailed ionophore from the membrane phase into the water phase. On the basis of the ion-exchange principle, the detailed dynamics mechanism of the decay behavior can be explained as follows: the addition of the analyte ion to the water phase causes, in the membrane phase, a nontailed ionophore to catch the analyte ion in the cavity and an anionic dye is subsequently deprotonated. The deprotonation of the dye brings about an increase in fluorescence of the dye. The leaching of the nontailed ionophore from the membrane phase into the water phase is accelerated by formation of the ion–ionophore complex because the ion in the cavity makes the ionophore become hydrophilized. As a result, the ion–ionophore complex in the membrane phase begins to leach into the water phase and the deprotonated dye in the membrane becomes protonated. The protonation of the dye gives rise to a decrease in fluorescence of the dye, which was observed as the decay behavior in the DD16C5-based optode shown in Figure 6b. It is noted that the decay rate of the fluorescence intensity of the dye indicates the leaching rate of the ion–ionophore complex from the membrane phase into the water phase. This dynamics mechanism also gives a qualitative explanation of the experimental results that the leaching rate becomes faster with an increasing concentration of analyte ion.

The results of the three profiles in Figure 6b clarify the use limit of the lipophilicity factor of log $P_{o/w}$, which is the criterion for leaching of the substance from the membrane in a bulk optode. In a micrometer-sized optode, the leaching of the ionophore cannot be explained only by the lipophilicity factor, because the tailed ionophore, ODM16C5 (log $P_{o/w} = 10.35$), has a lower lipophilicity value than the nontailed ionophore, DD16C5 (log $P_{o/w} = 11.78$). The hydrophobic interaction between the liquid membrane and the aliphatic tail of an ionophore has an important effect on the leaching in the micrometer-sized optode. This tail effect of the tailed ionophore is considered to be the anchor effect, because the aliphatic tail of the ionophore acts like an anchor attached to the liquid membrane. In the development of a micrometer-sized optode based on the liquid membrane, the chemical structure of the ionophore should be considered as well as the lipophilicity factor. The anchor effect can be evaluated as something like the hydrophile–lipophile balance (HLB) value of surfacants, estimated from the tailed ionophore including an ion of interest.

Response Features of the 3-μm-Sized Optode. With the 3-μm-sized optode incorporating the tailed ionophore of C14-DTM16C5 and the single-emission dye of the dibromofluorescein derivative, the optical responses for Na^+ at pH 7.4 were measured and the theoretical response characteristics were examined. Parts a and b of Figure 7 show a micrograph of the 3-μm-sized optode and its typical dynamic response for changes in Na^+ concentration in the sample solution, respectively. The response time of the optode is from 10 to ~200 s, dependent on the Na^+ concentrations of 3.8×10^{-4}–2.9×10^{-1} M. The sensor responses for Na^+ concentrations obtained from the dynamic response profile in Figure 7b are plotted in Figure 7c with closed circles. The solid curve in Figure 7c is the theoretical response curve calculated by fitting the plots with eq 5 using the computer software, Igor Pro (WaveMetrics, Inc.). On the basis of this fitting, $F_N = 3.2 \times 10^4$, $F_A = 6.2 \times 10^4$, and log $K = -4.85 \pm 0.07$ were obtained. This K value corresponded well with those obtained with the macrosized optodes having the same membrane composition in which the membrane was prepared using a spin-coating device.

Characterization of the 1.5-μm-Sized Optode. One of the greatest interests in the miniature optode based on the tailed

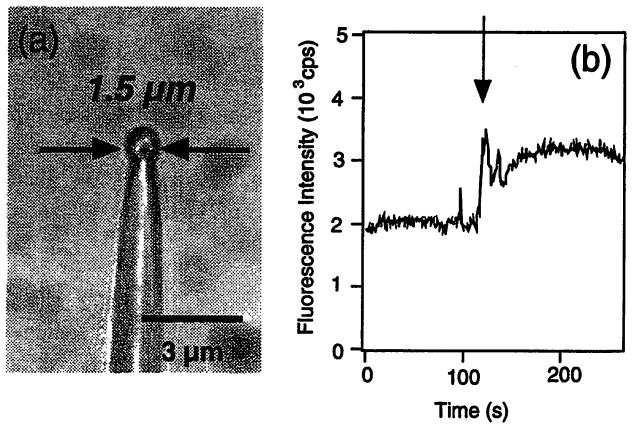

Figure 8. Characterization of a extremely miniature optode of 1.5-μm size based on the tailed ionophore C14-DTM16C5: (a) micrograph of the 1.5-μm-sized optode; (b) its optical response to a change in Na^+ concentration from 0 to 2.9×10^{-1} M. The arrow indicates the time when Na^+ droplets were added. The peak accompanying the mark is due to a light flash to check the droplets falling into the culture dish.

ionophore lies in the miniaturization limit. Therefore, a 1.5-μm-sized optode based on the tailed ionophore of C14-DTM16C5 and the single-emission dye of the dibromofluorescein derivative was prepared and characterized. A micrograph of the 1.5-μm-sized optode is shown in Figure 8a. The 1.5-μm-sized optode responded to a sodium ion but did not show a sensor response corresponding to the sodium ion concentration. Figure 8b shows a typical dynamic response of the 1.5-μm-sized optode for Na^+ concentrations from 0 to 2.9×10^{-1} M. A peak indicated by the arrow was caused by a light flash used to visually check the droplets of Na^+ sample falling into the culture dish. This sensor response of the 1.5-μm-sized optode indicates the possibility of preparing a submicrometer-sized ion optode, but it also indicates the technical limitations of its development. Usage of a tailed ionophore with a longer tail than the tailed ionophore C14-DTM16C5 would improve the leaching problem.

Demonstration of the Ratiometric Calibration Using a 8-μm-Sized Optode. Fluorescence distortion such as photobleaching due to the strong excitation and solvent effect in the sensing membrane is a major problem for the above-mentioned miniature optode using a single-emission dye, which can be solved by ratiometric calibration using a dual-emission dye. With the 8-μm-sized optode incorporating the tailed ionophore of C14-DTM16C5 and the dual-emission dye of a coumarin derivative, we demonstrated a high-performance micrometer-sized optode having the ratiometric calibration. The micrograph and the dynamic responses of the high-performance optode are given in parts a and b of Figure 9, respectively. The numbered arrows, 1–6, in Figure 9b indicate the time when the sodium ion concentration at pH 9 was changed by adding droplets of sodium ion solution into the dish. The profiles of F_1 and F_2 were obtained by measuring each emission of the dual-emission dye. The fluorescence of F_1 and F_2 ranged from 420 to ~500 nm and from ~360 to 385 nm, respectively. The sensor response of the optode having the ratiometric calibration is the profile of R, which was calculated by dividing the profile of F_1 by that of F_2. Judging from the profile of R, the response time of the optode is from 10 to roughly 500 s, depending on the concentration of the sodium ion

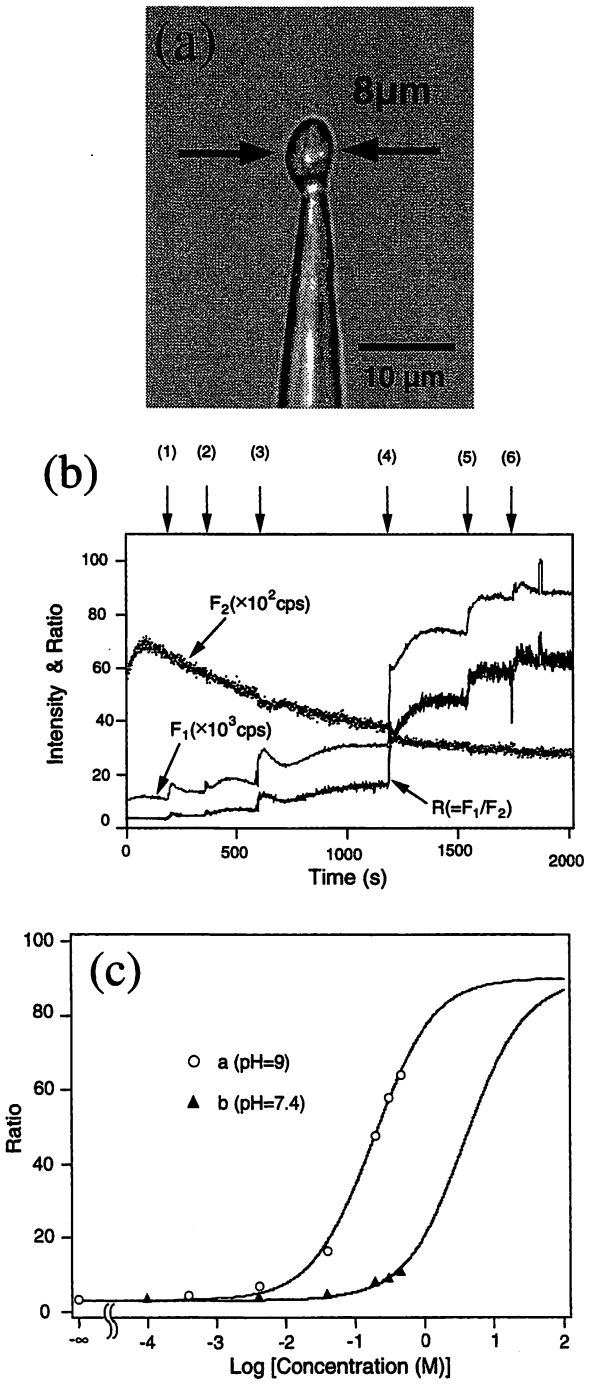

Figure 9. Characterization of a 8-μm-sized optode having ratiometric calibration based on the tailed ionophore C14-DTM16C5: (a) micrograph of an 8-μm sized optode; (b) dynamic responses of the 8-μm-sized optode. The profile of R is the dynamic response of the optode based on the ratiometric measurement. The profiles of F_1 and F_2 were obtained by measuring fluorescence intensities from the dual-emission dye at two different wavelengths. The profile of R is calculated by dividing the profile of F_1 by that of F_2. Arrows with a number indicate the point of a change in the Na^+ concentration: (initial state) 0, (1) 3.9×10^{-4}, (2) 4.1×10^{-3}, (3) 4.0×10^{-2}, (4) 1.9×10^{-1}, (5) 2.9×10^{-1}, and (6) 4.4×10^{-1} M. (c) Sensor responses and their response curves calculated by the theoretical equation (eq 22). Data a denoted by open circles come from the dynamic response of the profiles R. Data b denoted by closed triangles were obtained from the measurement of pH 7.4

(3.9×10^{-4}–4.4×10^{-1} M). The workings of the ratiometric calibration can be confirmed by some points: For example, the

profiles of F_1 and F_2 gradually increase from 0 to 70 s and then gradually decrease from 70 to 180 s, while the profile of R is constant during the measurement time because of the ratiometric calibration. The increase from 0 to 70 s can result from the solvent effect in the sensing membrane where the analyte ion concentration changes by movement of the analyte ion from the water phase into the membrane phase. The solvent effect in the sensing membrane causes enhancement of the entire fluorescence of the dye. On the other hand, the decrease from 70 to 180 s can be attributed to the photobleaching of the dye. The second example is found in the fact that the profile of R generally behaves as a step function rather than that of F_1. Here, the profile of F_2 plays a role in eliminating fluorescence distortion from the profile of F_1.

The sensor response of the optode having the ratiometric calibration is discussed using the theoretical response equation of eq 22, which is a suitable approximation of the exact theoretical equation of eq 20 at the relative concentration $r = 0.5$. Figure 9c shows the theoretical response curves fitting the sensor responses. The dynamic response of the profile R in Figure 9b corresponds to the open circles (data a) of Figure 9c. By fitting the data a with the theoretical curve of eq 20, $R_{min} = 3$, $R_{max} = 90$, and $\log K(S_{2A}/S_{2N}) = -7.24$ were obtained. To estimate the last value, we used $[H^+] = 10^{-9}$, $[S_{tot}] = 9.58 \times 10^{-2}$ (which was calculated from the specific gravity of BEHS, 0.914 g/cm^3), the molecular weight of the dual-emission fluorescent anionic dye is 400.6, and the ionophore is 200 mol % relative to the dye in the optode membrane. The theoretical response curve shown by the closed triangles (data b) in Figure 9c was obtained by measurement under the condition of pH 7.4, which causes the response curve of the data b to shift to a higher concentration side than that of the data a measured under the condition of pH 9.

There is great interest in the miniaturization limit of the optode having the ratiometric calibration. However, miniaturization smaller than an 8-μm optode has not yet been realized. The main reason is the excitation of UV light, which causes a kind of light denaturation in the copolymer of OH–PVC in the optode, although dual-emission anionic dyes for visible light excitation can avoid the light denaturation. In fact, as described above, we have successfully obtained a 3-μm-sized optode based on a single-emission dye for visible light excitation.

Anchor Effect of a Tailed Anionic Dye. The chemical structures of the anionic dyes in Figure 4 show that all the anionic dyes used in our experiment have a lipophilic long alkyl tail. It is quite natural that the tailed anionic dyes as well as the tailed neutral ionophore should have the anchor effect of the tail. Thus, one of the reasons why the leaching of the anionic dye was not observed in our experiment can be attributed to the anchor effect of the tailed anionic dye. In our micrometer-sized optode based on a liquid membrane, the anchor effect of the tail is used as an effective solution to the leaching problem.

CONCLUSIONS

The present paper demonstrated a micrometer-sized sodium-selective optode based on a liquid membrane using a tailed neutral ionophore such as C14-DTM16C5 and ODM16C5. This demonstration includes three important results. First, the micropipet fabrication method was accomplished as a method for immobilizing the optode membrane on the tip of the SNOM fiber probe. Second, as a solution to the leaching problem of an ionophore, the anchor effect of a tailed ionophore was discovered, which means that the tail of the ionophore functions as an anchor to prevent the leaching of the ionophore into the water phase because of the hydrophobic force. Third, two response theories of the intensity measurement using a single-emission dye and the ratiometric measurement using a dual-emission dye were presented and successfully applied to the experimental results.

The present paper has achieved the fundamental technology for a micrometer-sized optode using the existing liquid membrane-based technology. To develop a submicrometer-sized optode with a smaller size than the optical wavelength (0.4–0.8 μm), much greater improvement of the liquid membrane-based optode technology including an ionophore and an indicator dye is expected.

ACKNOWLEDGMENT

The authors thank Dr. R. U. Maheswari of the Kanagawa Academy of Science and Technology for critical reading and commenting on the manuscript. K.K. thanks the Nissan Science Foundation for financial support. This study was partially supported by a Grant-in-Aid for Scientific Research, the Ministry of Education, Science, Sports and Culture.

Received for review November 4, 1998. Accepted June 1, 1999.

AC981206+

Abstract e3.1b

Near field optical technology for high density optical storage and nano-deposition

M. Ohtsu
Interdisciplinary Graduate School of Science and Engineering,
Tokyo Institute of Technology, 4259 Nagatsuta-cho, Midori-ku, Yokohama 226-8502, Japan
Phone: +81-45-924-5455
Fax: +81-45-924-5599
E-mail: ohtsu@ae.titech.ac.jp

For optical disk memory of 1Tb/in^2 density and Gb/s data transmission rate, recent progress of storage and read out by a planar near field optical head array made of Si are reviewed. Chemical vapor deposition of nanometric metallic Zn stripes, closely spaced Zn dots, and blue-light emitting ZnO dots by UV optical near field are demonstrated for nanometric photonic integration,. Pump-probe spectroscopy of a single InGaAs quantum dot are reviewed to be used use as an integrated nanometric photonic switch. Basic concept for nano-photonic integrated circuit by optical near field technology is also presented.

Inst. Phys. Conf. Ser. No 165: Symposium 1
Paper presented at 2nd Conf. Int. Union Microbeam Analysis Societies, Kailua-Kona, Hawaii, 9–13 July 2000

Design and Application of an Ultra-high Spatial Resolution Mapping System Using Near-field Spectroscopy

[1]T Ikeda, [1]Y Narita, [2]T Williams and [3]M Ohtsu

[1]JASCO Corporation 2967-5, Ishikawa-cho, Hachioji, Tokyo 192-8537, Japan.
[2]JASCO International Co., LTD.,2-4-21, Sennin-cho, Hachioji Tokyo 193-0835 Japan.
[3] Interdisciplinary Graduate School of Science and Engineering, Tokyo Institute of Technology, 4259 Nagatsuda-cho, Midori-ku, Yokohama 226-8502 Japan

Recent advanced material technology puts demands on characterization in small regions of the sample. The Raman micro-spectrometer is a powerful tool for identification of impurity substances and estimation of residual stress in the materials. However, the spatial resolution of the instrument is determined by the diffraction limit ($\lambda/2$) of the exciting light and is insufficient for recent requirements. In 1928, Synge [1] proposed the concept of applying near-field optics to microscopes. In the 1990s, many researchers developed scanning near-field optical microscopes (SNOM). Applying Raman micro-spectroscopy has also been reported in spite of very weak Raman scattering in the near-field [2-5]. We have designed and developed an ultra-high spatial resolution micro Raman mapping system and photoluminescence (PL) mapping system using near-field spectroscopy technique with high throughput fiber probes.

Figure 1 shows the schematic illustration of our near-field Raman and PL micro-spectrometer. In the case of illumination-collection mode the exciting laser light is introduced into the fiber probe and irradiates the sample, then Raman scattering or photoluminescence is collected by the same fiber probe. On the other hand in the case of collection mode the laser irradiates the sample directly, then scattered light is collected by the fiber probe. The sample-probe separation is regulated by monitoring of a resonating probe to maintain the aperture of the probe in the near-field. The topographic image of the sample surface is then measured by monitoring variations in the position of the sample Z stage while XY scanning. The light from the probe is introduced to the monochromator and detected by a cooled CCD. A more detailed description of the system with illumination mode and optical fiber probe was reported elsewhere [3].

A scanning electron microscope (SEM) photograph of the probe is shown in Figure 2. The tip was fabricated using the chemical etching method, which gives high reproducibility. Many different types of probe can be fabricated simply by changing the composition of the etching solution. The probe surface is coated by a metal such as gold or aluminum. The aperture of 50 to 1000nm sizes was prepared by pushing the probe against a flat substrate.

The near-field Raman spectrum of a polydiacetylene (PDA) crystal using illumination-collection mode is shown in Figure 3. Raman spectra at a sample-probe separation of about 10 nm (A) and 1μm (B) were obtained in 1 second with an input laser power of 10 mW at 532 nm. The 300 nm aperture diameter probe was used to irradiate the sample and to collect the Raman scattering. PDA Raman was observed only in the near-field (A). The peaks at around

1420 cm^{-1} and 2120 cm^{-1} are assigned to a C=C and C≡C bond stretching respectively. The broad band spectrum at 1μm separation (B) is caused by the fiber probe itself. Mapping of near-field micro spectroscopy at low temperature (Liquid He) can be performed in a cryostat and several applications will be presented.

This work was funded by the Japan Science and Technology Corporation.

References

[1] Synge E H, 1928 Philos.Mag.**6**, pp 356-62
[2] Jahncke C L, Paesler M A, Hallen H D 1995 Appl. Phys. Lett **67**(17) pp 2483-5
[3] Narita Y, Tadokoro T, Ikeda T, Saiki T, Mononobe S, Ohtsu M. 1998 Appl. Spectrosc. **52** (9) pp 1141-4
[4] Webster S, Bachelder D N, Smith D A 1998 Appl. Phys. Lett. **72**(12) pp 1478-80
[5] Grausem J, Humbert B, Spajer M, Courjon D, Bruneau A and Oswalt J 1999 J. Raman Spectrosc. **30**, pp 833-40

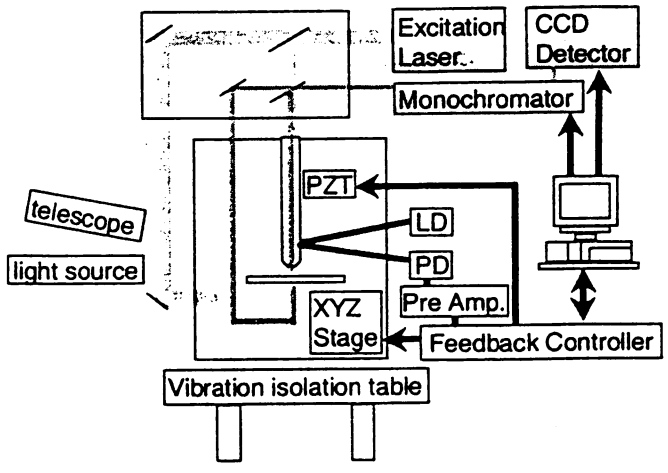

Fig. 1. The schematic illumination of the near-field micro-spectrometer

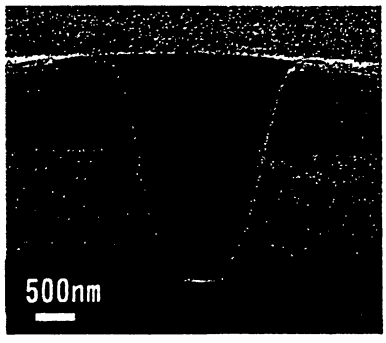

Fig. 2. SEM Photograph of a fiber probe

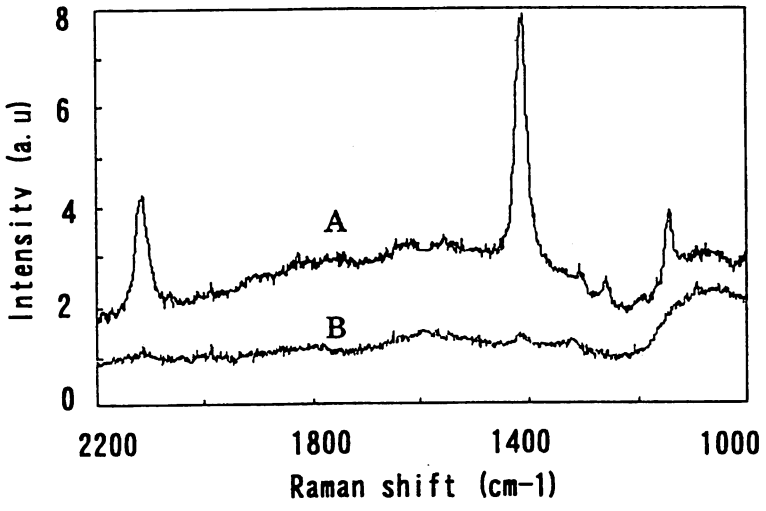

Fig. 3. The near-field Raman spectrum of a polydiacetylene crystal using illumination-collection mode at a sample-probe separation of about 10 nm (A) and 1μm (B)

CTuI7 **6:15 pm**

Extremely high throughput and resolution capability of an optical near-field slider

T. Yatsui, S. Kogiso, M. Kourogi,* K. Tsutsui, M. Ohtsu,* J. Takahashi,** *Interdisciplinary Graduate School of Science and Engineering, Tokyo Inst. of Tech., 4259 Nagatsuta, Midori-ku, Yokohama, Japan 226-8502; E-mail: yatsui@ae.titech.ac.jp*

For realizing high density/speed near-field optical recording/readout, we demonstrate here a new slider with silicon protruded probe array that is bonded to a glass substrate. The advantages of such a slider are: (1) The high refractive index of the silicon (n = 3.67, @ λ = 830 nm) leads to a short effective wavelength inside the probe, which results in high throughput and spatial resolution compared to conventional fiber probes.[1] (2) Data transmission rate increases in proportion to the number of probe in the array.[2] (3) The protruded silicon probe array has high durability because of its bonding to the thick glass substrate and surrounded by the bank.

By following the design criterion of a contact-type hard disk head,[3] the slider structure is fabricated from (100)-oriented silicon on insulator (SOI) wafer for realizing data transmission rate of 1 Gbps and data density of 1 Tb/in^2 with 100 probes: (i) The SOI is bonded to the glass substrate by anodic bonding [Fig. 1(a)]. (ii) After removing the silicon substrate, the oxide layer is patterned. (iii) The probe array, the bank, and pads are fabricated by anisotropic etiching (34 wt% KOH, 80°C) [Fig. 1(b)]. (iv) The slider is quarried by dic-

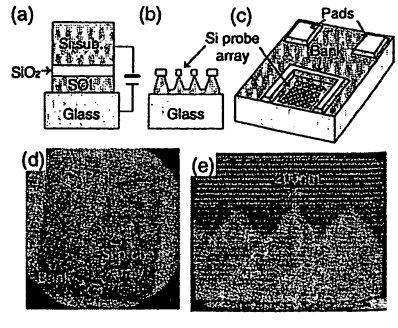

CTuI7 Fig. 1. Schematic of the fabrication process of an optical near-field slider with protruded silicon probe array.

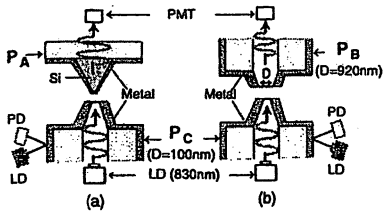

CTuI7 Fig. 2. Probe-to-probe method.[4] The separation between the probes is maintaining within several nanometers with shear-force technique. P_A: silicon protruded probe with 30-nm-thick aluminum coating, P_B: apertured probe with D = 920 nm, P_C: apertured probe with D = 100 nm.

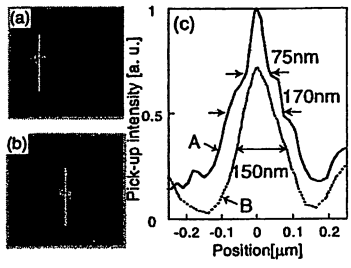

CTuI7 Fig. 3. Spatial distribution of the optical near-field intensity. (a) and (b) are for P_A (protruded silicon probe) and P_B (apertured fiber probe with D = 920 nm), respectively. Image size is 1.5 ~1.5 μm^2. Curves A (solid line) and B (dashed line) in (c) are the cross sectional profile along the white dashed line in (a) and (b), respectively.

ingsaw after removing the oxide layer. [Figs. 1(c) and 1(d)]. (v) The slider is coated with 30-nm-thick aluminum.

We confirmed that the height dispersion of silicon protruded probes is <10 nm [Fig. 1(e)], which is comparable to the thickness uniformity of the SOI layer.

By using an apertured fiber probe with aperture diameter (D) of 100 nm (P_C in Fig. 2), we evaluated the throughput and resolution of the silicon probe [P_A in Fig. 2(a)] in comparison with an apertured fiber probe with D = 920 nm [P_B in Fig. 2(b)], which is equal to cut-off diameter (D_C) at λ = 830 nm. As is described in detail in Ref. 4, the apertured probe with D = D_C has high throughput (10%) and very narrow peak [full width at half maximum (FWHM) = 150 nm] due to the resonance.

Figures 3(a) and 3(b) are observed spatial distribution for P_A and P_B. Curves A and B in Fig. 3(c) show the cross-sectional profile along the white dashed line in (a) and (b), respectively. The FWHM of curve A is 170 nm, to which a part of the leaked light can contribute because of the thin coating. However, one can find that a very narrow (75 nm) peak at the center of the curve and that the intensity is 1.5 times larger than that for curve B, which are attributed to the localized optical near field due to the high refractive index of the silicon. Taking the resolution of P_C into consideration, these results indicated that the protruded silicon structure led to high resolution (<100 nm) and high throughput (>10%) simultaneously.

From these results, it can be expected that the slider with protruded silicon probe array is a possible candidate for realizing high density/speed optical near field recording/readout.

*Also with Kanagawa Academy of Science and Tech., Japan
**Ricoh Co., Ltd., Japan

1. H.U. Dangebrink, T. Dziomba, T. Sulzbach, O. Ohlsson, C. Lehrer, L. Frey, "Nano-slit probes for near-field optical microscopy fabricated focused ion beams," J. Microscopy **194**, Pt 2/3, 335–339 (1999).
2. T. Yatsui, M. Kourogi, K. Tsutsui, J. Takahashi, M. Ohtsu, "Subwavelength-sized phase-change recording with a silicon planar apertured probe," in *Near-Field Optics: Physics, Devices, and Information Processing*, S. Jutamulia, M. Ohtsu, T. Asakura eds., Proc. SPIE **3791**, 76–84 (1999).
3. M. Yanagisawa, A. Sato, K. Ajiki, F. Watanabe, "Design concept for in-contact HDI system," TRIB-Vol. 6, Tribology of contact/near-contact recording for ultra high density magnetic storage, ASME, 25–32 (1996).
4. M. Kourogi, T. Yatsui, K. Tsutsui, J. Takahashi, M. Ohtsu, "Subwavelength-sized phase-change recording with a high throughput fiber probe" in *Near-Field Optics: Physics, Devices, and Information Processing*, S. Jutamulia, M. Ohtsu, T. Asakura eds., Proc. SPIE **3791**, 68–75 (1999).

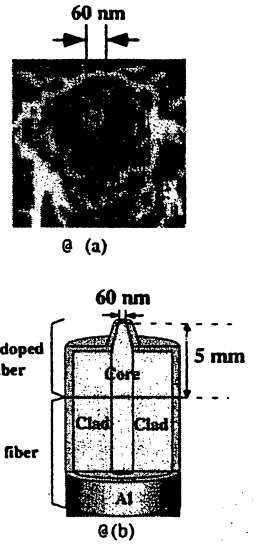

QMF4 Fig. 1. (a) SEM image of the tip region of a fiber probe with the aperture diameter of 60 nm and (b) illustration of the structure.

QMF4 **11:00 am**

In-situ fabrication of nanostructures by photo-enhanced chemical vapor deposition using optical near field

G.H. Lee, Y. Yamamoto,* M. Kourogi,**
M. Ohtsu,** *Japan Science and Tech. Corp., 687-1 Tsuruma, machida, Tokyo 194-0004, Japan; E-mail: ghl@ohtsu.jst.go.jp*

Photo-enhanced chemical vapor deposition (PE-CVD) offers the possibility for the lateral integration (i.e., side by side) of different structures (different sequence of layers, materials, thickness and dopants), without the need of any lithography or etching, in a single growth run. In the PE-CVD process, with utilizing optical near field with nanometric resolution as a light source, the technology allows one to fabricate and modify surface structure down to the nanometric level with high accuracy of controlling position and size. We have previously reported on the *in-situ* fabrication of Zn pattern with minimum width of 15 nm by prenucleation method.[1] Here, we demonstrate the method to directly deposit metal atoms by gas phase photodissociation of metalorganic gas. The method has the advantage that the lateral integration of various materials is easy.

Experiments were carried out by depositing directly Zn atoms on the substrate by means of photodissociation of diethylzinc (DEZ: $Zn(C_2H_5)_2$) gas with optical near field, which was generated from the subwavelength aperture at the tip of a fiber probe introduced into vacuum chamber. Because the second harmonic light of Ar+ laser (λ = 244 nm) was used as the light source, a fiber probe with low loss for the UV light was designed and fabricated by our group. In this work, UV fiber spliced with a fiber with GeO_2 core was used for the high reproducibility of aperture size. Figure 1 shows (a) the SEM image of the tip of an used fiber probe and (b) the illustration of the structure. The position control and the scanning of the probe were performed by typical optical near field microscope system.

Figure 2 shows (a) the shear force topographic image of Zn dots deposited on a glass by the fiber probe of Fig. 1 and (b) the cross sectional profile of the dots. The size of the two

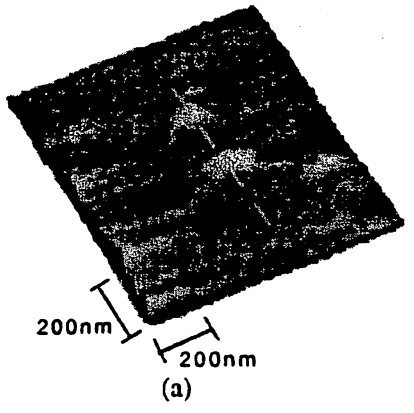

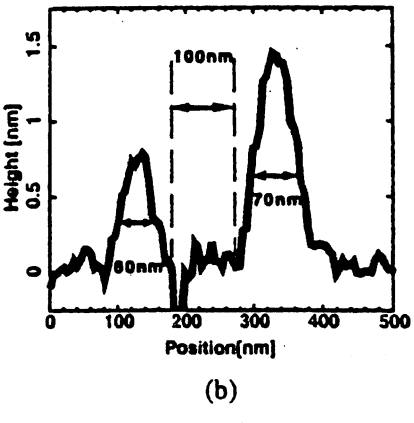

QMF4 Fig. 2. (a) Shear force topographic image of Zn nanodots fabricated on a glass by using the fiber probe shown in Fig. 1 and (b) cross sectional profile of the dots.

dots was comparable with the aperture diameter of the fiber probe, i.e., the FWHM were 60 nm and 70 nm, including the resolution of shear force microscope, which means that the lateral size of dot is determined by the aperture diameter of fiber probe. They were fabricated at distance close to 100 nm, which means that the fabrication position can be controlled on

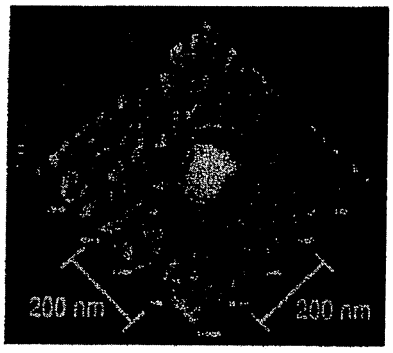

(a)

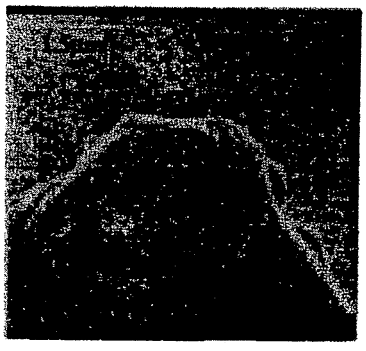

(b)

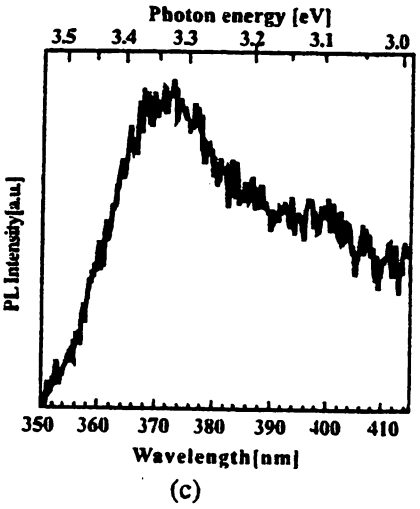

(c)

QMF4 Fig. 3. (a) Shear force topographic image of ZnO nanodot fabricated on an α-Al_2O_3 substrate by optical near field, (b) SEM image of a probe with submicrometer ZnO on the tip, and (c) room temperature emission spectrum from the tip of the probe.

the nanometric scale. The height of the dots increased in proportion to optical near field energy and the aspect ratio increased at the ratio of about 0.03/μJ.

As based on photochemical reaction, PE-CVD has no limitation regarding substrate and deposited materials. As a preliminary experiment, ZnO film was deposited on α-Al_2O_3 substrate to be insulator by a conventional far field propagating light using the reaction between photodissociated Zn atoms and oxygen. The substrate was heated over 150°C during the deposition. From the film, a strong free exciton emission of 380 nm was clearly observed even at room temperature, which we believe is the first observation of room temperature UV emission from the ZnO film deposited by PE-CVD. Furthermore, ZnO nanodot with the size smaller than the wavelength of the irradiating light (λ = 244 nm) was also successfully fabricated using optical near field [Fig. 3(a)]. On the other hand, the submicrometer ZnO was deposited on the tip of a fiber probe with submicrometer aperture [Fig. 3(b)], and room temperature UV emission of ZnO was also observed as shown in Fig. 3(c).

In-situ fabrication of nanostructures at desired position on the nanometric scale has been successfully realized by PE-CVD with optical near field. It is the best suitable for the development of nano-scale photonic IC composed of nanometer-scale structures showing quantum size effect, in which optical near field is used as a carrier for transmitting the signal.

*Tokyo Inst. of Tech., Japan

**Japan Science and Tech. Corp. and Tokyo Inst. of Tech., Japan

1. V. Polonski, Y. Yamamoto, M. Kourogi, M. Ohtsu, "Nanometric patterning of zinc by optical near field photochemical vapor deposition," J. Microscopy **194**, 545–551 (1999).

QTuA23

Nanometric probe-sample interactions via optical near fields: derivation and characteristics

Suguru Sangu, Kiyoshi Kobayashi, Motoichi Ohtsu,* *ERATO Localized Photon Project, Japan Science and Tech. Corp., 687-1 Tsuruma, Machida, Tokyo, 194-0004 Japan; E-mail: sangu@ohtsu.jst.go.jp*

Recent experimental studies have revealed distinct characteristics of optical near fields.[1] Highly localized optical near fields could be applied to not only a high-resolution microscope beyond the diffraction limit of light but also fabrication of nanometric devices. From this point of view, a theory, which quantitatively deals with interactions between a nanometric probe tip and sample, is required to describe the optical near-field systems. We have proposed a microscopic formulation of the optical near-field systems, and found that elementary excitation modes of exciton-polaritons, or virtual photons, give a good explanation for general properties of optical near fields.[2] In this report, we derive the effective interactions more rigorously, and elucidate characteristics of a nanometric probe-sample system.

In order to discuss the optical near-field system in terms of two-body interaction like the Coulomb interaction with the help of the projection-operator method,[3] we divide the total system into two subsystems, microscopic (probe tip-sample) and macroscopic (bath) subsystems. The macroscopic subsystem can be viewed as a set of excitons, free photons, and their interactions, and has characteristic elementary modes, that is, exciton-polariton modes. Finally, the potential operator is written as

$$\hat{V} = -i\sqrt{\frac{2\pi\hbar}{V_0}}\sum_{\alpha=A}^{B}\theta(z_\alpha)\sum_{j=1}^{3}[\hat{b}_j^\dagger(\vec{r}_\alpha) + \hat{b}_j(\vec{r}_\alpha)]\sum_{\vec{k}}[K'_{\alpha j}(\vec{k})\hat{\xi}(\vec{k}) - K^*_{\alpha j}(\vec{k})\hat{\xi}^\dagger(\vec{k})], \quad (1)$$

$$K'_{\alpha j}(\vec{k}) = \sum_{\lambda=1}^{2}\mu_\alpha[\vec{e}_j\cdot\vec{e}_\lambda(\vec{k})]\,f(k)e^{i\vec{k}\cdot\vec{r}_\alpha}, \quad (2)$$

where $(\hat{b}_j^\dagger, \hat{b}_j)$ and $(\hat{\xi}^\dagger, \hat{\xi})$ are the creation and annihilation operators of the electron excitation in the sample A and probe tip B, and of the exciton-polaritons in the macroscopic subsystem. If the eigenfrequency $\Omega(k)$ of the exciton-polaritons is approximated by using the effective mass m_p, *i.e.*, $\Omega(k) \approx \hbar k^2/2m_p + \Omega/2$, the coupling coefficient $f(k)$ is given by

$$f(k) = \frac{ck}{\sqrt{\Omega(k)}}\frac{\sqrt{\Omega(k)^2 - \Omega^2/4}}{\sqrt{2\Omega(k)^2 - \Omega^2/4 - c^2k^2}}$$

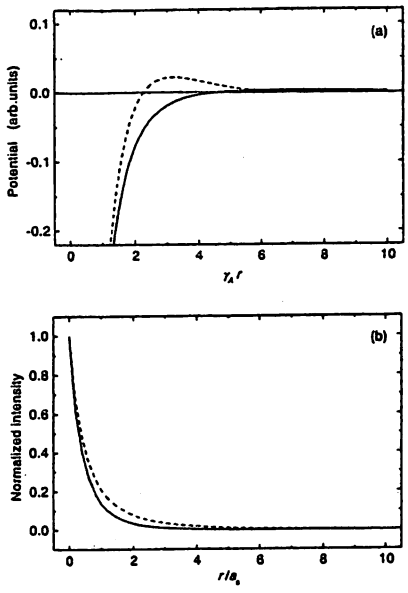

QTuA23 Fig. 1. (a) Effective interaction potentials between the probe tip and sample, and (b) intensity distribution from a spherical sample with the radius a_s = 10 nm. The solid and dashed curves represent the potentials in the cases of p = 0.1 and 0.9, respectively, where only the first term in Eq. (4) is calculated.

$$= \sqrt{\frac{m_p c^2}{\hbar}(k^2+\gamma_\alpha^2)}\left[\frac{A(p)}{k^2+\gamma_\alpha^2}+\frac{B(p)}{k^2+\delta^2}+\frac{C(p)}{k^2+i\delta^2/\sqrt{2}}+\frac{D(p)}{k^2-i\delta^2/\sqrt{2}}\right]^{1/2}, \quad (3)$$

where $\gamma_\alpha \equiv \sqrt{m_p(2\Omega_\alpha+\Omega/\hbar}$, $\delta \equiv \sqrt{m_p\Omega/\hbar}$, and $p \equiv \delta^2/\gamma_\alpha^2$, Ω_α being the eigenfrequency of the probe tip or the sample, and an approximation of $m_p c^2 \sim \hbar\Omega$ is adopted to give an insight for the characteristic behavior of the interactions. The effective interaction potential due to the coupling between the microscopic subsystem and the exciton-polaritons is, then, given by

$$V_{\text{eff}}(|\vec{r}_A-\vec{r}_B|) = -\frac{4\pi\mu_A\mu_B}{(2\pi)^3}\times\left\{\int\frac{f^2(k)e^{i\vec{k}\cdot(\vec{r}_A-\vec{r}_B)}}{k^2+\gamma_A^2}d^3\vec{k}+\int\frac{f^2(k)e^{-i\vec{k}\cdot(\vec{r}_A-\vec{r}_B)}}{k^2-\gamma_B^2}d^3\vec{k}\right\} \quad (4)$$

It follows that the effective interaction potential is determined by the sign and magnitude of the factors A, B, C, and D in Eq. (3), which depend on the unique parameter p. In Fig. 1(a), the effective interaction potential is plotted for p = 0.1 and 0.9 with $\hbar\Omega$ = 2 eV. In the latter case, both the positive and negative potentials appear because contributions from the third and fourth terms in Eq. (3), which include oscillating components, become more dominant than in the former case. Figure 1(b) shows intensity distribution as a function of the distance from a spherical sample with the radius a_s = 10 nm. In the case of p = 0.1, the decay length is comparable with the sample size while the positive potential for p = 0.9 induces somewhat a broaden decay.

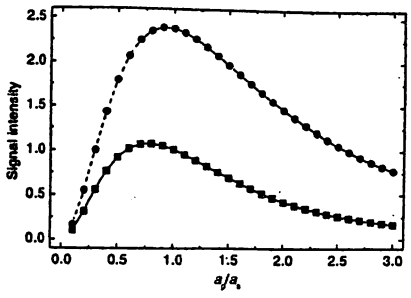

QTuA23 Fig. 2. Signal intensity of the optical near-field systems as a function of the probe-tip size normalized by the sample size. The square and circular dots represent the contrast in the cases of p = 0.1 and 0.9, respectively.

Our theoretical approach also has the advantage that intensity properties of optical near fields can be described without solving complex differential equations. As an example, we calculate the signal intensity that is defined as the ratio of the intensity integrated within a probe-tip sphere with the radius a_p to the geometrical cross-section (see Fig. 2). Size resonance between the probe tip and sample, which is a characteristic behavior of optical near-field systems,[4] can be observed in our numerical result. Moreover, it is found that the signal intensity becomes large with increase of the parameter p reflecting the eigenenergies of probe-tip/sample materials.

*Japan Science and Tech. Corp. and Tokyo Inst. of Tech., Japan

1. M. Ohtsu ed., "Near-field Nano/Atom Optics and Technology," (Springer-Verlag, Tokyo, 1998).
2. K. Kobayashi and M. Ohtsu, "Quantum theoretical approach to a near-field optical system," J. Microscopy **194**, 249–254 (1999).
3. P. Fulde ed., "Electron Correlations in Molecules and Solids," 3rd ed., 83–100 (Springer, Berlin, 1995).
4. K. Jang and W. Jhe, "Nonglabal model for a near-field scanning optical microscope using diffraction of the optical near field," Opt. Lett. **21**, 236–238 (1996).

Chemical vapor deposition of nanometric materials by optical near field toward nano-photonic integration

M. Ohtsu[1] and G.H. Lee[2]

1) Interdisciplinary Graduate School of Science and Engineering, Tokyo Institute of Technology, 4259 Nagatsuta-cho, Midori-ku, Yokohama 226-8502, Japan. ohtsu@ae.titech.ac.jp
Also with ERATO Localized Photon Project, Japan Science and Technology Corporation, 687-1 Tsuruma, Machida, Tokyo 194-0004, Japan

2) ERATO Localized Photon Project, Japan Science and Technology Corporation, 687-1 Tsuruma, Machida, Tokyo 194-0004, Japan, ghl@ohtsu.jst.or.jp

8.1 Introduction

Optical near field has been applied to varioud field, such as spatially high resolution microscopy, spectroscopy, ultra high density optical memory, atom manipulation and so on[1-3]. In the case of microscopy, high-resolution beyond the diffraction limit has been realized to observe the 4 nm –width image of a single strand DNA[4]. Spatial Fourier analysis has estimated that the resolution has reached as high as 0.8 nm[5]. Basic process governing near field optics is the short-range electromagnetic interaction between the probe tip and sample in optical frequency region. In case that this interaction is sufficiently strong, the sample structure and conformation can be optically modified, and thus, this modification can open new applications, such as the fabrication of nanometric materials and the manipulation of atoms.

Recently, there has been an interest in its application to nano-structure fabrication because of the possibility to realize nano-photonic integration[6]. For the realization of such a device, which uses the optical

near field as a carrier for signal transmission, various materials with nanometric size must be integrated laterally on a substrate. For this integration, we need an advanced nano-structure fabrication technique, which must realize spatially high resolution, precise control of size and position, and be applicable for various materials.

Conventional techniques popularly used for nano-structure fabrication are X-ray or electron beam lithography and self-organized growth technique[7]. The former makes it easy to produce the desired pattern, but is disadvantaged by the complexity associated with a multi-step proces that involves pattern definition and transfer. The latter easily produces high-quality nano-scale dots, but control over position and size is difficult.

So far, lithographic technology has been utilized for the fabrication of submicron structures using optical near field[8]. However, with the complexity of the process and with the damage of substrate and film by etchants, it has a lot of problems that still need to be solved. As a technology susceptible to solve those problems, photo-enhanced chemical vapor deposition (PE-CVD) method has been attracting attention. Based on photochemical reaction, PE-CVD offers not only the possibility for the lateral integration of different structures (different sequence of layers, materials, thickness and dopants) in a truly single growth run[9,10] but also the option of chemical selective growth by varying the wavelength of used light source.

Since the optical near field energy is concentrated within nanometric dimension smaller than the wavelength of light[1-3], it enables us to deposit various materials on nanometric dimension by utilizing photo-decomposition of chemical gases. Therefore, the combination of optical near field technology with the PE-CVD process appears to be the best suitable technology for the integration of nanometer scale elements because it not only allows us to fabricate nanostructures but also gives a dual advantage of the in-situ measurement of the optical properties of the fabricated nanostructures.

Based on this consideration, this paper reviews the recent progress of authors' works on fabricating nanometric materials toward the realization of a nanometric photonic integrated circuit[11].

8. 2 Principle

The PE-CVD combined with optical near field, i.e., near field optical –CVD (NFO-CVD), was carried out by utilizing the optical near field generated from the subwavelength aperture at the tip of a fiber probe introduced into a vacuum chamber. The scanning of the probe was performed by typical near field optical microscope system. As NFO-CVD is based on photodissociation reaction, it is necessary for a reactant molecule to absorb photons with higher energy than its dissociation energy. Hence, as the light source, light with higher energy than dissociation energy of reactant molecule should be used.

The deposition mechanisms using optical near field are represented in Fig.8.1, which demonstrates two methods. One is prenucleation method to fabricate prenuclei by decomposing only adsorbed molecules on the substrate with optical near field(Fig.8.1(a))[12]. The process consists of two-steps. In the first step, metalorganic gas is filled into the vacuum chamber for a few minutes and then evacuated, which leaves a few adsorbed monolayers on the substrate surface. By decomposing the adsorbed molecules with optical near field, nuclei for growth are formed, when patterning of the prenuclei is executed by scanning the probe. In the second step, conventional propagating light is directed onto the prenucleated area in the presence of a parent gas and then the decomposed atoms are selectively deposited on the pre-existing nuclei. This method has the advantage of being free from the deposition at the probe tip, otherwise has the drawback that the lateral integration of various materials is not easy due to using the propagating light in the second step.

The other is to directly deposit atoms by gas phase photodissociation of metalorganic gas with optical near field(Fig.8.1(b))[13]. The advantage lies in the possibility of selective deposition of various materials by changing parent gases, which is useful for lateral integration.

8.3 Depositing Zinc

Let us discuss the deposition of Zn as an example of NFO-CVD by using a diethlzinc(DEZ) as a parent gas. This molecule absorbs a light with photon energy higher than 4.76 eV (wavelength below λ = 260 nm) and photodissociation reaction occurs as follows.

$$Zn(C_2H_5)_2 + 2.256\ eV \rightarrow ZnC_2H_5 + C_2H_5$$
$$ZnC_2H_5 + 0.9545\ eV \rightarrow Zn + C_2H_5$$

Thus the second harmonic light (SH light) of an Ar^+ laser (λ = 244 nm) and an ArF excimer laser (λ = 193 nm) were used as the light source for photodissociation of DEZ gas. The SH light was generated in a BBO crystal placed in the built-up cavity. For the purpose of generating the UV optical near field with sufficient power density to decompose DEZ gas, an UV fiber with transmission los as low as 1.1 dB/m at 244 nm was used to fabricate a probe[14]. An UV probe was coated with 200 nm thick Al film after being tapered by chemical etching. The shape of this probe is shown in Fig.8.2. The throughput of the probe was 1 x 10^{-4} and the power density at the probe tip with a sub-100nm aperture for 1 mW of incident UV light was as high as 1 kW/cm^2. The separation between the probe and the substrate was maintained within several nanometers by shear-force technique using a tuning fork based probe[15].

Figure 8.3 shows the shear force image of the loop shaped Zn pattern on a glass substrate produced by prenucleation method[12]. The vacuum chamber was evacuated to below 10^{-5} Torr prior to the prenuclei fabrication stage, then filled with about 10 Torr of DEZ gas, maintaining at the pressure for 20 min. Next, the chamber was re-evacuated to the pressure of 10^{-5} Torr, which leaves a few adsorbed monolayer on the substrate surface. Prenucleation was performed by delivering the SH light on the substrate covered with adsorbed molecules using a probe. Nuclei of Zn were formed by the decomposition of DEZ gas adsorbed on the substrate with the optical near field at the probe tip. In the growth stage after nuclei fabrication, DEZ gas was refilled in the chamber with a few Torr and the unfocused ArF excimer laser with the maximum energy of 10mJ was directly irradiated on

the prenucleated substrate. Then the growth proceeded only on the pre-existing nuclei.

As seen in Fig.8.3, the minimum width of the pattern is as small as 20 nm. The width achieved here is two orders smaller than the minimum width reported so far by conventional PE-CVD using a far-field light[15]. Since the measured width includes the resolution of a vacuum shear-force microscope(VSFM)[17] depending on the shape of the used probe, the intrinsic width can be smaller than the value estimated from Fig.8.3.

Next, we discuss the results from the direct gas phase photodissociateion method. Figures 8.4(a) and (b) show the shear force image of deposited Zn dots and a T-shaped pattern. The gas pressure and input power of SH light were 1 mTorr and 10 mW, respectively. In the fabrication of the dots, optical near field on the probe tip was illuminated over five spots at the interval of 800 nm on the substrate for a few seconds. As shown in Fig.8.4(a), the position of the dots are spaced by 800 nm in excellent agreement with the spacings of the illuminated points, which establishes high controllability of the positioning in fabricating nanostructures by this technique. The T-shaped patten was prepared by scanning the substrate at a speed of 10 – 50 nm/s. A glance at Fig. 8.4(b) is sufficient to explain that NFO-CVD makes it possible to fabricate subwavelength-scale structures with control of their size and position. One disadvantage of this method is that the probe tip is also gradually covered with the depositing materials while fabricating a nano-structure on the substrate. In our experience, however, this only became a problem after a few hours of operation, while only a few seconds are necessary to fabricate nano-structure. Therefore, it is not a serious problem. NFO-CVD technique also allows us to fabricate nanostructure of oxides, inslators, and semiconductors as well as metals containing Zn, Al, Cr, and W.

In order to examine the effect of optical near field energy on the growth, an experiment was performed by varying illumination time at a constant gas pressure of 1 mTorr and input SH light power of 15 mW. The SH light power at the probe tip was estimated to be 300 nW. The value of

optical near field energy was evaluated by measured SH light power × illumination time. The substrate was kept at room temperature.

Figure 8.5 represents the variation of height and diameter of the shear force image of the dots as a function of optical near field energy. This figure shows that the Zn dots grew as the optical near field energy increased, i.e., the height increased linearly at the rate of about 5 nm/μJ in proportion to the increase of energy, while the diameter was almost constant with respect to the optical near field energy. It means that the dot size depends on the spatial distribution of the optical near field in the direction lateral to the substrate surface, while depends on the optical near field energy in the normal direction. Thus the aspect ratio of the dot, i.e., the ratio of its height to diameter increased proportionally with the increase of optical near field energy at the ratio of about 0.03/μJ.

One of the most attractive features of this technique is its high spatial resolution. The lateral size of fabricated pattern depends on the spatial distribution of the optical near field energy and its reproducibility also depends on the reproducibility of fabricating probes. Currently used probes are made of optical fiber with GeO_2 doped core, and have shown high resolution and high reproducibility. But the transmission loss for the light of 244 nm (96dB/m) is so high that the fiber cannot be used in UV region. To increase the reproducibility and spatial resolution of UV fiber probe, we spliced fiber probe with GeO_2 doped core to the UV fiber, as is schematically explained by Fig.8.6(a). The fiber probe was fabricated by the two-step etching process[18]. During the first step the cladding diameter was reduced by immersing in a buffered HF solution with a volume ratio of [40wt.% NH_4F aqueous solution] : [50%wt.% HF acid] : [deionized water] = 1.7 : 1 : 1. And in the next step, the fiber was selectively etched in the same kind of solution with a volume ratio of 10 : 1 : 1, while the temperature was kept at 25℃. After completing the etching process, the probe was coated with 200 nm thick Al by vacuum evaporation. In order to form an aperture, the Al film was removed from the probe tip by focused ion beam. Figure 8. 6(b) shows the SEM image of a fabricated probe with an aperture diameter of 60 nm. This probe is fabricated with highly reproducible aperture size less than 100

nm. Figures 8.7(a) and (b) show the shear force image of deposited dots by using a probe with aperture diameter of 60 nm and the cross sectional profile along the dashed line, respectively. Two dots with the diameter of 60 nm and 70 nm (full width at the half maximum of the cross sectional profile) were fabricated at a very close distance of 100 nm. The diameter of the dots was comparable with the aperture diameter of the used probe, which suggests that the smaller dots can be fabricated by using a fiber probe with smaller aperture. Since the measured diameter of the dot image includes the resolution of VSHM depending on the shape of the used probe, intrinsic diameter can be smaller than the value estimated from Fig.8.7.

8.4 Depositing Zinc Oxide

One of the advantages in this NFO-CVD is the fact that there is no limitation in regard to substrate and deposited materials. Another technique in which CVD is comined with scanning tunneling microscopy (STM) has been reported to be able to produce nanostructure with dimensions close to the atomic level[19]. However, the main drawback comes from the impossibility to use non-conductive substrates and grow patterns of non-conductive materials. However, this limitation is eliminated by using optical near field. As an example, let us demonstrate the nanofabrication of ZnO on α -Al_2O_3 substrate to be insulator by NFO-CVD[20].

As a preliminary experiment, ZnO films were deposited by PE-CVD method by using a propagating far-field light. Here, we used the reaction between oxygen and DEZ conveyed by a carrier gas (Ar) into the chamber during the irradiation by the propagating SH light (λ =244 nm) of an Ar^+ laser. (0001) α -Al_2O_3 was used as the substrate for the epitaxial growth of ZnO. The reaction chamber was initially evacuated to the pressure in the low 10^{-5} to 10^{-7} Torr range, then filled with the reactant gases with the ratio of DEZ : O of 1 : 10 at a working pressure of 10 mTorr. The chamber pressure was maintained at 10 mTorr during the growth. In order to find the optimal growth conditions, the crystallinity, stoichiometry, optical transmission, and photoluminescence were evaluated. The crystallinity and

the stoichiometry were evaluated by X-ray diffraction (XRD) measurement using Cu K α radiation and X-ray photoelectron spectroscopy (XPS) using Al K α X-ray. The optical transmission measurements were carried out by a double-beam monochromator in atmospheric ambient at wavelengths from 300 to 1000 nm to measure the optical energy band gap of films. The photoluminescence was measured at room temperature using a cw He-Cd laser as an excitation light source.

The PE-CVD of ZnO was carried out for 10 min within a range of the substrate temperature from room temperature to 300 ℃. The energy density of the laser source and the spot size were 10 mW and 600 μ m, respectively. The films were grown on only irradiated area and the photo-irradiation effect for the deposition rate was clearly observed for all substrates.

Figure 8.8 shows X-ray diffraction patterns of ZnO films deposited at various substrate temperatures. The rise in the surface temperature of the substrate from UV light was negligible for the light power was as low as 0.2 mW/cm^2, which means that the deposition resulted from photochemical reaction between DEZ and oxygen. The film deposited at room temperature exhibits no XRD reflection lines, which implies that it is essentially amorphous. Crystalline films were deposited at substrate temperature over 100 ℃ and the films with c-axis oriented crystalline, exhibiting the (002) XRD lines, were grown at substrate temperature above 150 ℃. With the increase of substrate temperature above 150 ℃, the intensity of X-ray peak from (002) planes became stronger, while other peaks such as the (101) peak became weaker. The c-axis lattice constant was estimated to be 0.5207 nm from the peak position of the (002) line, which is very close to the c-axis value of 0.5206 nm reported for bulk ZnO[21]. It indicates that these films have a high quality crystalline structure. The stoichiometry was confirmed from the XPS spectrum for the planar films. For the films deposited at the substrate temperature above 150 ℃, the atomic ratios of Zn : O were also 1.00 : 1.00 within the accuracy of a few percent.

The optical properties were also investigated. Figure 8.9 shows the optical transmission spectra of films deposited at substrate temperatures

from 150 ℃ to 300 ℃. Transmission fell off steeply at aroung 380 nm, characteristic of high quality ZnO film. From the plot of the wavelength vs. the absorption coefficient, optical band gap energies ranging from 3.26 to 3.31 eV were estimated, which is identical to the value recorded for high quality ZnO films[22]. The photoluminescence spectra were measured using the 325 nm line of a cw He-Cd laser. Figure 8.10 shows the emission spectra measured at room temperature from the films deposited at the substrate temperature from 150 ℃ to 300 ℃. The emission peak position is coincident with the expected energy of the free exciton, and even at room temperature a strong free exciton emission at 380 nm is clearly observed[23,24]. This confirms that if we use PE-CVD method at a low temperature, the ZnO film emitting UV light at room temperature can be fabricated. This is the first observation of the room temperature UV emission from the ZnO films deposited by PE-CVD.

Under the growth conditions studied by the previous experiments mentioned above, the ZnO nanostructure fabrication was carried out by NFO-CVD. The fabrication was performed by introducing the SH light of an Ar^+ laser onto the α -Al_2O_3 substrate surface through the fiber probe which is shown by Fig.8.6(a). The maximum power of the SH light was 10 mW, which means that the light power density at the probe tip was of the order of several kW/cm^2. During the deposition, substrate-probe tip separation was maintained at 10 nm by shear force technique.

Figure 8.11 shows the VSFM image of fabricated nanometric scale ZnO. The dot was 200 nm diameter and 5 nm height. The diameter is smaller than the wavelength of the irradiating light source. However, because this value includes the broadening due to the resolution of VSFM, the real diameter should be much smaller than that observed. We have actually succeedeed in making Zn dots and wires below 100 nm with the same probe by optimizing growth conditions, as shown in Fig.8.8.

8.5 Toward Nano-photonic Integration

Future optical transmission system requires an advanced photonic

integrated circuit(IC) for increasing speed and capacity. To meet this requirement, its size should become much smaller than that of a conventional diffraction-limited photonic IC, which is composed of diode lasers, optical switches, optical waveguides, and so on. A concept of such a nano-photonic IC is shown by Fig.8.12, in which metallic wires, light emitters, optical switches, input/output terminals, and photo-detectors, all controlled by nano-scale single dots and lines[6]. These devices use the optical near field as a carrier for signal transmission. For this integration, we need an advanced nano-structure fabrication technique, which realizes spatially high resolution, precise control of size and position. Further, various materials with nanometric size must be integrated laterally on a substrate, i.e., not a point-contact type but a planar-type near field optical system should be realized.

As having been demonstrated in the previous sections, the NFO-CVD constitutes very promising tool for in-situ patternig of nanostructures for this integration. Nanoscale Zn dots and lines with the size of sub-100 nm have been successfully realized in a single growth step. We also revealed that ZnO nanostructures, emitting UV light at the room temperature, can be fabricated. Further, This technique exhibits extraordinally high controllability and reproducibility in fabricating nanostructures at desired position, which have never been demonstrated by any other conventional self-organized growth technique of semiconductor nanostructures. What is excellent, as it is based on photodissociation reaction, selective growth of various materials, i.e., metals, insulators, and semiconductors, can be accomplished by the choice of light source, which allows us to realize the nano-photonic IC composed of nanostructures.

To operate the nano-photonic IC, several nonlinear and resonant optical phenomena such as dynamic Stark effect, optical bistability utilizing nonlinearity and plasmon-like field enhancement in a quantum dot [25], and so on should be utilized. In order to demonstrate, e.g., a nonlinear optical switching capability of a single quantum dot, we have measured the nonlinear absorption change in a single InGaAs quantum dot [26]. For this experiment, we used self-assembled quantum dots grown on a (100) GaAs

substrate by gas-source molecular beam epitaxy. Atomic force microscope studies confirmed that the average dot diameter was 30 nm and the height was 15 nm. The dot density was about 2 x 10^{10} dots/cm^2. These dots were covered with cap layers with a total thickness of 180 nm. As schematically explained in Fig.8.13(a), a probe light (λ = 900 - 980 nm) was introduced into the back of the sample, and the transmitted light is collected and detected by a high throughput fiber probe with double tapered structure[27] placed in the vicinity of the sample surface using shear force technique. When the sample was illuminated by a pump light(λ = 635 nm) passing through the fiber probe, carriers were generated in the barrier layer, and flew into the quantum dots. Then the ground states of the quantum dots were occupied with the carriers. The resultant reduction of the absorption of the quantum dots was measured by detecting the transmission change in the probe light. Experiments were carried out in a liquid helium cryostat, where a double modulation/demodulation technique was used for a detecting a very weak signal.

Figure 8.13(b) shows an experimental result demonstrating a deep modulation of the transmitted probe light power due to irradiation of the pump light. It is confirmed from this result that a single quantum dot works as an optical switch, and further, the switching operation can be detected by a conventional optical signal detection technique, which is advantageous for application to nano-photonic IC. Faster switching operation can be expected by utilizing nonlinear optical phenomena involving virtural transitions. Problems having to be solved for realizing a practical nano-photonic IC are; coupling with input/output ports, signal isolation, estimating the limits of bandwidth, gain/efficiency, switching time and power, and so on.

Combining the technique reviewed here with atom manipulation by optical near field[28], further progresses in depositing novel materials and operating more advanced photonic IC can be expected. For these progresses, theoretical works are required to establish the design criteria for optical near field system, for which quantum theoretical treatment of optical near field has been developed to establish an intuitive model of Yukawa potential[29].

8.6 Summary

This chapter reviewed the recent progress of application of interactions between optical near field and nanoscale materials. Photochemical vapor deposition of Zn dots and lines with the size of sub-100 nm has been realized by using an UV optical near field. Deposition of nanoscale ZnO was also revealed. Optical near field technology offers the opportunity to modify surfaces and develop new nanostructures that may exhibit quantum effect due to their extremely small size. Utilizing such a very high potential of this technology, a concept of nano-photonic IC was proposed. Optical switching operation of a single InGaAs quantum dot was demonstrated to be used for nano-photonic devices.

Acknowledgements

The authors would like to thank Mr. Y. Yamamoto (Tokyo Institute of Technology) and Dr. V. Polonski(Japan Science and Technology Corporation) for their devoted collaboration. They acknowledge Prof. H. Hori (Yamanashi University), Dr. K. Kobayashi (Japan Science and Technology Corporation), and Dr. M. Kourogi (Tokyo Institute of Technology) for their valuable comments and suggestions.

References

[1] M. Ohtsu, *Near-Field Nano/Atom Optics and Technology*, Springer-Verlag, Berlin, Tokyo, New York, 1998

[2] M. Ohtsu, J. Lightwave Technol., vol.13, p.1200 (1995)

[3] M. Ohtsu and H. Hori, *Near-Field Nano-Optics*, Kluwer Academic/Plenum Publishers, New York, 1999

[4] Uma Maheswari Rajagopalan, S. Mononobe, K. Yoshida, M. Yoshimoto and M. Ohtsu, Jpn. J. Appl. Phys., vol.38, p.6713 (1999)

[5] R. Uma Maheswari, H. Kadono and M. Ohtsu, Opt. Commun., vol.131, p.133 (1996)

[6] M. Ohtsu, Technical Digest of the 18th Congress of the International Commission for Optics, SPIE, vol.3749, p.478 (1999)
[7] D. Leonald, M. Krishnamurthy, C.M. Reaves, S.P. Denbaas, and P.M. Petroff, Appl. Phys. Lett., vol.63, p.3203 (1993)
[8] I.I. Smolyaninov, D. Mazzoni, and C.C. Davis, Appl. Phys. Lett., vol.67, p.3859 (1995)
[9] E. Maayan, O. Kreinin, G. Bahir, J. Salzman, A. Eyal, and R. Beserman, J. Crystal Growth, vol.135, pp.23-30 (1994)
[10] D. Bauerle, Appl. Surface Sci., vol.106, pp.1-10 (1996)
[11] M. Ohtsu, K. Kobayashi, H. Ito, and G.H. Lee, Proc. IEEE, to be published in 2000
[12] V.V. Polonski, Y. Yamamoto, M. Kourogi, H. Fukuda, and M. Ohtsu, J. Microscopy, vol.194, pp.545-551 (1999)
[13] Y. Yamamoto, V.V. Polonski, G.H. Lee, M. Kourogi, and M. Ohtsu, SPIE 44th Annual Meeting, 3791-18, Denver, CO, July 18-23, 1999
[14] S. Mononobe, T. Saiki, T. Suzuki, S. Koshihara, and M. Ohtsu, Opt. Commun., vol.146, pp.45-48 (1998)
[15] G.T. Ruiter, Appl. Phys. Lett., vol.71, pp.28-30 (1997)
[16] D. Ehrlich, R.M. Osgood, Jr., and T.F. Deutch, J. Vac. Sci. Technol., vol.21, pp.23-32 (1982)
[17] V.V. Polonski, Y. Yamamoto, J.D. White, M. Kourogi, and M. Ohtsu, Jpn. J. Appl. Phys., vol.38, p.L826 (1999)
[18] T. Pangaribuan, K. Yamada, S. Jiang, H. Ohsawa, and M. Ohtsu, Jpn. J. Appl. Phys., vol.31, pp.L1302-L1304 (1992)
[19] R. Wiesendanger, Appl. Surf. Sci., vol.54, pp.271-277 (1992)
[20] G.H. Lee, Y. Yamamoto, M. Kourogi, and M. Ohtsu, SPIE 44th Annual Meeting, 3791-18, Denver, CO, July 18-23, 1999
[21] O. Madelung, *Landolt-Bernstein New Series*, vol.17b, Springer-Verlag, Berlin, 1982
[22] T.Y. Ma, G.C. Park, and K.W. Kim, Jpn. J. Appl. Phys., vol.35, pp.6208-6211 (1996)
[23] Z.T. Tang, G.K.L. Wong, and P. Yu, Appl. Phys. Lett., vol.72, pp.3270-3272 (1998)

[24] D.B. Bagnall, Y.F. Chen, Z. Zhu, and T. Yao, Appl. Phys. Lett., vol.70, pp.2230-2232 (1997)

[25] S. Schmitt-Rink, D.A.B. Miller, and D.S. Chemla, Phys. Rev.B, vol.35, p.8113 (1987)

[26] T. Matsumoto, M. Ohtsu, K. Matsuda, T. Saiki, H. Saito, and K. Nishi, Appl. Phys. Lett., 75, 3246 (1999)

[27] T. Saiki, S. Mononobe, M. Ohtsu, N. Saito and J. Kusano, Appl. Phys. Lett., vol.68, p.2612 (1996)

[28] H. Ito, K. Sakaki, M. Ohtsu, and W. Jhe, Appl. Phys. Lett., vol.70, p.2496 (1997)

[29] K. Kobayashi and M. Ohtsu, J. Microscopy, vol.194, p.249 (1999)

Figure Captions

Fig.8.1
Principle of NFO-CVD. (a) Prenucleation method. (b) Gas phase direct photodissociation me+hod.

Fig.8.2
Cross sectional profile(a) and SEM image(b) of the fiber probe for UV light.

Fig.8.3
Shear force image of a loop shaped Zn deposited on a glass substrate by prenucleation method.

Fig.8.4
Shear force image of deposited Zn dots(a) and a T-shaped pattern(b) deposited on a glass substrate by gas phase direct photodissociation method.

Fig.8.5
Variation of the height(closed circles) and diameter(open circles) of the deposited Zn dots.

Fig.8.6
Cross sectional profile(a) and SEM image(b) of the spliced fiber probe for UV light.

Fig.8.7
(a) Shear force image of Zn dots fabricated by using a spliced fiber probe with an aperture diameter of 60 nm.
(b) Cross sectional profiles of the dots along the dashed line in (a).

Fig.8.8
X-ray diffraction patterns of ZnO films deposited at the substrate

temperatures of 150℃(A), 200℃(B), and 300℃(C).

Fig.8.9
Optical transmission spectra of ZnO films deposited at the substrate temperature of 150℃(A), 200℃(B), and 300℃(C). They were measured at the room temperature.

Fig.8.10
Photoluminescence spectra of ZnO films deposited at the substrate temperature of 150℃(A), 200℃(B), and 300℃(C). They were measured at the room temperature.

Fig.8.11
Shear force image of a ZnO dot deposited on the (0001) α -Al_2O_3 substrate by NFO-CVD.

Fig.8.12
Concept of a planar nano-photonic integrated circuit.

Fig.8.13
Saturated absorption spectroscopy of a semiconductor quantum dot. (a) Schematic explanation of the principle. (b) An experimental result of optical switching properties of a single InGaAs quantum dot.

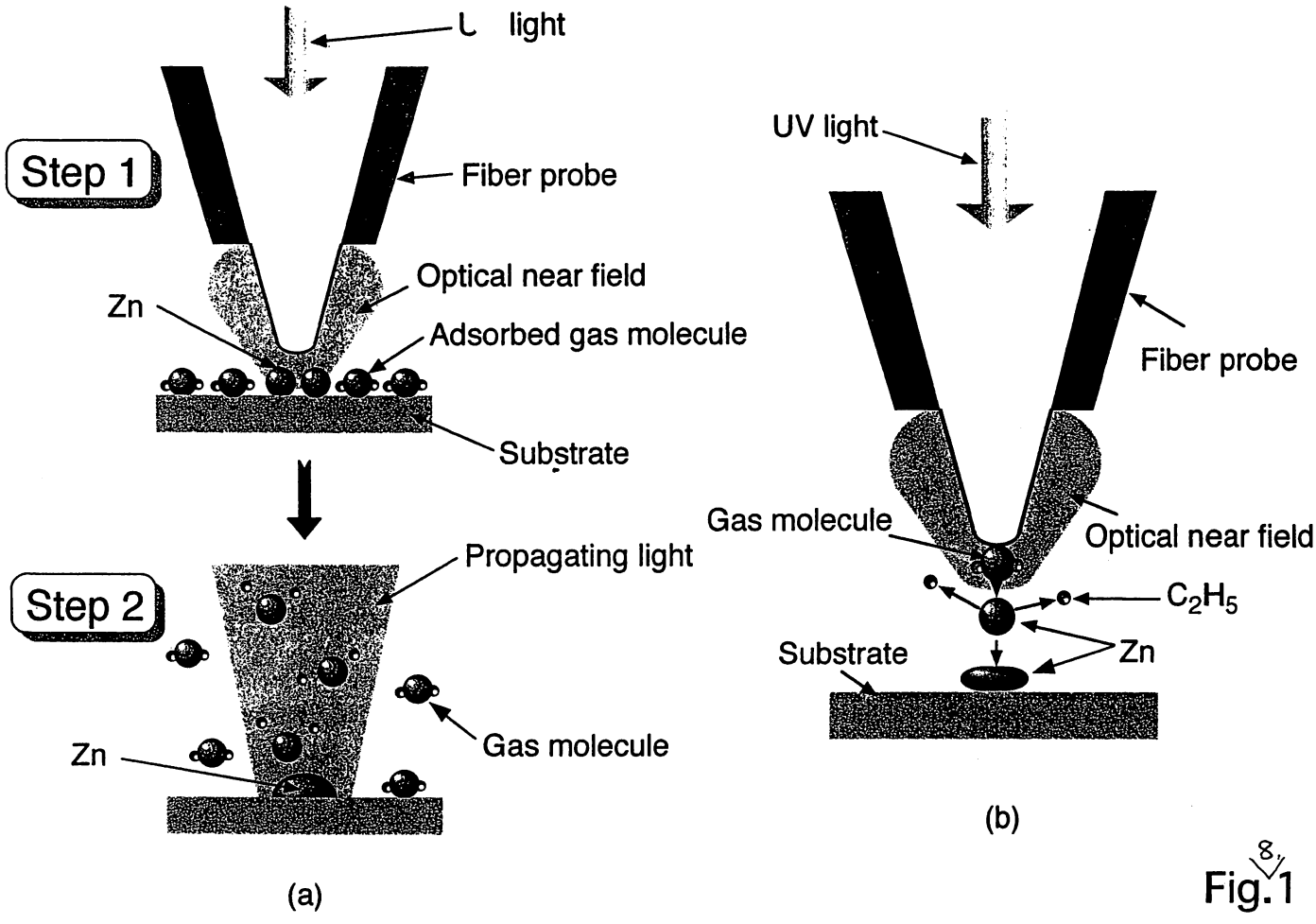
light
Step 1
Fiber probe
Optical near field
Zn
Adsorbed gas molecule
Substrate
Step 2
Propagating light
Zn
Gas molecule
(a)
UV light
Fiber probe
Gas molecule
Optical near field
C_2H_5
Substrate
Zn
(b)

Fig.1

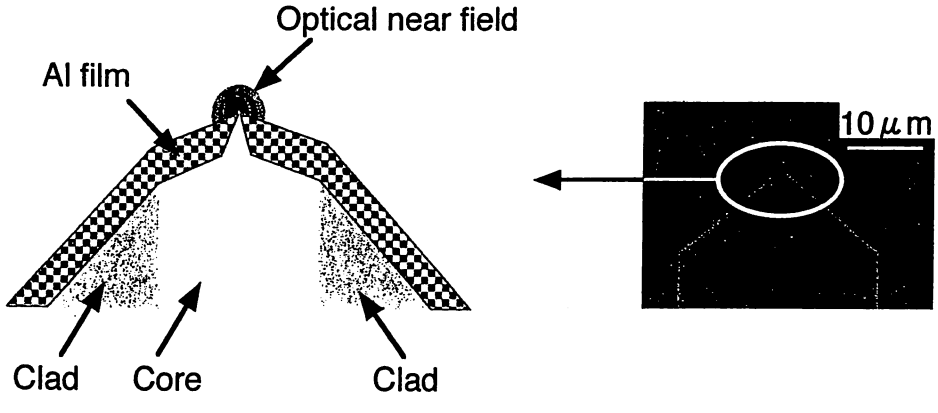
Optical near field
Al film
Clad
Core
Clad
(a)
10 μm
(b)

Fig.2

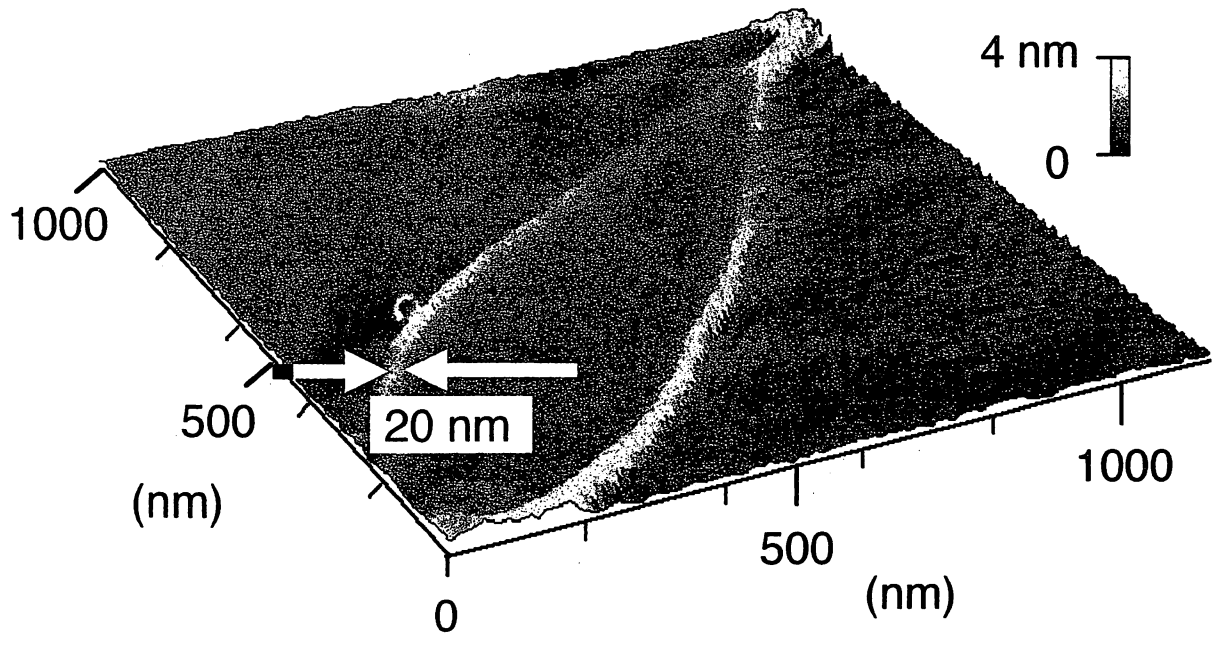

Fig.3

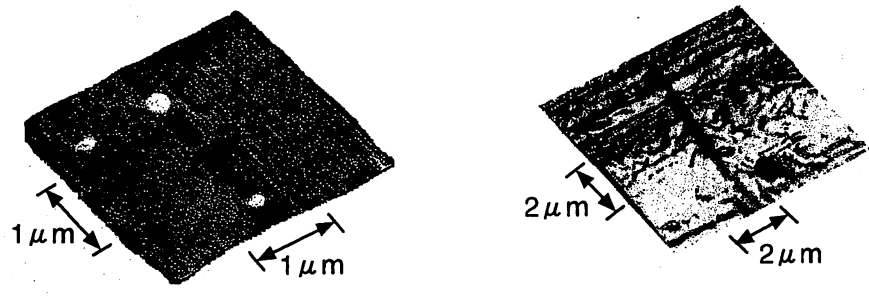

(a) (b)

Fig.4

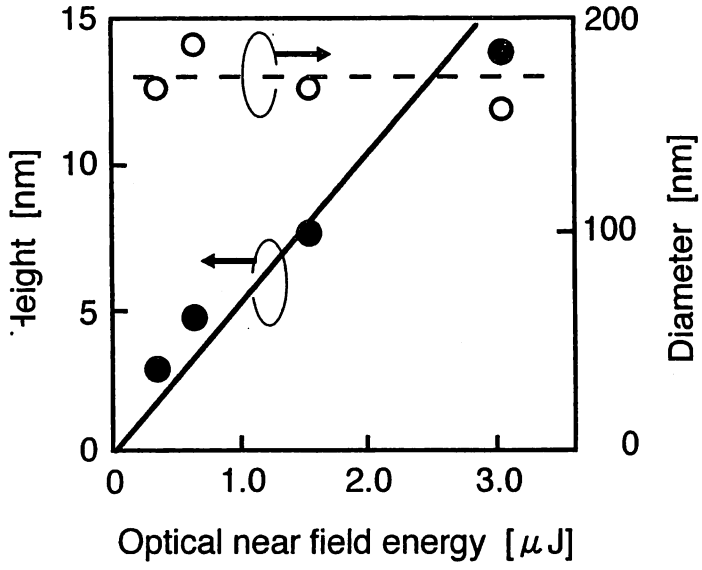
15
10
5
0
200
100
0
0
1.0
2.0
3.0
Diameter [nm]
Optical near field energy [μJ]

Fig.5

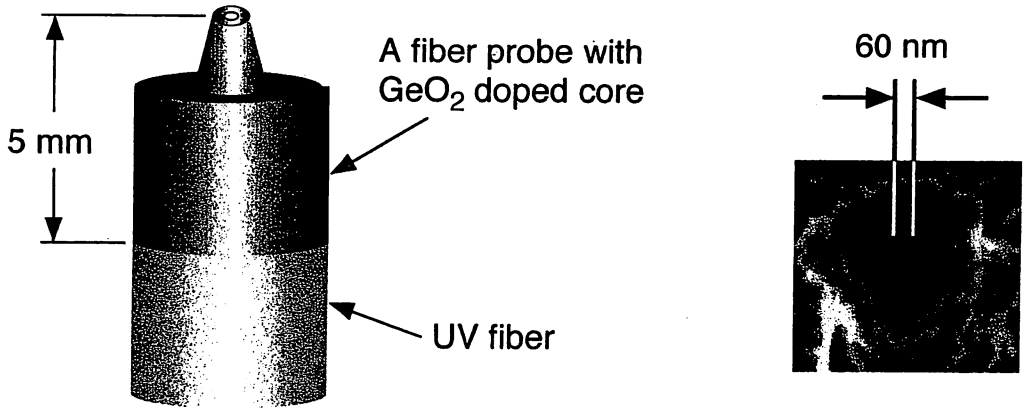
5 mm
A fiber probe with
GeO2 doped core
UV fiber
60 nm
(a)
(b)

Fig.6

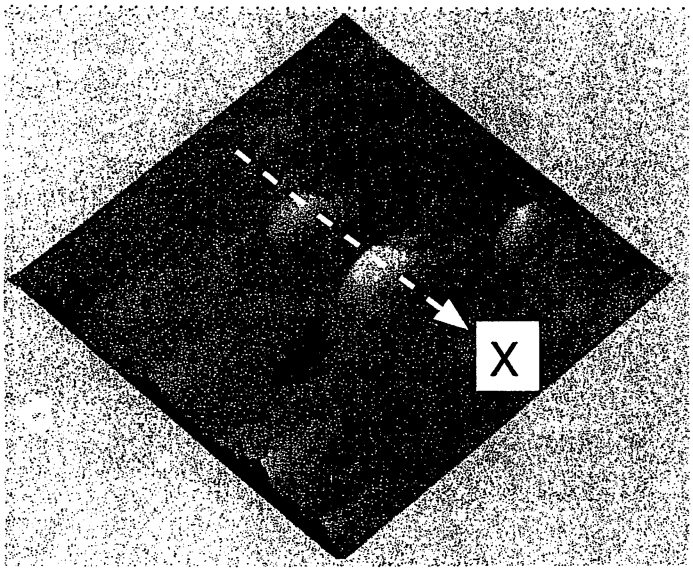
X

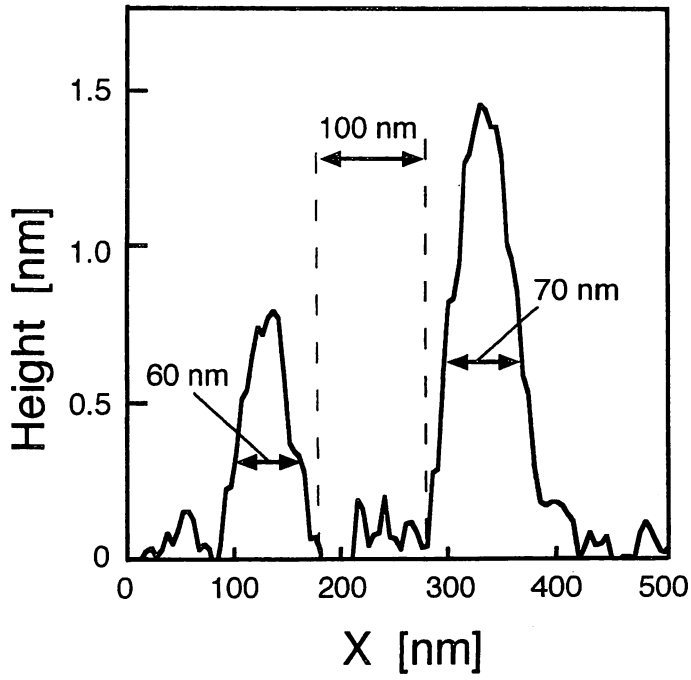
1.5
1.0
0.5
0
Height [nm]
100 nm
70 nm
60 nm
0
100
200
300
400
500
X [nm]

(a) (b)

Fig.7

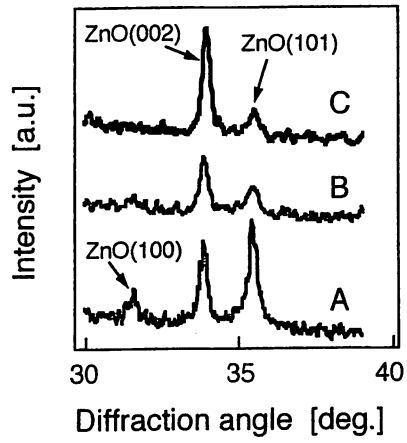
ZnO(002)
ZnO(101)
C
B
ZnO(100)
A
Intensity [a.u.]
30
35
40
Diffraction angle [deg.]

Fig.8

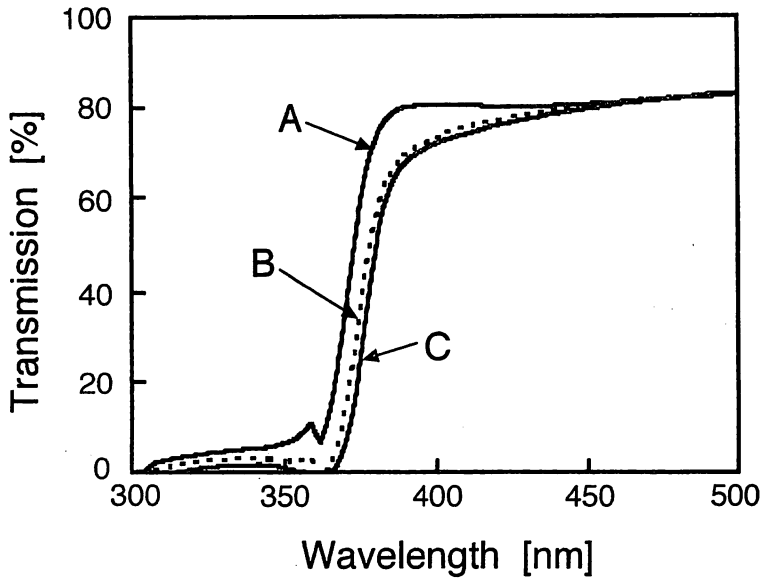
100
80
60
40
20
0
Transmission [%]
A
B
C
300
350
400
450
500
Wavelength [nm]

Fig.9

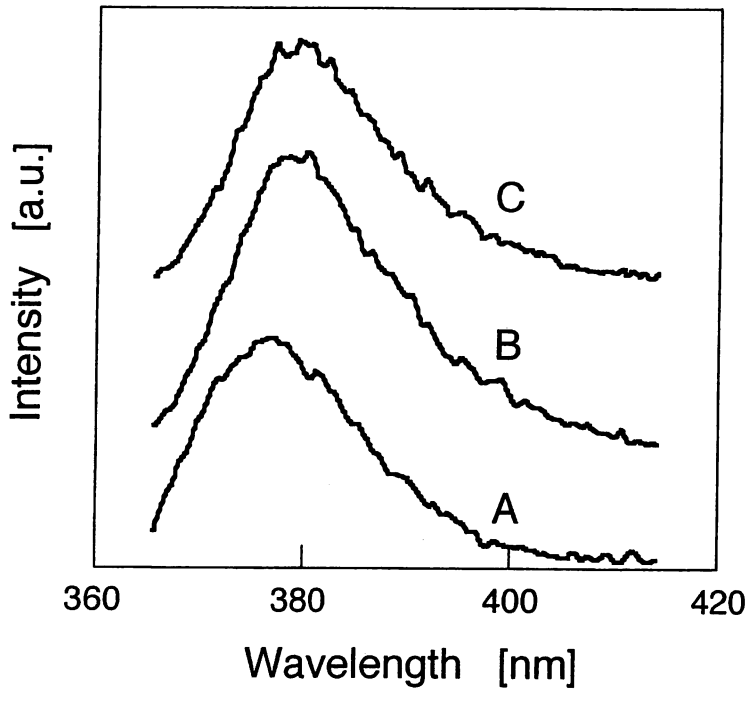
Intensity [a.u.]
C
B
A
360
380
400
420
Wavelength [nm]

Fig.10

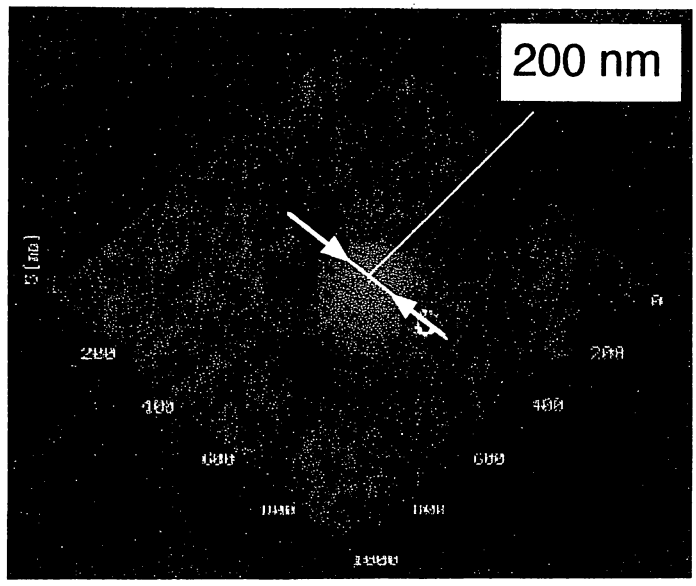
200 nm

Fig.11

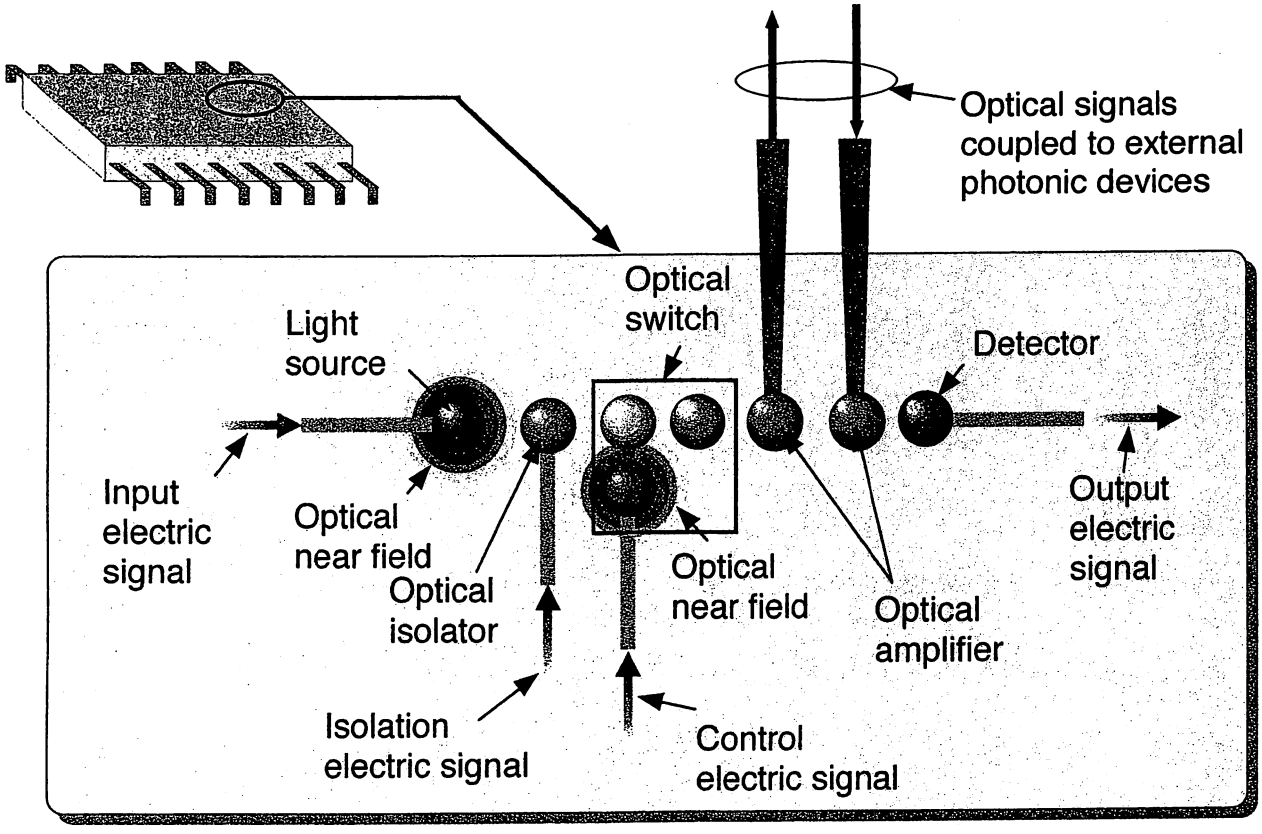
Optical signals coupled to external photonic devices
Optical switch
Light source
Detector
Input electric signal
Optical near field
Optical isolator
Optical near field
Optical amplifier
Output electric signal
Isolation electric signal
Control electric signal

Fig.12

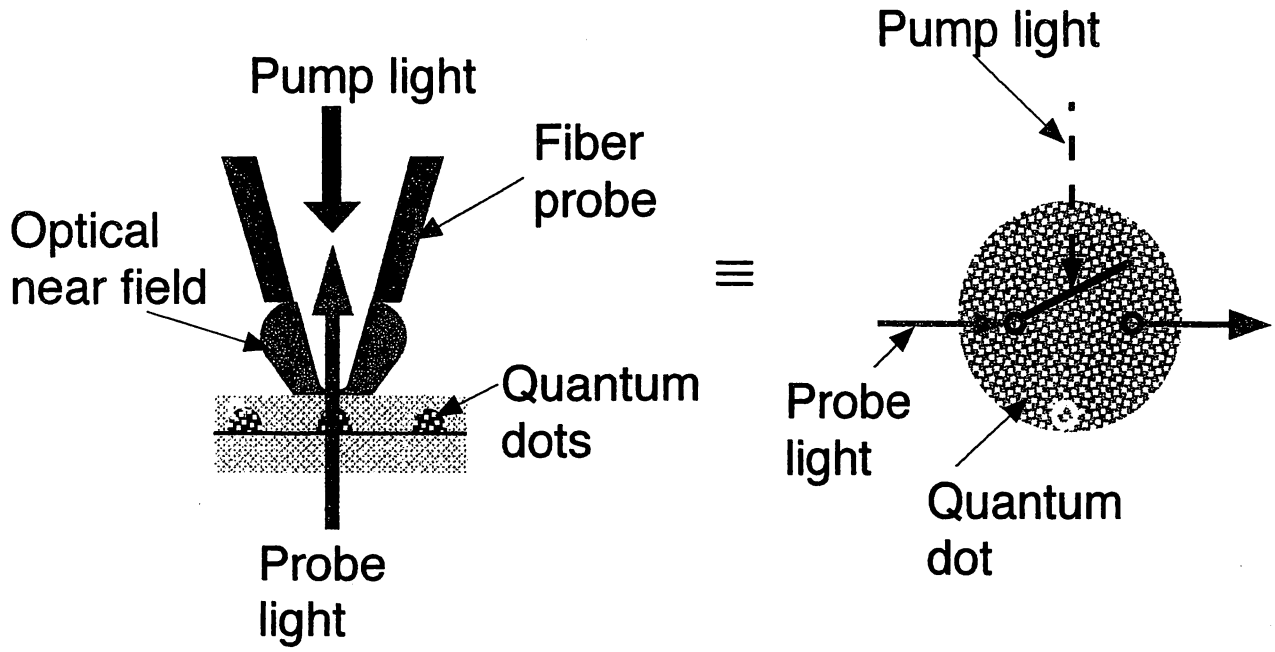
Pump light
Fiber probe
Optical near field
Quantum dots
Probe light
≡
Pump light
Probe light
Quantum dot

(a)

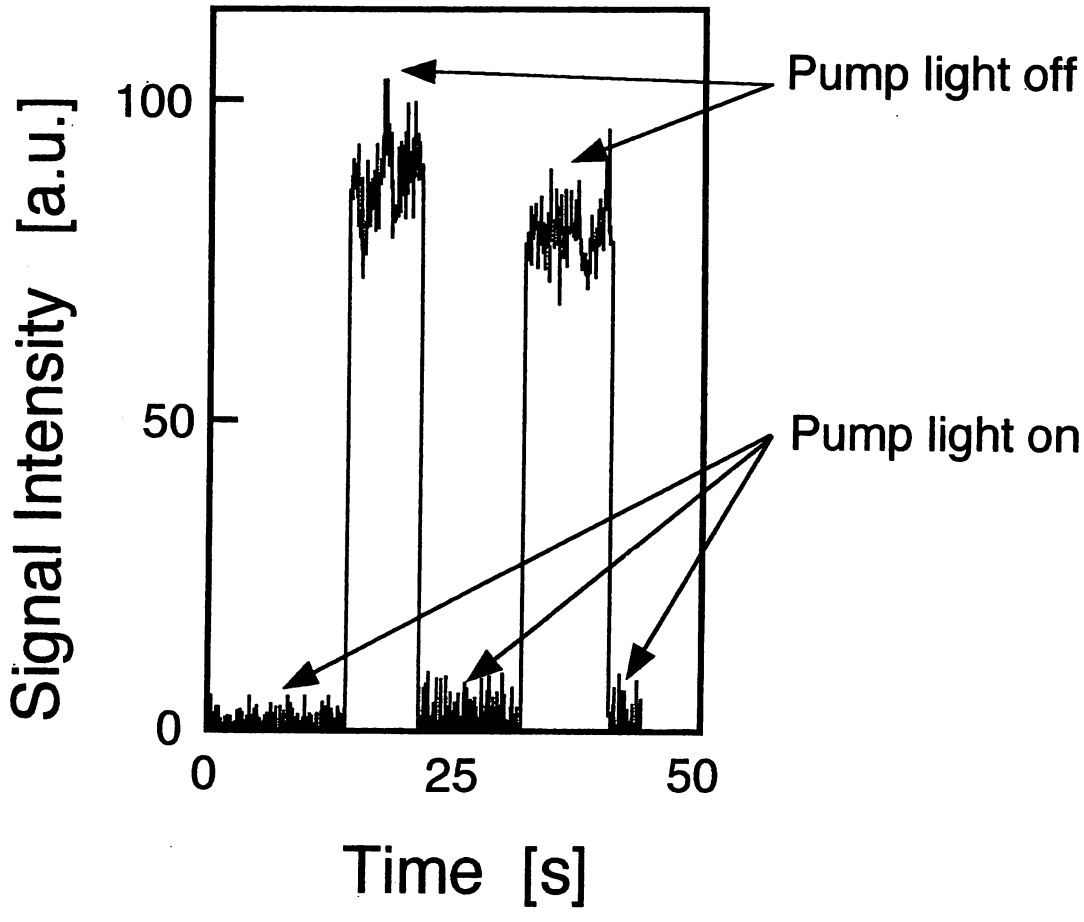
Signal Intensity [a.u.]
100
50
0
0
25
50
Time [s]
Pump light off
Pump light on

(b)

Fig.13

204

Applicability of Optical Near-Field for Depositing Nanoscale Patterns in Virtual Photon Environment

Vitali Polonski, Yoh Yamamoto, Geun-Hyong Lee and Motoichi Ohtsu

Japan Science and Technology Corporation (JST)
ERATO Localized Photon Project – Nanophotonics Group

Recently introduced concept of Optical Near-Field Photochemical Vapour Deposition (NFO-PCVD) has proven to be a viable tool for nanoscale studies and nanotechnology. The challenge of undertaked investigations – to verify whether PCVD processes, applicable for the conventional far-field light will work in "virtual photon" environment of induced optical near-field — has been positively answered experimentally. Versatility of conventional, typically using ultraviolet light, PCVD has turned it into semiconductor industry standard tool. According to International Technology Roadmap for Semiconductors 2000 edition, the year 2014 will see 35 nm minimum IC feature size. At the same time, economically viable implementation of a successful transition from submicro- to nano- and possibly molecular scale technology is still remains to be seen, especially given perfectionism standards required. First approach to cope with such an objective is creating nanoscale structures by removing the unwanted parts from the microscale structure. It essentially includes most of the nanofabrication methods being used currently, where selective etching plays a role of "removing". Second approach is a "bottom-up" synthesis of a nanoscale structure from its subunits (atoms and molecules), inherent to scanning probe techniques and chemosynthesis, including chemical self-assembly. Near-field incarnation of PCVD synthesize in itself these two principal approaches to nanofabrication, enabling etching-free maskless production of nanostructures with controllable size, chemical composition and morphology. This elegant solution, not requiring conductivity of the materials involved and allowing selective thin film growth depending on the wavelength used, offers integrity and a reproducibility not attainable by other developing methods of nanofabrication. Therefore, depositing variety of high-purity and crystallinity nanoscale structures, including metals, dielectrics and semicondustors, ultimately leading towards fabricating molecular scale devices, seems feasible. In addition to successfully deposited from different parent gases lines of Zn with observed few tens of nanometres, down to 15 nm, wide stripes and down to sub-nanometric scale height, recently we have achieved nanoscale ZnO dots, emitting blue and UV light. However, much work remains to be done to further elucidate the nature of associated with optical near-field phenomena, as well as to accumulate relevant expertise for further implementation of a suggested approach towards achieving drastic downscaling of pattern features and fabricating nanophotonic devices industry-wide.

Invited Paper

NEAR-FIELD NANO-OPTICS TOWARD NANO/ATOM DEPOSITION

M. OHTSU
Interdisciplinary Graduate School of Science and Engineering, Tokyo Institute of Technology
4259 Nagatsuta, Midori-ku, Yokohama 226-8502, Japan, e-mail: ohtsu@ae.titech.ac.jp

ABSTRACT: Chemical vapor deposition by UV-optical near field realized a 20 nm Zn stripes, two closely spaced Zn dots, and a ZnO dot with light emitting capability. Optical switching capability of a single InGaAs quantum dot was confirmed by near-field nonlinear absorption spectroscopy. Recent progress of atom manipulation for deposition is also reviewed.

I. INTRODUCTION

Sub-wavelength deposition of materials is required for photomask repair of DRAM, nano-photonic devices, and in-situ fabrication for the needs of microelectronics and for nanoscale electro-chemical studies. These trends signify the near field optical-chemical vapor deposition (NFO-CVD) as a means of overcoming diffraction limit and etch-damaging of the substrate[1]. Expected reproducibility of NFO-CVD for fabricating nanometric stripes and dots at desired positions is much higher than, e.g., the conventional self organized growth technique of semiconductor quantum dots. Moreover, by varying a photon energy and appropriate parent gases, selective growth can be accomplished. Among our several works near field optics in UV- visible-near IR region (,i.e., probe fabrication, imaging, single quantum dot spectroscopy, raman spectroscopy, optical storage/read-out[2,3], quantum optical theory[2-4], and atom manipulation[2,3,5]), this presentation reviews recent progress of nano-fabrication for future nano-photonics.

II. NANO-FABRICATION BY CHEMICAL VAPOR DEPOSITION

The core of the experimental setup is an illumination-mode near field optical microscope placed inside the reaction chamber. 244 nm-wavelength UV light was coupled into the fiber probe. A triple tapered fiber probe was developed by a 10 μ m pure silica core multimode UV fiber[6]. Transmission loss at 244 nm for this fiber was as low as 1.1 dB/m, by which the near field optical power density as high as 1 kW/cm^2 was realized. The same probe was used to obtain shear force image of the deposited Zn patterns. In order to avoid the decrease in the throughput of the probe by the deposited Zn, NFO-CVD is composed of the two steps. (1) Prenucleation: The reaction chamber was filled with Ar buffered dimethilzinc(DmZn) to produce a chemisorbed molecular layer with a thickness of few monolayers on the substrate(a Corning glass #7059). After the chamber was evacuated, patterning was performed by shining the area beneath the probe while keeping the probe in the near field region and scanning on the substrate. As a result, surface molecules of DmZn were decomposed selectively forming Zn nucleation centers. (5) Deposition: After reaction chamber was refilled with DmZn, the prenucleated area was irradiated from the far field using unfocused UV propagating light (193 nm-wavelength). Due to the presence of constant atom flux in the vicinity of the surface, the Zn around previously prenucleated centers was deposited and pattern was grown. **Figure1** shows the shear force image of deposited pattern with 20 nm Zn stripes. Quantitative verification estimated the average height of the deposited Zn to be about 50 atomic layers. Recent experiments employs the direct deposition of Zn by the UV optical near field because the decreases in the throughput of the probe by the deposited Zn was negligible. **Figure 2** shows the shear force image of the two closely spaced Zn dots of 60-70 nm diameters. Their heights were proportional to deposition time and optical power while their diameter depended only on the size of the probe. By introducing oxigen gas into the reaction chamber, ZnO dots were grown (**Fig.3**), which can be used as a blue-light emitter.

III. OPTICAL SWITCIHNG BY A SINGLE QUANTUM DOT

In order to confirm the optical switching capability of the nanometric materials, nonlinear absorption spectroscopy of a single quantum dot was carried out[7]. InGaAs quantum dots grown by conventional self-organized technique were used as the sample. For the measurement of the nonlinear transmission of single quantum dot, cw pump-probe technique was employed. Photo-excited carriers were generated in quantum dots by the pump beam (633 nm wavelength) passing through the fiber probe. The nonlinear change of the absorption coefficient due to the occupation of carriers in quantized states of single quantum dot was probed by the transmitted light (920 nm wavelength), which was collected through the same fiber probe. **Figure 4** shows the modulation characteristics of the signal intensity for the pump light on and off, by which the possibility of using the single quantum dot as a nanometric optical switch was confirmed.

IV. ATOM MANIPULATION

Atom guidance by optical hollow fiber and deposition experiment are in progress[8]. Their details will be also reviewed in the session.

Part of the 18th Congress of the International Commission for Optics: Optics for the Next Millennium
San Francisco, California • August 1999 SPIE Vol. 3749 • 0277-786X/99/$10.00

V. SUMMARY

Recent progress of our study has been reviewed. With regard to nano-fabrication, depositing several metals, oxides, and semiconductors on the common substrate can be expected by modifying the present technique. They can be used as light emitters, optical switches, etc. for novel integrated nano-photonic devices(**Fig.5**).

ACKNOWLEDGMENTS

Ohtsu would like to express his thanks to the members of Localized Photon Project of ERATO and Photon Control Project of KAST for their collaborations. Special thanks are to Dr. G.-H.Lee (ERATO) , V. Polonski and Y. Yamamoto(T.I.T.) for their works on nano-fabrication, and to T. Matsumoto(T.I.T.) and Dr.T.Saiki(KAST) for nonlinear absorption spectroscopy, and Prof. H. Ito(T.I.T.) for atom manipulation.

REFERENCES

[1] V. Polonski, et al., J. Microscopy, in press, 1999
[2] M. Ohtsu, *Near-Field Nano/Atom Optics and Technology*, Springer-Verlag, Berlin, 1998
[3] M. Ohtsu and H. Hori, *Near-Field Nano-Optics*, Plenum, New York, 1999
[4] K. Kobayashi and M. Ohtsu, J. Microscopy, in press 1999
[5] M. Ohtsu, Abstract, STM'97, Plenary 5, p.465, Hamburg, Germany 1997
[6] S. Mononobe, et al., Opt. Commun., vol.146 (1998) pp.45-48
[7] T. Matsumoto, et al., the 5th Int. Conf. on Near Field Opt., Shirahama, Japan, pp.38-39, Dec. 1998
[8] H. Ito, et al. Phys. Rev. Lett., vol.76 (1996) 4500

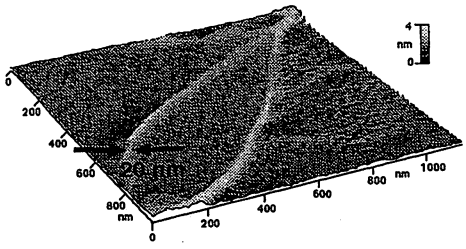

Fig.1 Deposited Zn looped-pattern.

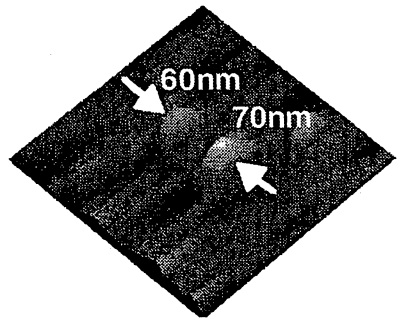

Fig.2 Two closely spaced Zn dots.

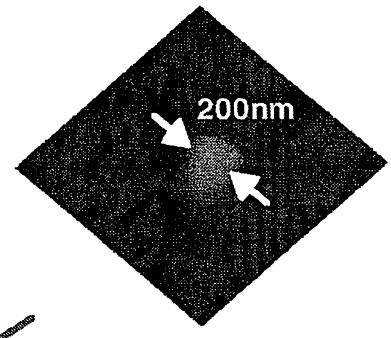

Fig.3 Deposited ZnO dot.

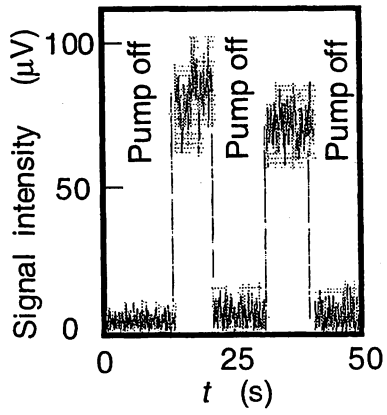

Fig.4 Optical switching properties of a single InGaAs quantum dot.

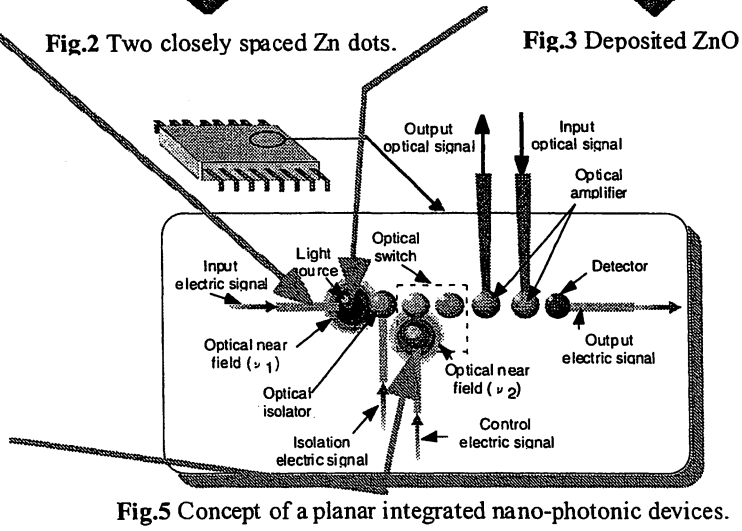

Fig.5 Concept of a planar integrated nano-photonic devices.

Invited Paper

Quantum theory and virtual photon model of near field optics

Kiyoshi Kobayashi[a] and Motoichi Ohtsu[a,b]

[a]ERATO Localized Photon Project, Japan Science and Technology Corporation,
687-1 Tsuruma Machida, Tokyo 194-0004 Japan
[b]Interdisciplinary Graduate School of Science and Engineering, Tokyo Institute of Technology,
4259 Nagatsuta-cho, Midori, Yokohama, Kanagawa, 226-8502 Japan

ABSTRACT

We point out that recent experimental results exemplify the need for quantum theoretical treatment of optical near-field problems, as well as the need for an intuitive model that provides clear insights into near-field optical systems. In this context, the virtual photon model as an intuitive model is discussed, and a quantum theoretical formulation of an optical near-field system is proposed on the basis of the projection-operator method. Special attention is paid to nanometric probe tip and quantum-mechanical sample systems such as atoms, molecules, and quantum dots. The effective probe tip-sample interaction is derived from the microscopic viewpoint; this interaction is essential for describing such phenomena as atom guidance and manipulation, or local excitation of a single quantum dot. The relationship to the virtual photon model is also discussed by focusing on the latter's empirical assumption of Yukawa-type interaction between the probe tip and sample. The key points are that a probe tip exists near the sample, and that the electron energies in the probe tip or sample are inversely proportional to the square of its size, owing to the confinement effect. Several applications and the future prospects of our theory are also briefly outlined.

Keywords: Quantum theory, projection operators, massive virtual photon, optical near field, Yukawa potential, nanometric sample, atom/molecule

1. INTRODUCTION

High-resolution imaging beyond the diffraction limit is now available for a variety of samples and materials by using optical near fields.[1] Local excitation with similar precision is also possible for a nanometric quantum dot,[2] or a single molecule.[3] From the spectroscopic observations thus obtained, we can learn about details of the internal structure of an object, such as its energy level structure, relaxation mechanism, and transition dynamics. Photochemical reaction as well as transition has been demonstrated on a sub-100-nm scale,[4] and has opened up a new way of developing nanometric photonics components, since optical near-field recording in both thermal[5,6] and photon modes[7] has been reported to be feasible on a sub-100-nm scale. As an ultimate component, an atom is also utilized in this context. For example, neutral atoms have been guided[8,9] through a micron-sized hollow fiber by using a blue-detuned optical near field. Moreover, atomic deposition with nanometric precision using very-low-energy atom deflection or manipulation has been proposed.[10]

These experimental advances imply that a quantum theoretical approach should be pursued even in near field optics. In addition, we should preserve the connection with an intuitive model such as the virtual photon model,[11,12] because such a connection plays a very important role as a bridge between conventional theories and recent and future experimental achievements. There are two alternative quantum theoretical approaches to near field optics. In one, called the semi-classical approach, electromagnetic fields are treated as classical, while matter fields are described by the Schrödinger equation with local[13–15] or non-local[16,17] susceptibility. In the other, called the full quantum approach, both fields are quantized. When we quantize the field, we usually employ a plane wave basis for infinite systems, but we have to consider how to include near fields.[18,19] From the elementary excitation point of view, exciton-polariton modes have been extensively studied both with[20–24] and without[25] matter absorption. In relation to cavity QED problems,[26,27] electromagnetic field has been quantized with spherical bases in atom-trapping by a microsphere.[28] Four-wave mixing experimental results have been analyzed from the exciton-polariton scattering picture, and the validity of boson expansion has been revisited.[29] In the near-field optical area, a

Further author information: (Send correspondence to K.K.)
K.K.: E-mail: kkoba@ohtsu.jst.go.jp
M.O.: E-mail: ohtsu@ae.titech.ac.jp

Part of the SPIE Conference on Near-Field Optics: Physics, Devices and Information Processing • Denver, Colorado • July 1999
SPIE Vol. 3791 • 0277-786X/99/$10.00

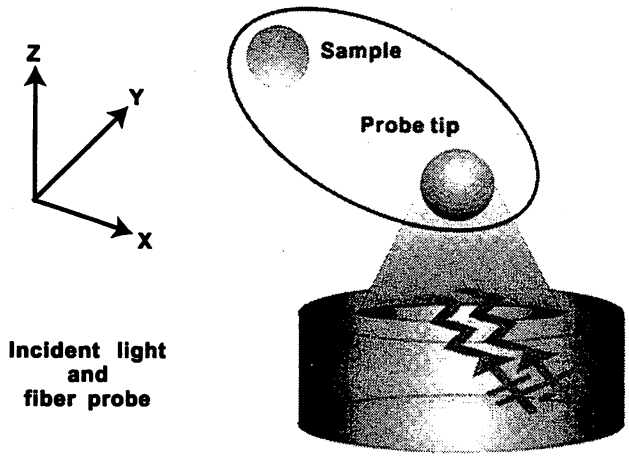

Figure 1. Schematically illustrated optical near-field system consisting of two subsystems: (1) an incident light and macroscopic matter system, and (2) a microscopic probe tip and sample system

quantum theoretical approach was proposed[30] on the basis of effective interaction by virtual mediation of exciton-polaritons. This approach provides a foundation for the massive virtual photon model — an intuitive model based on experimental results — that empirically assumes Yukawa-type interaction between a probe tip and a sample.

The paper is organized as follows. In the next section we propose a new theoretical formulation of optical near-field systems within the quantum theoretical framework. Taking note of the hierarchical structure of near field optics, namely, the existence of two subsystems, we apply the projection-operator method to it. The effective interaction between a nanometric probe tip and a sample system is then derived from the mediation of exciton-polaritons (massive virtual photons). It is shown to result in the Yukawa potential, which is an empirical assumption of the virtual photon model. In section 3, we discuss both conventional and quantum theoretical aspects of optical near-field problems, and finally we offer a summary in section 4.

2. THEORETICAL FORMULATION

Depending on our viewpoint as regards optical near-field systems, we may expect to reach a different formulation, as previously mentioned. It is appropriate to use classical electromagnetic theories for macroscopic descriptions of the behavior of light and matter such as a fiber probe. However, when the size of the probe tip or aperture is nanometric,[31] there is no guarantee that we can use the classical theories to correctly formulate optical near-field problems such as interactions between atom/nanometric samples and the probe. We therefore try to describe such problems within a quantum theoretical framework, paying special attention to the hierarchical structure of optical near-field systems.

2.1. HIERARCHICAL STRUCTURE IN NEAR FIELD OPTICS

The optical near-field system, as illustrated in Fig. 1, has characteristic structure in scale. There are two subsystems: in (1), incident propagating light consisting of real photons interacts with a macroscopic matter system (typically a prism in collection mode or a fiber probe in illumination mode). The other subsystem (2) consists of a nanometric probe tip and quantum-mechanical objects (atoms, molecules, and/or quantum dots). These two subsystems interact with each other, and their interactions should be treated consistently. This kind of problem can be formulated in a unified and systematic way by using the projection-operator method.

2.2. PROJECTION–OPERATOR METHOD

The projection-operator method is very appropriate for extracting an arbitrary number of degrees of freedom (P-space) from the many degrees of freedom of the system, and for renormalizing the effects of the other degrees of

freedom (Q-space). Even if we are, for example, not able to obtain all of the exact states for the total system, we can derive the exact effective interaction in terms of a few states for the subsystems. In the following discussion we can more generally obtain an effective operator $\hat{O}_{\rm eff}$ in the P-space, which is equivalent to an arbitrary operator $\hat{O}$ in the full space, corresponding to physical observables.

We follow the projection-operator method for steady states,[32,33] but readers interested in the relationship to the resolvent or time evolution of the operators may consult the publications listed in the references.[34–38] The starting point is that the eigenvalues and eigenstates of the total Hamiltonian $\hat{H}$ for the optical near-field system are written as E_λ and $|\Psi_\lambda\rangle$, respectively; that is,

$$\hat{H}\,|\Psi_\lambda\rangle = \left(\hat{H}_0 + \hat{V}\right)|\Psi_\lambda\rangle = E_\lambda\,|\Psi_\lambda\rangle\,, \tag{1}$$

where $\hat{H}_0$ consists of the Hamiltonians $\hat{H}_{\rm bath}$ for the subsystem (1) and $\hat{H}_{\rm A} + \hat{H}_{\rm B}$ for subsystem (2), while $\hat{V}$ denotes the interaction between the two subsystems. Defining the projection operators P and $Q = 1 - P$ in the usual manner as

$$\left|\Psi_\lambda^{(1)}\right\rangle = P\,|\Psi_\lambda\rangle\,, \qquad \left|\Psi_\lambda^{(2)}\right\rangle = Q\,|\Psi_\lambda\rangle\,, \tag{2}$$

$$P^2 = P\,, \qquad PQ = QP = 0\,, \tag{3}$$

$$\left[P, \hat{H}_0\right] = \left[Q, \hat{H}_0\right] = 0\,, \tag{4}$$

we divide the eigenstates $|\Psi_\lambda\rangle$ into two groups, $\left|\Psi_\lambda^{(1)}\right\rangle$ in P-space and $\left|\Psi_\lambda^{(2)}\right\rangle$ in Q-space. By using Eqs. (2)-(4), Eq. (1) is then rewritten as a set of equations:

$$\left(E_\lambda - \hat{H}_0\right) P\left|\Psi_\lambda^{(1)}\right\rangle = P\hat{V}P\left|\Psi_\lambda^{(1)}\right\rangle + P\hat{V}Q\left|\Psi_\lambda^{(2)}\right\rangle\,, \tag{5}$$

$$\left(E_\lambda - \hat{H}_0\right) Q\left|\Psi_\lambda^{(2)}\right\rangle = Q\hat{V}P\left|\Psi_\lambda^{(1)}\right\rangle + Q\hat{V}Q\left|\Psi_\lambda^{(2)}\right\rangle\,. \tag{6}$$

From the above equation Eq. (6), it is possible to formally express $Q\left|\Psi_\lambda^{(2)}\right\rangle$ by $P\left|\Psi_\lambda^{(1)}\right\rangle$ as

$$\begin{aligned} Q\left|\Psi_\lambda^{(2)}\right\rangle &= \left(E_\lambda - \hat{H}_0 - Q\hat{V}\right)^{-1} Q\hat{V}P\left|\Psi_\lambda^{(1)}\right\rangle\,, \\ &= J\left(E_\lambda - \hat{H}_0\right)^{-1} Q\hat{V}P\left|\Psi_\lambda^{(1)}\right\rangle\,, \end{aligned} \tag{7}$$

$$J = \left[1 - \left(E_\lambda - \hat{H}_0\right)^{-1} Q\hat{V}\right]^{-1}\,, \tag{8}$$

and the eigenstates $|\Psi_\lambda\rangle$ for the total Hamiltonian can then be expressed in terms of the eigenstates in P-space as

$$|\Psi_\lambda\rangle = (P+Q)\,|\Psi_\lambda\rangle = JP\left|\Psi_\lambda^{(1)}\right\rangle\,. \tag{9}$$

Since both of the states satisfy the normalization condition, we can rewrite this as

$$|\Psi_\lambda\rangle = JP\left(PJ^\dagger JP\right)^{-1/2}\left|\Psi_\lambda^{(1)}\right\rangle\,. \tag{10}$$

We thus obtain the effective operator $\hat{O}_{\rm eff}$ in the P-space as follows:

$$\langle\Psi_\mu|\,\hat{O}\,|\Psi_\lambda\rangle = \left\langle\Psi_\mu^{(1)}\right|\hat{O}_{\rm eff}\left|\Psi_\lambda^{(1)}\right\rangle\,, \tag{11}$$

$$\hat{O}_{\rm eff} = \left(PJ^\dagger JP\right)^{-1/2}\left(PJ^\dagger\hat{O}JP\right)\left(PJ^\dagger JP\right)^{-1/2}\,. \tag{12}$$

From the above Eqs. (11)-(12), it follows that relevant quantities such as the probe tip–sample interaction and transition dipole moments can be exactly expressed by using a small number of bases in P-space after renormalizing the effects from Q-space. This is one of the advantages of the method, and is desirable from the computational viewpoint.

2.3. ELEMENTARY EXCITATION: EXCITON–POLARITON

In the following subsections 2.3 and 2.4, components of the unperturbed Hamiltonian $\hat{H}_0$ for the two subsystems (1) and (2) will be discussed. There are basically no restrictions on the Hamiltonian, but for simplicity we assume that its eigenvalues and eigenstates are known.

Subsystem (1) can be viewed as a set of (i) excitons, (ii) real photons, and (iii) their interactions, if the induced electric polarization in three-dimensional infinite matter, or macroscopic matter is represented as excitons with energy $\hbar\Omega$. Such a system has characteristic elementary excitation modes, that is, exciton-polariton modes, and we can obtain the modes with energy $\hbar\Omega\left(\vec{k}\right)$ and momentum $\hbar\vec{k}$ as

$$\left[\hat{\xi}\left(\vec{k}\right), \hat{H}_{\text{bath}}\right] = \hbar\Omega\left(\vec{k}\right)\hat{\xi}\left(\vec{k}\right), \tag{13}$$

where the creation and annihilation operators of the exciton-polaritons ($\hat{\xi}^\dagger$, $\hat{\xi}$) are a linear combination of those of photons ($\hat{a}^\dagger$, $\hat{a}$) and excitons ($\hat{B}^\dagger$, $\hat{B}$), as follows:

$$\hat{\xi}\left(\vec{k}\right) = \sum_{\lambda=1}^{2}\left\{w_\lambda\left(\vec{k}\right)\hat{a}_\lambda\left(\vec{k}\right) + y_\lambda\left(\vec{k}\right)\hat{a}_\lambda^\dagger\left(-\vec{k}\right)\right\} + \sum_{\lambda'=1}^{3}\left\{x_{\lambda'}\left(\vec{k}\right)\hat{B}_{\lambda'}\left(\vec{k}\right) + z_{\lambda'}\left(\vec{k}\right)\hat{B}_{\lambda'}^\dagger\left(-\vec{k}\right)\right\}. \tag{14}$$

Here w, x, y, and z denote the mixing amplitude. This means that the states determined by the exciton-polariton modes are so-called "dressed" states of photons and excitons. The Hamiltonian $\hat{H}_{\text{bath}}$ is now given by

$$\begin{aligned}
\hat{H}_{\text{bath}} &= \sum_{\vec{k}}\sum_{\lambda=1}^{2}\hbar\omega\left(\vec{k}\right)\hat{a}_\lambda^\dagger\left(\vec{k}\right)\hat{a}_\lambda\left(\vec{k}\right) \\
&+ \sum_{\lambda'=1}^{3}\int d^3r\hbar\Omega\hat{B}_{\lambda'}^\dagger(\vec{r})\hat{B}_{\lambda'}(\vec{r}) - \int d^3r\hat{\vec{\mu}}(\vec{r})\cdot\hat{\vec{D}}(\vec{r}), \qquad (15) \\
&= \sum_{\vec{k}}\hbar\Omega\left(\vec{k}\right)\hat{\xi}^\dagger\left(\vec{k}\right)\hat{\xi}\left(\vec{k}\right), \qquad (16)
\end{aligned}$$

where the photon energy is denoted as $\hbar\omega\left(\vec{k}\right) = \hbar c\left|\vec{k}\right|$. The third term in Eq. (15) represents the interactions between photons and excitons in a multipolar QED Hamiltonian,[39] where $\hat{\vec{\mu}}(\vec{r})$ is the dipole operator of matter and $\hat{\vec{D}}(\vec{r})$ is the displacement field operator that is given by the conjugate momentum operator $\hat{\vec{\Pi}}(\vec{r})$ of the vector potential operator $\hat{\vec{A}}(\vec{r})$ expanded in terms of plane wave bases as

$$\begin{aligned}
\hat{\vec{D}}(\vec{r}) &= -4\pi c\hat{\vec{\Pi}}(\vec{r}), \qquad (17) \\
&= \sum_{\vec{k}}\sum_{\lambda=1}^{2} i\sqrt{\frac{4\pi\hbar\omega\left(\vec{k}\right)}{2V_0}}\vec{e}_\lambda\left(\vec{k}\right)\left\{\hat{a}_\lambda\left(\vec{k}\right)e^{i\vec{k}\cdot\vec{r}} - \hat{a}_\lambda^\dagger\left(\vec{k}\right)e^{-i\vec{k}\cdot\vec{r}}\right\}. \qquad (18)
\end{aligned}$$

Here the speed of light in vacuum, the normalization volume, and the unit vector for photon polarization are designated as c, V_0, and $\vec{e}_\lambda\left(\vec{k}\right)$, respectively. This Hamiltonian can be easily extended to include the absorption effects of matter. Moreover, it is possible to treat infinite matter with a two-dimensional boundary by using the step function $\theta(-z)$ as follows:

$$\begin{aligned}
\hat{H}_{\text{bath}} &= \sum_{\vec{k}}\sum_{\lambda=1}^{2}\hbar\omega\left(\vec{k}\right)\hat{a}_\lambda^\dagger\left(\vec{k}\right)\hat{a}_\lambda\left(\vec{k}\right) \\
&+ \sum_{\lambda'=1}^{3}\int d^3r\theta(-z)\hbar\Omega\hat{B}_{\lambda'}^\dagger(\vec{r})\hat{B}_{\lambda'}(\vec{r}) - \int d^3r\theta(-z)\hat{\vec{\mu}}(\vec{r})\cdot\hat{\vec{D}}(\vec{r}). \qquad (19)
\end{aligned}$$

Noting that the step function can be written as

$$\theta(-z) = \frac{1}{2}\int \delta(k_z)\, e^{ik_z z} dk_z + \frac{i}{2\pi}\int \frac{1}{k_z} e^{ik_z z} dk_z \ , \tag{20}$$

we find that the second term in Eq. (20) produces an infinite series of couplings with respect to k_z in the second and third terms of Eqs. (19). If the effect is negligible, as in the case where there is no absorption, however, we can rewrite Eq. (19) in a similar form to Eq. (15):

$$\begin{aligned} \hat{H}_{\text{bath}} &= \sum_{\vec{k}} \sum_{\lambda=1}^{2} \hbar\omega\left(\vec{k}\right) \hat{a}_{\lambda}^{\dagger}\left(\vec{k}\right) \hat{a}_{\lambda}\left(\vec{k}\right) \\ &+ \frac{1}{2}\sum_{\vec{k}} \sum_{\lambda'=1}^{3} \hbar\Omega \hat{B}_{\lambda'}^{\dagger}\left(\vec{k}\right) \hat{B}_{\lambda'}\left(\vec{k}\right) - \frac{1}{2}\sum_{\vec{k}} \hat{\vec{\mu}}\left(-\vec{k}\right) \cdot \hat{\vec{D}}\left(\vec{k}\right) \ . \end{aligned} \tag{21}$$

If the effect is not negligible, we have to choose some of the eigenstates of Eq. (21) as P-space, and to handle an effective Hamilitonian in order to renormalize the Q-space, as explained in the previous subsection. In all of the above cases, therefore, a near-field optical probe tip can be considered as interacting with nanometric samples or quantum-mechanical objects via exciton-polariton (massive virtual photon, or dressed photon) mediation.

2.4. NANOMETRIC PROBE TIP–SAMPLE SYSTEM

The Hamiltonian describing subsystem (2) depends, of course, on what kinds of material (atoms, molecules, nanometric samples, etc.) are taken into consideration. Instead of adopting specific Hamiltonians for $\hat{H}_{\alpha}$ (α=A, B), that is, specific atomic or molecular Hamiltonians, let us choose ones in which electrons with effective mass m_{e} and wave number k_{α} are confined in an infinite well potential of size $a(b)$. This can represent not only a characteristic situation in which the electrons are confined within a small area, but can also give a diagonalized form of the Hamiltonians, as follows:

$$\hat{H}_{\alpha} = \sum_{n} E_n(\alpha)\, \hat{c}_{n\alpha}^{\dagger} \hat{c}_{n\alpha} \ , \tag{22}$$

$$E_n(\alpha) = \frac{\hbar^2 k_{\alpha}^2}{2m_{\text{e}}} = \frac{\hbar^2}{2m_{\text{e}}}\left(\frac{n\pi}{a}\right)^2 \quad \text{or} \quad \frac{\hbar^2}{2m_{\text{e}}}\left(\frac{n\pi}{b}\right)^2 \ , \tag{23}$$

where the relevant energy levels are designated as $E_n(\alpha)$ for a positive integer n, the creation and annihilation operators are denoted as $\hat{c}_{n\alpha}^{\dagger}$ and $\hat{c}_{n\alpha}$, and electric dipole transitions between those levels are allowed.

2.5. EFFECTIVE INTERACTION BETWEEN PROBE TIP AND SAMPLE SYSTEM: YUKAWA POTENTIAL

The interaction $\hat{V}$ between the two subsystems described in the previous subsections 2.3 and 2.4 is written as

$$\hat{V} = -\sum_{\alpha=\text{A}}^{\text{B}} \theta(z_{\alpha})\, \hat{\vec{\mu}}_{\alpha} \cdot \hat{\vec{D}}(\vec{r}_{\alpha}) \ , \tag{24}$$

by assuming the dipole approximation of the multipolar QED Hamiltonian. Rewriting the photon operators as exciton-polariton operators, we can obtain the bare interaction in the exciton-polariton (elementary excitation mode) picture. Note that the word "bare" means that the interaction is not renormalized yet, or, that the effects of the Q-space are not consistently included yet.

$$\begin{aligned} \hat{V} &= -i\sqrt{\tfrac{2\pi\hbar}{V_0}} \sum_{\alpha=\text{A}}^{\text{B}} \theta(z_{\alpha}) \sum_{j=1}^{3} \left(\hat{b}_j^{\dagger}(\vec{r}_{\alpha}) + \hat{b}_j(\vec{r}_{\alpha})\right) \\ &\cdot \sum_{\vec{k}} \left[K'_{\alpha j}\left(\vec{k}\right) \hat{\xi}\left(\vec{k}\right) - K'^{*}_{\alpha j}\left(\vec{k}\right) \hat{\xi}^{\dagger}\left(\vec{k}\right)\right], \end{aligned} \tag{25}$$

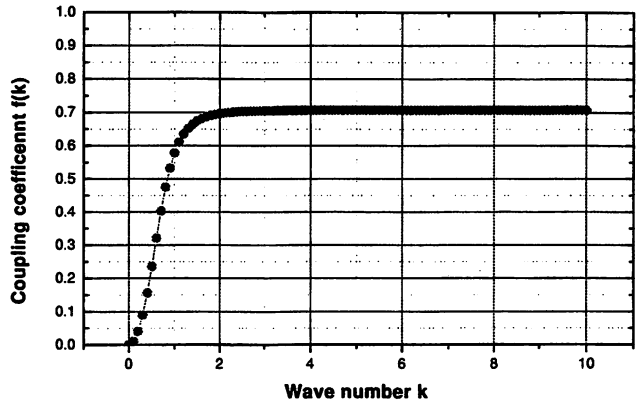

Figure 2. Dependence of the coupling coefficient $f(k)$ on the wave number k of incident light.

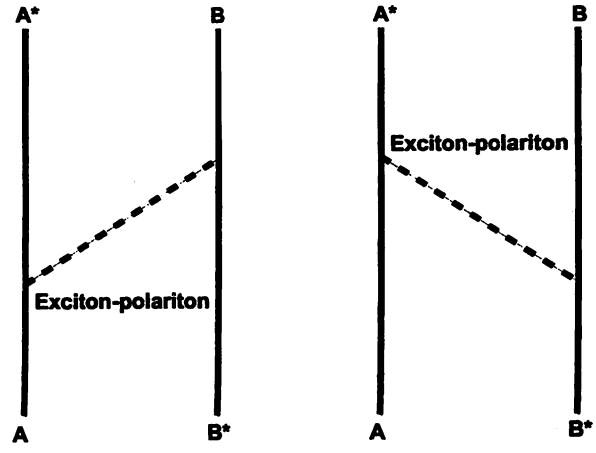

Figure 3. Elementary process in the second order: a virtual exciton-polariton, or a massive virtual photon, mediating between probe tip and sample.

$$K'_{\alpha j}\left(\vec{k}\right) = \sum_{\lambda=1}^{2} \mu_\alpha \left(\vec{e}_j \cdot \vec{e}_\lambda\left(\vec{k}\right)\right) f(k)\, e^{i\vec{k}\cdot\vec{r}_\alpha}, \tag{26}$$

$$f(k) = \frac{ck}{\sqrt{\Omega(k)}} \frac{\sqrt{\Omega^2(k) - \Omega^2/4}}{\sqrt{2\Omega^2(k) - \Omega^2/4 - c^2k^2}}, \tag{27}$$

where we used Eqs. (13) and (21) to calculate the eigenvalue $\Omega(k)$. The coupling coefficients between the probe (sample) and exciton-polaritons are denoted as $K'_{\alpha j}$ and $K'^{*}_{\alpha j}$, and $\hat{b}_j^\dagger$ and $\hat{b}_j$ are the creation and annihilation operators leading to electric dipole transitions of the sample–probe system, relating to Eq. (22). The unit vector $\vec{e}_j$ in Eq. (26) gives the direction of the dipole moment μ_α. It is worth reminding ourselves that there is no direct interaction between sample and probe tip in this Hamiltonian.

On the basis of the dispersion relation of an exciton-polariton (effective mass: m_{p}) obtained from Eq. (13), we make the usual effective mass approximation as

$$\Omega(k) = \frac{\Omega}{2} + \frac{\hbar k^2}{2m_{\mathrm{p}}}. \tag{28}$$

From Eqs. (26) and (27), the dependence of the coupling coefficient $f(k)$ on the wave number k of the incident light can be obtained as shown in Fig. 2. The horizontal and vertical axes in Fig. 2 are measured in units of $\sqrt{\frac{m_{\mathrm{p}}\Omega}{\hbar}}$ and $\sqrt{\frac{2m_{\mathrm{p}}c^2}{\hbar}}$, respectively. It thus follows that the coupling coefficients of the exciton-polariton modes to the nanometric subsystem (2) are constant when the wave number is larger than $k_c \sim 2\sqrt{\frac{m_{\mathrm{p}}\Omega}{\hbar}}$. Simple estimation gives $k_c^{-1} \sim 100$ nm by putting the excitation energy and effective mass as $\hbar\Omega \sim 1$ eV, $m_{\mathrm{p}}c^2 \sim 1$ eV.

Now let us discuss the effective interaction $\hat{V}_{\mathrm{eff}}$ according to the method described in subsection 2.2. As explained in that subsection, the relevant interaction can be exactly expressed by using the bare interaction $\hat{V}$ and a small number of bases in the P-space, after renormalizing the effects from the Q-space. We then choose a combination of the five states, $|\mathrm{A}\rangle$, $|\mathrm{A}^*\rangle$, $|\mathrm{B}\rangle$, $|\mathrm{B}^*\rangle$, and $|0\rangle$ as the P-space bases. Here the ground and excited states of $\hat{H}_\alpha (\alpha = \mathrm{A}$ or B) are designated as $|\mathrm{A}\rangle$, $|\mathrm{A}^*\rangle$, and $|\mathrm{B}\rangle$, $|\mathrm{B}^*\rangle$, while the ground state of $\hat{H}_{\mathrm{bath}}$ is expressed as $|0\rangle$. In order to evaluate the effective sample–probe interaction $V_{\mathrm{eff}}(\mathrm{AB})$ from Eqs. (11) and (12), we set $\left|\Psi_\lambda^{(1)}\right\rangle = |\mathrm{A}\rangle\,|\mathrm{B}^*\rangle\,|0\rangle$, $\left|\Psi_\mu^{(1)}\right\rangle = |\mathrm{A}^*\rangle\,|\mathrm{B}\rangle\,|0\rangle$, and have

$$\begin{aligned} V_{\mathrm{eff}}(\mathrm{AB}) &\equiv \left\langle \Psi_\mu^{(1)} \middle| \hat{V}_{\mathrm{eff}} \middle| \Psi_\lambda^{(1)} \right\rangle , \\ &= \left\langle \Psi_\mu^{(1)} \middle| \left(PJ^\dagger JP\right)^{-1/2} \left(PJ^\dagger \hat{V} JP\right) \left(PJ^\dagger JP\right)^{-1/2} \middle| \Psi_\lambda^{(1)} \right\rangle . \end{aligned} \tag{29}$$

The remaining task is to find an explicit form of the operator J that can be handled. Note that the state $P\left|\Psi_\lambda^{(1)}\right\rangle$ satisfies the following equation,

$$\left(E_\lambda - \hat{H}_0\right) P \left|\Psi_\lambda^{(1)}\right\rangle = P\hat{V}JP \left|\Psi_\lambda^{(1)}\right\rangle , \tag{30}$$

with the help of Eqs. (5) and (7). Using Eqs. (1), (9), and (30), we can then write down the equation to be solved as

$$\begin{aligned} \left[J, \hat{H}_0\right] P &= \left(E - \hat{H}_0\right) JP - J\left(E - \hat{H}_0\right) P , \\ &= \hat{V}JP - JP\hat{V}JP . \end{aligned} \tag{31}$$

If we expand J as $J = P + \sum_{n=1}^{\infty} g^{(n)} J^{(n)}$ and obtain perturbative solutions of it, we can determine $V_{\mathrm{eff}}(\mathrm{AB})$ perturbatively in the order of $\hat{V}$. Since there are no contributions in the lowest order of $\hat{V}$, because $P\hat{V}P = 0$, the

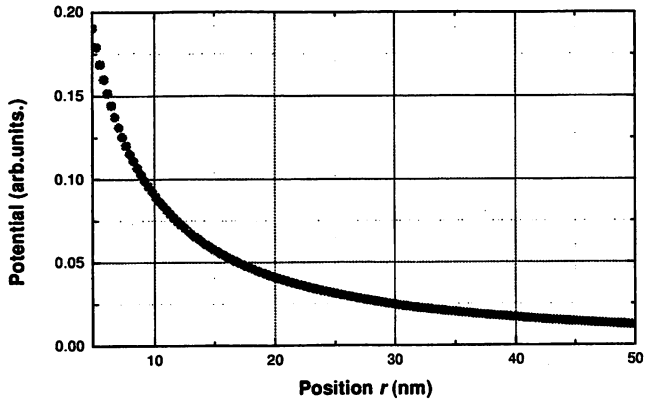

Figure 4. Yukawa potential: theoretical.

non-zero contributions to $V_{\text{eff}}(\text{AB})$ come from the second order of $\hat{V}$(see Fig. 3) as

$$V_{\text{eff}}(\text{AB}) = \langle \text{A}^* | \langle \text{B} | \langle 0 | \left[P\hat{V}Q \left(E_P^0 - E_Q^0\right)^{-1} \hat{V}P + P\hat{V} \left(E_P^0 - E_Q^0\right)^{-1} Q\hat{V}P \right] | \text{A} \rangle | \text{B}^* \rangle | 0 \rangle \ , \tag{32}$$

$$= \frac{4\pi}{(2\pi)^3} \int \mathrm{d}^3 k \left[\frac{K'_{\text{A}}\left(\vec{k}\right) K'^*_{\text{B}}\left(\vec{k}\right)}{\omega\left(\vec{k}\right) - \Omega_0(\text{B})} + \frac{K'_{\text{B}}\left(\vec{k}\right) K'^*_{\text{A}}\left(\vec{k}\right)}{\omega\left(\vec{k}\right) + \Omega_0(\text{A})} \right] . \tag{33}$$

Here the summation of $\vec{k}$ is replaced by integrating $\vec{k}$, and $\hat{H}_0$ in the denominators with respect to the corresponding eigenvalues. The excitation energies, $\hbar\Omega_0(\text{A})$ and $\hbar\Omega_0(\text{B})$, are

$$\hbar\Omega_0(\text{A}) = \frac{3\hbar^2}{2m_{\text{e}}} \left(\frac{\pi}{a}\right)^2 , \qquad \hbar\Omega_0(\text{B}) = \frac{3\hbar^2}{2m_{\text{e}}} \left(\frac{\pi}{b}\right)^2 , \tag{34}$$

from Eq. (23). We can similarly show how $\left\langle \Psi_\lambda^{(1)} \middle| \hat{V}_{\text{eff}} \middle| \Psi_\mu^{(1)} \right\rangle$ contributes to the effective sample–probe interaction $V_{\text{eff}}(\text{BA})$. Using the effective mass approximation of the exciton-polaritons given in Eq. (28) and the fact that $f(k) \sim$ constant, we obtain the explicit function form of

$$V_{\text{eff}}(\text{AB}) + V_{\text{eff}}(\text{BA}) \propto \frac{\exp\left[(i\gamma\pi r)/b\right]}{r} + \frac{\exp\left[-(\gamma\pi r)/a\right]}{r} + \frac{\exp\left[(i\gamma\pi r)/a\right]}{r} + \frac{\exp\left[-(\gamma\pi r)/b\right]}{r} , \qquad r = |\vec{r}_{\text{A}} - \vec{r}_{\text{B}}| , \tag{35}$$

where γ is the effective mass ratio for exciton-polaritons and electrons in the probe tip and sample system, and is defined as $\gamma = (3m_{\text{p}}/m_{\text{e}})^{1/2}$. This gives the effective sample–probe interaction derived from microscopic consideration, and the second and fourth terms are the Yukawa function (see Fig. 4), which was empirically assumed in the virtual photon model. We find that the Yukawa potential as the effective sample–probe interaction plays an important role in the near-field region, typically less than $k_{\text{c}}^{-1} \sim 100$ nm. The formula also shows that optical near field is effectively localized near the sample–probe system, and that the decay length is proportional to the inverse of the probe (sample) size and consistent with the experimental results.

3. APPLICATION OF THE THEORY

In the previous section, we formulated optical near-field problems, emphasizing the quantum theoretical viewpoint. It was shown that the Yukawa potential describes the effective interaction between the nanometric sample-probe

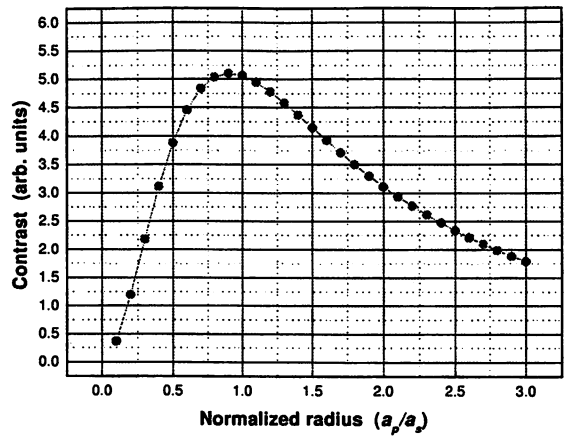

Figure 5. Size-resonant effect in the probe-sample system calculated by using the Yukawa potential.

system in the optical near-field region as a result of renormalizing or screening. This is the empirical assumption of the virtual photon model. We will take advantage of the characteristics of the model in order to develop applications of our theory for both the conventional and the quantum-mechanical aspects of optical near-field problems.

3.1. SIZE RESONANCE IN THE PROBE–SAMPLE SYSTEM

Let us investigate the contrast of signals picked up by a nanometric probe sphere (or aperture) interacting with a nanometric sample sphere (or aperture). We examine, in particular, how the contrast depends on the sizes ($a_{\rm p}$ for the probe and $a_{\rm s}$ for the sample). In the following we use the term "sphere," but the results are also applicable to the "aperture." Let the probe sphere scan above the sample sphere on a plane of constant height, where the height of d is the shortest distance between the top of the sample sphere and the bottom of the probe sphere. From Eq. (35), the Yukawa potential as the effective interaction is generated between the two arbitrary points ($\vec{r}_{\rm p}$, $\vec{r}_{\rm s}$) on the surfaces of the probe and sample spheres. Thus the pickup signal obtained from the whole of the probe sphere can be written as

$$I \propto \left| \int d\vec{r}_p \int d\vec{r}_s V_{\rm eff}\left(r_{ps}\right) \right|^2 , \qquad r_{ps} = |\vec{r}_{\rm p} - \vec{r}_{\rm s}| \, . \tag{36}$$

This might be regarded as showing that the Yukawa sources are distributed on both the spheres. Since we are interested in the effect of the existence of the probe sphere close to the sample sphere, we define the contrast as the signal I divided by the geometrical cross-section $\pi(a_{\rm s}^2 + a_{\rm p}^2)$, which corresponds to the case in which each sphere is individually located. Such a example is illustrated in Fig. 5, which shows that the contrast remains the highest when the probe size a_p is comparable or slightly less than the sample size a_s. This result is called the size-resonant effect, and has been obtained by numerical calculation based on classical electromagnetics,[40] but our approach is more convenient with respect to the computation time and applicability to an arbitrary shape.

3.2. ATOM DEFLECTION AS POTENTIAL SCATTERING

As an example of a quantum-mechanical system, we discuss the possibility of applying the formulation to atom deflection and manipulation with a sharpened fiber probe. These techniques are unique, and will be essential for carrying an atom to a desired point on a substrate with high spatial accuracy far beyond the diffraction limit.[41] Suppose that an incident atom with momentum $\hbar\vec{k}$ is deflected into momentum $\hbar\vec{k}'$ by an optical near field $V_{\rm eff}$. Then the differential cross-section or angular distribution of the deflected atom is given by

$$\frac{d\sigma}{d\Omega} = \left| \frac{M}{2\pi\hbar^2} \left\langle \vec{k}' \right| V_{\rm eff} \left| \vec{k} \right\rangle \right|^2 , \tag{37}$$

where M is the mass of the atom, and the Born approximation is assumed. This kind of evaluation and thorough investigation will be required in the design of atom guidance and manipulation systems using the optical near field, as well as in the discussion of basic experimental results. The above treatment is based on the Yukawa potential scattering of an atom, and it is an interesting issue to take into consideration the effect of effective dipole transition and energy-level shift caused by the optical near field. It is also important to apply the theory to local excitation of a molecule or an artificial atom/molecule (quantum dot). Those issues will be reported elsewhere in the near future.

4. SUMMARY

We have pointed out the need for quantum theoretical treatment and an intuitive model of optical near-field problems. Paying special attention to the hierarchical structure of optical near-field systems, we have developed a quantum theoretical formulation on the basis of the projection-operator method, and discussed the virtual photon model from the elementary excitation and effective interaction point of view. As an example of the application of the theory, we have numerically shown the so-called size-resonant effect, and outlined problems involving atom deflection and manipulation by using optical near fields.

ACKNOWLEDGMENTS

The authors gratefully acknowledge fruitful conversation with H. Hori, I. Banno of Yamanashi University, H. Ito, M. Kourogi of Tokyo Institute of Technology, and S. Sangu of Japan Science and Technology Corporation.

REFERENCES

1. *Near-Field Nano/Atom Optics and Technology*, M. Ohtsu, ed., Springer-Verlag, Berlin, 1998.
2. T. Saiki and K. Matsuda, "Near-field optical fiber probe optimized for illumination-collection hybrid mode operation," *Appl. Phys. Lett.* **74**, pp. 2773–2775, 1999.
3. J. Trautmann and W. P. Ambrose, "Near-field optical imaging and spectroscopy of single molecules," in *Single Molecule Optical Detection, Imaging and Spectroscopy*, T. Basché, W. E. Moerner, M. Orrit, and U. P. Wild, eds., pp. 191–222, VCH, Weinheim, 1997.
4. V. V. Polonski, Y. Yamamoto, M. Kourogi, H. Fukuda, and M. Ohtsu, "Nanometric patterning of zinc by optical near-field photochemical vapour deposition," *J. Microscopy* **194**, pp. 545–551, 1999.
5. E. Betzig, J. K. Trautman, R. Wolfe, E. M. Gyorgy, and P. L. Finn, "Near-field magneto-optics and high density data storage," *Appl. Phys. Lett.* **61**, pp. 142–144, 1992.
6. S. Hosaka, T. Shintani, M. Miyamoto, A. Kikukawa, A. Hirotsune, M. Terao, M. Yoshida, K. Fujita, and S. Kämmer, "Phase change recording using a scanning near-field optical microscope," *J. Appl. Phys.* **79**, pp. 8082–8086, 1996.
7. S. Jiang, J. Ichihashi, H. Monobe, M. Fujihira, and M. Ohtsu, "Highly localized photochemical process in LB films of photochromic material by using a photon scanning tunneling microscope," *Opt. Commun.* **106**, pp. 173–177, 1994.
8. H. Ito, T. Nakata, K. Sakaki, M. Ohtsu, K. I. Lee, and W. Jhe, "Laser spectroscopy of atoms guided by evanescent waves in micron-sized hollow optical fibers," *Phys. Rev. Lett.* **76**, pp. 4500–4503, 1996.
9. M. J. Renn, E. A. Donley, E. A. Cornell, C. E. Wieman, and D. Z. Anderson, "Evanescent-wave guiding of atoms in hollow optical fibers," *Phys. Rev. A* **53**, pp. R648–R651, 1996.
10. H. Ito, K. Sakaki, M. Ohtsu, and W. Jhe, "Evanescent-light guiding of atoms through hollow optical fiber for optically controlled atomic deposition," *Appl. Phys. Lett.* **70**, pp. 2496–2498, 1997.
11. H. Hori, "Quantum optical picture of photon STM and proposal of single atom manipulation," in *Near Field Optics*, D. W. Pohl and D. Courjon, eds., pp. 105–114, Kluwer, Dordrecht, 1993.
12. M. Ohtsu and H. Hori, *Near-Field Nano-Optics*, Kluwer, Dordrecht, 1999.
13. C. Girard, O. J. F. Martin, and A. Dereux, "Molecular lifetime changes induced by nanometer scale optical fields," *Phys. Rev. Lett.* **75**, pp. 3098–3101, 1995.
14. O. Keller, "Towards a microscopic theory of spatial confinement of light," *Ultramicroscopy* **71**, pp. 1–9, 1998.
15. K. Kobayashi, "Spin polarization in near-field optical microscopy," *Appl. Phys. A* **66**, pp. S391–S395, 1998.
16. K. Cho, "Nonlocal theory of radiation-matter interaction: Boundary-condition-less treatment of Maxwell equations," *Prog. Theor. Phys. Suppl.* **106**, pp. 225–233, 1991.

17. K. Cho, Y. Ohfuti, and K. Arima, "Theory of resonant SNOM (scanning near field optical microscopy): breakdown of the electric dipole selection rule in the reflection mode," *Surf. Sci.* **363**, pp. 378–384, 1996.
18. C. K. Carniglia and L. Mandel, "Quantization of evanescent electromagnetic waves," *Phys. Rev. D* **3**, pp. 280–296, 1971.
19. J. M. Vigoureux, L. D'Hooge, and D. V. Labeke, "Quantization of evanescent electromagnetic waves: Momentum of the electromagnetic field very close to a dielectric medium," *Phys. Rev. A* **21**, pp. 347–355, 1980.
20. M. Orrit, C. Aslangul, and P. Kottis, "Quantum-mechanical-model calculations of radiative properties of a molecular crystal. I. polaritons and abnormal decays of excitons in one- and two-dimensional systems," *Phys. Rev. B* **25**, pp. 7263–7280, 1982.
21. J. Knoester and S. Mukamel, "Intermolecular forces, spontaneous emission, and superradiance in a dielectric medium: Polariton-mediated interactions," *Phys. Rev. A* **40**, pp. 7065–7080, 1989.
22. B. Huttner and S. M. Barnett, "Quantization of the electromagnetic field in dielectrics," *Phys. Rev. A* **46**, pp. 4306–4322, 1992.
23. G. Juzeliūnas and D. L. Andrews, "Quantum electrodynamics of resonant energy transfer in condensed matter," *Phys. Rev. B* **49**, pp. 8751–8763, 1994.
24. M. S. Yeung and T. K. Gustafson, "Spontaneous emission near an absorbing dielectric surface," *Phys. Rev. A* **54**, pp. 5227–5242, 1996.
25. J. J. Hopfield, "Theory of the contribution of excitons to the complex dielectric constant of crystals," *Phys. Rev.* **112**, pp. 1555–1567, 1958.
26. *Cavity Quantum Electrodynamics*, P. R. Berman, ed., Academic Press, San Diego, 1994.
27. H. Cao, S. Pau, Y. Yamamoto, and G. Bjork, "Exciton-polariton ladder in a semiconductor microcavity," *Phys. Rev. B* **54**, pp. 8083–8086, 1996.
28. D. W. Vernooy and H. J. Kimble, "Quantum structure and dynamics for atom galleries," *Phys. Rev. A* **55**, pp. 1239–1261, 1997.
29. M. Kuwata-Gonokami, S. Inouye, H. Suzuura, M. Shirane, and R. Shimano, "Parametric scattering of cavity polaritons," *Phys. Rev. Lett.* **79**, pp. 1341–1344, 1997.
30. K. Kobayashi and M. Ohtsu, "Quantum theoretical approach to near-field optical system," *J. Microscopy* **194**, pp. 249–254, 1999.
31. M. Ohtsu, "Progress of high-resolution photon scanning tunneling microscope due to a nanometric fiber probe," *J. Lightwave Technol.* **13**, pp. 1200–1221, 1995.
32. H. Hyuga and H. Ohtsubo, "Breakdown of the siegert theorem and the many-body charge density operators," *Nucl. Phys. A* **294**, pp. 348–356, 1978.
33. K. Kobayashi and T. Kohmura, "Momentum-transfer dependence of nuclear spin-isospin transitions," *Prog. Theor. Phys.* **71**, pp. 327–338, 1984.
34. R. Zwanzig, "On the identity of three generalized master equations," *Physica* **30**, pp. 1109–1123, 1964.
35. H. Mori, "Transport, collective motion, and Brownian motion," *Prog. Theor. Phys.* **33**, pp. 423–455, 1965.
36. C. R. Willis and R. H. Picard, "Time-dependent projection-operator approach to master equations for coupled systems," *Phys. Rev. A* **9**, pp. 1343–1358, 1974.
37. P. Fulde, *Electron Correlations in Molecules and Solids, 3rd edn.*, Springer-Verlag, Berlin, 1995.
38. C. Cohen-Tannoudji, J. Dupont-Roc, and G. Grynberg, *Atom-Photon Interactions*, John Wiley, New York, 1998.
39. D. P. Craig and T. Thirunamachandran, *Molecular Quantum Electrodynamics*, Academic Press, London, 1984.
40. K. Jang and W. Jhe, "Nonglobal model for a near-field scanning optical microscope using diffraction of the optical near field," *Opt. Lett.* **21**, pp. 236–238, 1996.
41. H. Ito, K. Otake, and M. Ohtsu, "Near-field optical guidance and manipulation of atoms," *Proc. SPIE* **3467**, pp. 250–257, 1998.

Phase-change recording/readout with a high throughput fiber probe

Motonobu Kourogi *[a,b] ,Takashi Yatsui [a], and Motoichi Ohtsu [a,b]

[a] Interdisciplinary Graduate School of Science and Engineering, Tokyo Institute of Technology,
4259 Nagatsuta, Midori-ku, Yokohama 226-8502, Japan

[b] Kanagawa Academy of Science and Technology,
3-2-1, Takatsu-ku, Kawasaki 213-0012, Japan.

ABSTRACT

We applied a super- wavelength apertured fiber probe to phase-change recording/readout. Though the fiber probe had a super-wavelength aperture, the spot size at the aperture was as small as150nm ($< \lambda /5$). An as-deposited SiO_2/$AgInTe_2$/glass substrate was used as a recording medium. For recording, a laser diode with a pulsewidth of 2μs (λ =850nm) was used. By scanning the probe for reading, we obtained resolved images of the recorded dot with a width of 250 nm.

Keywords: optical near-field storage, phase-change recording, fiber probe

1. INTRODUCTION

In order to improve the data storage density, we must overcome the diffraction limit of light that governs the size of the focused beam spots. For realization of the higher density, near-field optics attract great attention. Preliminary experiments of the near-field optical recording have been carried out with various media such as magneto-optic materials[1,2] photochromic materials[3] and phase-change (PC) materials[4] using a metallic sharpened optical fiber probe with sub-wavelength apertures. A solid immersion lens[2] has been also used.

However, conventional scanning of a sub-wavelength aperture probe has been slow in its speed, which is due to low throughput of the probe. It is less than $1x10^{-5}$ with D<100nm, in conventional single-tapered probe where D is the aperture diameter. Therefore, signal-to-noise ratio is extremely low. Although recent development of fabrication methods of high throughput probes [5-7] shows the possibility of increase of the throughput, the realized throughput is still as low as 10^{-2}.

* Correspondance: Email: kourogi@ae.titech.ac.jp;Telephon:+81-45-924-5455;Fax:+81-45-924-5599

Part of the SPIE Conference on Near-Field Optics: Physics, Devices and Information Processing • Denver, Colorado • July 1999
SPIE Vol. 3791 • 0277-786X/99/$10.00

On the other hand, there were several reports of observing the images in the resolution of 150nm～ 200nm by using a fiber probe with super-wavelength aperture [8,9], where the wavelengths of the light sources were 0.8～1μm. This resolution is smaller than that obtained with a solid immersion lens. In Ref.7, it was pointed out that an optical intensity distribution has a very sharp and high intensity central peak even though the aperture diameter is larger than the wavelength, and it was also shown that the throughput of such a super-wavelength apertured probe is as high as 10%. These results means that the probe has high throughput and high resolution simultaneously. High density and high speed near-field recording can be expected by using this probe.

In this paper, we demonstrate the fabrication and characterization of such the probe. Further, optical near-field recording/ read-out is demonstrated using this probe.

2. CHARACTERISTICS OF THE PROBE

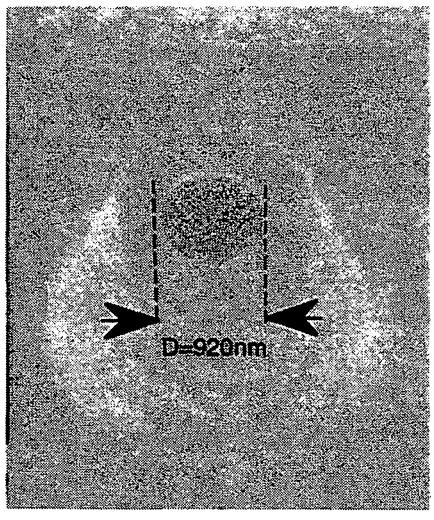

Figure.1: Scanning electron microscopic images of the apertured fiber probe.

A fiber probe was fabricated by three steps. (i)The GeO_2 doped core of the fiber was tapered by selective HF chemical etching to obtain the cone angle of 25 degree. (ii)The probe was coated with 500nm thick gold film. (iii) The aperture was fabricated at the end of the probe with a focused ion beam after metal coating, where the aperture diameter was coincident with the diameter where the TE_{12} propagation mode of the light inside the metalized probe is closed to be cut-off. Since we used 850nm wavelength laser for the experiment, the aperture diameter was made to be 920nm. Figures 1 shows the typical scanning electron microscopic images of the fabricated apertured probe.

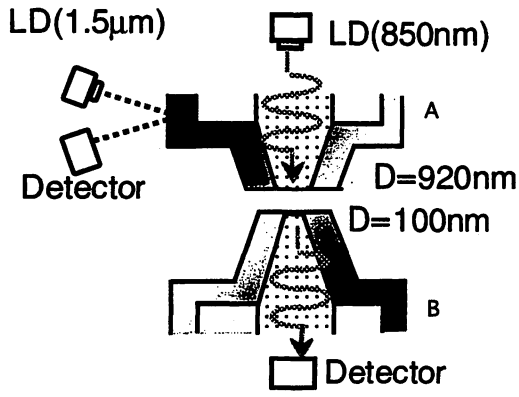

Figure 2: Apparatus for the measurement of the spatial distribution of the optical near-field intensity on the apertured probe.

We measured the spatial distribution of the optical near-field intensity on the apertured probe. Figure 2 shows an apparatus for the measurement. Linearly polarized light from a laser diode was coupled into the single-mode fiber with an apertured probe(probe A) on its end. The optical near-field generated on the apertured probe was observed by scanning with another probe (probe B) and detecting the scattered light with a photo-multiplier, while the separation between the two probes was maintained within several manometers with shear- force technique. We used an apertured probe with D=100 nm as the probe B.

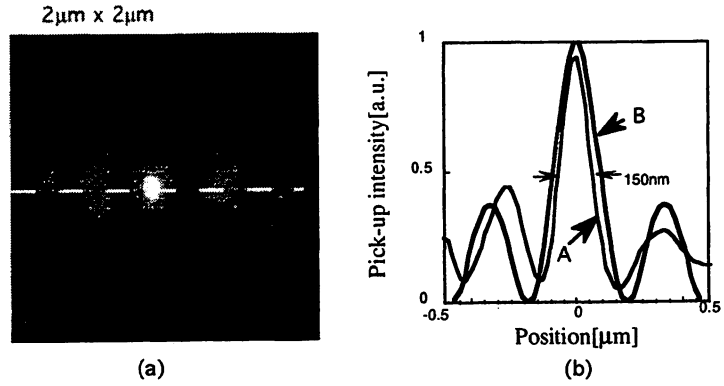

Figure 3:Spatial distribution of the optical near-field intensity on the aperture. (a):Two dimensional image. (b):Cross-sectional image. Curve A and B show the cross-sectional distribution along the white broken line in (a) and the calculated distribution, respectively.

Figure 3(a) shows the observed spatial distribution of the optical near-field intensity on the aperture. In Fig.3(b), curve A shows the cross-sectional distribution along the white broken line in Fig.3(a). One can find in this figure that there is a "focal point". Note that full width at half maximum (FWHM) of the central part of the curve was as small as 150nm, which is smaller than $\lambda/5$.

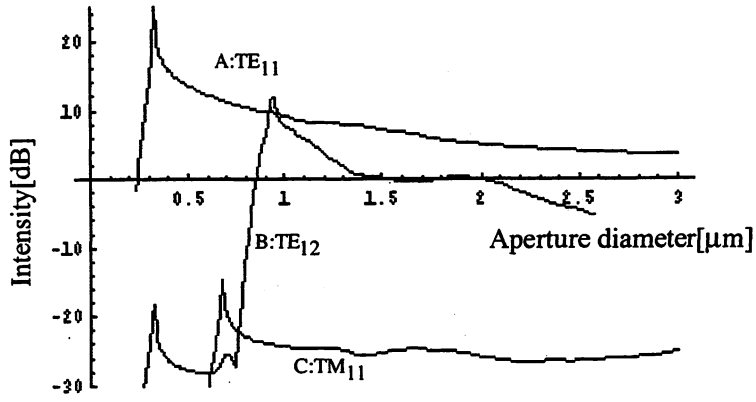

Figure 4:Calculated result of relative electric-field intensity of each propagation modes obtained by the analysis of tapered probe. Curves A, B and C shows TE_{11}, TE_{12}, and TM_{11} modes respectively.

Here we explain the reason why such a small spot was obtained. We assumed here that cladding is an ideal metal. Taking into consideration that only the symmetrical modes can exist inside this probe because the propagation mode in the single mode optical fiber is symmetrical, it is understood that modes which can exist the inside the probe at the aperture are TE_{11}, TE_{12} and TM_{11} modes. Figure 4 shows the calculated result of relative electric-field intensity of each propagation mode obtained by the analysis of tapered probe, where staircase concatenation method is used for the calculation. From this calculation it is known that the excitation efficiency of the TM_{11} mode is low and that of the TE_{12} mode is high at the cut-off aperture (D=920nm) due to the resonance. Therefore the spatial distribution on the aperture can be approximated as the sum of those of the TE_{11} and TE_{12} modes. In Fig.3(b), curve B shows the cross-sectional distribution on the apertured probe obtained by the calculation, where FWHM is 180nm with 30% sidelobe intensity even though the aperture diameter was as large as the wavelength of the light. This result is comparable to that of the curve A.

The principle of the generation of the near-field with this probe is summarized as followings,

1) Effective wavelength inside probe due to the high refractive index led the reduction of the spot size.

2) The propagation mode, which has a low spatial frequency component, does not exist.

3) The TE_{12} mode, which has the highest spatial frequency component, is excited most efficiently.

By the principle 1), the technique for the spot size less than 100nm should be possible using blue light and a material with very high index.

3. APPLICATION TO THE OPTICAL NEAR-FIELD RECORDING AND READOUT

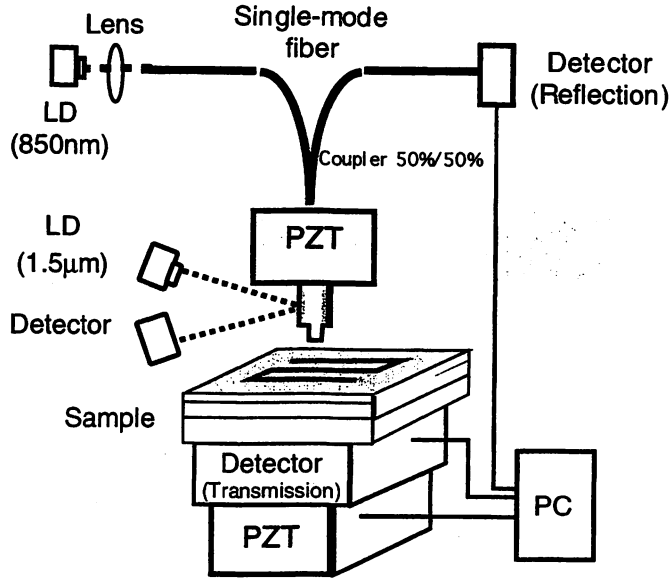

Figure 5: Schematic of the system used for near-field Phase-Change recording. PC: Personal computer.

We applied the probe for optical recording. We used an experimental setup shown in Fig.5. The linearly polarized laser beam from a light source (laser diode, wavelength=850nm) propagates in free space and enters into the single mode fiber to generate the optical near-field on the aperture of the probe at the end of the fiber. The separation between the probe and a recording medium was maintained within several nanometers with shear-force technique. The transmitted light through the aperture and the sample was detected with a photodetector under the medium. The reflected light was detected with a photomultiplier tube by using a fiber coupler. As-deposited phase change material was used as a recording medium.

The recording medium consisted of a 20-nm-thick SiO_2 film, a 25-nm-thick-$AgInTe_2$, and a glass substrate. The two layers were fabricated by RF sputtering. The phase-change film was covered with a 20-nm-thick SiO_2 layer for protecting the recording layer from deformation due to the laser light irradiation. We used an as-deposited $AgInTe_2$ film in an amorphous phase. In ref.10 one can find the dependence of the transmission efficiency of $AgInTe_2$ film on a phase by using a propagating laser beam.

We tried the phase-change recording with optical near-field generated on the probe, where irradiation time was fixed to 2 μs. By changing the optical power (coupling power into the fiber), optical near-field writing were performed. Then the spatial distributions of transmitted light were measured with the optical reading power of 0.2 mW. Figures 6(a) and (b) show the spatial distribution of the transmitted light power for the writing power of 7mW and 8.6mW, respectively. Figures

6(a) and (b) show the spatial distribution of the transmitted light power for the writing power of 7mW and 8.6mW, respectively.

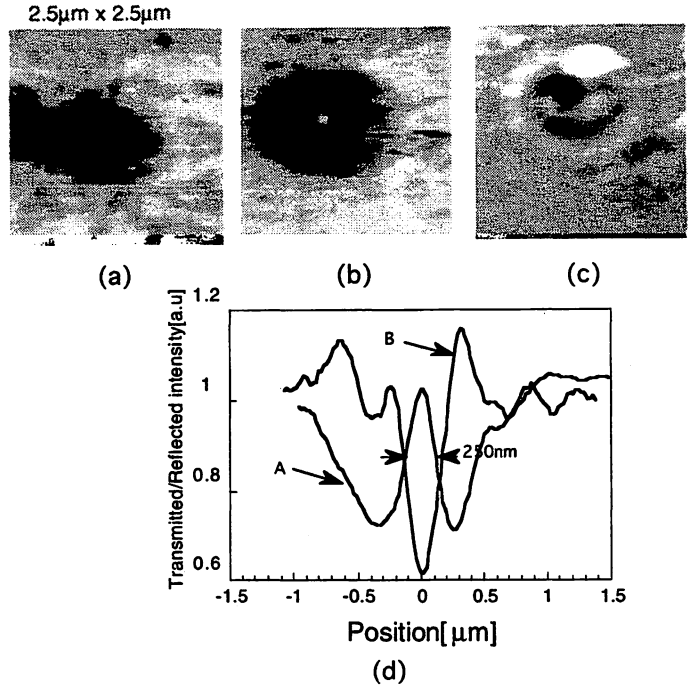

Figure 6: Spatial distribution of the optical near-field intensity Images of the phase-change recordings.(a) ,(b):Illumination mode. 7mW and 8.6 mW writing power writing power, respectively .(c): Illumination/Collection mode. 8.6mW writing power. (d) Curve A and B shows the cross-sectional distribution in (b) and (c), respectively.

When the writing power was 7mW(Fig.6(a)), darkening spot was seen. The darkening might be due to the photodarkening in thin films of amorphous chalcogenides.[11,12] Since Te, being a two-fold coordinated atom, has chain-molecule fragments,[13] structural changes without changing the phase were induced by being exposed to the light, which lead to increase in absorption coefficient.

When the writing power was 8.6mW(Fig.6(b)), one can find a small spot at the center of the photodarkening spot. Figures 6(c) shows the spatial distributions of reflected light when the writing power was 8.6mW, one can find a inverted small spot at the center and it can be seen that photo darkening effect is reduced. In Fig. 6(d), curve A is the cross-sectional profile of (b) . One can find that the full width at half maximum of this curve is 250 nm. Curve B is the cross-sectional profile of (c), from which one can find that the full width at half maximum of curve for the optical near-field writing is as narrow as that of curve A.

5. SUMMARY

We developed a high throughput fiber probe , and applied to the writing and reading of a phase-change material. Though the fiber probe had a super-wavelength aperture, the spot size was as small as150nm. As-deposited SiO_2/$AgInTe_2$/glass substrate was used as a recording medium. We used a laser diode (λ = 850nm) as the light souse, and drove it with a pulsewidth of 2μs for recording. By scanning with the probe for reading, we obtained resolved images of the recorded spot with a width of 250 nm.

6. ACKNOWLEDGMENTS

The authors would like to express their thanks to Dr. J. Tominaga(National Institute for Advanced Interdisciplinary Research), with their valuable discussions.

7. REFERENCES

1. E. Betzig, J. K. Trautman, R. Wolfe, E. M. Gyorgy, P. L. Finn, M. H. Kryder, and C.-H. Chang, "Near-field magneto-optics and high density data storage," *Appl. Phys. Lett.*, 61, 142 ,1992.

2. B. D. Terris, H. J. Mamin, D. Rugar, W. R. Studenmund, and G. S. Kino, "Near-field optical data storage using a solid immersion lens," *Appl. Phys . Lett.*, 65, 388 ,1994.

3. S. Jiang, J. Ichihashi, H. Monobe, M. Fujihira, and M. Ohtsu, "High localized photochemical processes in LB films of photochromic material by using a photon scanning tunneling microscope," *Opt. Commun.*, 106, 173 ,1994.

4. S. Hosaka, T. Shintani, M. Miyamoto, A. Hirotsune, M. Terao, M. Yoshida, K. Fujita, and S. Kammer, "Nanometer-sezed phase-change recording using a scanning near-field optical microscope with a laser diode," *Jpn. J. Appl. Phys.*, 35, 443 ,1996.

5. T. Saiki, S. Mononobe, M. Ohtsu, N. Saito, and J. Kusano, "Tailoring a high-transmission fiber probe for photon scanning tunneling microscope," *Appl. Phys. Lett.*, 68, 2612 ,1996

6. T. Yatsui, M. Kourogi, and M. Ohtsu, "Highly efficient excitation of optical near-field on an apertured fiber probe with an asymmetric structure," *Appl. Phys. Lett.*, 71, 1756 ,1997.

7. T. Yatsui, M. Kourogi, and M. Ohtsu, "Increasing throughput of a near-field optical fiber probe over 1000 times

by the use of a triple-tapered structure," *Appl. Phys. Lett.*, 73, 2090 ,1998.

8. Toshiharu SAIKI, Kenichi NISHI, and Motoichi OHTSU"Low Temperature Near-Field Photoluminescence Spectroscopy of InGaAs Single Quantum Dots" *Jpn. J. Appl. Phys.*, 37, 1638 ,1998.

9. T. Saiki and K. Matsuda "Near-field optical fiber probe optimized for illumination-collection hybrid mode operation" *Appl.Phys. Lett.*, 74, pp. 2773 ,1999.

10. T. Yatsui, M. Kourogi, K. Tsutsui, J. Takahashi, M. Ohtsu,"Subwavelength-sized phase-change recording with silicon planar apertured probe." *SPIE's 44rd Annual Meeting,* 3791-11 ,1999.

11. Ka. Tanaka, "Photo-Induce phenomena in amorphous semiconductors," *Fundamental Physics of AmorphousSemiconductors*, edited by F. Yonezawa, 104 (Springer Verlag, Berlin, 1981).

12. Ke. Tanaka, J. Non-Crys. Solids, 59&60, 925 ,1993.

13. B. W. Corb, W. D. Wei, and B. L. Averbach, "Atomic models of amorphous selenium," *J. Non-Crys. Solids*, 53, 29.1994.

Subwavelength-sized phase-change recording with a silicon planar apertured probe

Takashi Yatsui *[a], Motonobu Kourogi [a,b], Kazuo Tsutsui [a], Jun-ichi Takahashi [c], and Motoichi Ohtsu [a,b]

[a] Interdisciplinary Graduate School of Science and Engineering, Tokyo Institute of Technology, 4259 Nagatsuta, Midori-ku, Yokohama, Japan 226-8502.

[b] Kanagawa Academy of Science and Technology, 3-2-1, Sakado, Takatsu-ku, Kawasaki, Kanagawa, Japan 213-0012.

[c] Research and Development Center, Material and Device Research Group, Ricoh Co., Ltd. 16-1 Shin-eichou Tsuzuki-ku Yokohama, Kanagawa, Japan 224-0035.

ABSTRACT

We propose and demonstrate a new optical near-field slider with a planar apertured probe array for optical memory. The slider was fabricated by utilizing anisotropical etching of a silicon membrane and anodic bonding of a silicon membrane and glass substrate. We also present for the first time a subwavelength-sized phase-change recording/reading by using the planar apertured probe array. Apertures were fabricated at the bottom end of the pyramidal grooves. A SiO_2/$AgInTe_2$/glass substrate was used as the recording medium. By scanning the planar apertured probe array, we obtained resolved images with line width of 250 nm.

Keywords: optical storage, optical near-field, planar apertured probe array (PAPA), slider, silicon-on-insulator (SOI), anodic bonding, anisotropical etching, phase-change recording.

*Email: yatsui@ae.titech.ac.jp; Telephone: +81-45-924-5476; Fax: +81-45-924-5599

Part of the SPIE Conference on Near-Field Optics: Physics, Devices and Information Processing • Denver, Colorado • July 1999
SPIE Vol. 3791 • 0277-786X/99/$10.00

1. INTRODUCTION

In order to realize a high recording density in optical storage system, usage of a shorter wavelength light source, e.g., a blue-violet semiconductor laser, and a solid immersion lens[1] have been proposed. Furthermore, the usage of an optical near-field generated on a subwavelength aperture, where the spot size is not limited by the diffraction of light, has attracted a great attention as an ultrahigh density optical recording/reading method. Preliminary experiments of the near-field optical recording/reading have been carried out on various media such as magneto-optic materials,[2] photochromic materials,[3] and phase-change materials [4] using a metallic sharpened optical fiber probe with a subwavelength aperture.

Recent development of fabrication methods of high throughput probes [5-7] shows the possibility of realizing optical near-field recording/reading with the data transmission rate as high as or even higher than 100 Mb/s.[8] However, since the scanning speed as high as 30 m/s is required for realizing the data transmission rate of 1 Gb/s and the data density of 1 Tb/in^2, the optical near-field recording/reading system using the sharpened fiber probe has several drawbacks. First, the sharpened fiber probe is too fragile to scan at the speed as high as 30 m/s. Second, there is a difficulty of precise mechanical tracking of the single fiber probe maintaining the probe-medium separation within 10 nm by conventional actuators.

In order to overcome these difficulties, a silicon planar apertured probe array (PAPA) has been proposed.[9] Usage of the PAPA with **n** aperture elements reduces the required scanning speed to 1/**n** in comparison with the single probe. Furthermore, because of its planar head structure and reduction of the scanning speed, the array can be smoothly scanned over the storage medium maintaining a narrow gap as is the case of a contact-type hard disk.

However, since the silicon membrane such as a silicon-on-insulator (SOI) wafer is used to fabricate a PAPA with high homogeneous apertures, a problem on the silicon PAPA without backing is fragility. To solve this problem, we propose here a new micromachining method to fabricate a practical slider in which a PAPA is monolithically integrated. The slider is fabricated by utilizing the wet-etching process of a silicon membrane and anodic bonding of silicon membrane and glass substrate. Furthermore, optical near-field recording/reading is demonstrated using the single aperture of the PAPA.

2. A NEAR FIELD SLIDER WITH PLANAR APERTURED PROBE ARRAY

Figure 1 explains schematically the structure of a show a slider for optical near-field recording/reading. The slider consists of a glass substrate and two contact pads. Subwavelength aperture array was fabricated at the surface of the contact pad. The contact pad is made with silicon membrane, where apertures were fabricated at the bottom end of the pyramidal grooves. Note that the silicon PAPA with the thickness of about 10 μm could be durable due to the bonding with a thick (~ 1mm) glass substrate.

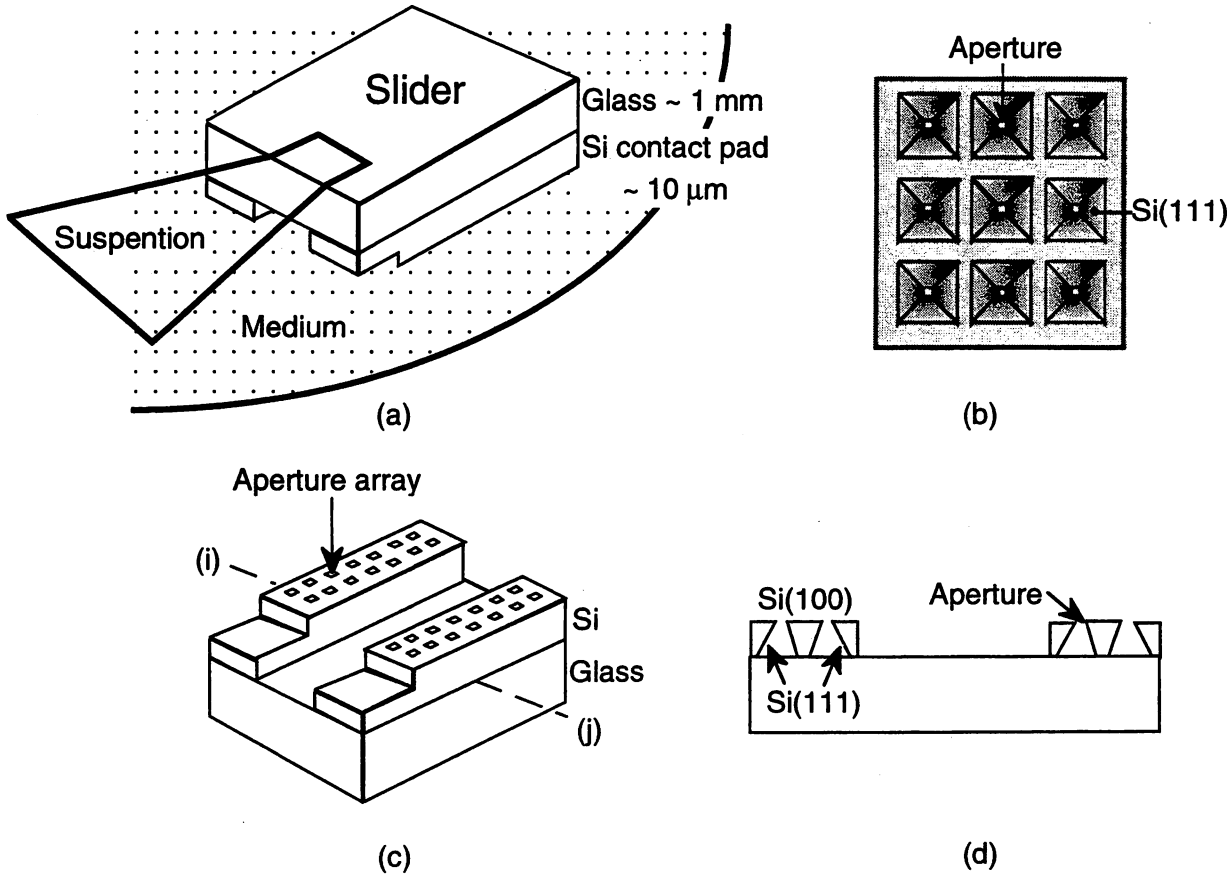

Figure 1: Schematic of the slider with PAPA: (a) bird's-eye view from the glass substrate side, (b) top view of the one of the silicon contact pad from the glass-silicon interface, (c) bird's-eye view from the air bearing surface, (d) cross section at (i)-(j) line in (c).

3. FABRICATION OF SLIDER WITH PLANAR APERTURED PROBE ARRAY

Figure 2 shows a schematic of the basic fabrication process of the optical near-field slider with PAPA. The slider was fabricated by following five steps from (100) oriented SOI wafer:

(i) The oxide layer on the SOI is patterned with the photolithography and the oxide layer is removed by buffered hydrofluoric acid (BHF) solution [Fig. 2(a)].

(ii) The SOI is etched with an anisotropic etchant (10 wt % KOH, 80 °C) until the buried oxide appears [Fig. 2(b)].

(iii) The SOI is bonded with the glass substrate by anodic bonding [10] (300V, 350°C, 10 min.) [Fig. 2(c)].

(iv) The silicon substrate is removed by wet-etching technique while the membrane surface is protected from etchant by the thick glass substrate [Fig. 2(d)].

(v) The buried oxide layer is removed by BHF solution to produce PAPA after quarrying the slider by dicingsaw [Fig. 2(e)].

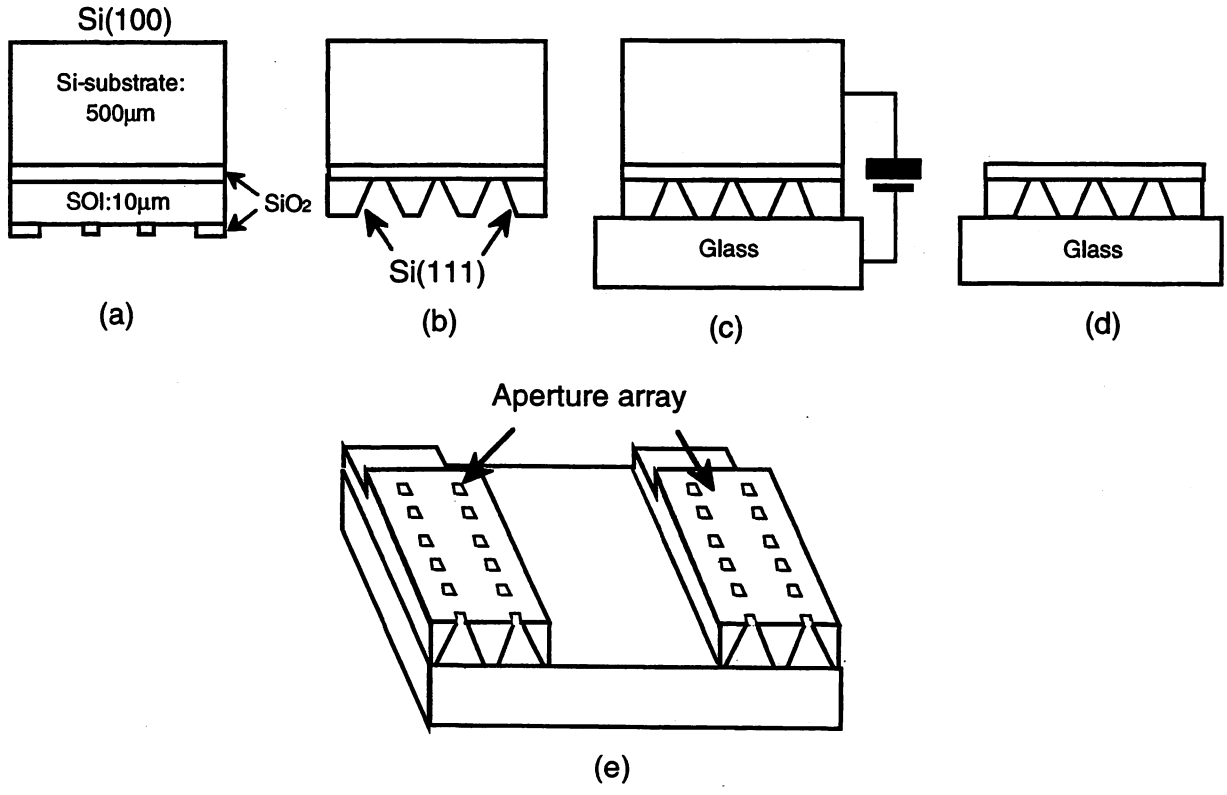

Figure 2: Schematic of the fabrication process of an optical near-field slider with PAPA.

The scanning speed of the PAPA with 1000 aperture elements require as small as 0.03m/s for realizing the data transmission rate of 1 Gb/s and the data density of 1 Tb/in^2. The slider structure is designed so that the gap between the slider and the medium is within 100 nm at scanning speed of 0.03m/s. Figures 3(a) and 3(b) show the image of the fabricated optical near-field slider with PAPA. Note that aperture size as small as 60 nm has been realized by using the same fabrication process.[9] Since the accuracy of the aperture size depends on the thickness of the wafer, the usage of a SOI wafer realizes a subwavelength aperture with high homogeneity.

4. DEMONSTRATION OF THE PHASE-CHANGE RECORDING

For the preliminary experiment of phase-change recording by the optical near-field generated on the PAPA, we used silicon PAPA without the glass substrate. The experimental setup for phase-change recording is shown in Fig. 4. The light from Ar^+ laser (λ = 514 nm) is focused on one of the grooves on the PAPA, where the aperture size was 150 nm $\times$ 150 nm (see Fig. 4(b)). The transmitted light through the aperture and the sample was detected with a photodetector. The PAPA was detached from the SOI wafer and glued to a beryllium copper suspension. The PAPA was put on a sample coated with thin lubricant (FOMBLIN Z-DOL) film.

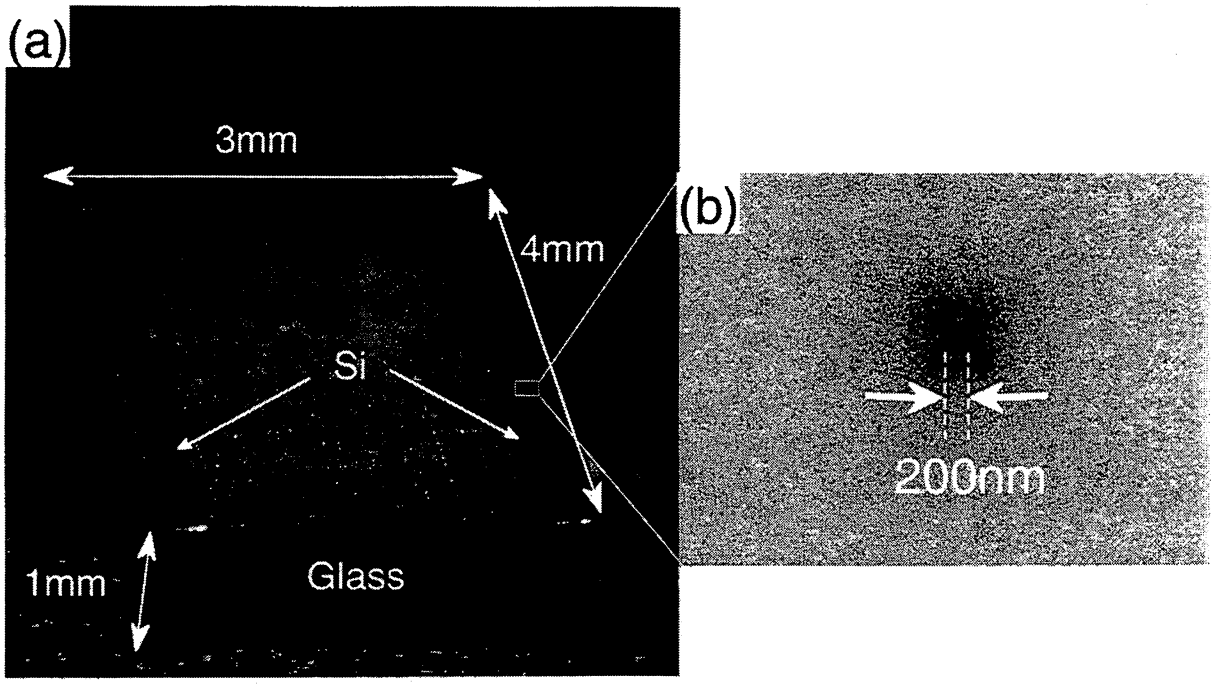

Figure 3: Fabricated optical near-field slider with PAPA: (a) optical microscope image of the slider, (b) magnified SEM image of one aperture.

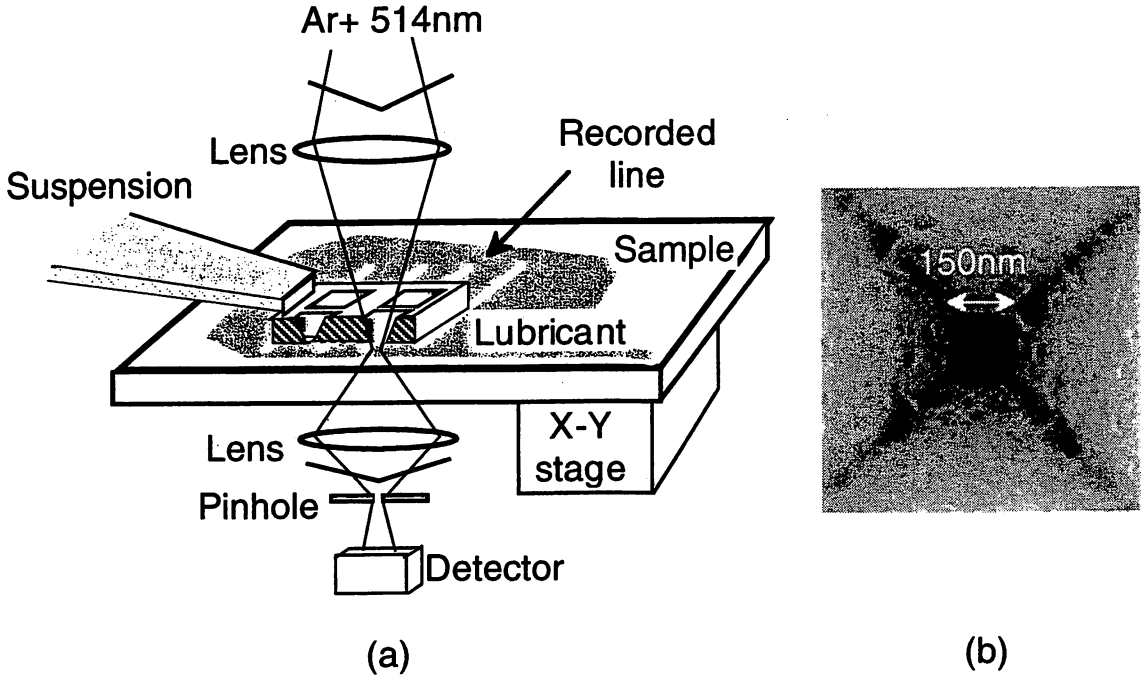

Figure 4: Schematic of the experimental setup for near-field recording: (b) SEM image of the apeture used for near-field recording.

The phase-change filim on a glass substrate consisted of a 20-nm-thick SiO_2 film and a 25-nm-thick-$AgInTe_2$ film. The two layers were fabricated by RF sputtering. It was covered with a 20-nm-thick SiO_2 layer for avoiding deformation due to the laser light irradiation. We used an as-deposited $AgInTe_2$ film of an amorphous phase.

As a preliminary experiment, we evaluated the transmission characteristics of $AgInTe_2$ film on a phase. For this purpose we observed the spatial distribution of transmission after recording with a constant optical power I_R. Here, I_R is the recording power of the conventional propagating light beam focused with objective lens ($\times 10$). The transmission is defined by

$$\text{Transmission} \equiv \frac{\text{Transmitted power}}{\text{Transmitted power through the unrecorded bit}}$$

Figure 5(a) shows a cross-sectional distribution of transmission on the recorded bit with the reading power of 1 mW. In Fig. 5(b), the transmission at center in Fig. 5(a) was plotted as a function of I_R.

One can find that the transmission rapidly increases in the range of 10 mW $\leqq I_w \leqq$ 15 mW. Since the spot size focused by objective lens ($10\times$) is about 2 μm, the optical power density for phase transition is estimated about 1 GW/m^2 at I_R = 10 mW.

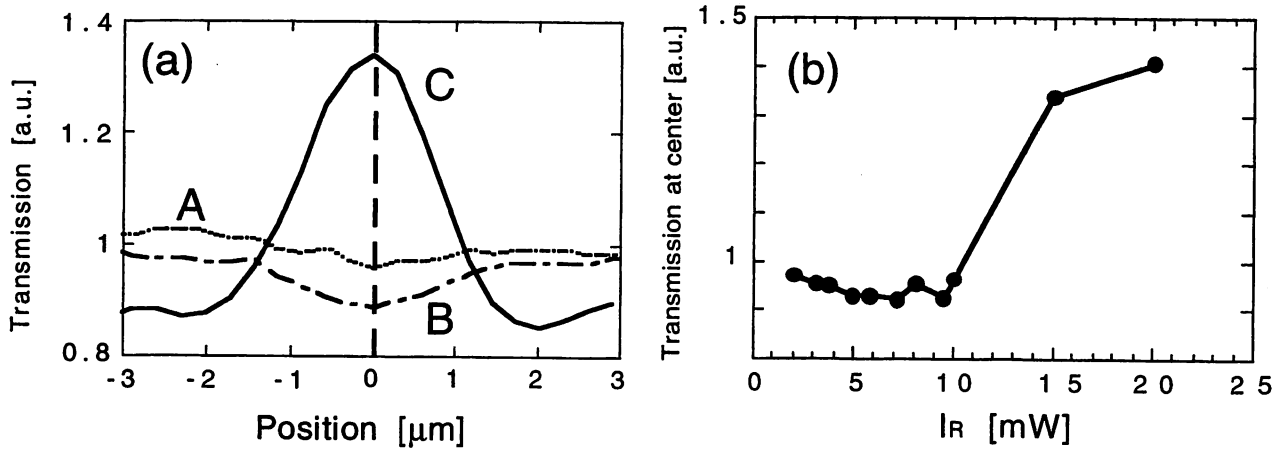

Figure 5: The relationship between transmission of $AgInTe_2$ film and the recording power (I_R): (a) cross-sectional profile, A: I_R = 2.0 mW, B: I_R = 4.9 mW, C: I_R = 15.0 mW, (b) relation between I_R and the transmission at center in (a).

By referring to the transmission characteristics evaluated by Fig. 5, we compared the phase-change recordings by focused propagating light and by optical near-field on the single aperture of PAPA. Recordings by focused propagating light and by optical near-field were performed by I_R = 3 mW with an object lens ($20\times$) and I_R = 30 mW with an aperture of 150 nm$\times$150 nm (see Fig. 4(b)), respectively, at scanning speed of 30 μm/s. Since the throughput (= scattered optical power from the aperture/input optical power) of single silicon probe with an aperture of 100 nm$\times$100 nm is 1×10^{-3},[9] the

power density at the aperture of 150 nm×150 nm is estimated about 1 GW/m^2, which is comparable to that of the optical power density for phase transition. The spatial distributions of transmission were observed through the aperture of 150 nm ×150 nm with the optical reading power of 1 mW. Figures 6(a) and 6(b) are the results for the recordings by the focused propagating light and by the optical near-field, respectively. Figure 6(c) shows cross-sectional profiles along the white dashed lines in (a) and (b).

One can find that the full width at half maximum of the curve of the recording by optical near-field is 250 nm, which is half as much as that by the focused propagating light. Major reason for wider line width (250 nm) than aperture size (150 nm) might be no coating over the silicon probe, by which the effective aperture size was larger due to the light penetration. The smaller bit should be recorded and read out by coating metal over the PAPA.

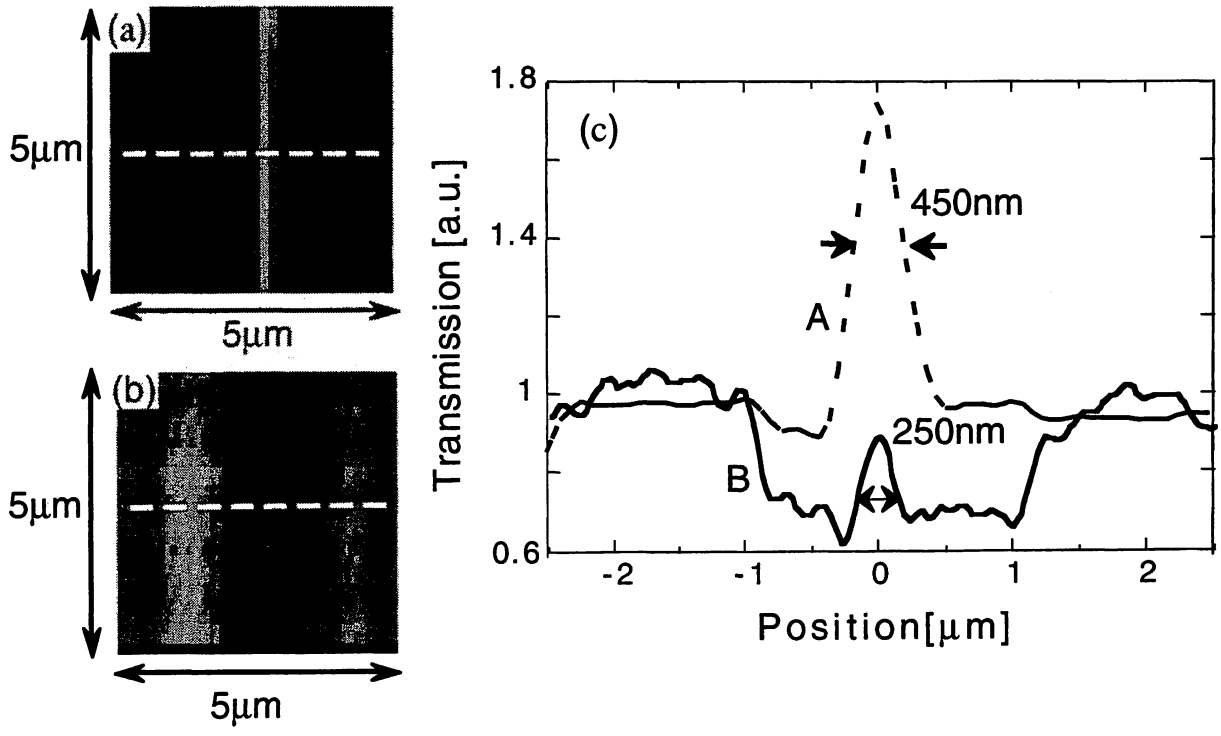

Figure 6: Spatial distribution of the transmitted light power: (a) recording by a focused propagating light, (b) by optical near-field, (c) curves A and B are the cross-sectional profiles along the white dashed lines in (a) and (b), respectively.

The darkening around the recorded line seen in Fig. 6(b) might be due to the photodarkening in thin films of amorphous chalcogenides.[11, 12] Since Te, being a two-fold coordinated atom, has chain-molecule fragments,[13] structural changes without changing the phase were induced by exposing to the light, which lead to increase in absorption coefficient.[11] As shown in Fig. 5(b), since the transmission decreases at I_R < 10 mW, the decrease in transmission around the recorded line (see Fig. 6(b)) might be due to the penetration of the light around the aperture.

5. SUMMARY

We proposed and demonstrated a new slider with a planar apertured probe array for optical near-field memory. The slider was fabricated by using wet etching technique of a silicon wafer and anodic bonding. Pyramidal grooves were formed on the silicon-on-insulator, and apertures were fabricated at the bottom of the pyramidal grooves. The phase-change recording was performed using the planar apertured probe array for the first time. We obtained resolved images with line width of 250 nm by scanning the planar apertured probe array. Higher density optical recording/reading can be expected using a near-field slider with a planar apertured probe array.

6. ACKNOWLEDGMENTS

The authors would like to express their thanks to Drs. J. Tominaga and N. Atoda (National Institute for Advanced Interdisciplinary Research), Profs. H. Ishiwara, and E. Tokumitsu (Tokyo Institute of Technology) for their valuable discussions.

7. REFERENCES

[1] B. D. Terris, H. J. Mamin, D. Rugar, W. R. Studenmund, and G. S. Kino, "Near-field optical data storage using a solid immersion lens," Appl. Phys. Lett., **65**, 388 (1994).

[2] E. Betzig, J. K. Trautman, R. Wolfe, E. M. Gyorgy, P. L. Finn, M. H. Kryder, and C.-H. Chang, "Near-field magneto-optics and high density data storage," Appl. Phys. Lett., **61**, 142 (1992).

[3] S. Jiang, J. Ichihashi, H. Monobe, M. Fujihira, and M. Ohtsu, "High localized photochemical processes in LB films of photochromic material by using a photon scanning tunneling microscope," Opt. Commun., **106**, 173 (1994).

[4] S. Hosaka, T. Shintani, M. Miyamoto, A. Hirotsune, M. Terao, M. Yoshida, K. Fujita, and S. Kammer, "Nanometer-sezed phase-change recording using a scanning near-field optical microscope with a laser diode," Jpn. J. Appl. Phys., **35**, 443 (1996).

[5] T. Saiki, S. Mononobe, M. Ohtsu, N. Saito, and J. Kusano, "Tailoring a high-transmission fiber probe for photon scanning tunneling microscope," Appl. Phys. Lett. **68**, 2612 (1996)

[6] T. Yatsui, M. Kourogi, and M. Ohtsu, "Highly efficient excitation of optical near-field on an apertured fiber probe with an asymmetric structure," Appl. Phys. Lett., **71**, 1756 (1997).

[7] T. Yatsui, M. Kourogi, and M. Ohtsu, "Increasing throughput of a near-field optical fiber probe over 1000 times by the use of a triple-tapered structure," Appl. Phys. Lett., **73**, 2090 (1998).

[8] M. Ohtsu, "High speed near-field optical technology for ultrahigh density storage," Tech. Digest of the Joint MORIS/ISOM Symp., 180 (1997).

[9] M. Kourogi, T. Yatsui, S. Ishimura, M. B. Lee, N. Atoda, K. Tsutsui, and M. Ohtsu, "A near-field planar apertured probe

array for optical near-field memory," Proceedings of SPIE's 43rd Annual Meeting, **3467**, 258 (1998).

[10] T. R. Anthony, "Dielectruuc isolation of silicon by anodic bonding," J. Appl. Phys., 58, (1998).

[11] K. Tanaka, "Photo-Induce phenomena in amorphous semiconductors," *Fundamental Physics of Amorphous Semiconductors*, edited by F. Yonezawa, 104 (Springer Verlag, Berlin, 1981).

[12] K. Tanaka, "*Mechanisms of photodarkening in amorphous chalcogenides,*" J. Non-Crys. Solids, **59&60**, 925 (1993).

[13] B. W. Corb, W. D. Wei, and B. L. Averbach, "Atomic models of amorphous selenium," J. Non-Crys. Solids, **53**, 29 (1994).

Photochemical vapor deposition by optical near-field

Y. Yamamoto [a], V. Polonski [a], G. H. Lee [b], M. Kourogi [a,b], M. Ohtsu [a,b]
a Interdisciplinary Graduate School of Science and Engineering, Tokyo Institute of Technology
4259 Nagatsuta, Midori-ku, Yokohama, Kanagawa 226-8502, Japan
b Japan Science and Technology Corporation
687-1 Tsuruma, Machida, Tokyo 194-0004, Japan

Abstract

In-situ patterning of nano-scale Zn dots and lines has been succeeded by photodissociation of a gas-phase diethylzinc in optical near-field. By using an optical fiber probe with the aperture diameter of 60nm, dots with full width at half maximum of ~60nm and~70nm, closely separated by 100nm were fabricated. It implies that finer patterns of a metal can be fabricated by using optical fiber probe with smaller aperture, allowing control of the size and position of nano-scale structures. Consequently, the technique is the one of most suitable for nano-photonic device fabrication

Keywords: near-field, photochemical vapor deposition, direct deposition, nano-photonic device

1. Introduction

Recently, optical near-field has been reported applicable in various fields, such as high resolution optical microscopy, localized spectroscopy of semiconductor quantum dots [1], optical memory [2] with ultra high density attainable to 1Tbit/in^2 and so on. Moreover, there has been an interest in its application to nano-fabrication techniques because of the possibility to realize nano-photonic device, composed of metallic wires and light emitting parts, photo-detectors, and optical switches, operated by nano-scale single dots. However, to do that, we need a high-level nano-fabrication technique, which is able to produce nano-scale structures of various materials with reliable control of their size, position and topography.

Conventionally, nano-fabrication has been accomplished by X-ray or electron beam lithography and self-organized growth technique [3]. The former makes it easy to produce the desired pattern, but has a disadvantage of damaging the substrate by etchants, etc. The latter easily produces high-quality nano-scale dots, but it is difficult to control their position and size.

As a nano-fabrication technique, in-situ patterning using scanning probe microscopy such as STM [4] has been also investigated. Though STM enables fabrication of nano-scale structures, it has a fatal disadvantage setting a limit to deposited materials, because of the impossibility to deal with insulators. Therefore, none of present methods is adequate enough to integrate nano-structures of various materials.

On the other hand, chemical vapor deposition (CVD) by optical near-field, which we previously proposed [5], can eliminate the damage and substrate contamination, and better still, can deposit various materials as metal, semiconductor, and

Correspondence: Email: yoh@ae.titech.ac.jp; Telephone: 045-924-5476; Fax: 045-924-5599

Part of the SPIE Conference on Near-Field Optics: Physics, Devices and Information Processing • Denver, Colorado • July 1999
SPIE Vol. 3791 • 0277-786X/99/$10.00

insulator. Based on photochemical reaction, this technique has also the option of chemical selective growth by varying the wavelength of used light source. In addition, by using optical near-field, it becomes possible to easily fabricate nano-scale structures composed of various materials on the same substrate with reliable control of their size, position and topography, which consequently raises the expectation of this technique as the best suited for the nano-photonic device realization.

In our previous work, we succeeded in producing various patterns of zinc (Zn) by prenucleation [5], which involves the formation of nuclei by optical near-field and consequent selective growth of the prenucleated pattern by propagating far-field light (Fig.1 (a)). We obtained topographic images with minimum line width of 15nm employing the high-resolution shear-force microscopy placed in vacuum [6]. This technique has the advantage of avoiding possible deposition on the top of the probe tip, and it is convenient for the nano-fabrication of a single material, for example, suitable for the repair of photomasks etc. However, the lateral integration of various materials is difficult due to use of the propagating far-field light in the second step of final pattern formation. In order to solve this problem, in this work, we directly deposited Zn by photodissociation of gas-phase diethylzinc (DEZ) by optical near-field generated at the probe tip (Fig.1 (b)). Since only optical near-field is utilized in this technique, closely spacing nano-scale structures of various materials can be produced in a single step.

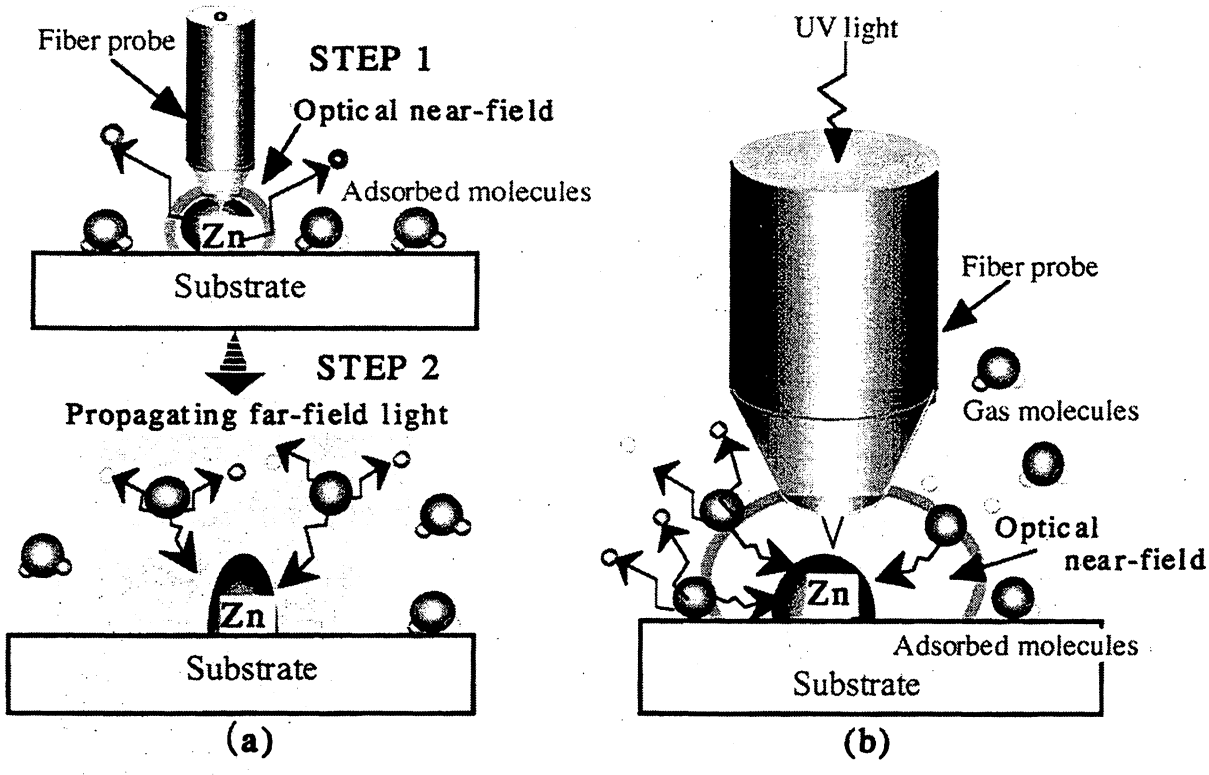

Fig. 1 Principle of CVD by optical near-field (a) prenuclation STEP1: prenuclation by optical near-field STEP2: development of pattern by propagating far-field light (b) direct deposition

2.Experimental setup

As photochemical vapor deposition is based on photodissociation reaction, for deposition, it is necessary for reactant molecule to absorb photon with higher energy than dissociation energy.

We used diethylzinc (DEZ) as a parent gas for deposition of Zn. This molecule has adsorption below $\lambda = 260$nm and it is photodecomposed via the following step.

$$Zn(C_2H_5)_2 + 2.256eV \rightarrow ZnC_2H_5 + C_2H_5$$

$$ZnC_2H_5 + 0.9545eV \rightarrow Zn + C_2H_5$$

Figure 2(a) shows schematic diagram of the experimental set up. We used second harmonic light (SH light) of Ar ion laser (λ=244nm: 5.08eV) as a light source for photodissociation of DEZ. SH light was generated in BBO crystal placed in built-up cavity, and the light was directed into the vacuum chamber through the UV fiber. As the optical fiber probe, we used UV triple tapered probe coated with 200nm-thick aluminum film after being tapered by chemical etching [7]. (Except for section 3.3 in this paper) The shape of this probe is shown in Fig.2 (b). Transmission loss at 244nm for this fiber is as low as 1.1dB/m, which means the throughput of the used probe was 1×10^{-4} (@100nm:aperture diameter), and the power density for 1mW of light couple into the fiber was as high as 1kW/cm^2. The vacuum chamber was evacuated to below 1×10^{-5}Torr and then filled with a few mTorr of DEZ. Corning grass 7092 was used as a substrate, and the separation between the probe and the substrate was maintained within several nanometers by shear-force technique using tuning fork based probe [8] during deposition. Deposits were measured by vacuum shear-force microscopy (VSFM) [6] with the same probe. All experiments were performed at room temperature.

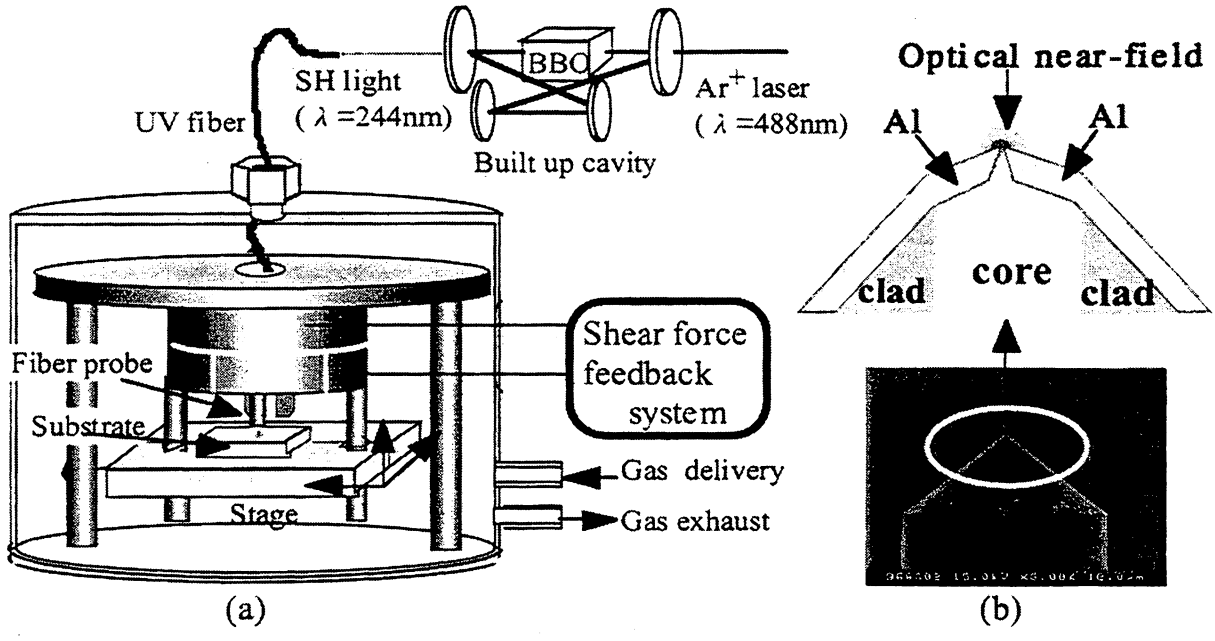

Fig. 2 Experimental setup (a) schematic diagram of experimental setup

(b) fiber probe: above~cross-section of the tip below~SEM image

3. Result

3.1 Fabrication of nano-scale patterns

Figures 3 (a) and (b) show the shear-force image of deposited Zn dots and the cross-sectional profile along the white dashed line in (a), respectively. We deposited Zn in 1mTorr of DEZ. The input power of SH light was 10mW, and optical near-field on the tip was illuminated to five spots at intervals of 800nm on the substrate for a few seconds. As shown in Fig.3 (a), we can see deposited Zn dots on the illuminated point. The size of these dots (FWHM) was ~ 155nm in width and 1~6nm in height depending on illumination time, as shown in Fig.3 (b). The positions of dots are spaced by 800nm, comparable with illuminated point. This indicates that this technique has high precision of positioning in fabrication of nano-scale dots.

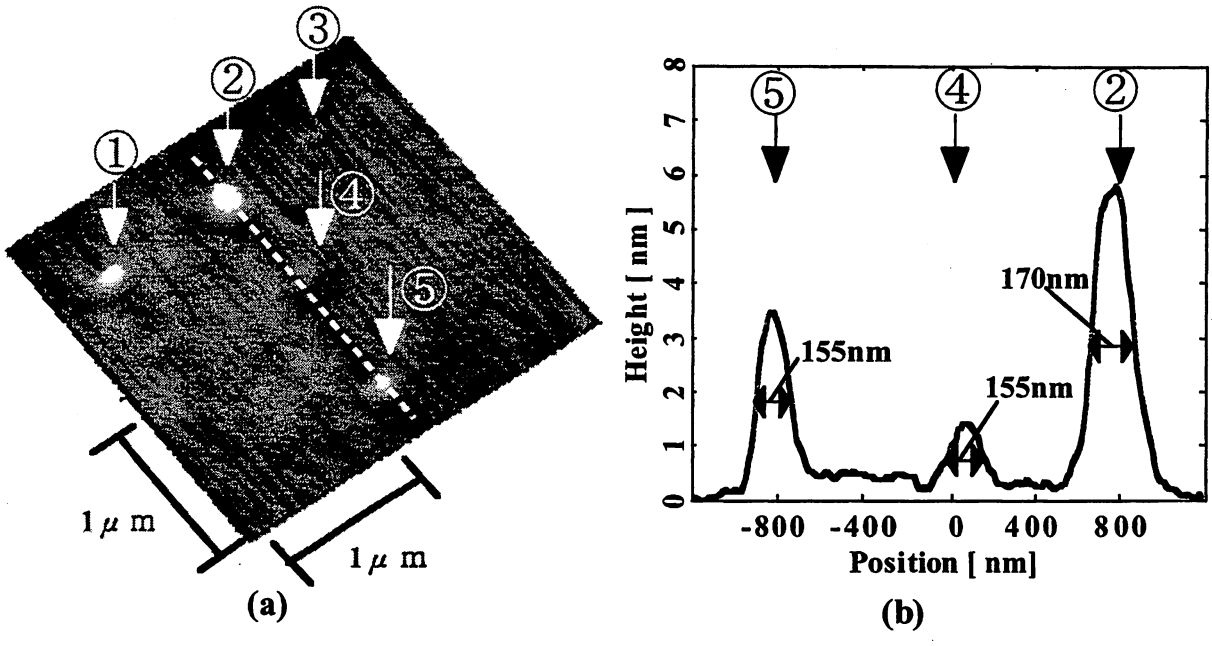

Fig. 3 Nano-scale dots of Zn (a) shear-force image of five dots (①~⑤) (b) cross-sectional profile along the white dashed line in (a)

Next, we demonstrated fabrication of nano-scale lines. In this experiment, the gas pressure of DEZ was ~5mTorr, and the input light power was 3mW. T-shaped lines were produced by scanning the substrate at a speed of 10~50nm/s. Figures 4 (a) and (b) show the shear-force image of fabricated Zn lines, and the cross-sectional profile along the black dashed line in (a), respectively. The width (FWHM) of this pattern was ~200nm, and the height was 16nm. The minimum width of lines fabricated by conventional photo-CVD does not lie below 2~3 μ m[9], and this result was one-tenth as small as it.

In this section, we showed that photo-CVD by optical near-field make it possible to fabricate subwavelength-scale structures with control of their position. Incidentally, the tip of used probe was gradually covered with depositing materials.

However, it took 2～3 hours until the near-field light could not be generated at probe tip due to the deposit contamination. Therefore, there is no serious problem, since only a few seconds are necessary to fabricate nano-structure.

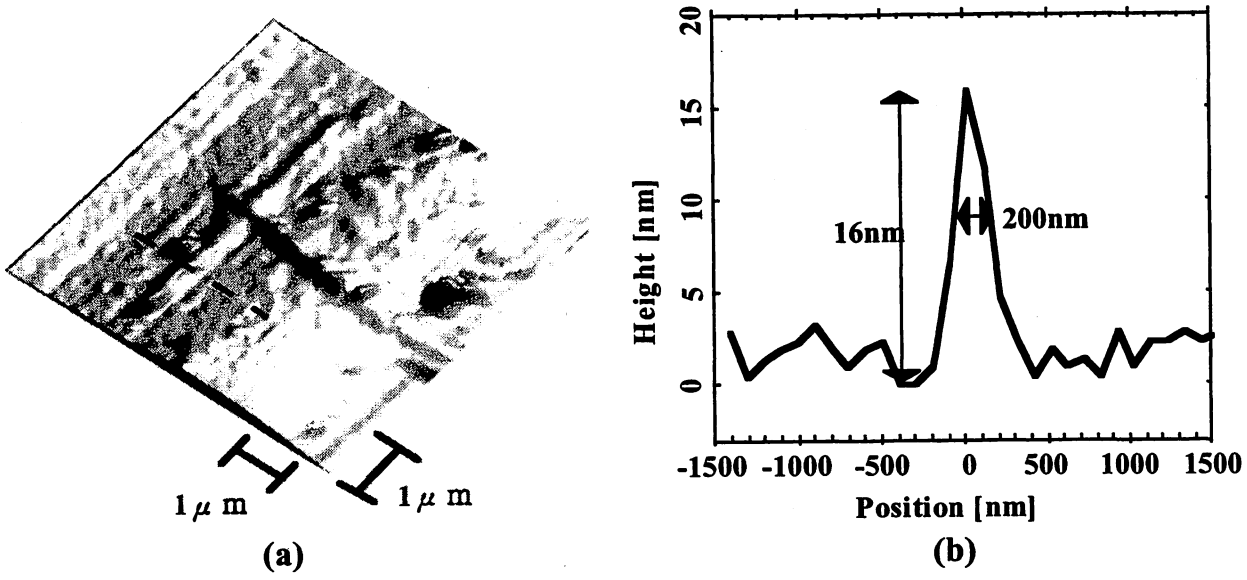

Fig. 4 Nano-scale line of Zn (a) shear-force image of T-shaped lines (b) cross-sectional profile along the black dashed line in (a)

3.2 The dependence on optical near-field energy (deposition time)

This section presents the effect of optical near-field energy on growth. This experiment was performed by varying illumination time at a constant gas pressure of 1mTorr and input SH light power of 15mW. The temperature of the substrate was room temperature. SH light power at the tip was 300nW, measured with a broad-area Si photo-diode (sensor area: 5.8× 5.8 mm^2) at a distance of a few mm apart from the tip. The value of optical near-field energy was estimated by measured SH light power×illumination time.

Figure 5 (a) shows the shear-force image of deposited Zn dots. Dots①,②,③,④ were fabricated on condition that optical near-field energies were 0.3, 0.6, 1.5, and 3.0 μJ (illumination time: 1s, 2s, 5s, 10s), respectively. Dot⑤ was excepted from the following discussion because input SH light power varied while it was deposited. We could observe that Zn dots grew as optical near-field energy increased. Figure 5 (b) shows the variation of height and width (FWHM) of fabricated dots as a function of optical near-field energy. FWHM was about 175nm and it is almost constant with respect to optical near-field energy. On the other hand, height increased linearly at the rate of～5nm/μJ, as optical near-field energy increased. It was found from this result that the size of fabricated dots depends on spatial distribution of optical near-field in the horizontal direction to substrate, while does energy of optical near-field in the perpendicular direction to substrate. As a result, its ratio of height to width, i.e. its aspect ratio increased in proportion to the increase of optical near-field energy, with the rate of ～ 0.03/μJ.

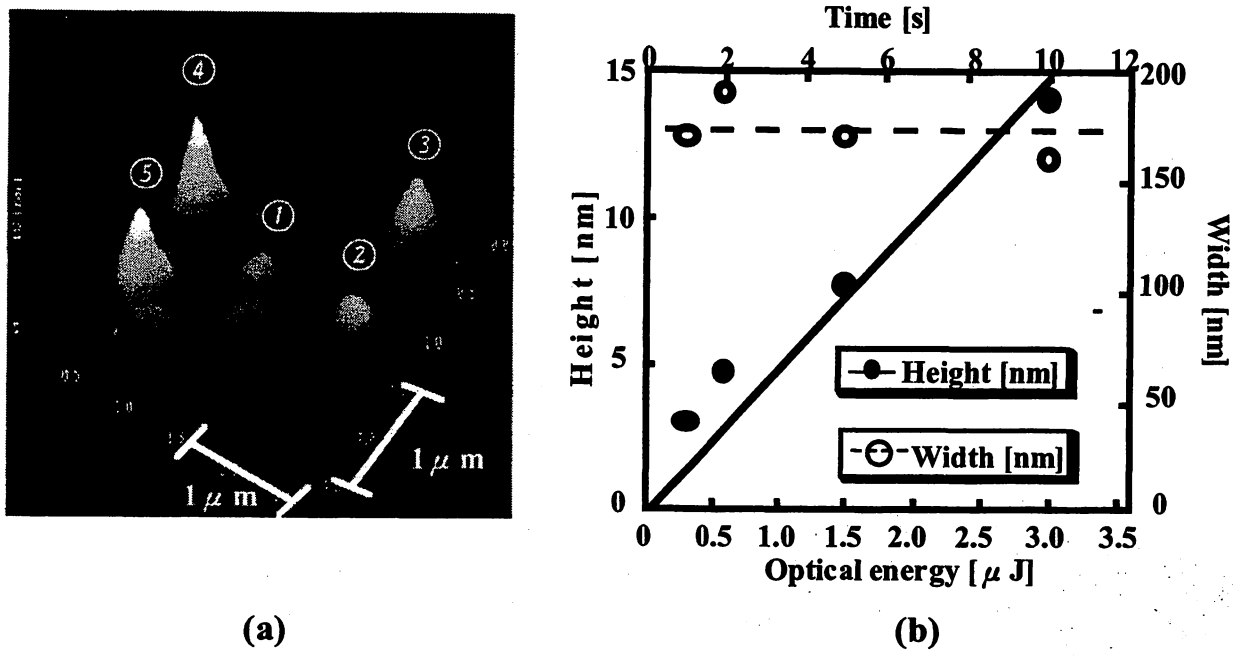

Fig. 5 The effect of optical near-field energy on growth of Zn (a) shear-force image (b) variation of height (open circles) and FWHM (closed circles) of fabricated Zn dots (①~④) as a function of optical near-field energy

3.2 The consideration to the improvement of spatial resolution and reproducibility

One of the most attractive points of this technique is its high spatial resolution. As we mentioned in the previous section, lateral size of fabricated pattern depends on the spatial distribution of the optical near field, that is, it depends on the property of used probe. Its reproducibility consequently depends on the reproducibility of fabricating probes. Currently, various probes are made of optical fiber with GeO_2 doped core applied its use. Especially, high-resolution probe[10] was realized, and its reproducibility is very high. However, because of high transmission loss for 244nm(~96dB/m) of this fiber, such a probe is difficult to use in UV region. Therefore, the property of usable in UV region probe is limited. In order to increase the flexibility of the UV probe, we spliced fiber probe with GeO_2 doped core to UV fiber. This probe is shown in Fig.6. In this work, we spliced single-tapered apertured probe[11], which is easily fabricated with small aperture reproducible and

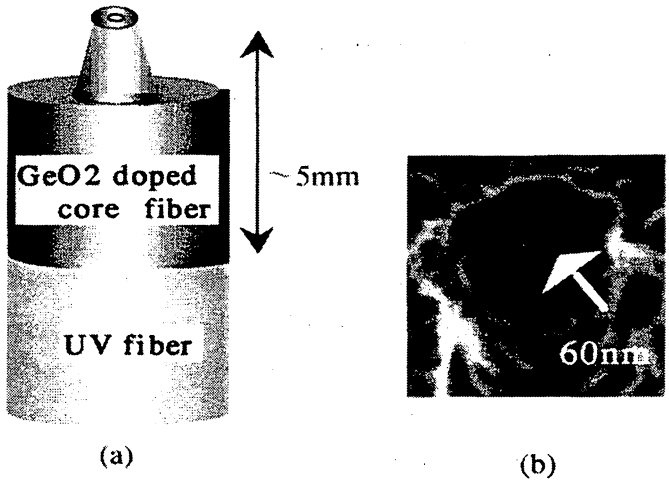

Fig. 6 Fiber probe for UV (a) the illustration of structure (b) SEM image

controllable of its size, to UV fiber. Figure 7(a) and (b) show the shear-force image of deposited dots by using a probe with aperture diameter of~60nm and cross-sectional profile along the white dashed line in (a), respectively. The experimental condition were gas pressure of 1mTorr, input light power of 3mW, and illumination time of 300s. In addition, as a result of careful adjustment of separation between probe and substrate, we successfully fabricated two dots with the size of 60nm and 70nm at a very close distance of 100nm. FWHM of dots was comparable with aperture diameter of used probe. This result indicates that we can fabricate patterns of Zn with smaller size by using optical fiber probe with smaller aperture. Measured size of fabricated patterns includes the resolution of VSFM depending on the shape of the used probe, so we can obtain smaller image of fabricated patterns by using a probe with higher resolution. We expect that we can fabricate and measure patterns of Zn with smaller size by splicing high-resolution probe to UV fiber in the future.

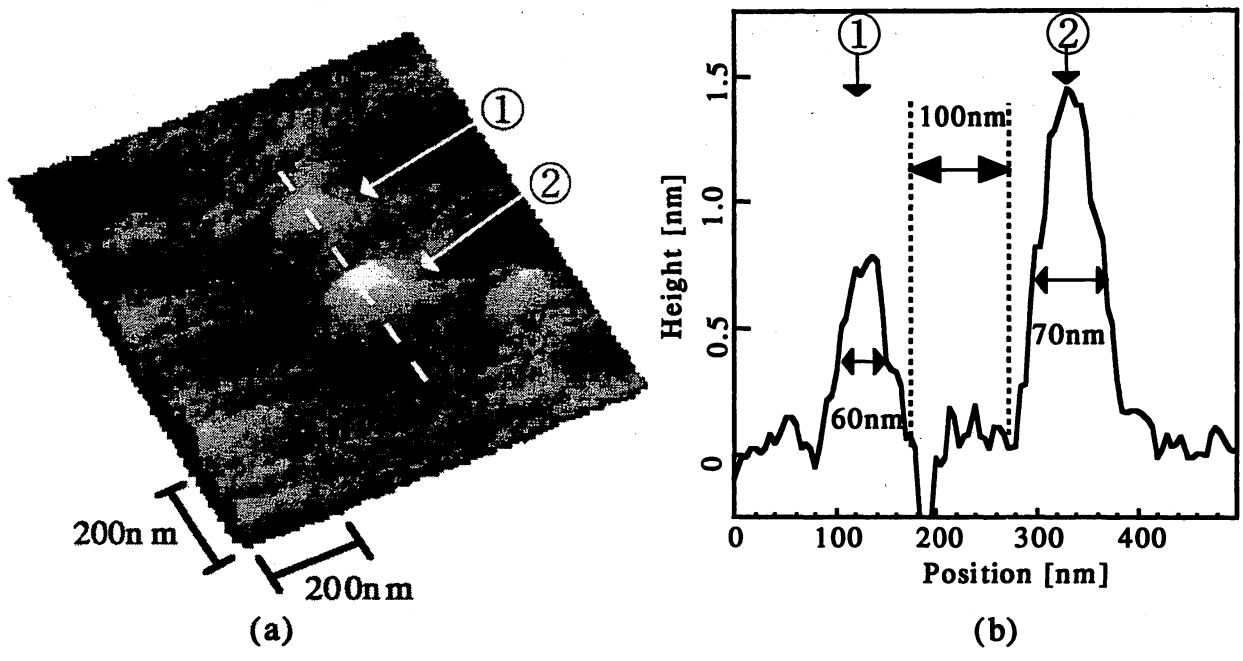

Fig. 7 Closely deposited nano-scale Zn dots (a) shear-force image of two dots (①,②)
(b) cross-sectional profile along the white dashed line in (a)

4. Conclusion

In conclusion, we successfully fabricated nano-scale dots and lines of Zn by direct deposition with optical near-field at desired positions. In addition, we observed that the lateral size of patterns depended on the distribution of optical near-field, and the vertical size grew in proportion to the increase of energy of optical near-field. These results show that this technique makes it possible to fabricate various nano-scale structures controlling their position and size. It is applicable to the deposition of not only Zn but also other metals, semiconductors and insulators, therefore, is suitable for the realization of nano-photonic device.

Acknowledgments

Authors would like to thank to Mr. S. Mononobe of Kanagawa Academy of Science and Technology for his irreplaceable help and advice in the art of making fiber probes and to H. Fukuda of Ricoh Co. Ltd. for useful discussions. We are also grateful to Professors M. Konagai and A. Yamada of Tokyo Institute of Technology for useful advice for development of instrument.

References

1. T. Saiki, et al., "Low temperature near-field photoluminescence spectroscopy of InGaAs single quantum dots" Jpn. J. Appl. Phys., 37, 1638 (1998)
2. M. Ohtsu, et al., "Near field optics and its application to optical memory", Elect. Comm. in Japan Part :Electronics, 8(18), 41(1998)
3. D. Leonald, et al., "Direct formation of quantum-sized dots from uniform coherent islands of InGaAs on GaAs surface", Appl. Phys. Lett., 63(23), 3203(1993)
4. R. Wiesendanger, "Fabrication of nanometer structure using STM", Applied Surface Science 54, 271(1992)
5. V. Polonski, et al., "Nanometric patterning of zinc by optical near field photochemical vapor deposition", J. Microscopy 194, (1999) in press
6. V. Polonski, et al., "Vacuum shear-force microscopy: Application to high resolution imaging", Jpn. J. Appl. Phys (To be published)
7. S. Mononobe, et al., "Fabrication of a triple tapered probe for near-field optical spectroscopy in UV region based on selective etching of a multistep index fiber" , Optics Comm., 146, 45 (1998)
8. G. T. Ruiter, et al., "Dynamic behavior of tuning fork shear-force feedback", Appl. Phys. Lett. 71(1), 28 (1997)
9. D. J. Ehrlich, et al, "Spatial delineated growth of metal films via photochemical prenucleation", Appl. Phys. Lett. 38, (11) 946 (1981)
10. S. Mononobe, et al., "Development of a fiber used for fabricating application oriented near-field optical probes", IEEE Photonics Technol. Lett. 10, 99 (1998)
11. T. Yatsui, et al., "Enhancing throughput over 100Times by a triple-tapered structure for near-field optical fiber probe", Proceeding of SPIE, 3467-13 (1998)

Fabrication of ZnO nanostructure using near-field optical technology

G.H. Lee*[a], Y . Yamamoto[b], M. Kourogi[a,b], M. Ohtsu[a,b]

[a]Japan Science and Technology Corp., 687-1 Tsuruma, Machida, Tokyo 194-0004, Japan
[b]Interdisciplinary Graduate School of Science and Engineering, Tokyo Institute of Technology, 4259 Nagatsuda, Midori-ku, Yokohama, Kanagawa 226, Japan

ABSTRACT

ZnO nanodots have been successfully fabricated on a (001) Al_2O_3 substrate by photo-enhanced chemical vapor deposition (PE-MOCVD) combined with near-field optical technology. The optical near-field generated from an optical fiber probe tip allowed ZnO dots to selectively grow on the irradiated substrate surface, with a size smaller than the wavelength of the light source (λ=244nm). The crystallinity and composition of ZnO were evaluated from planar films using x-ray diffraction analysis, optical transmittance and x-ray photoelectron spectroscopy (XPS). The planar films were grown using PE-MOCVD with a direct irradiation by an ultraviolet light source without probe tip. Above a deposition temperature of 150 °C, stoichiometric ZnO films (R O:Zn=1), strongly the c-axis oriented and exhibiting a band gap of about 3.3 eV were obtained.

Key words: ZnO nanodot, Photo-enhanced chemical vapor deposition (PE-MOCVD), Optical near-field.

1. INTRODUCTION

Nowadays, with the development of optical communications and for the sake of higher integration tantamount of higher performances (speed, capacity), it is of crucial importance to minimize the constituents size in optical devices. The light, however, is localized in a space whose dimensions are in the order of its wavelength. This forces the size of optical elements not to be decreased below that wavelength. If one could use a light wave localized within dimension smaller than its wavelength, that will overcome the wavelength limit. Such a localized light exists and is called optical near-field. The optical near-field is spatially localized within a distance comparable to the diameter of the object generating it [1), 2)]. So, in order to use the optical near-field in an optical integrated circuit, the position of optical elements must be controlled and fabricated with high accuracy for the effective interaction at a sub-wavelength distance between two nanometric-sized

* Correspondence: E-mail: ghl@ohtsu.jst.go.jp; Telephone:+81-42-788-6039; Fax: +81-42-788-6031

Part of the SPIE Conference on Near-Field Optics: Physics, Devices and Information Processing • Denver, Colorado • July 1999
SPIE Vol. 3791 • 0277-786X/99/$10.00

elements. What is more, the optical near-field having its energy concentrated within dimension smaller than its wavelength, it constitutes also very promising tool to fabricate nanostructures.

So far, in the field of semiconductor industry, lithographic technology has been utilized widely for the fabrication of sub-micron structures. However, with the complexity of the process and with the damage of substrate and film by etchants, it has a lot of problems that still need to be solved. As a technology susceptible to solve those problems, photo-enhanced chemical vapor deposition (PE-MOCVD) method has been attracting attention for the last few decades.

PE-MOCVD allowing of in-situ patterning, it offers the possibility for the lateral integration (i.e. side by side) of different structures (different sequence of layers, materials, thickness and dopants), without the need of any lithography or etching steps, in a truly single growth run [3), 4), 5)]. Moreover, PE-MOCVD has an inherent potential to change the lateral pattern during growth. It is therefore expected to become a key technology for the manufacture of optoelectronic circuits. The combination of near-field optical technology with the PE-MOCVD process is even a more promising technology since it allows the integration of nanometer scale elements. On the other hand, another technique in which MOCVD is combined with Scanning Tunneling Microscopy (STM) [6)] has been reported to successfully be able to produce nanostructures with dimensions close to the atomic level. However, the main drawback associated with this process comes from the impossibility to use non-conductive substrates and to grow non-conductive films.

On the contrary, there is no limitation regarding substrate and film materials in MOCVD combined with near-field optical technology. Moreover, this technology not only allows us to fabricate nanostructures, it allows also and at the same time the in-situ measurement of the optical properties of the fabricated nanostructures. MOCVD combined with near-field optical technology appears to be the best suitable method for the realization of photonic devices making use of nanostructures. Based on this consideration, we have proposed PE-MOCVD by optical near-field and succeeded in deposition a 20 nm linewidth Zn strip on a glass substrate[7)]. After this, further works have been carried out to fabricate a variety of subwavelength Zn patterns [8)].

In this paper, the nanofabrication of ZnO by NOM will be presented. ZnO, as a wide-gap semiconductor, has attracted a great deal of attention due to efficient exciton emission that occurs even at room temperature [9), 10)] due to its large exciton binding energy of 60 meV. Another interesting property that has been reported recently is the second harmonic generation from ZnO thin films deposited on sapphire substrate [11)]. ZnO appears to be a very promising material with important potential application in integrated optics.

2. EXPERIMENTAL

ZnO films were obtained using the reaction between diethylzinc [DEZ: $Zn(C_2H_5)_2$], conveyed by a carrier gas (Ar) into the chamber, and oxygen during the irradiation by the second harmonic light (λ=244nm) of Ar^+laser. (001) Al_2O_3 was

selected as the substrate for the (001) epitaxial growth of ZnO. The reaction chamber was initially evacuated to pressures in the low 10^{-5} or 10^{-7} Torr range, then filled with the reactant gases with the ratio of DEZ:O of 1:10 at a working pressure of 10 mTorr. The chamber pressure was maintained constantly at 10 mTorr during growth. The substrates were cleaned using acetone, alcohol, and de-ionized water, and blown dry with N_2 to ensure good reproducibility of the film properties.

The films for crystallinity, surface morphology and transmittance measurements were prepared by direct laser irradiation on the substrates. The energy density of the laser source and the minimum spot size were 10 mW and 600 μm, respectively. The substrate temperature was varied in the range of room temperature - 300 °C. The crystallinity and surface morphology were evaluated by x-ray diffraction (XRD) measurement using Cu Kα radiation and scanning electron microscopy (SEM), while the optical transmission measurements were carried out by a double-beam monochromator in atmospheric ambient at wavelengths from 300 to 1000 nm to obtain the optical energy band gap of the films. The stoichiometry was measured by x-ray photoelectron spectroscopy (XPS) using Al Kα x-ray.

On the other hand, the fabrication of nanometric structures was performed by delivering the laser light on the substrate using a low-loss (1.1 dB/m) optical fiber that was specially developed by our group [12]. In this study, an UV fiber spliced with a fiber with GeO_2 core was used for the reproducibility of aperture size. The fiber was sharpened by chemical etching, resulting in the fabrication of an aperture of nanometric size, thus increasing the power density the fiber tip to about 1 kW/m^2. We have fabricated nanostructures by keeping a sample-fiber tip separation distance of about 10 nm, a distance that was controlled by shear force technology. The schematic diagram of the experimental deposition setup is shown in Fig. 1.

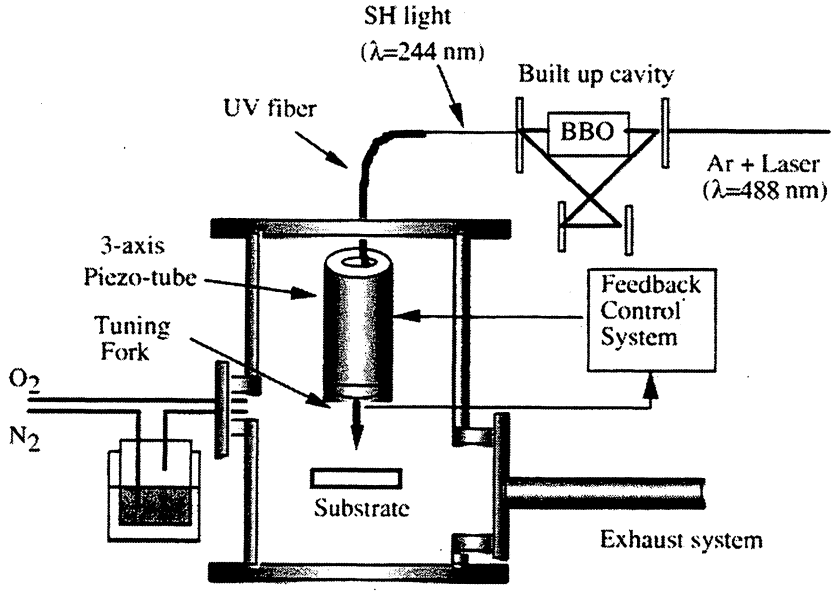

Fig. 1. Schematic diagram of the experimental setup.

3. RESULTS AND DISCUSSION

3.1 Characteristics of ZnO film deposited by PE-MOCVD

The photodeposition of ZnO was carried out for 10 min within a range of the substrate temperatures from room temperature to 300 °C. The photo-irradiation effect on the deposition rate was clearly observed for all substrates. The thicknesses of films were 150 nm, 170nm and 140 nm for the substrate temperatures of 150 °C, 200 °C and 300 °C, respectively. Figure 2 represents X-ray diffraction patterns that were obtained for ZnO films deposited by PE-MOCVD at different substrate temperatures. The increase of substrate surface temperature caused by UV light irradiation is negligible because the light power density on the substrate is as low as 0.2 mW/cm^2, which means that the deposition resulted from

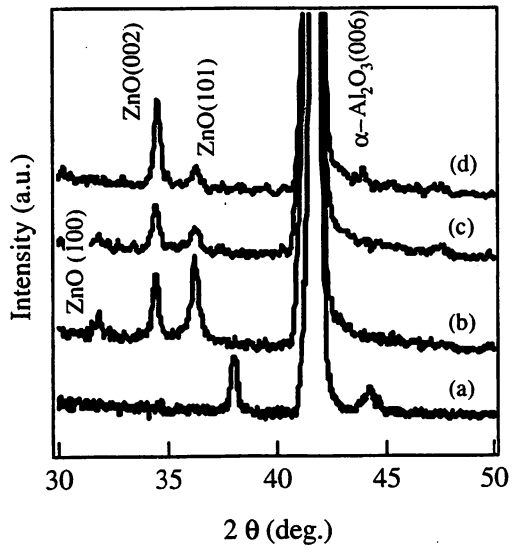

Fig. 2. X-ray diffraction patterns of ZnO films grown at the substrate temperatures of (a) 100 °C, (b) 150 °C, (c) 200 °C, and (d) 300 °C.

photo-chemical reaction between DEZ and oxygen. The film deposited at room temperature was found to be essentially amorphous, with no sharp XRD reflection lines. Crystalline films could be grown at substrate temperatures over 100 °C. C-axis oriented films exhibiting the (002) XRD lines were grown at substrate temperatures above 150 °C. With the temperature increase, a strong X-ray peak from (002) planes appears while other peaks such as the (101) peak become weak. Since it is well known that the (001) direction in ZnO has the lowest surface energy, and therefore equilibrium growth conditions lead to a (001) orientation, the higher the deposition temperature, the stronger the intensity from (002) planes. The c-axis lattice constant, estimated from the peak position of the (002) line was 0.5207 nm, to be comparable with the c-axis lattice value of 0.52066 nm recorded for ZnO powder [13], which indicates that these films have a high-quality crystalline structure. The stoichiometry of the films was further confirmed from the XPS spectrum, as shown in Fig. 3. This figure shows XPS spectrum of a ZnO film deposited at 200 °C. It showed that the O 1s peak is actually composed of only a single

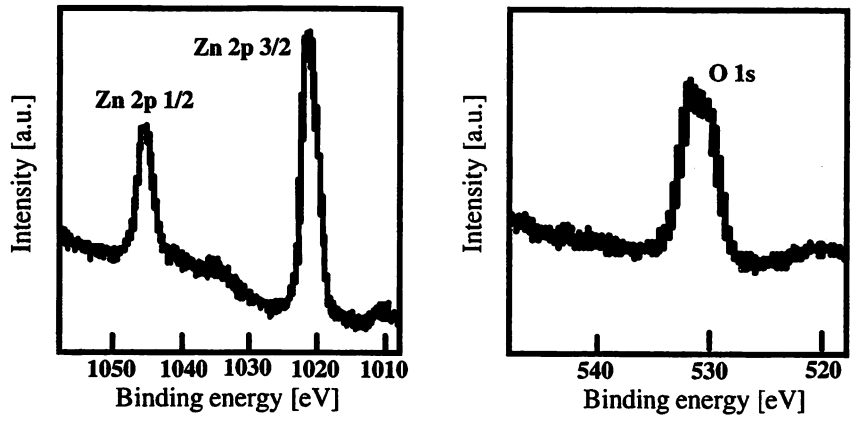

Fig. 3. XPS spectra of ZnO films deposited at the substrate temperature of 200 °C. The atomic ratio Zn:O was determined to be 1.0:1.03.

component at 531.8 eV binding energy. The displayed XPS spectra were charge-corrected to the adventitious C 1s peak at 284.1 eV binding energy. The O 1s component is attributed to O-Zn bonds. The Zn 2p 3/2 and 1/2 peaks appear with the center at 1022 eV and 1045 eV, respectively, which are similar to the values of the bulk crystal. The atomic ratio of Zn:O was determined to be 1.0:1.03 within the accuracy of XPS. For the films deposited at the substrate temperature higher than 150 °C, the atomic ratios of Zn:O were 1.0:1.0 within the accuracy of a few percent. The optical transmittance of the films was also investigated. Figure 4 shows the optical transmittance spectra for ZnO films deposited at substrate temperatures from 100 °C to 300 °C. Transmittance fell off steeply at around 380 nm, which is an intrinsic characteristic of high-quality ZnO films[14), 15)]. From the plot of the absorption coefficient versus wavelength in the region of high optical absorption, an optical band gap energy ranging from 3.26 to 3.31eV was estimated, which is identical to the value recorded for high-quality ZnO films[9), 10), 16)].

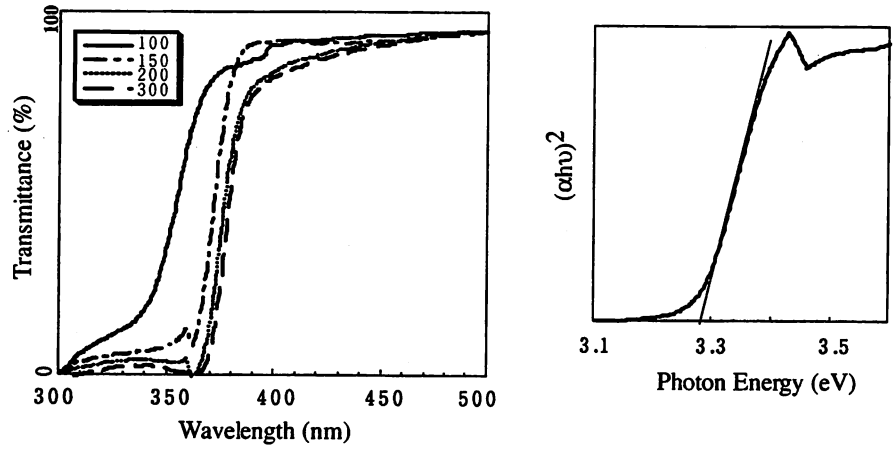

Fig.4. (Left); Transmittance spectra of ZnO films measured at room temperature. (Right); the band gap (Eg) obtained by plotting $(\alpha h\upsilon)^2$ vs. $h\upsilon$, where α is the absorption coefficient and $h\upsilon$ is the photon energy (for a film grown at the temperature of 200°C).

By these evaluations, we have finally confirmed that high quality ZnO films in terms of crystallinity and optical properties have been obtained at substrate temperatures above 150 °C. The films represented strong (002) XRD reflection lines and had the atomic ratio of Zn:O of 1.0:1.0. The optical band gaps were evaluated in the range of 3.26-3.31eV, which is a proof of very high-quality ZnO thin film.

3.2 Fabrication of nanometric scale ZnO dot

The fabrication of nanometric scale ZnO dot was performed by introducing the ultraviolet light source onto the surface through an optical fiber using the previously mentioned conditions. The fiber probe tip was prepared by a two-step etching process [17]. When the shear force technique is employed to control the sample - probe separation, the cladding diameter is one of the important parameters governing the resonance frequency of a dithering probe. Therefore the cladding diameter must be reduced effectively for the precise control of the sample-probe distance. Figure 5(a) shows a schematic diagram of the fabrication method. During the first step the cladding diameter was reduced by immersing in BHF with a volume ratio of [40wt.%NH_4F aqueous solution]:[50wt.%HF acid]:[deionized water]=1.7:1:1. And in the next step, the fiber was selectively etched in the same kind of solution with a volume ratio of 10:1:1, while the temperature was kept at 25 °C to obtain single-tapered apertured probe. After completing the etching process, the probe was coated with 200 nm thick Al by vacuum evaporation. In order to form an aperture, the Al film was removed from the tip of the probe by FIB. Figure 5(b) shows SEM micrograph of a fabricated probe with an aperture of 60 nm. The second harmonic light from an Ar^+ laser, with a maximum optical power of 10 mW and a spot size of 3 mm^2, was coupled into the UV optical fiber. The light power density

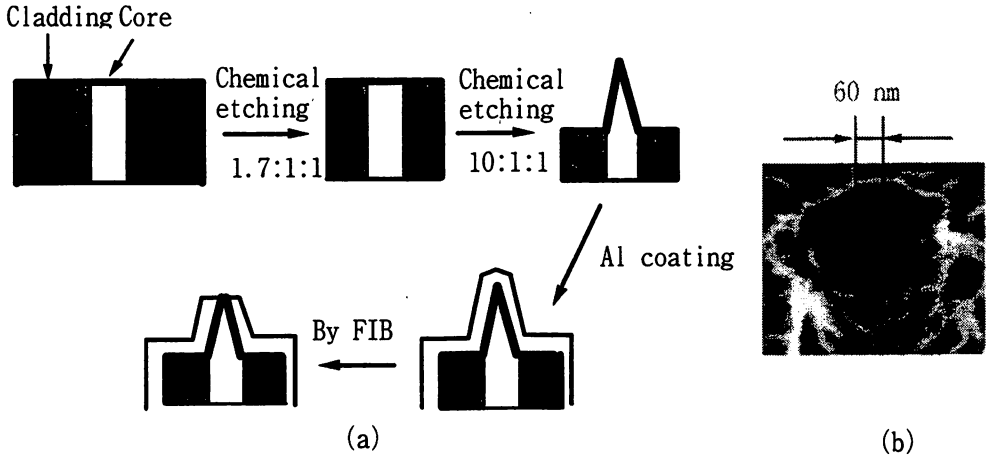

Fig. 5. (a) Fabrication method of a fiber probe, (b) SEM micrograph of the tip region of the fabricated fiber probe. The thickness of the Al film and the aperture size are 150nm and 60nm, respectively.

shining the substrate was estimated to be of the order of several kW/cm^2. An experiment was carried out using (001) Al_2O_3 substrates. Figure 6 shows the nanometric scale ZnO dot fabricated at room temperature. During this experiment the total

reactor pressure was kept at 10 mTorr and the ratio of DEZ : O_2 was 1:10. The dot was 5 nm high and 200 nm wide (including broadening due to the resolution of shear-force microscopy). The width of the dot is smaller than the wavelength

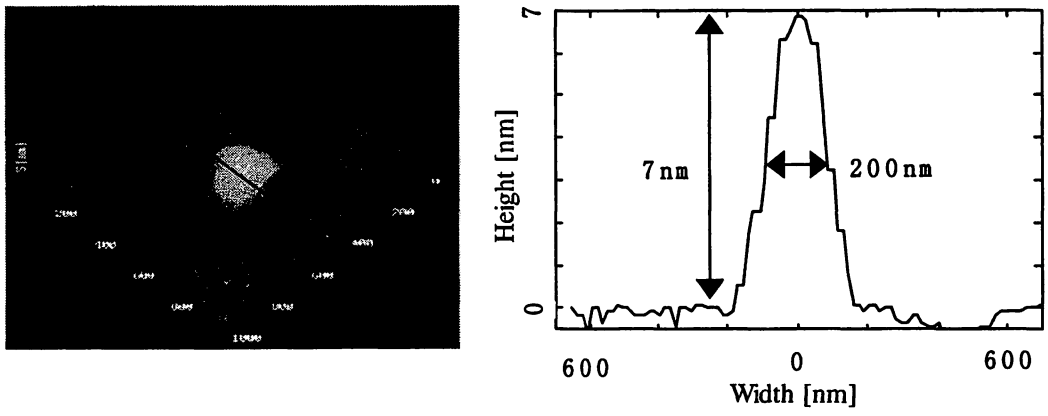

Fig. 6. Shear-force topographic image of ZnO dot fabricated by introducing UV light through an optical fiber onto the (001) Al_2O_3 substrate.

of the irradiating light source (λ=244 nm). A glance at the result is sufficient to explain that the size and position of the structure can also be controlled. In particular, the result on ZnO reveals that we can actualized the fabrication of ZnO nanostructures emitting the light even at room temperature with fabricating under the proper growth condition.

4. SUMMARY

High-quality ZnO films were fabricated using PE-MOCVD method combined with near-field optical technology, where DEZ and O_2 as reactant gases. It was found that UV light irradiation during the growth is very effective in the enhancement of the deposition rate. Under suitable film growth conditions, the formation of ZnO nanodots has been achieved using an optical near-field generated from the sub-micron scale aperture of an optical fiber tip, through which an UV light source was introduced onto the substrate. The dot diameter was smaller than the wavelength of the light source used. It suggests that near field optics offer the opportunity to modify surfaces and develop new nanostructures that may exhibit quantum effect due to their extremely small size.

5. REFERENCES

(1) M. Ohtsu, Near-Field Nano/Atom Optics and Technology, Springer, Tokyo, 1998.

(2) M. Ohtsu, "Progress of High-Resolution Photon Scanning Tunneling Microscopy Due to a Nanometric Fiber Probe", J. Lightwave Tech. 13, pp 1200-1221, 1995.

(3) E. Maayan, O. Kreinin, G. Bahir, J. Salzman, A. Eyal and R. Beserman, "Selective growth of GaAs/ InGaP

heterostructures by photo-enhanced organometallic chemical vapor deposition", J. Crystal Growth 135, pp 23-30, 1994.

(4) D. Bauerle, "Laser-chemical processing: recent developments", Appl. Surf. Sci. 106, pp 1-10, 1996.

(5) D. J. Ehrlich, R. M. Osgood, Jr. , and T. F. Deutsch, "Spatially delineated growth of metal films via photochemical prenucleation", Appl. Phys. Lett 38, pp 946-948, 1981.

(6) R. Wiesendanger, "Fabrication of nanometer structures using STM", Appl. Surf. Sci. 54, pp 271-277, 1992.

(7) V. Polonski, Y. Yoh, M. Kourogi, and M. Ohtsu, "Nanometric patterning of zinc by optical near field photochemicalvapor deposition", J. Microscopy 194, 1999 (in press).

(8) Y. Yamamoto, V. Polonski, G. H. Lee, M. Kourogi, M. Ohtsu, "Photochemical vapor deposition by optical near field", SPIE's 44th Annual Meeting, 3791-18, 1999.

(9) Z. T. Tang, G. K. L. Wong, and P. Yu, "Room-temperature ultraviolet laser emission from self-assembled ZnO microcrystallite thin films", Appl. Phys. Lett. 72, pp 3270-3272, 1998.

(10) D. B. Bagnall, Y. F. Chen, Z. Zhu, and T. Yao, " Optically pumped lasing of ZnO at room temperature", Appl. Phys. Lett. 70, pp 2230-2232, 1997.

(11) H. Cao, J. Y. Wu, H. C. Ong, J. Y. Dai, and R. P. H. Chang, "Second harmonic generation in laser ablated zinc oxide thin films", Appl. Phys. Lett. 73, pp 572-574, 1998.

(12) O. Madelung, Landolt-Bornstein New Series , Springer, Berlin, 1982, Vol. 17b.

(13) S. Mononobe, "Fabrication of a triple tapered probe for near-field optical spectroscopy in UV region based on selective etching of a multistep index fiber", Optics Communication 146, pp 45-48, 1998.

(14) V. Craciun, J. Elders, J. G. E. Gardeniers, and Ian W. Boyd, "Characteristics of high quality ZnO thin films deposited by pulsed laser deposition", Appl. Phys. Lett. 65, pp 2963-2965, 1994.

(15) D. H. Zhang, R. W. Gao, and H. L. Ma, "Burstein shift and UV photoresponse in IBAD-deposited transparent conducting ZnO films", Thin Solid Films 293, pp 83-869, 1995.

(16) T. Y. Ma, G. C. Park, and K. W. Kim, "Substrate Temperature Dependence of ZnO films Prepaired by Ultrasonic Spray Pyrolysis", Jap. J. Appl. Phys. 35, pp 6208-6211, 1996.

(17) T. Pangaribun, K. Yamada, S. Jiang, H. Ohsawa, and M. Ohtsu," Reproducible fabrication technique of nanometric tip diameter fiber probe for photon scanning microscope" Jpn. J. Appl. Phys. 31, L1302, 1992.

[III] REVIEW PAPERS

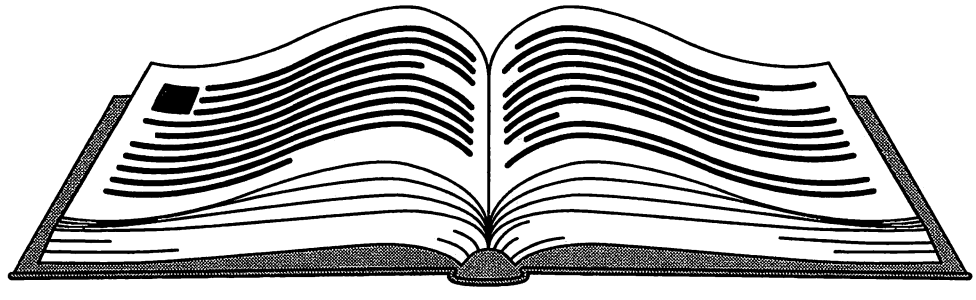

巻頭言

向かい風の中に立つ?

大津元一*

本号の特集で扱う光技術では光を利用し，さらにそのために新しい光や物質を作る．この分野では1960年のレーザー発明以降，日本の技術者のレベルの高さに支えられ日本が先導する技術（ファイバー，半導体レーザーなど）が成長したのは周知のとおりである．

社会はこの技術の順調な進歩を信じ，ますます多くの要求をつきつけており，厳しい事態が21世紀初頭には生まれそうだ．例えば2010年には光メモリーについてはDVDの100倍程度の大容量化が必要と予想されており，これは原理的に従来の光技術の能力を越えている．このことは光技術の原理に関する新しいアイディアを生み出す必要があること，光技術のパラダイムシフトが必要であることを意味している．

今までの光技術の進歩を顧みると，日本が先導したといってもそれはあくまでも技術的内容が主であって，原理は欧米で生まれている．しかし幸か不幸か今回実現すべきパラダイムシフトは原理と技術の両方が足並みをそろえて改革されないと実現しないような高度なものである．従来の光技術でもこの足並みのそろいは必要であったが，今回はそれが必須である．しかしそうであるならば，技術に強いわが国が原理も含めたパラダイムシフトの騎手となる可能性を秘める．

科学は西洋貴族の趣味，暇つぶしから発展したといわれており，したがって人まねや二番煎じが入り込む余地はなかった．この原点に立ち返れば新しいアイディアを得ることができよう．ただし現代では社会への貢献も求められるので，これが周りから吹いてくる強い向かい風となる．一番手の研究者・技術者はその向かい風の中に立ち，耐えることを余儀なくされ，体力を非常に消耗する．欧米で発した話題を日本で最初に着手することに意義を感じる人たちは一番手の後ろで風をよけている二番手であり，体力の消耗はきわめて少なく，しかしそれゆえに新アイディアを生み出す知的刺激も受けない．状況分析能力の高い人はきたるべき追い風の強さをいち早く認識でき，それを回避するので，これは何番手かという議論からはずれる．

一方，欧米の研究成果や論文の安易な崇拝は研究者・技術者が自ずから向かい風を発することになる．

最近では各省庁での大型プロジェクト研究が多数行われているが，欧米に対して追いつけ追い越せ型の育成支援，予算の悪平等配分などは再考を要する．さらに，プロジェクト遂行の段階で硬直な運用体制をとると厭世観さえ生まれる．このような状況は研究者・技術者のぜい肉を増やすのみであり，体力増強にはならない．したがって向かい風の中ではやがて自身の体重のために倒れる．

以上のように考えると，将来の光技術に関し尊重すべきことは農耕民族としての日本人の長所に裏打ちされた新アイディアの出現，排除すべきは日本の村社会的な慣習からくる弊害であり，結局はわれら日本人の長所，欠点を認識することが大事であろうという月並みな結論に落ちついてしまう．

*東京工業大学・大学院総合理工学研究科

近接場光技術とその展開*

大津元一**

Near-field Optical Technology and Its Overlook / Motoichi OHTSU

Key words: probe, fiber, microscope, nano-fabrication, optical memory

1. まえがき

近接場光とはエネルギーの集中する空間的寸法がナノメートル程度の小さな光である．それは光源からの光が三次元的形状を持った微粒子（その寸法は光源からの光の波長に比べてずっと小さい）に照射されたとき，微粒子中に誘起された電気双極子から発生する第二次電磁場のうちの非伝搬成分であり，微粒子と同程度の空間的広がりを有する局所的電磁場である．近接場光を用いることにより回折限界を越えて波長非依存の光科学技術が実現したが，これは従来の伝搬光や二次元的形状を持った物質平面および一次元的形状をもった線状物質表面に発生するエバネッセント光では到底達成しなかったものである[1)~3)]．本稿では近接場光にかかわる歴史と現状，将来展望について概説する．

2. 歴史と現状

近接場光は非伝搬なので，それを検出するためにはプローブにより試料との間の近距離電磁相互作用を誘起して近接場光を散乱すること，すなわち微粒子内に誘起された電気双極子を再配列することが不可欠であり，これは局所電磁場の破壊を意味する．したがって試料とプローブ間の近距離電磁相互作用が強まれば試料自身の形状や構造さえも変化する．このことは近接場光の本質的応用分野が物質の加工や操作であることを意味する．なお，近接場光を顕微鏡という計測に応用する提案は1928年にさかのぼるが[4)]，それは光学の枠組みの中にとどまっており，加工の可能性を示唆するものではなく，かつ近接場光の本質的特性について言及するものでは決してなかった．さらに半世紀の空白期の後に1980年代に入って始まった近接場光の研究開発の方向も長い間顕微鏡技術，走査プローブ顕微鏡技術の枠組みの中にとどめ置かれた．現に欧米ではいまだに有機化学，バイオなどの試料を計測するための応用としての限定された小さな研究分野にとどまっている観がある．

しかし幸いなことに日本では1980年代初頭に世界の数研究機関と同時期かつ独立に開始された研究開発の開拓期においてすでに加工の重要性に着目し，まずファイバ技術に支えられたプローブ加工技術において勝利をおさめ，それを当面顕微鏡に応用して優越性を実証した．この優れたプローブ技術はその後，分光分析，記録，加工，さらには原子操作へと体系的につながり，光学の枠組みを越えた新理論も構築されている[5)]．このような体系的発展，さらに開拓期から現在に至る継続的発展は欧米ではみられない．以上で述べた近接場光の研究開発に関する歴史を概観すると**表1**のようになる[6)]．以下ではこのような歴史的進展を経た研究開発の現状を概説する．

2.1 プローブ技術

プローブは少なくとも次の2つの性能を兼備しなければならない．すなわち，(I) 微小な近接場光を扱うのでその先端が小さいこと，(II) 微小な近接場光と伝搬光との間の変換を担うインタフェース機能を有すること，である．特に (II) は (I) に比べ注目されていないが近接場光の発生と検出の効率を左右する重要なものであり，これこそが近接場光を観測者が認識し，科学の対象，技術の手段とするために根本的なものである．現在使われているプローブはこの2つの性能を向上させるように開発され，次の3種

* 原稿受付 平成12年2月24日

** 東京工業大学大学院総合理工学研究科（横浜市緑区長津田町4259）
1978年東京工業大学大学院理工学研究科博士課程電子物理工学専攻修了．工学博士．同年同大学助手，1982年同助教授，1991年同教授，現在に至る．研究分野：ナノフォトニクス，著書：Near-Field Nano-Optics，ほか

表1　近接場光技術の研究開発の歴史的経緯（文献6）中の表4.1.1を著者が要約した）

分　類	年　代	トピックス
提案期	1928年	・微小開口により発生する光を用いた高分解能顕微鏡の提案
シミュレーション期	1970年代	・マイクロ波を用いた実験
開拓期	1980～1983年	・IBMチューリッヒ研究所（スイス），コーネル大学（米国），マックスプランク研究所（独），東工大（日）で独立に実験開始，特許取得 ・初期の特許競争 ・欧米では微小開口，毛細ガラス管，加熱引張法によるファイバ等をプローブとして使用 ・日本では選択エッチングによるファイバをプローブとして使用
移動期	1980年代中期	・上記欧米の若手研究者が大学やベル研究所（米）等に移動し，特に米国で研究推進（分解能は低いが各種特許取得．研究機関間での特許抗争） ・欧米でのプローブ開発技術の停滞．日本でのプローブ性能の進展（光エレクトロニクス，ファイバ技術の支援を受ける．） ・欧米では顕微鏡として有機化学，バイオ分野が進展 ・ベル研究所（米），東工大（日）による光メモリの原理実験
成長期	1980年代後期～1990年代初期	・研究人口の増加 ・米国の民間研究機関での応用志向研究方針によりベル研究所等で研究グループの消滅 ・日本では光エレクトロニクス分野への応用が進展し，かつ量子光学分野の実験と理論が出現
発展期	1990年中期～	・欧米でのプローブ製作関連のナノテクノロジーの出遅れによる技術の沈滞．擬似近接場光技術としてはSIL技術のみ．しかし，2000年に入り，米国政府のナノテクノロジー技術重点化始まる ・日本では近接場光技術を光関連ナノテクノロジーととらえて研究開発が進展．特に産業界では光メモリ応用に興味集中

類に大別される．

(1) ファイバプローブ：先鋭化したファイバコアの先端寸法に依存する空間的広がりを有する近接場光を発生または検出する．その製作法に関し，日本で発明された選択エッチング法はその性能の高さ，製作の再現性・量産性の高さ故に加熱引張法などの他方法を圧倒した[7]．光検出器へ到達する信号光が近接場光を介したプローブ先端と試料との間の近距離電磁相互作用に起因するものだけであることを保証するには光源からの伝搬光が直接光検出器に達するのを防がなくてはならないが，このために不透明な金属膜を先鋭化コアの根本に塗布する．なお，このファイバプローブは開口付きプローブと呼ばれる場合があるが，この呼称は不適当である．なぜなら分解能の観点から注意すると，分解能を決めているのはファイバコア先端直径であり，塗布された金属膜の開口部の働きは上記のように伝搬光を遮断することだからである．

選択エッチング法の高精度性と高再現性により先端曲率半径1 nm程度のものが作製され，上記(I)の性能が実現している[8]．一方，ファイバの伝搬モード解析をもとに，テーパ部の形状を2段階[9]や3段階[10]として上記(II)の性能を高め，近接場光の発生および検出効率が10%にも達するファイバプローブが実現している．近赤外，可視域のみでなく紫外域での使用も可能となった[11]．さらに先端に色素分子を付着させた発光型[12]，金属微粒子を塗布したプラズモン共鳴型[13]などが開発されている．これらのファイバプローブにより計測，分光分析，加工の実験が急速に進歩し，さらには光記録再生の基礎データの取得[14]，原子操作の基礎実験[15]などに結びついた．

(2) 金属プローブ：走査型トンネル顕微鏡（STM）のプローブなどを流用したものであり，(1)のプローブ加工技術の配備不可能な場合に便宜的に使われる．金属は光に対する散乱効率が高いので近接場光の検出効率を稼ぐことができる[16]．開口なしプローブなどとも呼ばれている．その名のとおり，(1)でも述べたような，光検出器へ到達する信号光が近接場光を介したプローブ先端と試料との間の近距離電磁相互作用に起因するものだけであることを保証するための機能を持たない．このことはキャリアの拡散の影響を受けない分光分析，堆積加工，原子操作，さらには光記録再生のための高速走査への適用を不可能にしている．

(3) 集積型プローブ：原子間力顕微鏡（AFM）のカンチレバーを基本型とし，これに光導波路や光検出器等を同時に作りつけるものであるが[17]，現在のところ微細加工技術の応用例として試作されているのみで，これらの大半はいまだに近接場光の空間的特性に基づいた設計が行われていない．しかしながらAFM技術とは独立に上記(1)のモード解析による設計に基づいたピラミッド型プローブアレイがシリコン平面加工プロセスにより開発された．これは光記録再生用で，近接場光発生効率は10%に達している[18]．

2.2　形状計測

近接場光学顕微鏡と呼ばれる形状計測への応用である．バイオ試料が最も興味のある計測対象とされているが，この試料には必ずしも近接場光が十分に利用されているわけではなく，今のところ平面表面上のエバネッセント光によ

る照明などの方が多く使われている．プローブ性能の向上による測定時定数の短縮などを図る必要がある．しかしながらすでにファイバプローブによる水中での計測[19)20)]，AFMなどの補助手段は使わず幅4 nmのDNA単一分子画像取得などの高分解能計測が実現している[21)]．さらには現状でのプローブ走査の低速性の問題を解決するために，測定部位でプローブを固定し，プローブで時系列信号を高速検出する方法が試みられている[22)]．有機・無機化学の分野ではユーザとしてのみ近接場光技術を使っており，近接場光技術自身を進展させる動きはあまりない．しかしながら2.1節(1)に示すようにプローブ先端に色素分子を固定し，オプトード（optode）と呼ばれる化学センサの微小化，高速応答性の追求が試みられている[12)]．

なお，多くの研究機関ではいまだに高分解能プローブ技術の配備が不可能なため，形状測定は分解能の高いAFMやSTMなどに任せ，近接場光学顕微鏡の分解能を高くすることを後回しにしている場合が多いが，これは今後の進展を考えると不利である．言うまでもなく近接場光技術のすべての成果はプローブの性能によって律則されるからである．

2.3 分光分析

ドナー分子からアクセプター分子へのエネルギー移乗という古くからある研究課題[23)]にかかわる実験の延長上で，単一色素分子からの蛍光の測定が欧米を中心に活発に行われているが[24)]，これは微弱光を扱うため分解能を犠牲にせざるを得ないのが現状である．ただしこの場合に測定している蛍光は伝搬光の球面波なので分解能が低くても測定可能なので，平面表面上のエバネッセント光を利用するなどすれば既存の光技術でも測定でき，時間分解分光も可能である[25)]．一方，凝縮系試料である半導体の量子井戸，量子ワイヤのフォトルミネッセンス分光では試料形状が二次元的，または一次元的に広がっているため簡単なプローブにより低分解能測定が可能であったが[26)]，量子ドットのような三次元的微粒子からのフォトルミネッセンスでは高分解能・高感度の測定が不可欠である．特にキャリアの拡散による分解能低下を防ぐことが必須で，2.1節(1)のプローブによってのみ実現している．現在までに極低温でのフォトルミネッセンス分光により均一広がりスペクトルの評価や励起子のエネルギー状態の同定が実現し[27)]，さらに室温における測定[28)]，時間分解分光[29)]へと展開している．

さらには紫外域での量子ワイヤのフォトルミネッセンス分光[30)]，半導体材料のエレクトロルミネッセンスや光励起電流分光[31)]，有機・無機材料のラマン分光[32)]などが行われ，最近では日本の産業界から世界初の分光分析装置の市販化に至っている．

2.4 加　工

冒頭にも記したように近接場光の検出過程が局所電磁場の破壊である以上，ナノメートル寸法の加工が近接場光の本来の応用分野である．形状計測への応用は破壊の弱極限近似に基づいているのにすぎない．近接場光によるナノ加工としては既存の半導体デバイス製作のための微細加工への応用が考えられるが，これは必ずしも広く普及しないと思われる．なぜなら既存の半導体デバイスの微細加工に用いられている短波長光，X線，電子ビーム法のもつ問題点（設備投資，特殊環境下での動作）などを補うほどの長所をもっていないからである（たとえば作業速度，一括処理性など）．今後は一括露光可能なスタンプ光リソグラフィなどの方法により[33)]，長所が伸長することを期待したい．

上記の不都合は既存の技術の枠組みの中で使われているデバイスを新技術である近接場光により加工しようとすることに起因する．必要なことはまず近接場光を使って動作する新概念に基づいた高機能デバイス（電子デバイス，光デバイスを問わず）を考案することである．この新デバイスの製作は既存の加工技術では不可能で，近接場光による加工が必須だからである．このような新デバイスの例は超高密度光ディスクメモリとナノ寸法光集積回路であり，これらについては2.5節，2.6節に示すが，本節では以上の事情に注意しながら加工に関する現状を概観する．

(1) 既存のデバイスの製作にかかわる加工：ファイバプローブを用いてリソグラフィ用フォトレジストへの露光が行われ，数十nmの幅のパターンが描画されている[34)35)]．ただし，最終的な加工精度はこの後のエッチング，ドーピング，成膜の各プロセスに左右される．短パルス光を用いてアブレーションが行われている[36)]．ただし，その分解能は既存のレーザアブレーションのそれと大差ない．使用しているプローブの性能が低いためである．

(2) 近接場光で動作する新デバイスの製作にかかわる加工：2.6節で概説するように半導体量子ドットなどの微粒子表面に近接場光を発生させ，それを情報キャリアとして信号伝達する光トンネルデバイス，そのための発光，スイッチング，受光デバイスが提案されている[37)38)]．その製作には金属，誘電体，半導体などの異種材料を共通の半導体基板の上の希望する位置に，希望する寸法で作りつけなければならない．量子サイズ効果を援用するにはその寸法は30 nm以内，加工精度は数nm以内の必要がある．これには既存の量子ドット製作に用いられている自己組織化法などは無力である．また上記のリソグラフィはあらかじめ堆積した物質を周囲から削り取る多段階プロセスなので作業効率が低い．これらの問題を解決する方法として，紫外域の近接場光を用いた光化学気相堆積が行われている．すでに亜鉛金属の幅20 nmの曲線[39)]，ドット[40)]などが形成され，さらに青色発光を示す酸化亜鉛などが堆積されている[41)]．使用する有機金属気体とそれを光解離するのに十分に高いフォトンエネルギーを有する光源の組合せにより，亜鉛のほかにアルミニウムなどの金属，絶縁体，さら

には化合物半導体の堆積が可能とされている．このほか走査プローブ顕微鏡による陽極酸化法と組み合わせて酸化チタンを形成する方法[42]なども試みられている．

2.5 光記録再生

2010年の光技術の動向の予測調査により，光ディスクメモリに関し，記録密度1 Tb/in^2，再生速度100 Mb/s以上の性能が必要であることが指摘されている[43]．これらは回折限界のために既存の光ディスクメモリ技術では達成不可能な値である．これを達成するために近接場光による実現が検討されている．近接場光技術の応用に関して日本の産業界が最も興味を持っているのはこの光記録再生であり，この点において欧米の近接場光研究開発動向とは方向が大きく異なっている．上記のような超高密度記録・超高速再生能力を有する光メモリに対する製作者，使用者のとらえ方の発想変換が要求されているが，このようななかですでに記録再生ヘッドのデバイス，記録媒体，メカトロニクス，ソフトウェア，標準化などの各課題を有機的に関連付けた技術開発方針が詳細に検討され，産業的戦略とともに技術開発の段階に入っている．もはや学会レベルでの議論や研究開発の域を脱して実用化のための開発段階に入った様相を呈しているが，この現状では今後これらの戦略から外れる技術は，それが独創的であったとしても採用されない可能性が出てくる．

なお，近接場光の多くの応用のなかで，光記録再生は近接場光により動作するデバイスを近接場光で加工しようとする典型例である．すなわち2.4節中の分類(2)に属する．Super-RENS (Super-resolution near-field structure)と呼ばれ，記録媒体上に作りつけた非線形光学薄膜に伝搬光を照射したときに自己形成される微小開口により近接場光記録再生する方式[44]，シリコン基板加工によるピラミッド突起状二次元アレイ[18]，などによる記録再生が行われ，さらには面発光レーザを用いた記録再生ヘッドの開発[45]など，点接触型から平面積層型へ脱却した近接場光技術が進展している．これらの方法はすでに光学の枠組みから脱却したアイデアに基づいた，日本で生まれた独創的な技術であるが，米国で提案された固侵レンズ (Solid immersion lens：SIL)[46]のように光学の枠組みのなかにとどまり回折限界に律則された方法に比べ，性能および将来の発展性の点で優れている．

2.6 ナノ寸法光集積回路

既存の光集積回路は主に光通信システムの送信，受信端で用いられ，半導体レーザ，光導波路，光変調器などから構成される．これらは回折限界の枠組みのなかで動作するので，電子デバイスである半導体集積回路の寸法に比べ巨大であり，したがって光電混成集積回路の技術は成熟していない．また，2010年に光通信システムに要求される光交換の速度5 Tb/sを達成するための光マトリクススイッチの集積化（既存のデバイス基板に100×100の光スイッチングデバイスを集積化することが必要[47]．これは各光スイッチングデバイス寸法を30～50 nmまで微小化する必要があることを意味する．）を実現することもできない．このようなナノ寸法の微小な光デバイスとその集積化のために単一量子ドットによる発光デバイスの提案[37)38]，スイッチング機能の検証実験[48]，さらには2.4節で述べたように，これらのデバイスを製作するための光化学気相堆積法の開発が進んでいる．

このようなナノ寸法の光デバイスに至る前段階での試みも行われている．それは半導体量子井戸のなかの励起子によるポラリトン波動を利用して寸法の光導波路を作り，干渉型の光スイッチを構成する方法[49]，金属細線を光導波路として利用する方法[50]などである．これらの方法は媒質の屈折率を高め，そのなかの伝搬光の波長を短くしてデバイスの小型化を図る方法なので，依然として回折限界の枠組みのなかの技術であるが，ナノ光集積回路と外部回路との入出力インタフェースとしての利用可能性を有する．

3. 将来展望

近接場光技術が回折限界の壁を越える手法であることは周知の事実である．ただし国内外の機関から発表されるデータの空間的分解能はまだ必ずしも高くはなく，波長の1/10程度にとどまっているものも多く見られ，またAFMなどを併用したものである場合が多い．さらに近接場光に本質的な三次元形状微粒子を扱っておらず，平面表面や線状物質上のエバネッセント光を扱っているにすぎないものが多い．これらは近接場光技術にとって本質的なプローブ関連デバイスの作製にかかわるナノ加工の開発がまだ未成熟であり，今後の発展にはこれを成熟させるのが必須であることを意味している．

しかし一方では2010年に向けたロードマップに連携して技術開発が進んでおり，ようやく形状計測への応用という回り道を経て近接場光技術本来の使われ方が始まった感がある．本稿では近接場光による原子の操作と堆積の試み[51]については割愛したが，今後ナノ加工にとどまらず，原子寸法加工への展開の可能性も持っている．このように近接場光技術は従来の光技術では不可能だった微小化，ひいては大容量の情報を扱う新技術を実現しつつあり，そのカバーする領域はきわめて広範にわたると考えられる．

4. まとめ

近接場光に関連する技術動向について概観したが，ここで注意すべきはこの技術を使いこなすには光技術のパラダイムシフトを実現することが必要であるという問題を提起している点である．この実現のためには素粒子物理学などの関連分野とも融合し（なぜなら試料とプローブとの間の

近距離電磁相互作用を媒介する近接場光は，原子核の中で陽子と中性子の間の近距離相互作用を媒介する中間子と類似だからである[52]，「近接場光の学」[53]を発展させ，その技術を産業界で大成させて，社会の要求にこたえる必要がある．

現在のところ日本の研究成果がリードしていることは喜ばしい限りであるが，その優越性，先進性は今後どのくらい長く続くかは予断を許さない．今後もリードを保つにはここまで育ってきた近接場光の技術を短期間のうちに成熟させるための集中的努力を払う以外にない．

参 考 文 献

1) 大津元一：ナノ・フォトニクス，米田出版，東京，(1999).
2) M. Ohtsu：Near-Field Nano/Atom Optics and Technology, Springer-Verlag, Tokyo/Berlin/New York, (1998).
3) M. Ohtsu and H. Hori：Near-Field Nano-Optics, Kluwer Academic/Plenum Publishers, New York, N. Y., (1999).
4) E. A. Synge：A Suggested Method for Extending Microscopic Resolution into the Ultra-Microscopic Region, Phil. Mag., **6**, (1928) 356.
5) K. Kobayashi and M. Ohtsu：Quantum Theoretical Approach to a Near-Field Optical System, J. Microscopy, **194**, 2/3, (1999) 249.
6) (財)光産業技術振興協会編：極限光インフォニクス技術に関する調査研究報告書，(財)光産業技術振興協会，東京，(2000) 129.
7) T. Pangaribuan, K. Yamada, S. Jiang, H. Ohsawa and M. Ohtsu：Reproducible Fabrication Technique of Nanometric Tip Diameter Fiber Probe for Photon Scanning Tunneling Microscope, Jpn. J. Appl. Phys., **31**, 9 A, (1992) L 1302.
8) S. Mononobe and M. Ohtsu：Fabrication of a Pencil-shaped Fiber Probe for Near-Field Optics by Selective Chemical Etching, J. Lightwave Technol., **14**, 10, (1996) 2231.
9) T. Saiki, S. Mononobe, M. Ohtsu, N. Saito and J. Kusano：Tailoring a High-Transmission Fiber Probe for Photon Scanning Tunneling Microscopy, Appl. Phys. Lett., **68**, 19, (1996) 2612.
10) T. Yatsui, M. Kourogi and M. Ohtsu：Increasing Throughput of a Near-Field Optical Fiber Probe over 1 000 Times by the Use of a Triple-tapered Structure, Appl. Phys. Lett., **73**, 15, (1998) 2090.
11) S. Mononobe, T. Saiki, T. Suzuki, S. Koshinara and M. Ohtsu：Fabrication of a Triple Tapered Probe for Near-Field Optical Spectroscopy in UV Region Based on Selective Etching of a Multistep Index Fiber, Opt. Commun., **146**, 1/6, (1998) 45.
12) K. Kurihara, M. Ohtsu, T. Yoshida, T. Abe, H. Hisamoto and K. Suzuki：Micrometer-Sized Ion-Selective Optodes Based on a "Tailed" Neutral Ionophore, Anal. Chem., **71**, 16, (1999) 3558.
13) M. Matsumoto, T. Ichimura, T. Yatsui, M. Kourogi, T. Saiki and M. Ohtsu：Fabrication of a Near-Field Optical Fiber Probe with a Nanometric Metallized Protrusions, Opt. Rev., **5**, 6, (1998) 369.
14) S. Jiang, J. Ichihashi, H. Monobe, M. Fujihira and M. Ohtsu：Highly Localized Photochemical Processes in LB Films of Photochromic Material by Using a Photon Scanning Tunneling Microscope, Opt. Commun., **106**, 4/6, (1994) 173.
15) H. Ito, A. Takamizawa, H. Tanioka and M. Ohtsu：Precise Control of Atoms with Optical Near-fields: Deflection and Trap, Proc. SPIE Conf. Near-Field Optics, Denver, Colorado, July 1999, SPIE Vol. 3791, p. 2.
16) Y. Inoue and S. Kawata：Near-field Scanning Optical Microscope with a Metallic Probe Tip, Opt. Lett., **19**, 3, (1994) 159.
17) K. Fukuzawa and H. Kuwano：Conversion of Evanescent into Propagating Light in Near-Field Scanning Optical Microscopy, J. Appl. Phys., **79**, 11, (1996) 8174.
18) T. Yatsui, S. Kogiso, M. Kourogi, K. Tsutsui and M. Ohtsu：Extremely High Throughput and Resolution Capability of an Optical Near Field Slider, Conf. Lasers and Electro-Optics, San Francisco, California, May (2000) in press.
19) M. Naya, R. Micheletto, S. Mononobe, R. Uma Maheswari and M. Ohtsu：Near-Field Optical Imaging of Flagellar Filaments of Salmonella in Water with Optical Feedback Control, Appl. Opt., **36**, 7, (1997) 1681.
20) H. Muramatsu, N. Chiba, K. Homma, K. Nakajima, T. Ataka, S. Ohta, A. Kusumi and M. Fujihira：Near-Field Optical Microscopy in Liquids, Appl. Phys. Lett., **66**, 24, (1995) 3245.
21) R. Uma Maheswari, S. Mononobe, K. Yoshida, M. Yoshimoto and M. Ohtsu：Nanometer Level Resolving Near Field Optical Microscope under Optical Feedback in the Observation of a Single-String Deoxyribo Nucleic Acid, Jpn. J. Appl. Phys., **38**, 12 A, (1999) 6713.
22) R. Micheletto, M. Denyer, M. Scholl, K. Nakajima, A. Offenhauser, M. Hara and W. Knoll：Observation of the Dynamics of Live Cardiomyocytes through a Free-Running Scanning Near-Field Optical Microscopy Setup, Appl. Opt., **38**, 31, (1999) 6648.
23) H. Kuhn：Classical Aspects of Energy Transfer in Molecular Systems, J. Chem. Phys., **53**, 1, (1970) 101.
24) X. S. Xie and R. C. Dunn：Probing Single Molecule Dynamics, Science, **265**, (1994) 361.
25) T. Funatsu, Y. Harada, M. Tokunaga, K. Saito and T. Yanagida：Imaging of Single Fluorescent Molecules and Individual ATP Turnover by Single Myosin Molecules in Aqueous Solution, Nature, **374**, (1995) 555.
26) T. D. Harris, G. Gershoni, R. D. Grober, L. Pfeiffer, K. West and N. Chand：Near-Field Optical Spectroscopy of Single Quantum Wires, Appl. Phys. Lett., **68**, 7, (1996) 988.
27) T. Saiki, K. Nishi and M. Ohtsu：Low Temperature Near-Field Photoluminescence Spectroscopy of InGaAs Single Quantum Dots, Jpn. J. Appl. Phys., **37**, 3 B, (1998) 1638.
28) K. Matsuda, T. Saiki, H. Saito and K. Nishi：Room-temperature Photoluminescence Spectroscopy of Self-Assembled InGaAs Single Quantum Dots by Using Highly Sensitive Near-field Scanning Optical Microscope, Appl. Phys. Lett., **76**, 1, (2000) 73.
29) M. Ono, K. Matsuda, T. Saiki, K. Nishi, T. Mukaiyama and M. Kuwata-Gonokami：Time-Resolved Emission from Self-Assembled Single Quantum Dots Using Scanning Near-Field Optical Microscope, Jpn. J. Appl. Phys., **38**, 12 A, (1999) L 1460.
30) M. Arai, S. Koshihara, M. Ueda, M. Yoshimoto, T. Saiki, S. Mononobe, M. Ohtsu, T. Miyazawa and M. Kira：Observation of Polysilane by Near-Field Scanning Optical Microscope for Ultraviolet Region, J. Lumin., in press.
31) T. Saiki, N. Saito and M. Ohtsu：Near-field Optical Study of Semiconductor Photonic Devices, Mater. Sci. Eng. B **48**, (1997) 162.
32) Y. Narita, T. Tadokoro, T. Ikeda, T. Saiki, S. Mononobe and M. Ohtsu：Near-field Raman Spectral Measurement of Polydiacetylene, Appl. Spectroscopy, **52**, 9, (1998) 1141.
33) S. Tanaka, M. Nakao, Y. Hatamura, M. Komuro, H. Hiroshima and M. Hatakeyama：Printing Sub-100 Nanometer Features Near-Field Photolithography, Jpn. J. Appl. Phys., **37**, 12 B, (1998) 6739.
34) I. I. Smolyaninov, D. Mazzoni and C. C. Davis：Near-Field Direct-write Ultraviolet Lithography and Shear Force Microscopic Studies of Lithographic Process, Appl. Phys. Lett., **67**, 26, (1995) 3859.
35) 光岡靖幸，中島邦雄，千葉徳雄，村松　宏，安宅龍明：AFM制御型SNOMによる光加工，応用物理学会・日本光学会・近接場光学研究グループ，第5回研究討論会予稿，和光市，

(1996. 6) 71.
36) K. Liberman, Y. Shani, I. Melnik, S. Yoffe and Y. Sharon : Near-Field Optical Photomask Repair with a Femtosecond Laser, J. Microsc., **194**, 2/3, (1999) 537.
37) M. Ohtsu : Near-Field Nano-Photonics toward Nano/atom Deposition, Tech. Digest of the 18th Congress of the International Commission for Optics, San Francisco, California, August 1999, SPIE Vol. 3749, p. 478.
38) M. Ohtsu, K. Kobayashi, H. Ito and G. H. Lee : Nano-Fabrication and Atom-Manipulation by Optical Near Field and Relevant Quantum Optical Theory, Proc. IEEE, **87**, (2000) in press.
39) V. V. Polonski, Y. Yamamoto, M. Kourogi, H. Fukuda and M. Ohtsu : Nanometric Patterning of Zinc by Optical Near-field Photochemical Vapour Deposition, J. Microsc., **194**, 2/3, (1999) 545.
40) Y. Yamamoto, V. V. Polonski, G. H. Lee, M. Kourogi and M. Ohtsu : Fabrication of Nanometric Zinc Pattern with Photoassociated Gas-Phase Diethylzinc by Optical Near-field, Appl. Phys. Lett., **76**, (2000) in press.
41) G. H. Lee, Y. Yamamoto, M. Kourogi and M. Ohtsu : Fabrication of ZnO Nanostructure Using Near-Field Optical Technology, Proc. SPIE Conf. Near-Field Optics, Denver, Colorado, July 1999, SPIE Vol. 3791, p. 132.
42) 小貫哲平，時崎高志，谷　俊朗：SNOM プローブチップによる金属薄膜のナノサイズ陽極酸化加工とその光学的観測，応用物理学会・日本光学会・近接場光学研究グループ，第8回研究討論会予稿，川崎市，(1999. 6) 37.
43) (財)光産業技術振興協会編：光テクノロジーロードマップ報告書―情報記録分野―，(財)光産業技術振興協会，東京，(1998) 18.
44) J. Tominaga, T. Nakano and N. Atoda : An Approach for Recording and Readout beyond the Diffraction Limit with an Sb Thin Film, Appl. Phys. Lett., **73**, 15, (1998) 2078.
45) S. Shinada, F. Koyama, K. Suzuki, K. Goto and K. Iga : Near-field Analysis of Micro-Aperture Surface Emitting Laser for High Density Optical Data Storage, Opt. Rev., **6**, 6, (1999) 486.
46) B. D. Terris, H. J. Mamin and D. Ruger : Near-Field Optical Data Storage Using a Solid Immersion Lens, Appl. Phys. Lett., **65**, 4, (1994) 388.
47) (財)光産業技術振興協会編：光テクノロジーロードマップ報告書―情報通信分野―，(財)光産業技術振興協会，東京，(1998) 34.
48) T. Matsumoto, M. Ohtsu, K. Matsuda, T. Saiki, H. Saito and K. Nishi : Low-Temperature Near-Field Nonlinear Absorption Spectroscopy of InGaAs Single Quantum Dots, Appl. Phys. Lett., **75**, 21, (1999) 3246.
49) 勝山俊夫：(株)日立製作所・基礎研究所，私信，2000年1月.
50) J. Takahara, S. Yamaguchi, H. Taki, A. Morimoto and T. Kobayashi : Guiding of One-Dimensional Optical Beam with Nanometer Diameter, Opt. Lett., **22**, 7, (1997) 475.
51) 伊藤治彦，大津元一：近接場光を用いた原子の制御，光学，**28**, 11 (1999) 610.
52) 大津元一：0（ゼロ）を制御する工学―光による新しい「真空」の工学―，真空，**36**, 5 (1993) 461.
53) 大津元一：「近接場の光学」それとも「近接場光の学」?，光学，**26**, 10 (1997) 509.

近接場光学用プローブの作製法*

物部秀二** 大津元一***

Fabrication of Near-field Optical Probes /
Shuji MONONOBE and Motoichi OHTSU
Key words: microscopy, near-field optics, optical fiber, pulling, etching

1. はじめに

近接場光学顕微鏡は光を情報媒体とする走査型プローブ顕微鏡であり，プローブはそれを構成する最も重要なデバイスである．1980年以降，図1(a)～(c)に示すようなillumination モード (i-mode)[1)~4)]，collection モード (c-mode)[5)~14)]，illumination-collection モード (i-c mode)[15)] などの顕微鏡システムが開発され，それに伴って，テーパ化ファイバプローブ[6)~8)]，金属製 Tip[9)]，半導体製 Tip[11)~13)]，金属コートファイバプローブ[2)~4)10)14)~17)] などが提案された．ここで，プローブはi-modeにおいては，近接場光の発生器として，c-modeにおいては近接場光の散乱・検出器としてそれぞれ働き，3つの方式はそれぞれ異なる応用範囲を持つ．多様な顕微鏡方式が存在することは他のプローブ顕微鏡にはない特徴であるが，同時にそれは個々の応用のためにどのようなプローブをどのように設計・作製・操作するかという技術的課題を生じる．一方，各プローブと顕微鏡方式の関係を見ると，金属コートファイバプローブが3つの顕微鏡方式のすべてに関して実績を持ち，汎用性が高い．本稿では，金属コートファイバプローブの作製法について概説する．

* 原稿受付 平成12年3月3日
** 神奈川科学技術アカデミー（川崎市高津区坂戸3-2-1）
*** 東京工業大学大学院総合理工学研究科（横浜市緑区長津田町4259）
物部秀二
1993年大阪府立大学大学院工学研究科博士前期課程修了．同年財団法人神奈川科学技術アカデミー常勤研究員．1999年博士（工学）．現在に至る．研究分野：近接場光学，光ファイバ，石英ガラスのエッチング，無電解めっき
大津元一
本号 p. 661 に掲載

2. 作製法

金属コートプローブを作製するためには，まず光ファイバをテーパ化し，次にそのテーパ面をアルミニウム (Al)，金 (Au) などの遮光性金属によってコートする手法が有効である．技術的には，溶融延伸[2)]，メニスカス・エッチング[17)~19)]，選択エッチング[8)16)17)]，複合選択エッチング[16)17)] のテーパ化法と真空蒸着[2)]，スパッタリング[15)~17)]，無電解めっき[17)] の金属化法を組み合わせて行う．

2.1 溶融延伸と真空蒸着

溶融延伸は炭酸ガスレーザによって石英系光ファイバの一部を加熱後，ある一定の張力をかけて光ファイバを延伸・破断するものである．現在では炭酸ガスレーザを搭載したマイクロピペットプラー（例えば米国Sutter社製，P 2000）が市販されており，これに光ファイバ用のプラー・

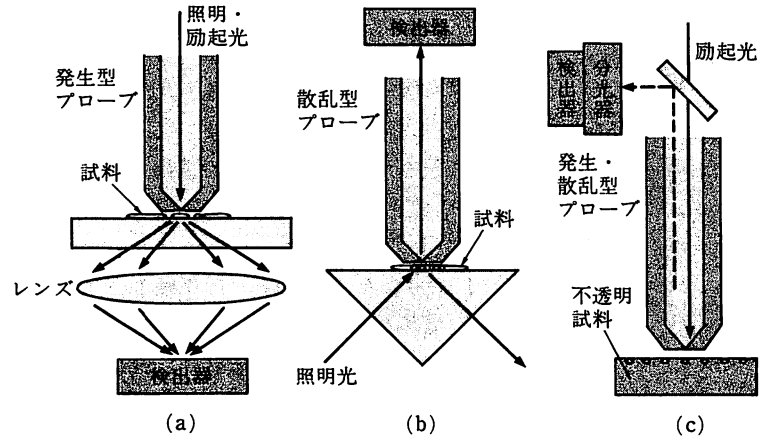

図1 近接場光学顕微鏡の3つの顕微鏡方式
(a) 照明モード (i-mode)，(b) 集光モード (c-mode)，(c) 照明・集光モード (i-c mode)

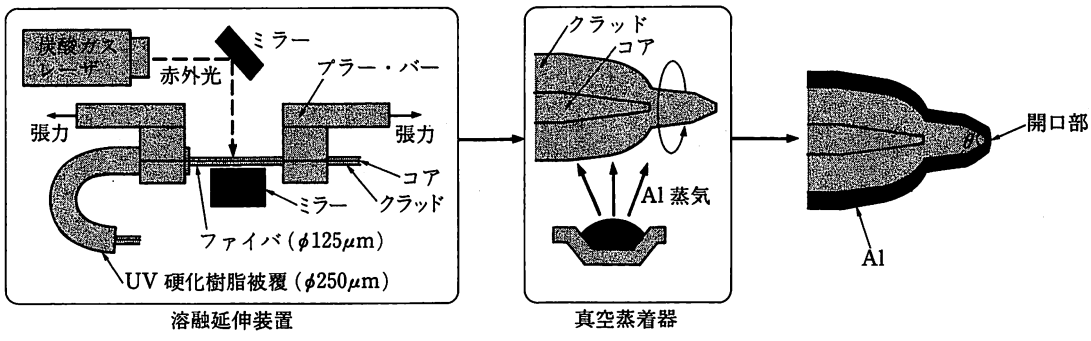

θ：先鋭角

図2　光ファイバの溶融延伸と金属の真空蒸着の説明図

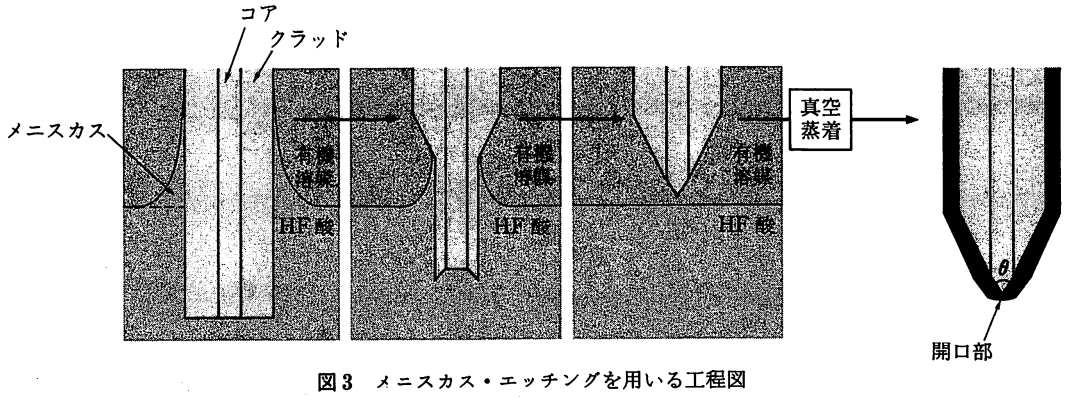

図3　メニスカス・エッチングを用いる工程図

バーを装備することにより，図2に示すような光ファイバ溶融延伸装置が構築される．加熱と延伸の強度およびタイミングを調整することにより，50 nm の最小先端径，20～40° 程度の先鋭角を持つテーパ化プローブを作製できる．ただし，先端径 50 nm を維持しながら先鋭角を厳密に制御することは困難である．

マイクロピペットプラーによりテーパ化された後，図に示されるように，真空蒸着器を用いて遮光用金属でコートされたプローブが作製される．このとき，テーパ化プローブは高真空中にて回転されながら蒸着される．金属としてアルミニウム，金などがよく使用され，その典型的な膜厚は 150 nm 程度である．このプローブは専ら i-mode のために用いられており，c-mode での実績はない．

2.2　メニスカス・エッチング

メニスカス・エッチングは有機溶媒を浮かべたふっ化水素酸に光ファイバを浸漬することにより行われる．元々ファイバ型マイクロレンズ作製のために考案された技術であるが，80年代末に暗視野照明 c-mode 用テーパ化プローブの作製法として使用された．図3はメニスカス・エッチングの工程を説明する図である．まず，石英製光ファイバがふっ化水素酸に浸漬されると，光ファイバの周りにふっ化水素酸のメニスカスが形成され，ふっ化水素酸との接触部分が溶解するので，ファイバ径が減少する．次に，ファイバ径の減少に伴ってふっ化水素酸のメニスカスの高さが低くなるので，有機溶媒とふっ化水素酸の境界でテーパ化が進行する．最後に，メニスカスが消失しふっ化水素酸が光ファイバから解離してエッチングが停止する．金属化のためには，溶融延伸でテーパ化されたプローブと同様に真空蒸着法が用いられる．最近は金属化コートしたものが i-mode のために用いられている．

上述のエッチングにおいては，有機溶媒の種類を変えることにより，先鋭角は数度から 35° 程度まで変化する．ただし，先鋭角を 35° 以上の範囲で制御することはできない．また我々が 630 nm 用の市販光ファイバとシリコンオイルを浮かべた 50% ふっ化水素酸を用いてテーパ化を実行し，先端形状を電子顕微鏡で調査したところ，先端断面が短軸方向先端径 20 nm 程度，長軸方向先端径 60～100 nm の楕円あるいは多角形になっていることが分かった．このようなばらつきは，形成されるテーパ部分の幾何学的異常およびテーパ中心とコア中心の不一致による．最近，この影響を軽減するため，耐ふっ化水素酸性樹脂コートされた光ファイバを用いる方法[19]が提案されている．

2.3　選択エッチング

図4に示す選択エッチングは端面をカットした分散補償ファイバを緩衝ふっ化水素水溶液（BHF）に浸漬してファイバのコア領域をテーパ化する方法である．ここで，BHF 中におけるコアとクラッドの溶解速度を R_1，R_2（$>R_1$）とし，コアの半径を r とすると，浸漬時間 t が

$$t=\frac{r}{R_1}\left(\frac{R_1+R_2}{R_2-R_1}\right)^{1/2}$$

のとき，コア領域のテーパ化が完了し，その先鋭角 θ は次式で表される．

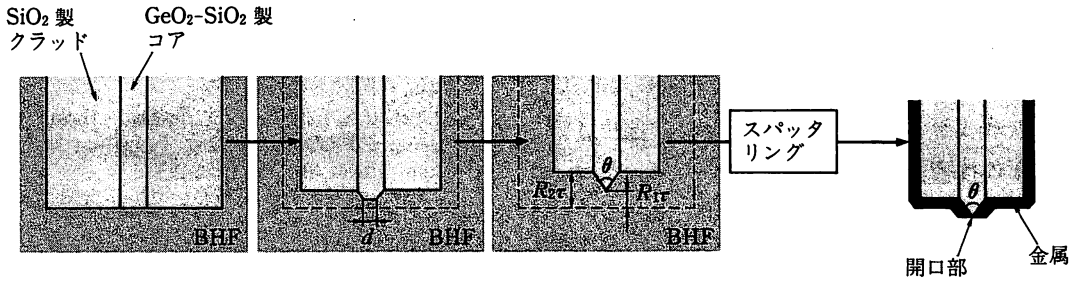

d：先端径，R_1, R_2：コアとクラッドの溶解速度，τ：エッチング時間

図4　選択エッチング法に基づくプローブ作製工程図

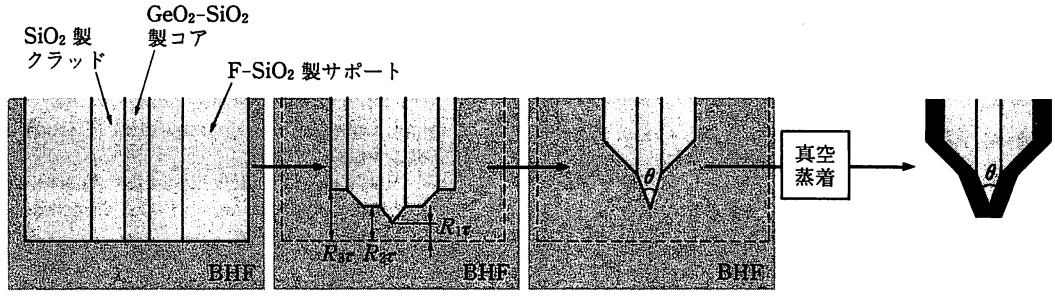

R_3：サポートの溶解速度

図5　多段屈折率型ファイバの複合選択エッチングによるプローブ作製法

$$\sin\frac{\theta}{2}=\frac{R_1}{R_2}$$

ゲルマニウム添加石英製ファイバに関しては，BHF の組成を変えると上式左辺の値が変化し，さらにコア径 2 μm，比屈折率差 2.5% の分散補償ファイバを用いた場合，先端径＜10 nm に対して先鋭角を 20° 以上の範囲で制御できる．それゆえ，この方法は前述の 2 つの手法に比べて高い形状再現性を持つ．選択エッチされたプローブに対して真空蒸着の金属化法は有効ではないので，金属化工程ではしばしばスパッタリングが用いられる．このとき，テーパ部分と同程度の膜厚でプローブ先端も金属コートされるので，測定前にプローブ先端を試料基板で機械的に研磨するか，選択的樹脂コーティングに基づく化学的手法[17]を導入する必要がある．スパッタリング以外では，我々は無電解めっきによる湿式コーティング[17]を開発中で，今後の成果が期待される．分散補償ファイバの選択エッチングを応用して作製されるプローブ群[17]は 3 つの顕微鏡方式で実績を持つ．

2.4　複合選択エッチング

複合選択エッチングは二酸化ゲルマニウム添加石英コア，純粋石英クラッド，ふっ素添加石英サポートからなる多段屈折率型ファイバを用いるテーパ化技術である．コア，クラッド，サポートの BHF による溶解速度をそれぞれ R_1, R_2, R_3（$R_1<R_2<R_3$）とすると，BHF に浸漬された多段屈折率型ファイバのコア領域とクラッド領域はそれぞれ

$$\sin\frac{\zeta}{2}=\frac{R_1}{R_2}$$

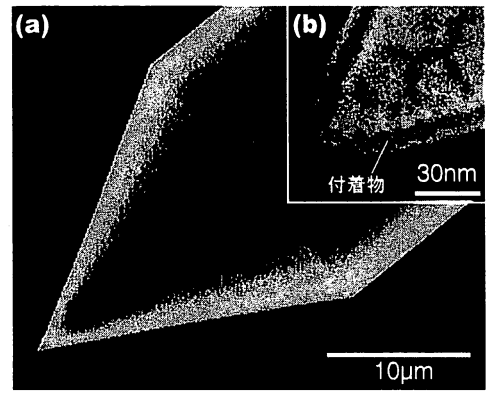

図6　複合選択エッチングによって作製された先鋭角 30° のテーパ化プローブの (a) 電子顕微鏡写真と (b) 先端付近の拡大図

$$\sin\frac{\psi}{2}=\frac{R_2}{R_3}$$

で表される先鋭角 ζ と ψ でテーパ化される．さらに，クラッド領域のテーパ化が完了した後もエッチングを継続すると，コアは

$$\sin\frac{\theta}{2}=\frac{R_1}{R_3}$$

で表される先鋭角 θ でテーパ化され，テーパ化プローブが作製される．金属化は真空蒸着により行われる．

図 6 は複合選択エッチングによってテーパ化されたプローブの電子顕微鏡写真とその先端部分の拡大写真である．ここで，$\theta=30°$，$\psi=62°$，先端径 $d<10$ nm である．この方法は前節で述べた選択エッチングと同様に高い先鋭角制御性（$\theta>17°$）と形状再現性を持つ．

我々はファイバプローブの応用範囲を拡充するために，

既出の手法で作製される単純テーパ化プローブに加えて，三重テーパ化プローブ，Protrusion型プローブ，金属-誘電体-金属コートプローブ，単一モード多モードファイバプローブ，純粋石英コアを持つファイバプローブ等[17]を開発しており，その技術の実用化[20]に努めている．複合選択エッチングは三重テーパ化プローブや単一モード多モードファイバプローブ等の作製に応用できるので，この技術を元として，ファイバプローブのフレキシブル生産を展望する．

3. ま と め

近接場光学顕微鏡用ファイバプローブのための作製法として代表的な溶融延伸と真空蒸着，メニスカス・エッチング，分散補償ファイバを用いる選択エッチング，多段屈折率型ファイバを用いる複合選択エッチングについて概説した．これらの中では複合選択エッチングが最もフレキシブルなプローブ生産に対応できる作製法であった．

参 考 文 献

1) D. W. Pohl, W. Denk and M. Lanz : Optical Stethoscopy: Image Recording with Resolution $\lambda/20$, Appl. Phys. Lett., **44**, (1984) 651.
2) E. Betzig and J. K. Trautmann : Near-field Optics: Microscopy, Spectroscopy, and Surface Modification beyond the Diffraction Limit, Science, **257**, (1992) 189.
3) Z.-Y. Shi and R. Kopelman : Development of Submicron Chemical Fiber Optic Sensors, Anal. Chem., **64**, (1992) 2985.
4) R. Uma Maheswari, H. Tatsumi, Y. Katayama and M. Ohtsu : Observation of Subcellular Nanostructure of Single Neurons with an Illumination Mode Photon Scanning Tunneling Microscope, Opt. Commun., **120**, (1995) 325.
5) E. Betzig, M. Isaacson and A. Lewis : Collection Mode Near-field Scanning Optical Microscopy, Appl. Phys. Lett., **51**, (1987) 2088.
6) R. C. Reddick, R. J. Warmak and T. L. Ferrell : New Form of Scanning Optical Microscopy, Phys. Rev. B, **39**, (1989) 767.
7) D. Courjon, K. Sarayeddine and M. Spajer : Scanning Tunneling Optical Microscopy, Opt. Commun., **71**, 23, (1989).
8) S. Jiang et al. : Nanometric Scale Biosample Observation Using a Photon Scanning Tunneling Microscope, Jpn. J. Appl. Phys., **31**, (1992) 2282.
9) Y. Inoue and S. Kawata : Near-field Scanning Optical Microscope Using a Metallic Probe Tip, Opt. Lett., **19**, (1994) 159.
10) M. Naya et al. : Imaging of Biological Samples by a Collection-mode Photon Scanning Tunneling Microscope, Opt. Commun., **124**, (1996) 9.
11) F. Zenhausern, M. P. O'Boyle and H. K. Wickramasinghe : Scanning Interferometric Apertureless Microscopy: Optical Imaging of at 10 Angstrom Resolution, Science, **269**, (1995) 1083.
12) S. Akamine, H. Kuwano and H. Yamada : Scanning Near-field Optical Microscope Using an Atomic Force Microscope Cantilever with Integrated Photodiode, Appl. Phys. Lett., **68**, (1996) 579.
13) W. Noell et al. : Micromachined Aperture Probe Tip for Multifunctional Scanning Probe Microscopy, Appl. Phys. Lett., **70**, (1997) 1236.
14) R. Uma Maheswari, S. Mononobe, K. Yoshida, M. Yoshimoto and M. Ohtsu : Nanometer Level Resolving Near Field Optical Microscope under Optical Feedback in the Observation of a Single-string Deoxyribo Nucleic Acid, Jpn. J. Appl. Phys., **38**, (1999) 6713.
15) T. Saiki et al. : Spatially Resolved Photoluminescence Spectroscopy of Lateral p-n Junctions Prepared by Si-doped GaAs Using a Photon Scanning Tunneling Microscope, Appl. Phys. Lett., **67**, (1995) 2191.
16) S. Mononobe : Probe Fabrication, in *Near-Field Nano/Atom Optics and Technology*, M. Ohtsu ed., Springer-Verlag, Tokyo, (1998) Chap. 3.
17) 物部秀二：学位論文，東京工業大学，(1999). http://www.kast.or.jp/Mononobe.pdf.
18) K. M. Takahashi : Meniscus Shapes on Small Diameter Fibers, J. Colloid and Interface Sci., **134**, (1990) 181.
19) P. Lambelet et al. : Chemical Etching of Fiber Tips through the Jacket: A New Process for Smoother Tips, Tech. Digest of NFO-5, Shirahama, Dec. (1998) 218.
20) http://www2.odn.ne.jp/kawaguchi-opt/

近接場光を用いた原子の制御

伊藤　治彦*,**,***・大津　元一*,***

近接場光は物質表面に留まって外部には伝搬していかない光の場である．光波の全反射の際に生じるエバネセント光[1]が古くから知られており，ドップラーフリー分光法のひとつとしても用いられてきた．近年における関連研究の拡大と展開[2,3]の過程で「場の局在性」が大きな比重を占めるようになり，従来のエバネセント光（次第に消えゆく光）という名称では物理的特性を正確にいい表せないとの認識から，現在ではより適切な表現として近接場光（near field）の名称が定着している．この用語は伝搬光（far field）との対比においても便利なものになっている．

近接場光を用いる研究の基盤のひとつとなっているのは，一端をナノ寸法に尖らせた先鋭化ファイバーをつくる技術である[2,3]．この技術の確立によってナノ領域に局在化した近接場光をさまざまな場面で使用する可能性が開けてきた．たとえば，回折限界をはるかに超えた分解能をもつ光学顕微鏡への応用は周知であろう[2,3]．また，単なる顕微システムにとどまらず，量子ドットや生体試料の観測にも大きな威力を発揮している[2]．

先鋭化ファイバーの先端近傍につくられる近接場光の局在範囲は，波長に依存せず先端の曲率半径程度であることが実験結果などから示されている[2,3]．すなわち近接場光は回折の影響を受けず，伝搬光の場合に現れるような空間分解能の回折限界をもたない．近接場光の局在性を利用すれば原子のような微粒子の運動も非常に高い位置精度で制御できることが期待される．本稿ではすでに確立している近接場光を用いて原子を反射したり誘導したりする手法に触れたあと，先鋭化ファイバーによって原子を操作する可能性について筆者らの研究に基づいて概観する．

*東京工業大学大学院総合理工学研究科電子機能システム専攻（〒226-8502 横浜市緑区長津田町 4259 番地）
E-mail: ito@ae.titech.ac.jp
**科学技術振興事業団さきがけ研究 21「場と反応」領域グループ（〒700-0904 岡山市柳町 1-1-1　住友生命岡山ビル 17 階）
***神奈川科学技術アカデミー光科学重点研究室第 2 研究グループ（〒213-0012 川崎市高津区坂戸 3-2-1　かながわサイエンスパーク東棟 408 号室）

1. 近接場光による原子の反射

空間的に強度が一様でない共鳴からわずかに離調した光の場に原子が置かれているとき，強度の変化する方向に原子は双極子力[4]と呼ばれる力を受ける．双極子力の強さは光強度の勾配と周波数離調に比例する．近接場光は指数関数的に強度が減衰するため，原子の熱運動を大きく変化させるほどの強い双極子力を原子に及ぼすことができる．他方，力の向きは原子の共鳴周波数と光周波数の兼ね合いによって決まる．近接場光の場合，光周波数が共鳴周波数よりも高い場合（正離調）には光の場からはじく向き（斥力）に作用し，低い場合（負離調）には光の場に引き込む向き（引力）に作用する．近接場光による原子の制御では基本的にこのような双極子力が用いられる．

図 1 に，近接場光によって原子を反射する方法を示す．プリズム表面でレーザー光を全反射させ表面近傍に近接場光を誘起する．このときレーザー光が正離調されていれば，近接場光領域に進入してきた原子は斥力を受けて反射される．この種の最初の実験は Balykin らによって Na 原子を用いて行われた[5]．その後，Aminoff らは近接場光上で重力落下する Cs 原子がトランポリンのように繰り返し反射されるのを観測した[6]．

原子反射実験は基礎研究にも応用されている．誘電体表面近傍ではファン・デル・ワールス力が原子に働くことが知られているが，これまで基底状態の原子に対しては精密に測定する方法がなかった．Aspect らは近接場光による原子反射の実験において双極子力の強さが周波数離調にも依存することを利用して，双極子力（斥力）とファン・デ

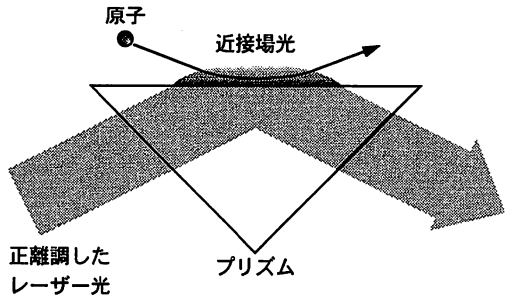

図1　正離調したレーザー光の全反射によりプリズム表面に誘起された近接場光による原子の反射.

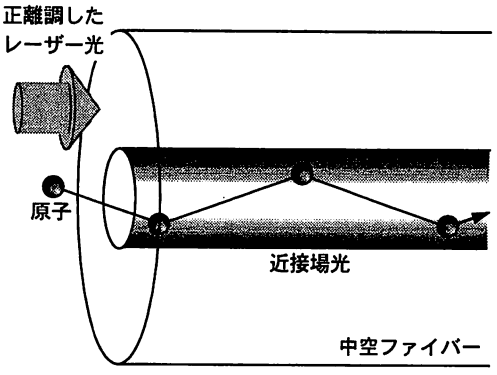

図2　中空ファイバーを用いた原子の誘導. 正離調したレーザー光のコア部分への結合によって中空領域に誘起された近接場光が内壁表面に近づいてきた原子を反射する.

ル・ワールス力（引力）が釣り合い原子が反射されなくなる場合を調べ，基底準位の原子に対するファン・デル・ワールス力を見積もった[7].

2. 中空ファイバーによる原子の誘導

原子を反射する近接場光のトンネルをつくることにより，原子をその中に閉じこめて誘導することができる. 図2に光を導波するコアの中心に穴がある中空の光ファイバーを用いた原子誘導路の概略を示す. レーザー光（誘導光）を中空ファイバーに結合させると伝搬モードに付随して近接場光が内壁表面を覆うようにして励起される. 正離調の場合，中空領域に進入してきた原子は内壁表面に近づくと近接場光から斥力を受け，反射を繰り返しながらファイバーの中を進んでいく.

原子の誘導実験は共鳴波長780 nmのRb原子を用いて行われた[8,9]. 図3に筆者らのグループが用いた中空ガラスファイバー（中空径2 μm，コア厚4 μm）の断面写真を示す. 原子の誘導に適した近接場光を伴う伝搬基本モードであるLP_{01}モードが励起されている[2]. 図4に中空径7 μmの中空ファイバーから誘導されて出てきたRb原子（細い原子ビーム状にして中空ファイバーの中空領域に導入している）の2段階光イオン化スペクトルの一例を示す[9]. ここ

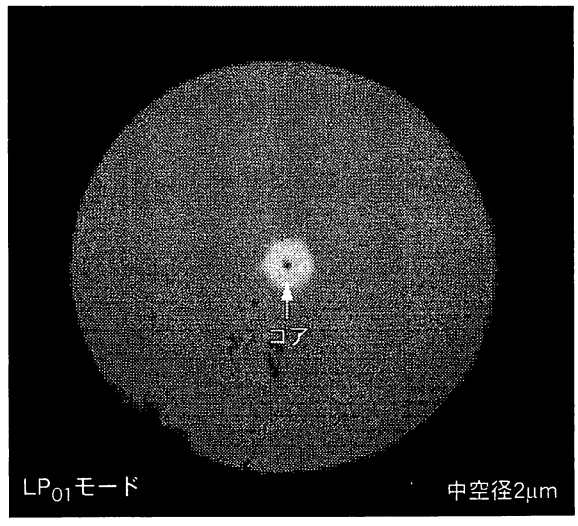

図3　中空径2 μmの中空ガラスファイバーの断面写真. 中心の中空部分のまわりに厚さ4 μmのコアがあり，さらにそのまわりにクラッドがある. 基本伝搬モードであるLP_{01}モードが励起されている.

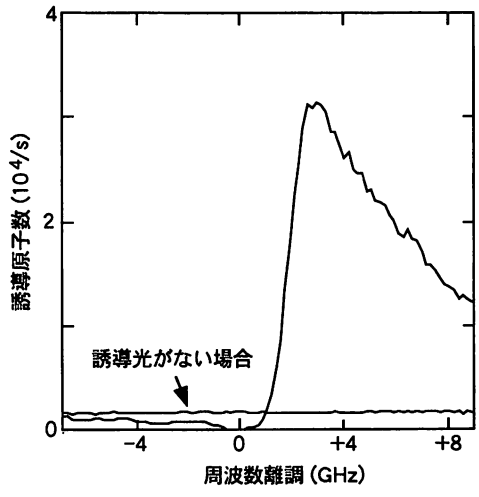

図4　中空径7 μmの中空ファイバーによって誘導されたRb原子の2段階光イオン化スペクトル. 5S基底状態のRb原子を半導体レーザーによって5P状態に励起した後，波長476.5 nmのアルゴンイオンレーザーによってイオン化しチャネル電子増倍管で検出している.

では中空ファイバーから出てきた5S基底準位にあるRb原子を波長780 nmの半導体レーザーで5P準位に励起した後，波長476.5 nmの高出力アルゴンイオンレーザーでさらにイオン化レベルに励起している. イオン化されたRb原子はチャネル電子増倍管によって検出されている. 誘導光がない場合の結果と比べると，正離調領域では原子が誘導されるため検出原子数が大幅に増加しているのがわかる.

近接場光による原子制御では共鳴的な双極子力を利用しているため，原子の種類や量子状態を光周波数によって選

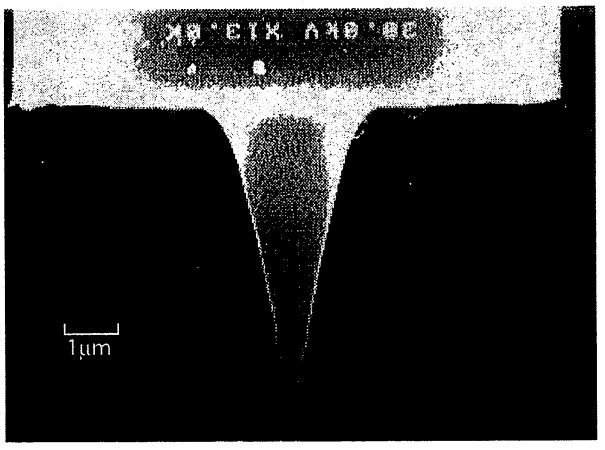

図5　化学エッチング法によって作製した先鋭化ガラスファイバーのSEM像．先端の曲率半径は2 nm（またはそれ以下）と見積もられる．

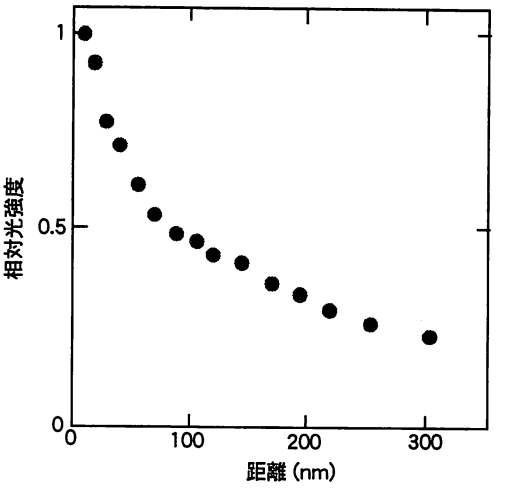

図6　曲率半径200 nmの先鋭化ファイバー先端近傍の光強度分布（波長780 nm）．曲率半径40 nmの金コート先鋭化ファイバーを用いて，散乱光強度を近接場光をつくっている先鋭化ファイバー先端からの距離の関数として測定している．

択することができる．実際，筆者らは上述の原子誘導路を用いて質量数85と質量数87の2つのRb同位体の分離を試みている[9]．また，微小な中空径をもつ中空ファイバーの内部では原子と真空場との相互作用の結果生じる共振器量子電気力学効果の増大が期待されるが，原子誘導の手法を応用することによりその観測が可能になると思われる[2]．

3.　先鋭化ファイバーによる原子の操作

光を用いた気体原子の制御に関する研究のひとつの方向が低温化と高密度化であったのに対して，もうひとつの方向は位置制御の高精度化や少数化に向けられている．後者は特に単一原子の操作を視野に入れたものであり，ナノファブリケーションへの応用に期待が寄せられている．

表面に付着した原子の操作はscanning tunneling microscopy技術を用いることによって可能になっているが，自由な気体原子の場合はどうであろうか．大津と堀らは先端をナノ寸法に尖らせた先鋭化ファイバーによって単一の気体原子を操作することができる可能性を示した[10,11]．また，Letokhovらは原子をトラップするための近接場光の空間分布を計算によって求めている[12]．以下の3.2節では，先鋭化ファイバーを用いた原子操作の有効な方法として，先の大津と堀らによって提案されたものとは異なる機構を導入する．

3.1　先鋭化ファイバー先端近傍の近接場光

先鋭化ファイバーの作製技術の進歩のおかげで，使用目的に応じて種々の大きさや形状をもったものがつくれるようになっている．図5に化学エッチング法によって作製した先鋭化ファイバー[2,3]のSEM像を示す．先端の曲率半径は2 nm（またはそれ以下）と見積もられる．その先端だけを残して側面は金などでコーティングすることにより伝搬光成分を除去している．

先鋭化ファイバー先端近傍の光強度分布は別の先鋭化ファイバー（プローブとして使用）の先端を近づけたときに散乱される光をそれ自身でピックアップすることにより調べることができる．図6に先端曲率半径（$=a$）が200 nmの先鋭化ファイバーに波長780 nmの光を結合させたときに生じる先端近傍の光強度分布の測定結果のひとつを示す．ここでは$a=40$ nmの先鋭化ファイバーをプローブとして用いて得た光強度を，近接場光を生じている先鋭化ファイバーの先端表面からの距離（$=r$）の関数として描いてある．なお，光強度は$r=10$ nmの位置での値で規格化されている．図6では$r=100$ nm程度までが近接場光成分と考えられ，それよりも遠いところでは伝搬光成分が混ざってきている．この場合，先端近傍の近接場光の強度分布は式$I(r)=I_0\exp(-1.85\,r/a)$で近似的に表すことができる．

近接場光の強度分布は原理的にマクスウェル方程式を数値的に解いて求めることができるが，物理的直感と結びついたものとして湯川型の強度分布式が提案されている．すなわち湯川型ポテンシャル

$$\phi(r)=\iint\frac{\exp\left(-\frac{r}{a}\right)}{r}\,\mathrm{d}S$$

から強度分布を

$$I(r)\sim\left|\nabla\phi(r)\right|^2+\frac{1}{a^2}\left|\phi(r)\right|^2$$

の形で与える[3,11]．最近，小林らは湯川型ポテンシャルが近接場光の3次元的強度変化をよく表すことを理論的に導出

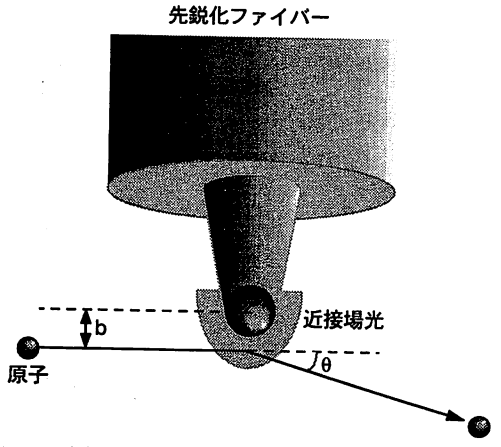

図7　先鋭化ファイバーを用いた原子の運動の偏向.

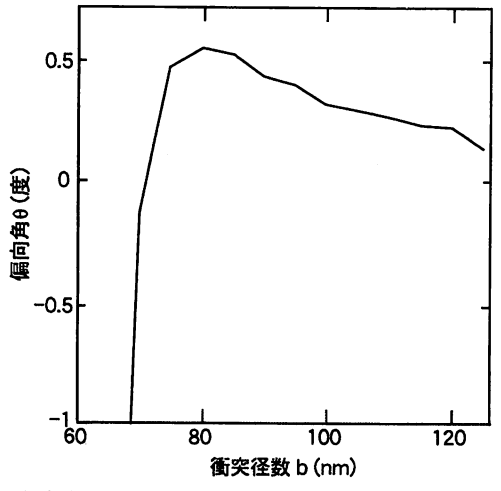

図8　曲率半径50 nmの先鋭化ファイバーによる速度10 m/sのRb原子の偏向（計算）．先鋭化ファイバーへの結合光パワーから見積もった先端近傍における近接場光パワーを50 nWとしている.

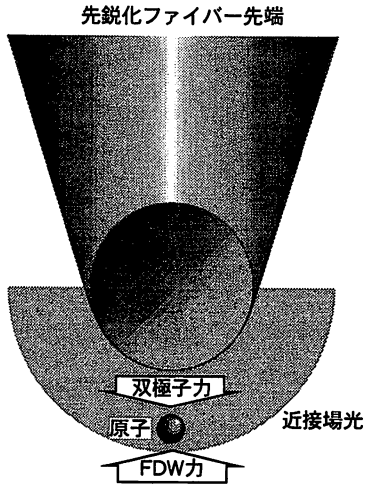

図9　先鋭化ファイバーによる原子の捕獲．斥力の双極子力と引力のファン・デル・ワールス（FDW）力の釣り合いによってトラップが形成される.

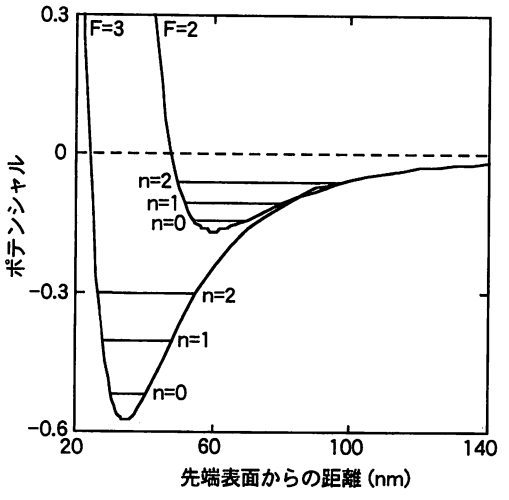

図10　曲率半径20 nmの先鋭化ファイバー先端近傍に誘起されたトラップポテンシャル(周波数離調+1 GHz, 近接場光パワー600 nW)．^{85}Rb原子の2つの超微細基底準位$F=2$および$F=3$に対して示す．原子は量子振動準位（nでラベル）にトラップされうる.

している[13]．前述した先鋭化ファイバー先端近傍の強度分布の測定結果は湯川型強度分布に近いものになっている.

3.2　原子の運動の偏向とトラップ

湯川型強度分布に基づいて，先鋭化ファイバーによる原子の操作として偏向とトラップの2つの場合を考えることにする[2]．図7に正離調した近接場光からの双極子力（斥力）による原子の運動の偏向を示す．近接場光領域に進入した原子はファン・デル・ワールス力と双極子力を受けるが，光強度が十分に強い場合には双極子力が勝り，先端からはじかれる向きにその運動が曲げられる．図8は$a=50$ nmの場合に速さ10 m/sで飛来したRb原子の偏向角θを衝突径数bの関数として数値的に見積もったものである．ここではRb原子を散乱または偏向するポテンシャル障壁となる双極子力の光ポテンシャルを湯川型強度分布式から算出している（周波数離調+1 GHz，近接場光パワー50 nW）．図8では$b=80$ nmにおいて最大の偏向角0.5度が得られているが，この値は10 cm後方で原子の位置が入射方向から100 μm程度変位することを示す（市販されている粒子検出器の分解能で検出可能）.

先鋭化ファイバー先端近傍で原子に作用する双極子斥力とファン・デル・ワールス引力とを釣り合わせて（図9），原子をトラップするためのポテンシャルを形成することができる．図10に$a=20$ nmの場合において2つの超微細基底準位$F=2$と$F=3$にある^{85}Rb原子に対して見積もったトラップポテンシャル（光ポテンシャルとファン・デル・ワールス・ポテンシャルの和）を示す．ここで周波数離調は基底下準位$F=2$に対して+1 GHzとなるように取ら

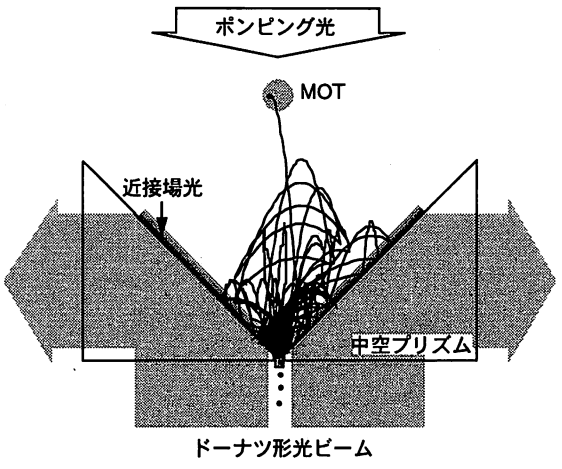

図11　近接場光を用いた原子ファネル．磁気光学トラップ（MOT）から落下する冷却原子は中空プリズムの内壁に誘起された近接場光によって反射されると同時に運動エネルギーをも失い，冷却原子ビームとして出射される．

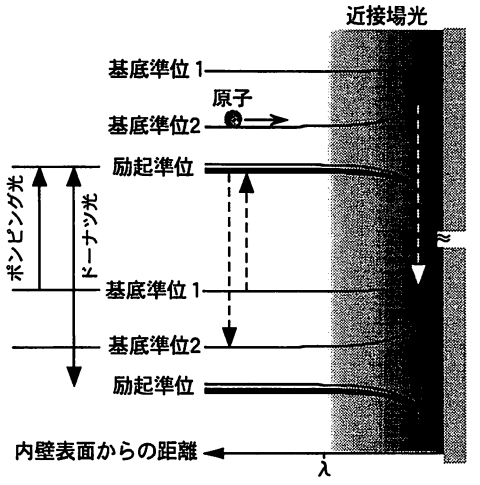

図12　近接場光誘起 Sisyphus 冷却の原理．近接場光との相互作用の結果として表面近傍で原子のエネルギー準位が変化する．その変化分（エネルギーシフト）は光ポテンシャルとほぼ等価であり，おおよそ光強度に比例し周波数離調に反比例する．Rb 原子のようなアルカリ金属原子は2つの超微細基底準位をもっており，両準位に対して正離調となるように光周波数を選んでおく（ドーナツ光と書いた矢印）．このとき，反射の際に両準位間の遷移が起きる（白破線矢印）と，周波数離調の違いから生じる両準位間の光ポテンシャルの差の分だけ原子の運動エネルギーが失われることになる．この過程はポンピング光によって繰り返される（黒破線矢印）．

れている（近接場光パワー 600 nW）．Rb 原子はこのポテンシャル内につくられる量子振動準位（図10に n でラベルした）のひとつにトラップされうる．たとえば基底上準位 $F=3$ に対するポテンシャル内の $n=0$ 振動準位には温度換算で 30 μK の ^{85}Rb 原子がトラップされる．

先鋭化ファイバー先端には完全に球形の光近接場がつくられるわけではなく，またナノメートルのオーダーの距離変化では重力ポテンシャルも原子を捕まえておくには十分でない．したがって図9に示したような場合でも鉛直上方に原子が逃げる可能性がある．より安定なトラップのためには複数の先鋭化ファイバーを組み合わせたものが必要となると考えられるが，そのひとつは正四面体の各面の重心に4つの先端を配置することにより実現されうる[2]．

4. 近接場光ファネル

先鋭化ファイバーによる原子の操作では，ナノ寸法の近接場光と原子との間に相互作用が生じるためには原子の運動の速さが遅いことが必要となると同時に，効率よく近接場光領域に原子を送り込まなければならない．そこで冷却した原子ビームをそのソースとして使用することが考えられる．図11に筆者らが提案している磁気光学トラップ（MOT）からの冷却原子集団を原子ビームに変換する近接場光で構成した光ファネル（漏斗）を示す[14]．中空のプリズムの鉛直下方からドーナツ形の正離調した光ビームを照射し内表面で全反射させて近接場光を誘起する．MOT から落下してきた原子は近接場光からの斥力を受けて反射され，プリズム下部に設けた出射口に集められビーム状になって出ていく．

このファネルでは反射だけでなく，その際に原子の冷却が行われる点に特徴がある．図12にその原理を示す．近接場光領域に原子が進入してくると双極子相互作用によってエネルギー準位が光強度に比例して変化するが，Rb 原子のように2つの基底準位をもつ場合，両方の準位に対して正離調となるように光周波数を選んでやる（ドーナツ光と書いた矢印参照）と下準位（基底準位2）の方が離調が小さいためエネルギーシフトが上準位（基底準位1）より大きくなる．このようなエネルギーシフトは光ポテンシャルと等価である．そこで，基底準位2にいた原子が反射の際に基底準位1に遷移する（白破線矢印）と両基底準位間のポテンシャルエネルギーの差の分だけ運動エネルギーを失うことになる．この過程はファネルの鉛直上方から弱いポンピング光を照射することによって原子を基底準位1から2に戻してやれば（黒破線矢印）繰り返させることができる（Sisyphus 冷却[15]）．図11には平均温度 10 μK のマクスウェル・ボルツマン分布をもつ MOT から落下する ^{85}Rb 原子のモンテカルロシミュレーションによって求めた軌跡のひとつを示してある．ファネル実験は現在進行中である．

先鋭化ファイバーを用いた原子操作技術は，伝搬光を主体とした従来の原子光学技術では不可能と思われていた位置制御性をわれわれに提供してくれるものと期待される．実際に実験を行う上での克服すべき課題が多く残されてい

るものの，その実現によってもたらされる成果を考えるならば取り組む価値の高いものであろう．たとえば，先鋭化ファイバーで捕まえた原子を所望の位置にまで運び，光周波数を負離調にして放してやればatom-by-atomに結晶成長を行うことが可能となるかもしれない．

湯川型光強度分布式を用いた評価では伝搬光理論から得られた光ポテンシャルの表式をそのまま使用している．また，ファン・デル・ワールス・ポテンシャルもマイクロメートル領域で得られた結果を援用している．これらが近接場領域で本当に成り立つかどうかは理論的にも残された問題である．特に光子の概念を直接結びつけられない近接場光と原子の相互作用に関する理論的研究もまだこれからの課題である．Sisyphus冷却では光子数状態に基づいたdressed atom理論が用いられているが，近接場の場合にこれが正確にはどのようになるか明らかとはいえない．このような点においても近接場光を含む場の量子化の問題は重要な未解決課題となっている．

近接場光の強度分布を知ることは原子操作用の先鋭化ファイバーを設計する上で重要であるが，本稿でも述べた先鋭化ファイバー同士による測定では場を大きく乱して測定しているために正確な情報が得られていないと考えるべきである．先鋭化ファイバーによる偏向技術は原子の運動を高精度に制御できるばかりでなく，近接場光そのものの研究においても有用である．すなわち原子をプローブとして用いることにより近接場光をより非破壊に近い状態で調べることができる．これは湯川型光強度分布の検証にも役立つであろう．

文　献

1) 諸　元鎬，堀　裕和："エバネッセント波とは何か？"，パリティ，Vol. 11, No. 12 (1996) 14-22.
2) *Near-Field Nano/Atom Optics and Technology*, ed. M. Ohtsu (Springer-Verlag, Berlin, 1998).
3) M. Ohtsu and H. Hori: *Near-Field Nano-Optics* (Kluwer/Plenum, New York, 1999).
4) J. P. Dowling and J. Gea-Banacloche: "Evanescent light-wave atom mirrors, resonators, waveguides, and traps," *Advances in Atomic, Molecular, and Optical Physics Vol. 37*, eds. B. Bederson and H. Walther (Academic Press, San Diego, 1996) pp. 1-94.
5) V. I. Balykin, V. S. Letokov, Yu. B. Ovchinnikov and A. I. Sidorov: "Quantum-state-selective mirror reflection of atoms by laser light," Phys. Rev. Lett., **60** (1988) 2137-2140.
6) C. G. Aminoff, A. M. Steane, P. Bouyer, P. Desbiolles, J. Dalibard and C. Cohen-Tannoudji: "Cesium atoms bouncing in a stable gravitational cavity," Phys. Rev. Lett., **71** (1993) 3083-3086.
7) A. Landragin, J.-Y. Courtois, G. Labeyrie, N. Vansteenkiste, C. I. Westbrook and A. Aspect: "Measurement of the van der Waals force in an atomic mirror," Phys. Rev. Lett., **77** (1996) 464-467.
8) M. J. Renn, E. A. Donley, E. A. Cornell, C. E. Wieman and D. Z. Anderson: "Evanescent-wave guiding of atoms in hollow optical fibers," Phys. Rev. A, **53** (1996) R648-R651.
9) H. Ito, T. Nakata, K. Sakaki, M. Ohtsu, K. I. Lee and W. Jhe: "Laser spectroscopy of atoms by evanescent waves in micron-sized hollow optical fibers," Phys. Rev. Lett., **76** (1996) 4500-4503.
10) M. Ohtsu, S. Jiang, T. Pangaribuan and M. Kozuma: "Nanometer resolution photon STM and single atom manipulation," *Near-Field Optics*, eds. D. W. Pohl and D. Courjon (Kluwer, Dordrecht, 1993) pp. 131-139.
11) H. Hori: "Quantum optical picture of photon STM and proposal of single atom manipulation," *Near-Field Optics*, eds. D. W. Pohl and D. Courjon (Kluwer, Dordrecht, 1993) pp. 105-114.
12) V. V. Klimov and V. S. Letokhov: "New atom trap configurations in the near field of laser radiation," Opt. Commun., **121** (1995) 130-136.
13) K. Kobayashi and M. Ohtsu: "Quantum theoretical approach to near-field optical system," J. Microscopy, **194** (1999) 249-254.
14) H. Ito, K. Sakaki, W. Jhe and M. Ohtsu: "Atomic funnel with evanescent light," Phys. Rev. A, **56** (1997) 712-718.
15) J. Söding, R. Grimm and Yu. B. Ovchinnikov: "Gravitational laser trap for atoms with evanescent-wave cooling," Opt. Commun., **119** (1995) 652-662.

(1999年6月30日受理)

電子材料ナノメータ領域評価技術
近接場光によるナノメートル寸法物質の堆積

特集解説

李　謹炯
科学技術振興事業団
山本　洋
興梠元伸
東京工業大学
正員　大津元一
東京工業大学，科技団

キーワード
近接場光，ファイバープローブ，光化学気相堆積法，単一行程，ナノ構造

1. まえがき

光通信、光情報処理システムの今後の一層の高速化、高容量化のためには光デバイスの小型化が最も重要な技術となる。しかし、光は回折の性質をもつため、光素子の寸法は光波長以上でなくてはならないという制限が課せられている。この制限（回折限界と呼ばれている）は光を電磁波としてとらえ、利用していることに起因する。しかし光波長以下の寸法の空間での制御された電磁相互作用を媒介する場として光をとらえ、利用すればこの制限は無くなる。そのような光の場を近接場光と呼ばれる[1][2]。近接場光は物質表面のごく近い領域に存在し、光波長より小さなナノメートル寸法の領域にエネルギーが集中している光なので、ナノメートル寸法の光加工にも利用可能であり、特に最近では光化学気相堆積法（光 CVD）に利用され、微小物質が作製されている。

半導体産業などに広く利用されている微細加工技術の中にリソグラフィー技術がある。しかし、その技術は複数の行程を必要とし、かつバルクの材料を削る方式なので、基板と薄膜に損傷が起こりやすい。これに対し光CVDは単一行程でのパターニングが可能である。従来の光CVDは次のような特徴を有する。1.低温プロセスが可能、2.基板への損傷や汚染が少ない、3.原料ガスとの共鳴相互作用に基づき、入射光の光子エネルギーを調節することにより堆積物質の選択性および多様性がある、4.多種材料の水平集積化が可能、5.堆積物質と基板の制約がない等[3][4][5]。さらにこの方法に近接場光を用いることにより、ナノメートル寸法の光機能材料、デバイスの堆積、作製が可能になると考えられる。本稿では近接場光を用いたナノメートル寸法の微小物質の堆積について記述する。

2. 近接場光を用いた光化学気相堆積法の原理

堆積は真空チャンバー内に設置されたファイバプローブ（以下、プローブと記す）先端に発生する近接場光を用いて行われる。プローブの走査方法は近接場光学の応用システムとして代表的な近接場光学顕微鏡に採用されているものと同等である。ここでは光CVDの例として亜鉛（Zn）金属の堆積を紹介する。

光CVDのためには原料となる分子にその解離エネルギーより大きなエネルギーを持つフォトンを吸収される必要がある。実験では原料ガスとしてジメチル亜鉛[$Zn(CH_3)_2$:以下DEZと記す]を用いるので、光分解反応によりZnを堆積するためには以下の反応式で示すように解離エネルギー3.76 eV

$$Zn(CH_3)_2 + h\nu(<338\ nm) \longrightarrow Zn + 2CH_3$$

以上（波長338 nm以下）のフォトンエネルギーを有する紫外域の近接場光が必要となる。そのための光源としてAr^+レーザの第二高調波発生器、及びArFエキシマレーザ(波長=193 nm)を使用した。Ar^+レーザの第二高調波発生器はビルドアップ共振器中に収めたBBO結晶である。これにより波長224 nmの第二高調波光（以下SH光と記す）が発生する。十分に高いパワー密度を持つ近接場光を発生させるため、紫外光に対する伝送損失が1.1 dB/mの純粋石英コアファイバーを用いてプローブが作製された[6]（従来の光通信用ファイバーの伝送損失は96 dB/mである)。このファイバーを化学エッチングにより先端を先鋭化し、その表面に200 nm程度の膜厚のアルミニウム膜を蒸着してプローブを作製した。図1には作製したプローブのSEM像とその断面を示す。プローブが基板に10 nm以内に接近して走査されるようにせん断応力を用いて位置制御された。

堆積は二つの方法で行われる。（1）前期核形成法を援用する方法（図2(a)）：これは基板上の吸着層だけを近接場光により分解し成長核を形成する方法である。すなわち、まず基板をDEZガス中に数分さらす。その後、ガスを完全に排出すると、基板方面上には1分子層程度の吸着層が残るので、プローブから発生する近接場光によりこの吸着層を分解し、Znの成長核を形成する。その時、プローブを走査してZnの成長核のパターニングを行う。次に再びガスを満たしてArFエキシマレーザを基板全体に照射することにより成長核の上に選択的に堆積を行う。この方法の利点は

Deposition of Nanometer-Sized Materials by Optical Near-Field. By *Geun-Hyoung Lee*, Non-member (Japan Science and Technology Corp.), *Yoh Yamamoto*, Non-member, *Motonobu Kourogi*, Non-member (Tokyo Institute of Technology), *Motoichi Ohtsu*, Member (Tokyo Institute of Technology, Japan Science and Technology Corp.).

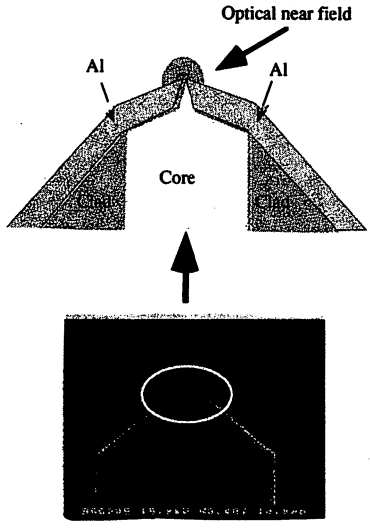

図1．作製された紫外用プローブの SEM 像とその断面図.

プローブ先端での堆積が回避できることである。ただし、多様な物質のパターンの2次元的な集積化には制限がある。（2）気相分解を用いる方法（図2(b)）：これは DEZ ガスを反応チャンバーに満たし、プローブからの近接場光を用いて光化学反応により Zn を堆積させる方法である。この方法は原料ガスの交換によって多様な物質を選択的に堆積できる利点を持つので、2 次元集積化に適している。ただし、基板上だけではなく、近接場光が発生するプローブ先端でも堆積が起こり、最後には堆積された膜により近接場光が発生しなくなる可能性がある。しかし実際にはプローブ先端が膜に被覆され、近接場光が出なくなるのには数時間かかるので、ナノメートル寸法のパターンの作製（数分で終了）には問題にならないことが分かっている。ナノ寸法光機能材料やデバイスの作製には多様な材料の 2 次元集積化が必要なので、そのためには（2）の方法が有利である。

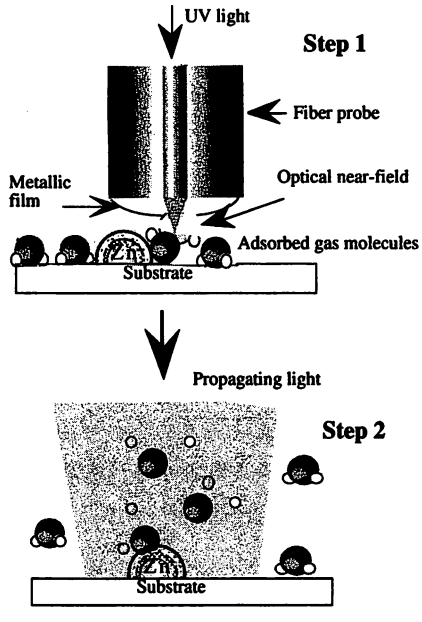

(a)

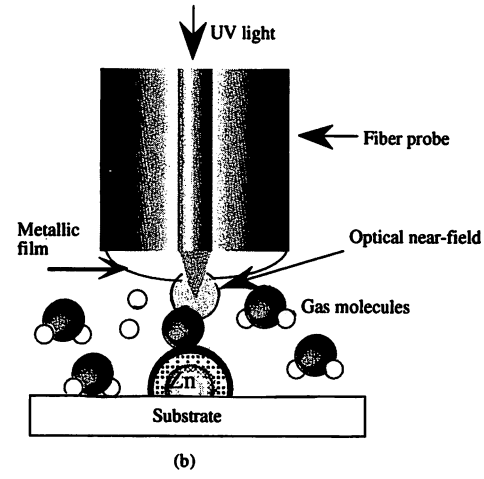

(b)

図2．近接場光 CVD の原理 (a) 方法（1）：Step 1; 近接場光による成長核形成、Step 2; 伝搬光によるパターン形成. (b) 方法（2）.

最近では走査トンネル顕微鏡（STM）を用いたナノ構造の作製が報告されている[7]。この方法では基板と STM チップの間のトンネル電流により発生する熱を用いて有機金属ガスを分解することによりナノメートル寸法の物質を作製する。しかし、この方法は、絶縁体に適用できないという制限がある。それに対して本方法では基板と堆積物に関する制限は大幅に緩和されている。

3. パターンの作製

方法（1）では堆積を行う前、真空チャンバーは 10^{-6}Torr まで排気し、その後、約 10 Torr の DEZ ガスを満たして 20 分間維持する。チャンバーの真空度が 10^{-5}Torr になるまで再度ガスを完全に排出してからファイバー後端に Ar^{+}レーザを照射し、先端の近接場光により基板上の吸着層を分解して成長核を形成する。基板はコーニングガラス(#7092)であ

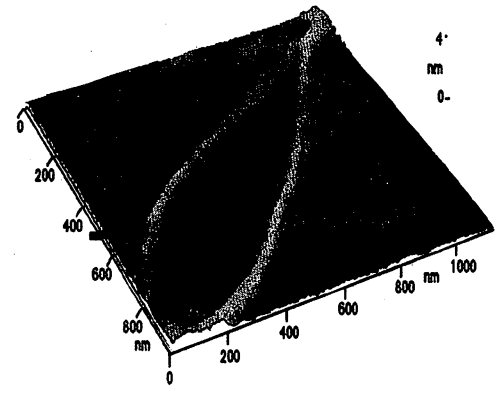

図3．方法（1）により作製されたリング状の Zn パターンのせん断応力顕微鏡像[8].

る。成長核形成後、再度原料ガスを満たし、ArFエキシマレーザ光を直接基板に照射して成長核の上にZnを堆積、成長させる。近接場光を用いる場合の利点はプローブの走査により曲線や点などの任意のパターンが描けることである。図3にはこの方法（1）で作製されたリング状のZnパターンのせん断応力顕微鏡像を示す[8]。この図中の矢印で示した部分の細線パターンの幅は20 nmである。従来、同じ光源からの伝搬光を用いて光CVDにより得られたZnパターンの最小幅は2～3 μmなので[9]、図3中のパターンの幅はこの1/100以下である。

次に方法（2）について記す。図4(a),(b)は作製されたドット状のZnパターンのせん断応力顕微鏡像及びその断面を示している。実験はガス圧約1 m TorrのDEZ中にて行われた。10 mWのAr+レーザSH光をプローブ後端に照射し、プローブ先端に発生する近接場光を基板に数秒間照射した。また、光照射は800nm間隔に5箇所に対して行った（図4(a)矢印部）。図4(a)に示すように光照射部のみに堆積されたZnを確認することができた。また、図4(b)に示すように、これらのドットの幅（半値全幅）は約155 nmであった。なお、ここでは堆積用のプローブを再び用いてせん断応力顕微鏡像を観察した。ただし、このプローブはせん断応力顕微鏡像の観察のためには必ずしも高い分解能を与えるものではないので、図4中のドットの幅は真値よりもかなり大きくなっていると考えられる。真値の推定は今後の課題である。

一方、ドットの高さは照射時間に依存し、1～6 nmであった。ドットの間隔は約800 nmであり、これは光を照射した位置とほぼ一致しており、本方法がナノメートル寸法のドットの作製の際に高い位置精度を持つことを示している。

図5には方法（2）により作製されたT字細線状のZnのせん断応力顕微鏡像を示している。実験はガス圧約5 m TorrのDEZ中で行われた。プローブ後端にSH光を3 mW照射し、先端に発生した近接場光を照射しながら基板を10～50nm/s

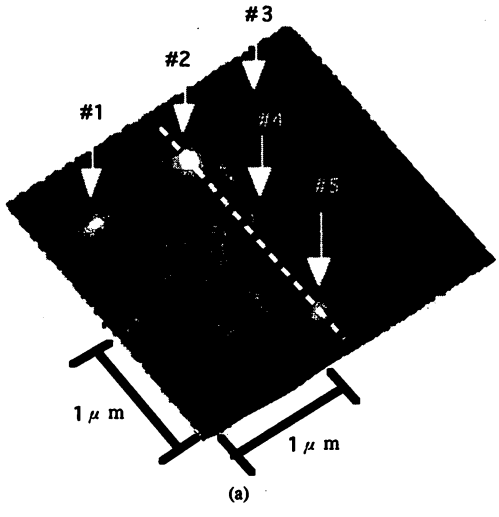

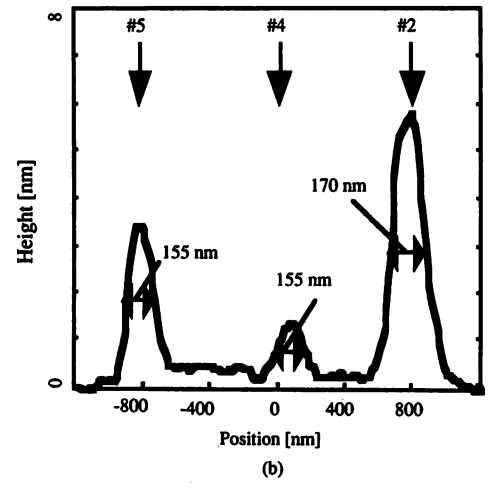

図4．方法（2）により作製されたドット状のZnパターンのせん断応力顕微鏡像とその断面図.

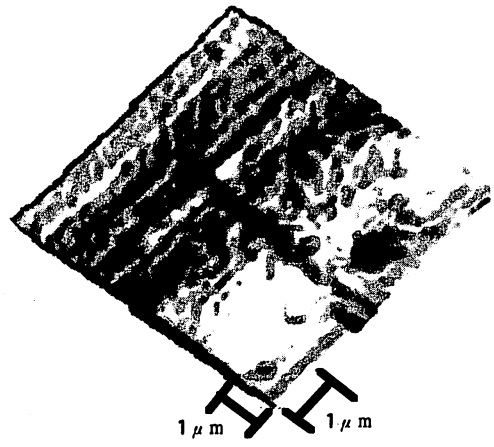

図5．方法（2）により作製されたT字細線状のZnパターンのせん断応力顕微鏡像.

の速度で走査することによりT字細線状のZnパターンを作製した[10]。このパターンの幅(半値全幅)は約200 nm、高さは16 nmである。測定したパターンの寸法には図4の場合と同様、プローブの形状によって決まるせん断顕微鏡の分解能も含まれているので、より高い分解能の測定をすれば、さらに狭い幅となるはずである。

以上の方法（1）、（2）によればZnのみではなく、Al, Cr, Wなどの金属や酸化物[11]および化合物半導体[12]のナノメートル寸法の堆積も可能であると推察されている。

4. 作製されたパターン形状の近接場光エネルギー（堆積時間）依存性

次に方法（2）による堆積の光エネルギー依存性について説明する。実験としてはDEZガス圧力、Ar^+レーザのSH光パワーは各々1 mTorr, 15 mWの一定値とし、照射時間

を変化させ、ドット状のZnパターンを作製した。プローブの先端でのSH光パワーは先端より数mm離れた地点において大受光面積Siフォトダイオード（受光面積5x5 mm^2）で測定した結果、300nWであり、近接場光エネルギーはこの測定された光パワー×照射時間とした。図6(a)は堆積されたドット状パターンのせん断応力顕微鏡像を示している。①,②,③,④のドットは近接場光エネルギーをそれぞれ0.3、0.6、1.5、3.0[μ J]（照射時間：1s,2s,5s,10s）として作製したものである。また、⑤のドットは堆積中、SH光入射強度が大きく変動したため、これからの議論からは省く。照射時間と共にドットが成長してゆく様子が確認される。図6(b)は作製されたドットの高さ、幅（半値全幅）の近接場光エネルギー（堆積時間）依存性を示している。半値全幅は、近接場光エネルギーによらず約175 nm程度でほぼ一定である。それに対し、高さは時間と共に5nm/μ Jの割合でほぼ線形に増加する。このことから、基板面内方向の寸法

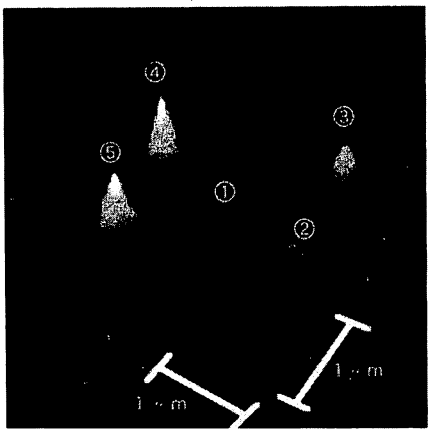

(a)

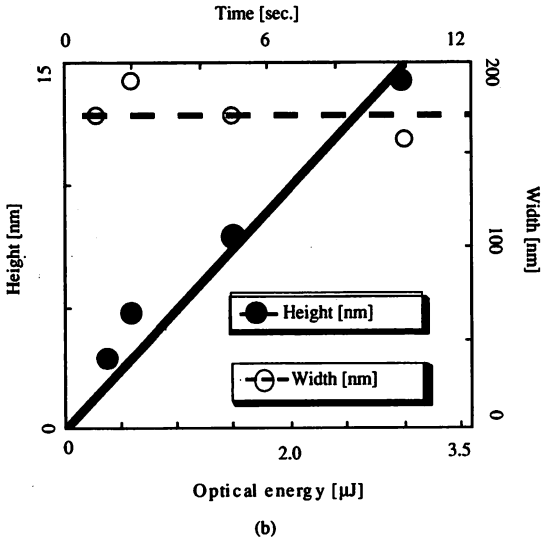

(b)

図6.(a) 方法（2）により作製されたドット状のZnパターンのせん断応力顕微鏡像. (b) その高さと幅の近接場エネルギー（堆積時間）依存性.

は近接場光の空間的分布によって決まり、法線方向には近接場光エネルギーに依存して成長することがわかる。従って、その比、つまりアスペクト比は、0.03/μ Jの割合で近接場光エネルギーと共に線形に増加する。

5. 一層の微細化と作製の再現性の向上の為の検討

本方法の最大の利点の一つは加工の微細性であるが、前節で確認されたように作成されるパターンの基板面内の形状は近接場光の空間的分布によって決まる。つまり、その形状は使用するプローブの性能に強く依存する。従ってその再現性もプローブ作製の再現性により決まる。現在、GeO_2ドープコアファイバーを用いて各用途に合わせた多様なプローブが製作されており、特に高分解能用プローブ[13]が実現し、その作製の再現性も極めて高い。そこで、本方法で用いるプローブの自由度を大きくするため、紫外用ファイバーにGeO_2ドープコアファイバーを接続した物を作製した。作製したプローブのSEM像とその断面構造を図7(a),(b)

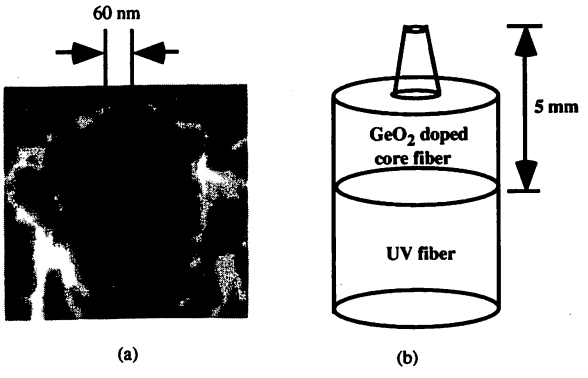

(a) (b)

図7.(a) 紫外用ファイバーにGeO_2ドープコアファイバーを接続して作製された開口60 nmのプローブのSEM像. (b) 断面構造図.

に示す。このプローブの開口作製には集束イオンビーム装置が使えるので、微小開口を再現性良く得ることができ、その寸法の制御も容易に行える。図8(a),(b)は図7のプローブにより堆積したドット状のZnのせん断応力顕微鏡像、及び破線部の断面図を示している。実験は、DEZガス圧1 mTorr、Ar^+レーザのSH光パワー3 mWで、また、堆積時間は300 sで行われた。更に基板とサンプル間の距離等にも注意を払いながら堆積を行った結果、半値全幅60 nm、70 nmの2つのドットを100 nmと非常に近接した位置に作製することに成功した。作製されたドットの半値全幅は使用したプローブの開口径にほぼ一致している。これはプローブの開口径をさらに小さくすることにより作製されるパターンの寸法も小さくなることを示している。また、観測されたパターンの寸法にはプローブ先端の形状に依存される分解能も含まれているため、より高分解能な測定を行うことにより更に微少な像を得ることが出来る。今後、同様の方法でさ

らに高分解能の紫外用プローブを作製することにより、一層微小な構造をもつ微小物質の作製が可能となると期待される。

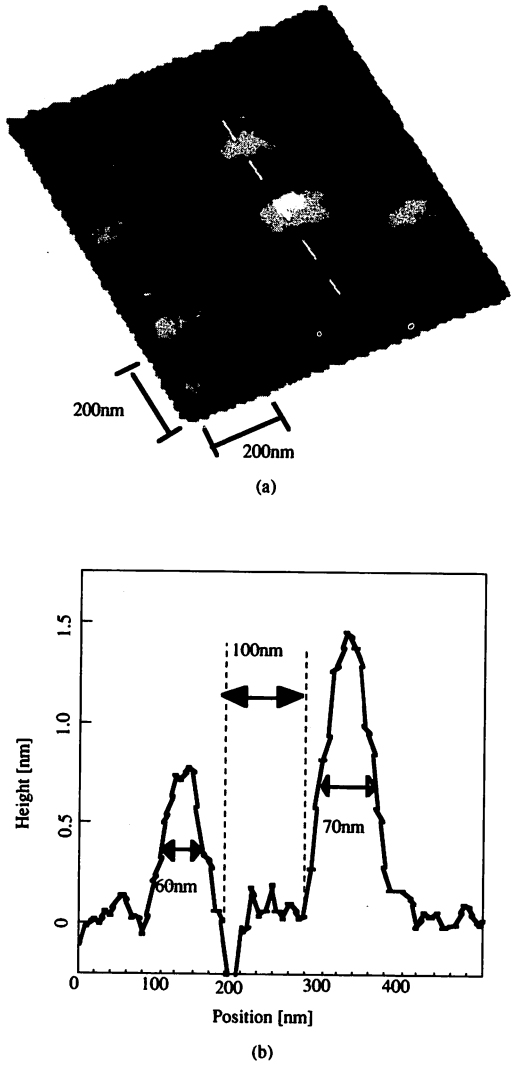

図8. (a) 図7のプローブにより作製されたドット状のZnパターンのせん断応力顕微鏡像. (b) その断面図.

6. むすび

本稿では近接場光を用いたナノメートル寸法の物質の堆積の原理と現状について概説した。プローブ先端からしみ出す近接場光を用いてナノ構造の作製が可能になり、光機能素子の開発、さらに量子サイズ効果を有するナノ構造で構成される未来のナノフォトニクス用デバイスの実現に適した手法であることを示した。

さらにナノ構造の作製と同時にその場で作製された構造の光物性が測定ができ、実験結果により物理的な直感で訴える新しい理論モデルの開発にも期待できる。

謝　辞

光CVDに関してご指導賜った、東京工業大学工学部小長井誠教授、山田明助教授、さらに有用なご討論を賜った東京工業大学大学院総合理工学研究科福田浩章氏、V. Polonski氏に感謝します。

(平成11年8月10日受付)

文　献

(1) M. Ohtsu, Near-Field Nano/Atom Optics and Technology, Springer, Tokyo, 1998.
(2) M. Ohtsu, "Progress of high-Resolution Photon Scanning Tunneling Microscopy Due to a Nanometric Fiber Probe", J. Lightwave Tech. 13, pp 1200~1221, 1995.
(3) E. Maayan, O. Kreinin, G. Bahir, J. Salzman, A. Eyal and R. Beserman, "Selective growth of GaAs/InGaP heterostructures by photo-enhanced organometallic chemical vapor deposition", J. Crystal Growth 135, pp 23~30, 1994.
(4) Y. Aoyagi, M. Kanazawa, A. Doi, S. Iwai, and S. Namba, "Characteristics of laser metalorganic vapor-phase epitaxy in GaAs", J. Appl. Phys. 60, pp 3131~3135, 1986.
(5) D. Bauerle, "Laser-chemical processing: recent developments", Appl. Surf. Sci. 106, pp 1~10, 1996.
(6) S. Mononobe, T. Saiki, T. Suzuki, S. Koshihara and M. Ohtsu, "Fabrication of a triple tapered probe for near-field optical spectroscopy in UV region based on selective etching of a multistep index fiber", Opt. Commun. 146, 45 (1998).
(7) R. Wiesendanger, "Fabrication of nanometer structures using STM", Appl. Surf. Sci. 54, pp 271~277, 1992.
(8) V. Polonski, Y. Yamamoto, M. Kourogi, and M. Ohtsu, "Nanometric patterning of zinc by optical near field photochemical vapor deposition", J. Microscopy 194, pp 545 ~ 551, 1999.
(9) D. J. Ehrlich, R. M. Osgood, Jr., and T.F. Deutsch, "Spatially delineated growth of metal films via photochemical prenucleation", Appl. Phys. Lett. 38, pp 946~948, 1981.
(10) 山本　洋, V. Polonski, 李　謹炯, 興梠元伸, 大津元一, "近接場光による化学気相堆積法 (Znの堆積)", 1998年秋季第59回応用物理学会学術講演会、15 pD 12 (1998).
(11) K. Tokita, F. Okada, "Growth of metal oxide thin films by laser-induced metalorganic chemical vapor deposition", J. Appl. Phys. 80, 1996.
(12) A. Toda, F. Nakamura, K. Yanashima, A. Ishibashi, "Blue-green laser diode grown by photo-assisted MOCVD", J. Crystal Growth 170, pp 461~466, 1997.
(13) S. Mononobe, et al.,"Development of a fiber used for fabricating application oriented near-field optical probes", IEEE Photonics Technol. Lett. 10, p 99, 1998.

李　謹炯　(非会員) 1987年韓国延世大学金属工学科卒業。1990年同大学大学院金属工学科修士課程修了。1998年東京工業大学大学院総合理工学研究科博士課程修了。1998年科学技術振興事業団創造科学技術推進事業大津局在フォトンプロジェクト研究員になり、現在に至る。近接場光による原子レベルでの堆積・表面処理・結晶成長・原子操作に関する研究に従事。

山本　洋　(非会員) 1996年早稲田大学電気工学科卒業。1998年東京工業大学大学院総合理工学研究科電子システム専攻修士課程修了。1998年東京工業大学大学院総合理工学研究科電子システム博士課程に入学し、現在に至る。近接場光による原子レベルでの堆積・結晶成長に関する研究に従事。

興梠　元伸　（非会員）1987年静岡大学工学部卒.1992年東京工業大学大学院総合理工学研究科物理情報後期博士課程修了。同年同大学助手現在に至る。レーザ制御、近接場光学の研究に従事。

大津　元一　（正員）1973年東京工業大学工学部卒。1978年同大学院総合理工学研究科博士課程修了。同年同大学助手、1982年助教授、1991年教授、現在に至る。この間、1986~87年、東工大休職、AT&Tベル研究所研究員。1998年より科学技術振興事業団創造科学技術推進事業大津局在フォトンプロジェクト統括責任者。近接場光に関する研究に従事。